

The  
University  
Of  
Sheffield.

Department  
Of  
Mechanical  
Engineering

# Low Maintenance Bearings for Aircraft Landing Gear

Peter Krier

---

Thesis submitted for the Degree of Doctor of Philosophy

Department of Mechanical Engineering

The University of Sheffield

October 2016

---



## Abstract

Pin joints are utilised in many engineering structures, where movement is required between two components. Typically the joint consists of a shaft rotating through a limited range of motion between the two components, within a bush or set of bushes. Grease lubrication is often incorporated to minimise and ideally prevent direct metal to metal contact. However very seldom is separation achieved, and therefore wear and friction occur. In an aircraft landing gear application, pin joints are widely utilised in the extension retraction mechanism. The replacement of these lubricated metallic bushes with a lightweight polymer alternative could not only lead to reduced maintenance and expensive overhaul of components, but also brings significant weight savings and hence increases in aircraft efficiency from a reduction in fuel burn.

A bespoke radial load test rig has been designed and manufactured to simulate the loading conditions imposed upon a pin joint, located in the bracing strut of an aircraft landing gear extension retraction mechanism, as the aircraft manoeuvres on the ground. Four self-lubricating polymer composite materials were tested for three aircraft lives and an assessment of the wear and deformation occurring as a result.

The co-efficient of friction was evaluated for the four self-lubricating materials and also the current technology in both the lubricated and unlubricated states. The re-lubrication interval was also investigated. The effect of the articulation angle on the co-efficient of friction was investigated for the lubricated and self-lubricating materials.

A load displacement model was developed to predict the displacement and contact angle of polymer composite materials under an applied radial load and was experimentally validated. The model uses only geometrical and material parameters, and was shown to be more accurate at higher loads than the current models used.

[Blank Page]

## Contents

Abstract

Contents

Nomenclature

Acknowledgements

<b>1. Introduction</b> .....	<b>1</b>
1.1. Statement of the Problem .....	2
1.2. Aims and Objectives.....	4
1.3. Statement of Novelty.....	5
1.3. Layout of the Thesis .....	6
<b>2. Background</b> .....	<b>7</b>
2.1. Landing Gear .....	8
2.1.1. Pin Joints in Landing Gear .....	9
2.2. Lubrication Regimes.....	12
2.2.1. Boundary Lubrication.....	12
2.2.1.1. Tribology of Dry Sliding.....	13
2.2.1.2. Polymer Bearings .....	15
2.2.2. Mixed Lubrication .....	18
2.2.2.1. Lubrication in a Landing Gear Application.....	18
2.2.2.2. Grease Lubrication.....	19
2.2.2.3. Design of Lubricated Bearings .....	21
2.3. Performance of the Pin Joint .....	22
2.4. Conformal Contact.....	24
2.5. Material Selection for Pin Joints .....	28
2.5.1. Viscoelasticity .....	28
2.6. Conclusion.....	30
<b>3. Experimental Techniques</b> .....	<b>33</b>
3.1. Loading of a Landing Gear Pin Joint.....	34
3.2. Pin Joint Radial Load Tester .....	34

3.2.1. Loading Clevis.....	35
3.2.2. Single Axis Test Frame .....	36
3.2.3. Instrumentation .....	37
3.2.3.1. Load cells – Structure and Configuration.....	37
3.2.3.2. Instrumented Load Pin.....	38
3.2.3.3. LVDT Structure and Configuration .....	43
3.2.4. Servo Valves and PID Control.....	44
3.2.5. Specimen Temperature and Humidity.....	49
3.2.6. Fitting and Removal of Bearings .....	50
3.2.7. Loading Conditions .....	51
3.3. Pin Joint Function Tester.....	53
3.3.1. Loading Clevis.....	54
3.3.2. Bi-axial Test Frame.....	55
3.3.3. Instrumentation .....	56
3.3.4. Sample Raw Results .....	58
3.3.5. Loading Conditions .....	60
3.3.6. Test Specimens .....	61
3.3.7. Procedure .....	61
3.4. Conclusion.....	62
<b>4. Characterisation of Specimens .....</b>	<b>63</b>
4.1. Specimens .....	64
4.2. Surface Roughness of Bushes .....	67
4.2.1 Pin Characteristics.....	69
4.3. Mass of Bushes .....	70
4.4. Deviation from Roundness Plots.....	71
4.5. Conclusion.....	73
<b>5. Static Deformation of a Radially Loaded Pin Joint.....</b>	<b>75</b>
5.1. Theoretical Modelling of Displacement .....	76
5.2. Static Deformation.....	85

5.3. Experimental Validation .....	86
5.3.1. Aircraft Geometry .....	88
5.3.1.1. Maximum Static Displacements .....	91
5.4 Conclusion .....	91
<b>6. Wear of a Radially Loaded Pin Joint .....</b>	<b>93</b>
6.1. Dynamic Load Testing and Wear .....	94
6.2. Talyrond Roundness.....	97
6.3. Visual Inspection .....	112
6.3.1. Failure of Vespel 21 Flange .....	123
6.4. Size of Contact .....	125
6.5. Conclusion.....	130
<b>7. Articulation of a Pin Joint.....</b>	<b>133</b>
7.1. Lubrication Performance in an Oscillating Journal Bearing.....	134
7.2. Dry Contact .....	134
7.3. Lubricated Contact.....	136
7.4. Effect of Lubricants on the Contact .....	138
7.5. Effect of Articulation on Re-lubrication Interval.....	139
7.5.1. Aerospace Grade Grease .....	140
7.5.2. General Purpose Grease .....	142
7.5.3. Number of Cycles.....	146
7.6. Self-lubricating Bushes.....	147
7.6.1 Co-efficient of Friction Comparison.....	149
7.7. Commercial Self-lubricating Bushes .....	150
7.7.1. Angle of Articulation .....	153
7.7.2. Assessment of Wear and Dimensional Change .....	154
7.8. Conclusion.....	161
<b>8. Conclusions and Recommendations .....</b>	<b>163</b>
8.1. Wear Performance of Self-lubricating Bearings .....	164
8.2. Load Displacement Model .....	166

8.2.1. Experimental Validation.....	167
8.3. Effect of Articulation Angle on COF .....	168
8.4. COF for Reciprocating Journal Bearings.....	169
8.5. Metrology of Self-Lubricating Bushes.....	170
8.6. Summary of Materials Tested.....	170
8.7. Future Work.....	172
<b>References .....</b>	<b>175</b>
<b>Appendix</b>	
Appendix A – Material Data Sheets	
Appendix B – Radially Loaded Pin Joint	
Appendix C – Grease Lubricated Testing	

## Nomenclature

A	Contact area
b	Half contact width
bl	Bush length
bt	Bush thickness
$D_1$	Diameter of pin
$E_1$	Elastic Modulus of pin
$E_2$	Elastic Modulus of bush
$E^*$	Modified Elastic Modulus
e	Eccentricity
F	Applied load
f	Reciprocal frequency
H	Hersey Number
h	Height of arced portion
lo	Original length
$P$	Mean contact pressure
$P'$	Load per unit length
$R_a$	Arithmetic surface roughness (2D)
$R_b$	Internal radius of the bush
$R_p$	External radius of the pin
$R_q$	Root mean squared surface roughness (2D)
$R'$	Reduced radius
$\Delta R$	radial clearance
S	Sliding distance
$S_a$	Arithmetic surface roughness (3D)
$S_q$	Root mean squared surface roughness (3D)
$S_{sk}$	Skewness of surface roughness (3D)
U	Sliding velocity
V	Volume of wear debris removed
$V_1$	Poisson's ratio of pin

$V_2$	Poisson's ratio of bush
$K$	Dimensionless wear constant
$X_{bm}$	calculated contact width
$\delta$	Shaft Displacement
$\gamma$	Half arc of contact
$\eta$	Lubricant Viscosity
$\omega$	Angular Velocity
$\theta$	Angle of articulation
$\mu$	Co-efficient of friction
$\Phi$	Angle of pin rotation

## Acknowledgements

The author would like to thank Prof. Rob Dwyer-Joyce for his help, support and guidance throughout this project. The experience and knowledge in tribology research and research in general will benefit him a lifetime. Without him the completion of this thesis would not have been possible.

Thanks are also extended to Airbus UK for the financial support, and to DuPont, GGB Bearing Technology, Kamatics RWG, and Saint-Gobain for their co-operation and involvement with the project.

Thanks to Mr. David Butcher, Mr. Luke Callaghan and Mr. Richard Kay for their technical assistance. Thanks are also extended to Mr. Mike Rennison for the invaluable knowledge in mechanical testing and servo-hydraulics.

The author would like to thank the group in the Lea Lab for all their support and in creating a positive environment for working and testing in, a time that will never be forgotten. Thanks to Dr. Christopher Hardwick, Dr. Thomas Howard, Dr. Stephen Lewis, Dr. Robin Mills, Dr. Pedrom Tayefi, Dr. Richie Louks, Hugh Price, Mike Hayward, Andy Cartledge and Adam Cox for all the help and support. Thanks also to Dr. Paniel Reyes for celebrating and encouraging the author when the opportunity was accepted.

Finally the author would like to thank his parents and his soon to be wife Miss Ellen Ashbourne, to whom this thesis is dedicated, for the continued encouragement throughout.

[Blank Page]

# 1.

## Introduction

In this chapter a background to the growth of air travel is given along with some of the ways in which to improve aircraft efficiency. A brief introduction to aircraft landing gear and some of the developments made in design that have reduced weight and enabled the industry to continue growing are also presented. An introduction to the problem of landing gear joints is given, along with the projects main aims and objectives.

## 1.1 Statement of the Problem

Air travel has rapidly become the preferred method of fast transportation (Lee et al, 2001). It is predicted that approximately twice the number of aircrafts will have to be manufactured by 2033 (Airbus, 2000; Boeing, 2014) to both replace existing aircrafts and to meet the growing demand. This coupled with the increasing cost of fuel (Airbus, 2008; Cranfield University, 2010; Dillingham, 2014) and growing environmental pressures (Lee et al., 2001) means that the efficiency of the aircraft must continue to increase (Airbus, 2008). Emissions are typically controlled by engine design, but improvements in fuel efficiency can also be used to reduce them (Lee et al., 2001). Reducing fuel burn and therefore increasing efficiency can be achieved in a variety of ways, one of which is to reduce the weight of the aircraft (Airbus, 2008). Landing gear typically accounts for 3 to 6% of the aircraft maximum take-off weight (Krüger, 2001), approximately 10 tonnes (Airbus, 2005), this can often be seen as a deadweight which impairs flight performance (Krauss, 1995; Raymer, 1999), therefore any weight reductions on the landing gear would lead to significant savings in terms of fuel burn.

The difficulty is that although the landing gear is not utilised while the aircraft is in the air, it is still a safety critical component (Krüger, 2001), and cannot yet be removed. In 1903, when wheeled landing gear was first attached to Santos Dumont's "No. 14 bis", (Curry, 1988) it was of a much simpler form: a rigid external structure. Just under 30 years after its introduction retractable landing gear was developed in attempts to reduce aerodynamic drag (Krüger, 2001). By 1939 retractable landing gear had become common on many fighter aircrafts (Curry, 1988). A common design had been settled on during the fifties, with two or more main gears and a steerable nose gear (Curry, 1988; Krüger, 2001; Vincenti, 1994). Figure 1.1 shows a labelled schematic diagram of one of the typical retractable main gears which is fitted to many aircraft in operation today (Raymer, 1999).

Landing gear such as this typically consists of a bogie (axel beam) which the wheels are connected to, an oleo (shock absorber), bracing between the airframe and the oleo to prevent lateral movement of the gear. An extension retraction actuator to move the gear, and a down lock to hold the gear in the extended position.

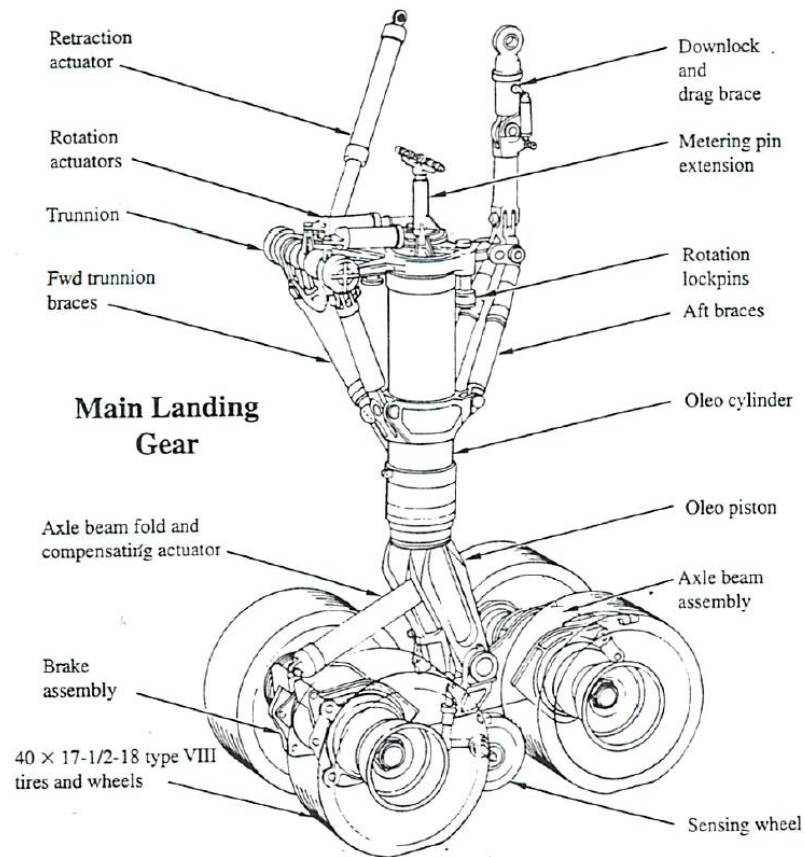


Figure 1.1: Typical multi wheel main landing gear.

Pin joints, a shaft rotating through a limited range of motion within a set of bushes, are widely utilised in the extension retraction mechanism of landing gear (McCarthy, Haines, & Newley, 1994). This is to avoid it disrupting the structure of the airframe if fully retracted or affecting the aerodynamic properties if left partly exposed to the slipstream (Curry, 1988; Raymer, 1999). At present the joints typically consist of a chrome plated steel pin and aluminium bronze bushes or a stainless steel pin (17-4PH) and aluminium nickel bronze bushes, both types are lubricated with aircraft grease (Curry, 1988). Lubrication intervals are left to the discretion of the airline but are typically between 500 to 700 hours. Although it was reported that one airline lubricates critical joints every 24 hours (Curry, 1988).

The replacement of these lubricated metallic bushes with a lightweight polymer alternative could lead to significant weight savings with approximately 80 joints on aircraft landing gear, which when translated into a potential saving of fuel this becomes 3.4 kilograms (Airbus, 2008). With the price of jet fuel set to continue quadrupling every 9 years (Dillingham, 2014), airline operators could save in excess of \$3,500 per aircraft per year on material change

alone. Additional savings could also be realised from a reduction in both lubricants, and maintenance which is the 3<sup>rd</sup> largest cost after fuel and pilot's salaries (Lee et al., 2001).

However the application of composites to landing gear is not an easy task, and is one that is breaking new ground in terms of strength and safety (McCarthy et al., 1994). The joints must be able to cope with a wide range of demanding conditions over the 20 year life of the aircraft, or at the very least until a scheduled overhaul of the landing gear. This research project was intended to investigate the feasibility of some aviation approved self-lubricating bushing materials, under realistic loading conditions.

## 1.2 Aims and Objectives

The aim of this thesis is to investigate the performance of alternative materials in the application of aircraft landing gear joints in both dynamic radially loaded and oscillatory motion:

- Investigate the wear performance of self-lubricating bearings under fatigue style loading.
- Develop a model to predict displacement and arc of contact of self-lubricating polymer bushes accounting for bush thickness.
- Verify the model with experimentation to determine the displacement and contact size.
- Conduct experimentation to investigate the effects of the articulation angle in both lubricated and self-lubricating contacts.
- Evaluate the co-efficient of friction of commercial self-lubricating bearings and compare to the current technology.

### 1.3 Statement of Novelty

The work presented here aims to address the development of a contact model for polymer composite bearings with significant elastic dissimilarity between the Young's Modulus  $E$  for the bush material and the shaft material. The two current models commonly used for the contact of conformal cylinders give some consideration to the difference in elasticity however this is generally applicable for bush materials such as Aluminium Bronze running against a steel shaft, which has a small difference in elasticity compared to that of a polymer composite bushing against a steel shaft. Additionally the thickness of the bush material has often been neglected, with the normal assumption that it is infinite.

The second body of work investigates the micro slip and wear between several commercial polymer composite bushes radially loaded against a steel aircraft landing gear pin in a cyclic load application. To the best of the author's knowledge no work has been conducted focusing on the micro slip and wear between the bushing and shaft of self-lubricating materials, where no oscillatory motion between the bush and shaft is present, especially under a cyclic radial load.

While some research and experimentation has been conducted on reciprocating oscillatory journal bearings some areas have been left untouched, such as the effect of the articulation angle on the COF for both grease lubricated journal bearings and the state of the art self-lubricating materials. Therefore the third body of work investigates the COF in a reciprocating oscillatory motion for both the grease lubricated bearings and the self-lubricating cases to investigate the feasibility of replacing grease lubricated bearings with self-lubricating ones in an aircraft landing gear application.

## 1.4 Layout of the Thesis

In Chapter 2 the background information about aircraft landing gear and the application of pin joints within it is presented, along with the boundary and mixed lubrication regimes and the commonly used conformal contact models.

Chapter 3 describes the experimental equipment used in this thesis and how it was applied to test self-lubricating bushes in both a dynamic radially loaded application and also a reciprocating oscillatory motion. Chapter 4 identifies the self-lubricating bushes to be tested and their geometrical and material properties, along with how they have been measured.

Chapter 5 presents the results from a static radially loaded pin joint with elastically dissimilar materials. A model for conformal contact of a steel pin against a polymer bush is developed using only geometrical and material parameters.

Chapter 6 investigates the dynamic testing of the joint and presents the measurement of wear and deformation occurring. The arc of contact is also investigated using the model developed, experimental results and is compared to Persson's model.

Chapter 7 deals with the results from testing the bushes in a reciprocating oscillatory manner, where the COF is determined for the current technology and also the state of the art bushes identified in Chapter 4. Investigations into the effect of the articulation angle for both grease lubricated and self-lubricating contacts along with the re-lubrication interval are conducted.

Chapter 8 is a discussion addressing the performance of the materials tested in both methods, and the conclusions that can be drawn from the investigation. Recommendations for further work in the area are also presented.

# 2.

## Background

In this chapter background information is given on aircraft landing gear and the application of pin joints. The boundary and mixed lubrication regimes are presented along with the developments made with regards to self-lubricating materials for bearing applications, and a review of the work regarding oscillating journal bearings. The current models for conformal contact of a pin joint are also discussed.

## 2.1. Landing Gear

Aircraft Landing gear is primarily required to absorb the vertical energy of the touchdown (McCarthy et al. 1994; Krüger 2001), typically at a speed of 3.05 m/s (Krüger 2001), and provide a comfortable ride for both passengers and crew (Kirk 1973; Krüger 2001). This can be challenging when landing on rough runways (Krüger 2001; McCarthy et al. 1994) and even more so for military aircraft which are occasionally required to land on bare soil (Curry 1988). Much research has been conducted into changing the damping properties of the oleo, to provide both a smooth ride, and absorption of the vertical energy (Krüger 2001).

The secondary requirements are to do with ground handling, which also put a very different but demanding set of loading conditions on the landing gear. The main gear is required to hold 85% to 92% of the aircrafts weight (Krüger 2001), while the nose gear is subjected to towing and push back operations which can cause nose gear collapse (Hinson 1993; Aarrass et al 2008). Additionally braking and turning forces (Krüger 2001; McCarthy et al. 1994) are developed.

Runway roughness has recently received more attention, as aircraft are becoming larger and more flexible therefore reducing the fatigue life of the entire aircraft (Curry 1988). Detailed analysis of runways is not given here, but it should be noted that it has been studied by other authors. Fabre et al. (2004) conducted an experimental investigation comparing the effects of different bogies on the runway. Zhejun (1987) highlights modifications that can be made to the oleo for landing on rough and bomb damaged runways. Krüger (2001) presents data of two typically rough runways to enable improvements of passenger and pilot comfort.

Other sources of vibrations and oscillations have been identified by numerous authors, and further researched to determine how to minimise them. Vibrations and oscillations in the cabin can be caused by, wheelbase length, gear position (Silsby 1962), gear walk (Denti & Fanteria 1995), nose wheel shimmy (Depei 1989), brake squeal (Biehl 1983; Krabacher 1995) and tyre size and pressure (Raymer 1999). While fuselage vibration control techniques such as semi-active front gear may make the ride more comfortable for the crew and passengers (Wentscher et al. 1995), landing gear components such as the side braces must still be able to withstand the loads imposed upon them.

Taxiing induced vibrations caused by runway and taxiway unevenness have been found to be a significant factor in the fatigue of aircrafts (Kirk 1973). Paved runways are made from

many individual concrete sections joined with rubber. As the runway ages the sections settle unevenly resulting in a rough runway (Wentscher et al. 1995).

The tertiary requirement of the landing gear is such that it must be retractable in order for it not to affect aerodynamic principles and reduce aircraft efficiency. However the gear must fit into a small space that that has been predefined by the airframe engineers in order to maximise the cargo carrying capacity of the aircraft (Raymer 1999; Krauss 1995).

The use of pin joints fulfils the requirement of the landing gear to not only meet the demands mentioned above, but also allows the gear to be stowed in a restricted space typically, through means of folding, shortening (McCarthy et al. 1994) and rotating bogies as the gear is retracted (Curry 1988). Braces such as the side brace are used to minimise the lateral and braking loads exerted on the oleo (Raymer 1999) and therefore are subjected to tensile and compressive loads as the gear tries to deflect laterally, and hence any joints must be able to support all the loads mentioned above.

### 2.1.1. Pin Joints in Landing Gear

The joint investigated in this study is located on the drag stay brace of the Nose Landing Gear (NLG) for a narrow bodied aircraft. The joint is one that experiences relatively low loads in comparison to those on the Main Landing Gear (MLG), as the NLG typically only carries 6-20% of the aircraft weight when on the ground (Curry 1988). The location of the joint is shown in Figure 2.1, (Airbus 2005).

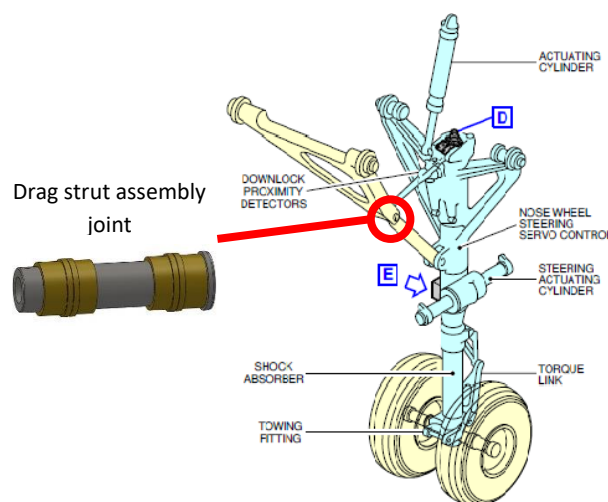


Figure 2.1: Location of the Drag Strut Assembly Joint on the Nose Landing Gear

The pin is of hollow chrome plated steel construction, 42 mm OD, 30 mm ID, and 175 mm long, and is constrained using a cross bolt to prevent lateral pin movement and rotation. The pin slides against Aluminium Bronze bushes to prevent the likelihood of galling (Curry 1988), they typically contain circumferential H grooves machined internally for the distribution of grease.

The joint is part of the extension retraction mechanism, and therefore operates only through a limited range of motion. The speed of the extension retraction system typically occurs at 12 deg/sec, however this varies slightly for each type of aircraft (Curry 1988). Under emergency conditions faster deployment may be required (Curry 1988). The location of the joint is highlighted in both the extended (solid circle) and retracted (dashed circle) positions in the schematic below (Airbus n.d.).

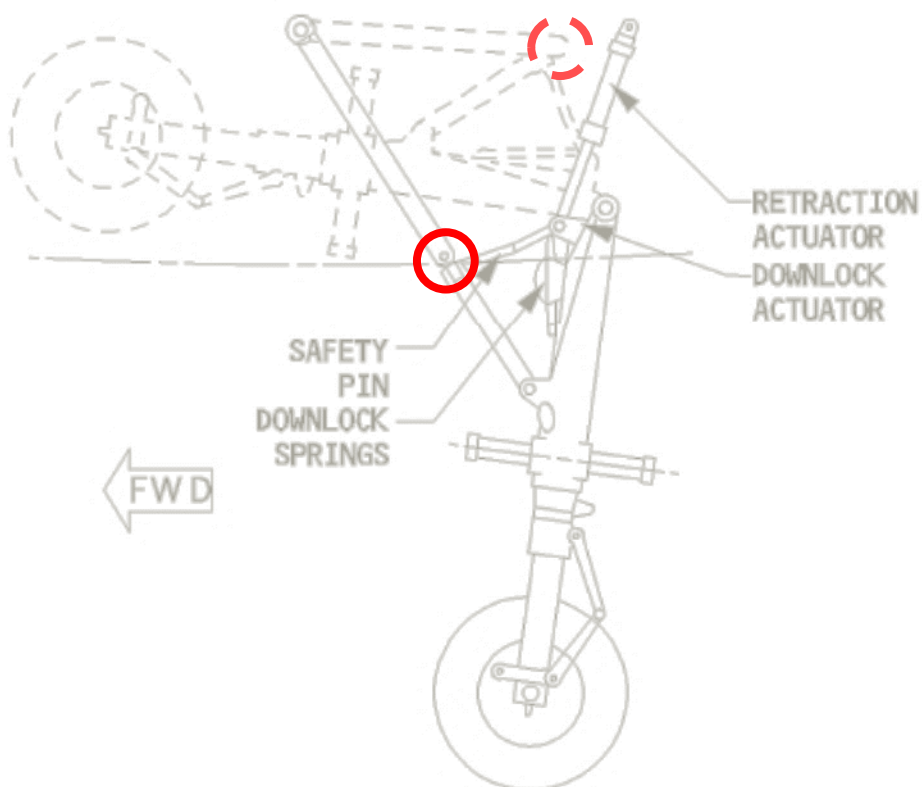


Figure 2.2: Location of the joint in the extended and retracted positions

Airline operators have indicated that a higher initial cost of aircraft may be offset by a reduction in operating costs (Lee et al. 2001; Krüger 2001), therefore landing gear manufacturers are considering the use of polymer composites in designs, to the extent of replacing entire components (McCarthy et al. 1994). Assessments envisage the potential for a 30% to 40% weight saving through the use of composites (Lee et al. 2001; Curry 1988). Weight is of great concern in aircrafts, a reduction of 100 kg can save between \$3500 and \$6500 per year on a single aircraft (Airbus 2008). Airline operators have already realized the potential savings resulting from weight reductions, and as a result manufacturers have seen increased orders for new more fuel efficient models (Dillingham 2014). For some applications such as polymer composite bearings, additional benefits such as reduced maintenance can also be offered. If this can be provided at a reasonable acquisition cost, landing gear manufacturers will still be able to maintain their competitive advantage (Krüger 2001; McCarthy et al. 1994). This then brings with it the savings associated with removing the aircraft grease itself. Finally consideration should be given to the weight of the grease, excessive greasing would not only be a waste of grease but it would also remain on the aircraft, and add to the weight. Therefore the potential of self-lubricating polymer composites for bearing materials in aircraft landing gear is one that offers great rewards.

## 2.2. Lubrication Regimes

For lubricated journal bearings, a Stribeck-Hersey curve is used to assess the lubrication performance, over a range of conditions. A typical Stribeck curve is shown in Figure 2.3 where the COF is plotted against the Hersey number, a non-dimensional parameter.

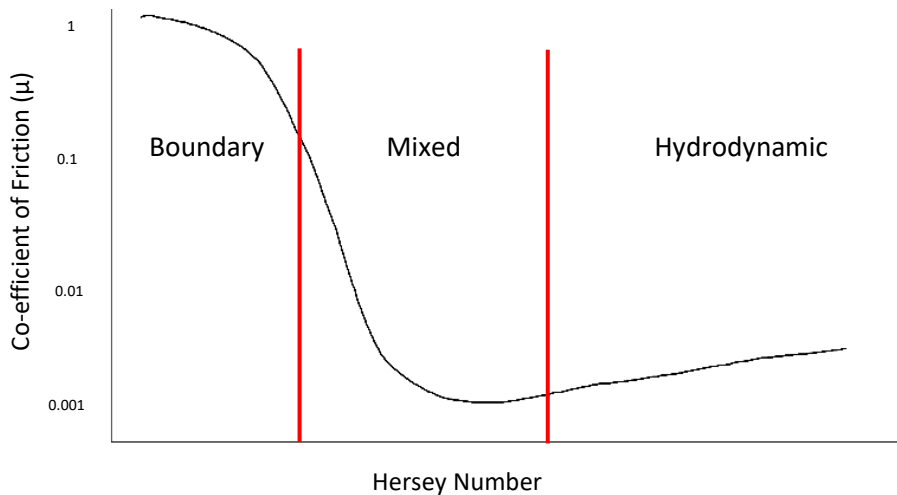


Figure 2.3: Stribeck-Hersey Curve

The Hersey number is defined as

$$H \equiv \frac{\eta\omega}{p} \quad (2.1)$$

Where  $P$  is the mean contact pressure,  $\omega$  is the angular velocity of the pin, and  $\eta$  is the lubricant viscosity. The Stribeck curve, can typically be split into three regions, boundary, mixed and Hydrodynamic Lubrication.

### 2.2.1. Boundary Lubrication

The boundary regime of the Stribeck diagram occurs when asperity to asperity contact dominates, there is insufficient pressure to separate the surfaces as a result of either low relative sliding speeds, or high loads. In these circumstances self-lubricating or dry bearing materials show significant advantages up to approximately 10m/s (Lancaster 1972b) without damaging the metallic mating surface (Holligan 1968). Self-lubricating bearings are becoming increasingly popular in the engineering world, they are generally used where:

- Oscillatory motion is present, which prevents the generation of a hydrodynamic oil film e.g. construction equipment (Strand 2005),

- Environments are hostile e.g. space (Briscoe 1990),
- The use of lubricants is prohibited e.g. food industry (Unal & Mimaroglu 2003),
- The provision of lubrication systems becomes too complex or inconvenient to provide e.g. aircrafts (Holligan 1968).

The Engineering Sciences Data Unit (ESDU) conducted a large amount of work on dry rubbing bearings (ESDU 87007 2010). Included was an attempt to summarise a characteristic Pressure Velocity PV curve for current self-lubricating bearing technologies (Lancaster 1972b). This is a useful parameter for comparing dry bearing performance which is the product of the pressure and rubbing velocity PV (Pinchbeck 1961; Holligan 1968). The maximum pressure is generally limited by the strength or creep resistance of the material, while the velocity is generally constrained by the maximum operating temperature that the bearing can withstand (Evans 1981). It has been well established over the years that an increase in PV also results in an increase in bearing temperature (Holligan 1968; Pinchbeck 1961), so care should be taken when considering PV limits.

PV values however are only guidelines, as bearings can be successfully operated outside of the quoted PV limits. Lancaster comments on some limitations of PV especially with regards to thermoplastic bearing materials, bearing size and temperature (Lancaster 1971). There is much criticism of only the PV relationship being used for design purposes (Pinchbeck 1961; Pratt 1973). Hooke et al. (1996) shows that the temperature rise generated by friction is of great significance, and should be considered along with PV. However Holligan (1968) highlights that certain materials have a greater effect as a result of either pressure or velocity and therefore that it can be unreliable for design, and full scale testing is often required.

#### 2.2.1.1. Tribology of Dry Sliding

One of the two mechanisms that is widely acknowledged to contribute to the friction force is the shearing of junctions formed between the two mating surfaces (Quaglioni et al. 2009). This is of great significance in the boundary lubrication regime where significant asperity to asperity contact is occurring.

The friction and wear performance of dry bearings is governed by third bodies in the contact (Play & Godet 1977). For dry rubbing surfaces the less well defined form of the “third body” is generally formed from the compaction of wear debris (Williams 2005). The generation of

the wear debris, occurs through one, or a combination of wear mechanisms such as adhesion, abrasion or erosion.

Therefore in polymer bearing applications where a metallic shaft is commonly used as a counter-face, consideration should be given to the surface roughness. A rough and comparably hard counter face such as steel against a polymer is a classic example for the generation of wear debris through the mechanism of abrasion (Williams 2005). While the development of the transfer film is more prominent where 'rough' metallic surfaces are used (Kennedy et al. 1985), which may seem counterintuitive at first however, the effects on the wear rate must also be taken into consideration which tend to rise significantly (Gay 2013). A large amount of research has been conducted into the tribological behaviour of polymers, and it has been well documented that for polymer metal junctions, a transfer film forms on the metallic face and results in a decrease in friction (Quaglioni et al. 2009). For many self-lubricating dry bearings the third bodies are utilised as a sacrificial layer to generate a protective or lubricating layer (Bahadur 2000) dependent on the contact normal to the sliding direction (Play & Godet 1977).

This reduces the adhesive and ploughing wear mechanisms taking place between the moving surfaces (Fusaro 1990), but only if the transfer film has adhered to the counter face material, otherwise the process is repeated, resulting in wear (Bahadur 2000).

PTFE, an important engineering material is a classic example of this. It known for its low coefficient of friction which is achieved through the transfer of a layer of PTFE to the mating surface (Fusaro 1990) through the adhesion of the two materials, and the shearing of the polymer (Bahadur 2000). This however occurs at the expense of a high wear rate (Biswas & Vijayan 1992), which controls the bearing life (Play & Godet 1977).

For PTFE under sliding with a hard counter face, the PTFE chain undergoes scission and chemically reacts with the counter face to provide a coherent transfer film (Biswas & Vijayan 1992). The sliding velocity of PTFE was shown to have little significance on the wear rate, however an increasing load resulted in a higher wear rate but a decrease in the co-efficient of friction (Unal, Mimaroglu, et al. 2004). An extensive review of the friction and wear of PTFE was conducted by Biswas & Vijayan (1992), where it was concluded that continuous transfer film results in low friction, whereas a non-coherent film is a result of high friction.

Polyoxymethylene (POM) behaves in a similar manner to that of PTFE, generating a relatively thin transfer layer (Bahadur 2000), and greater wear rates than that of other unfilled

polymers Polyamide 6 (PA 6) and Ultra High Molecular Weight polyethylene (UHMWPE) (Unal & Mimaroglu 2003). Unal & Mimaroglu (2003) identified that for PA 6, UHMWPE and POM, all materials were more sensitive to sliding velocity than the applied load in terms of wear, differing from that of PTFE. Wang et al. also confirmed this for UHMWPE (Wang & Li 1999).

Low Density Polyethylene (LDPE), Poly-Propylene (PP) and Nylon 66 however tend to form a relatively thick lumpy film (Bahadur 2000). There is still some disagreement however if Poly-Propylene forms a transfer layer at all (Briscoe & Sinha 2002).

Gay (2013) provides a brief summary of the extensive work conducted by the Laboratoire de Mécanique des Contacts (Laboratory of Contact Mechanics) of the tribological properties of dry sliding materials. Perhaps the most significant piece of work conducted was that of Godet et al (1980) where it was determined that the geometry and motion of the contacting bodies can displace or help to retain the wear debris between the moving surfaces (Williams 2005). This was observed by Play (1985) in the non-uniform distribution of wear debris and the resultant lower co-efficient of friction for an oscillating motion was attributed to it.

### 2.2.1.2. Polymer Bearings

Polymer bearings made their debut in about 1931 with the 'bakelised' bearing (Pinchbeck 1961), since then there has been a growing interest in plastic bearings. There are two types of plastics that can be used for bearings in engineering applications, thermosetting and thermoplastics. Some examples are shown in Table 2.1 (Pinchbeck 1961).

<i>Thermoplastic</i>	<i>Thermosetting</i>
Nylon (Polyamide)	Epoxy
Polycarbonate	Melamine- Formaldehyde
PTFE (Polytetrafluoroethylene)	Phenol- Formaldehyde
Polypropylene	Polyester
Polyvinyl acetal	Urea- Formaldehyde

Table 2.1: Examples of some Thermoplastic and Thermosetting bearing materials

Thermoplastics can be reheated and re-shaped after their initial moulding, whereas thermosetting plastics cannot. This remoulding is as a result of their chemical composition. Thermoplastics have weak forces between the polymer chains, which can easily be broken and reformed upon heating and re-cooling. Thermosetting plastics however form covalent

bonds between the polymer chains resulting in strong cross links (Pfestorf et al. 2000), which means that on the addition of heat the polymer chains themselves will be broken at the same time as the cross link bonds are broken (Thorp 1982).

In order to improve the performance of polymers as bearings, they may either be reinforced or filled to improve their tribological properties. Pure PTFE for example has exceptional frictional properties and performs well under low speeds but high loads, unfortunately it has poor wear resistance in the unfilled state (Holligan 1968). Lancaster (1972b) presents numerically a comparison of Acetal and Epoxy in their natural and reinforced forms for 5 important parameters when considering bearing applications.

The tribological properties of polymer bearing materials such as Polytetrafluoroethylene (PTFE), Polyamide (PA), Polyethylene (PE) in its various forms (LDPE, HDPE, UHMWPE), Polypropylene (PP), Polyoxymethylene (POM) and (PEEK) has been conducted by a number of authors over the years, (Briscoe 1981; Wang & Li 1999; Unal & Mimaroglu 2003; Unal et al. 2004; Unal et al. 2004; Stuart 1998) under a variety of benchtop tests and therefore by no means is an exhaustive list given here.

While other works regarding the application of polymers for bearings has been evaluated by a number of authors (Ünlü et al. 2009a; Ünlü & Atik 2007; Ünlü et al. 2009b; Ünlü 2011). Friction and wear of journal bearing materials can be measured under test in a variety of ways. A common method is to use a continuously rotating shaft, with the bearing loaded against it using a deadweight, and to measure the deflection or displacement for friction and wear measurements respectively (Ünlü & Atik 2007).

Unfortunately there are some inherent problems with plastics that significantly affect their performance as bearings. It has already been briefly mentioned about the heating effects in self-lubricating bearings with regards to PV, however this is more of a problem for thick polymer based materials which struggle to conduct the heat away, in contrast to thin liner materials. Movement occurs between two surfaces and the resistance due to friction generates heat in a self-lubricating bearing application, this heat must be dissipated through the housing and or shaft due to the lack of cooling provided by a lubricant (Holligan 1968). With polymer materials this becomes a problem due to the poor dissipation of heat as a result of the significantly lower thermal conductivity (one to two orders of magnitude) than that of their metallic counterparts (Lancaster 1972b). Pinchbeck (1961) briefly mentions an intensive study conducted by Keil, and the findings that if the bearing material is fitted to the

shaft, then the rate of heat transfer can be increased, and therefore higher loads and speeds can be achieved than in conventional designs. Failure to remove this frictional build-up of heat will result in increased molecular vibration until the molecular chains forming the material break, and the material melts (Pinchbeck 1961). Therefore this limits performance of a polymer bearing either as a result of overheating and seizure, or by the amount of wear (Pfestorf et al. 2000).

Polymer bearings are difficult to constrain to a housing (Wilson n.d.), due to the increased tolerances that are required to prevent seizure from thermal expansion and moisture absorption (Pinchbeck 1961; Holligan 1968). An increase in clearance of just 200  $\mu\text{m}$  resulted in 50% more start-up torque for PTFE specimens (Colbert et al. 2010). Pinchbeck (1961) also comments that machining tolerances of 0.002 in must be accepted, due to the uncertainty in the machining and the measurement of plastic bearings.

A reduced wall thickness will improve the load carrying capacity of a self-lubricating bearing, and also the dissipation of heat generated, along with any dimensional changes as a result of temperature or moisture absorption. However due to their poor tensile and impact resistance the wall thickness of a polymer bearing will typically have to be greater than that of their metallic counter parts (ESDU 87007 2010).

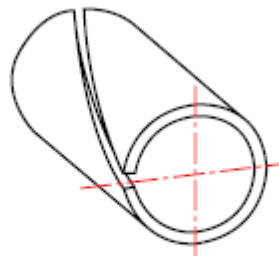


Figure 2.4: Loose tape bearing liner (ESDU)

To improve this, a tape bearing such as that shown in Figure 2.4 could be used, or alternatively a plastic lined metallic backed bearing. Pratt (1973) investigates the latter for a steel backed porous bronze impregnated with PTFE and Lead.

### 2.2.2. Mixed Lubrication

Mixed lubrication as the name suggests is a combination between the boundary lubricated regime and the hydrodynamic regime. The hydrodynamic regime is the ideal lubrication regime for many lubricated contacts. As one surface moves relative to the other with a converging geometry, a pressure is generated lifting one surface and separating the contact. For a rotating journal bearing the same is true. As the shaft rotates lubricant is dragged into the contact, generating a pressure and lifting the shaft. Figure 2.5 shows that there is also a slight eccentricity produced as a result.

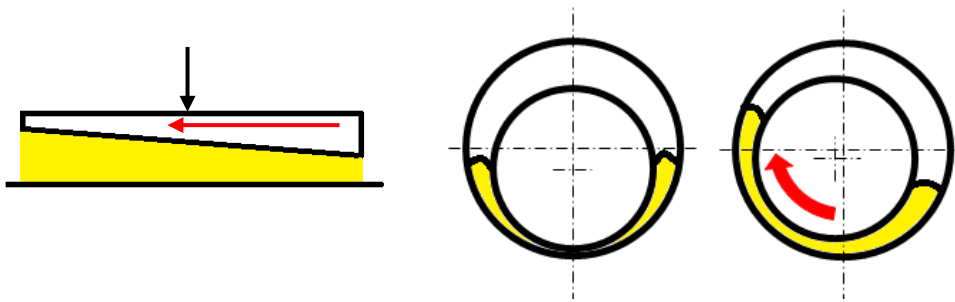


Figure 2.5: Converging geometry in (left) two plates, generating a full hydrodynamic film, (right) non-rotating journal bearing with no film, and (far right) rotating journal bearing with a fully developed film

In the mixed regime there is a lubricating film however there is still asperity to asperity contact as the thickness of the film is comparable to that of the surface roughness. This would typically occur during the start-up of a rotating journal bearing. For metallic contact between the surfaces, methods such as electrical contact resistance may be used (Clarke et al. 2014), this however is obviously not possible for polymer bearings.

#### 2.2.2.1. Lubrication in a Landing Gear Application

Given that a limited range of motion is observed and the slow velocities used, rolling element bearings are unsuitable unless substantially oversized (Strand 2005). At present most landing gear extension-retraction mechanisms, still favour the use of the greased journal bearing.

Curry (1988) provides some recommendations for grease lubricated aircraft bearings, mainly that lubrication should typically be completed every 500-700 hours, but there is no fixed re-lubrication interval and is left to the discretion of the airline operators. Using the average number of annual flight hours and cycles (Airbus 2008) it may be calculated following Curry's recommendation that the gear should be lubricated every 250 flight cycles. The average plane life is 90,000 flight cycles (Khapane 2003), meaning that over the lifetime of the aircraft the gear would be lubricated approximately 360 times.

Careful consideration must be given when selecting any lubricant for a specific application. In the case of aircraft landing gear, it is believed that the limited motion and the low speeds of 12 deg/sec do not provide adequate lubrication, as the bearing is always operating in either the mixed or boundary lubrication regime, and never develops a full film (Zhu et al. 2012). Lu & Khonsari (2007b) showed that greased journal bearings perform well at slow to moderate rotational speeds in highly loaded contacts. Additional work further proved that for mixed and boundary lubrication regimes, grease lubricated journal bearings perform better than those lubricated with oil (Bradford et al. 1961; Horth 1968; Godfrey 1964).

Some joints on the landing gear may be adequately lubricated with oil however this would require the addition of a complex and heavy oil supply system, rendering it less attractive with regards to the greased journal bearing which can provide the same load carrying capacity (Reinhoudt 1970). Mullet (1973) comments further on some of the advantages of a grease lubricated system. However since the grease is not continuously recycled, and filtered like oil lubricated systems, replenishment is required at specific intervals. The lubrication requirements vary for the different joints on the aircraft, therefore require different re-lubrication intervals. Often the optimum re-lubrication interval cannot be achieved for economic and logistical reasons, as it is more efficient to re-lubricate all of the landing gear at once, rather than one at a time. Not only do the re-lubrication intervals vary, but also the greases used, Aeroshell 17 for example, is designed to be used for heavily loaded sliding surfaces such as the bogie pivot pin, while Aeroshell 22 is a multipurpose grease for items such as wheel bearings (Shell n.d.). It is important not to mix the different greases as in the example above as this could lead to inadequate lubrication of the mating surfaces and therefore result in seizure of main components (Careless 2008). Aviation grease spans a wider operating temperature range and therefore is one of the reasons that it has been specially developed for the aerospace industry, and hence is expensive in comparison to that of multipurpose general grease (Mullet 1973).

#### 2.2.2.2. Grease Lubrication

Grease lubrication has been greatly studied over the years, and therefore only brief comments will be made here. Greases consist of a liquid lubricant gelled with a thickening agent, usually soaps based on Lithium, Calcium, Sodium Barium or Aluminium (Yousif 1951). By altering the ratio of thickener and different manufacturing techniques, the stiffness of the grease can be altered. The National Lubricating Grease Institute (NLGI) number is used to categorise greases according to their hardness on a scale of 000 to 6 where a lower number

represents a softer grease. Numbers 2 and 3 are the most commonly used in bearing applications (Mullet 1973). Cann & Lubrecht (1999) summarise the understanding of grease lubrication mechanisms in rolling element bearings, highlighting the two mechanisms proposed, over rolling and oil bleeding.

The first is outlined by Scarlett (1996), where a thin layer of grease forms on the surface and the remaining grease forms a protective seal, preventing the lubricating high viscosity grease layer from escaping. Experimentation showed that no base oil escaped from the contact.

The oil bleed theory has however been more widely accepted though ball on disc testing where it is thought that the grease releases or bleeds the base oil out of the grease which lubricates the contact, with the majority of the grease being pushed aside forming a reservoir (Cann 1999). Unfortunately however there is still little direct evidence for this, only visual observations during ball on glass disc testing (Cann & Lubrecht 1999).

Cann (2007; 2001) conducts a large amount of work with regards to the performance of greases, thickeners, and their importance, largely in rolling element bearings, concluding that at slow speeds an inverse Stribeck curve is produced. Investigation of grease degradation in bearings using SKF R0F and R2F test rigs is then made using IR spectroscopy (Cann et al. 2001; Cann et al. 2007).

Mota & Ferreira (2009) investigated the effects of base oil viscosity and percentage of soap in rolling contact wear. Concluding that greases with a higher value of base oil viscosity, and a higher percentage of soap led to reduced wear. Yousif (1983) also uses a twin disc machine to study the effect of frictional traction with time, to which he found that there is a continual increase unlike mineral oils, and comments that they are not ideal lubricants, as they can lead to failure through starvation at high slip.

Lu & Khonsari (2007b) experimentally investigate load, bushing material and the type of grease on the co-efficient of friction in journal bearings, and develop a mixed elasto-hydrodynamic model for line contact. They also comment on their findings of a reduction in the co-efficient of friction when the load is increased when operating in the hydrodynamic regime, and the higher value of the friction co-efficient due to the thickener, when comparing grease with the same base oil viscosity of that of an oil.

### 2.2.2.3. Design of Lubricated Bearings

Many authors, have commented on the non-Newtonian behaviour and reluctance to flow unless the yield value is exceeded (Scarlett 1996; Cann & Lubrecht 1999). Yousif (1951) investigated the rheological properties of greases, concluding that at higher shear rates, the grease begins to flow as a Newtonian liquid, but has a higher viscosity than would be expected from the base oil. When distributing grease through lubrication channels, the flow of greases becomes of great importance. Therefore many designs of grease grooves in metallic bushings have been developed. Different designs have been investigated, by a variety of authors. Russo (2013) shows some of the more common designs (Figure 2.6).



Figure 2.6: Some common designs of lubrication channels in journal bearings

Brito et al. (2012) compared a single and twin axial groove distribution with particular attention to the flow rates and pressures used and Ahmad et al. (2013) investigated the effects of varying the pressure input with axially grooved bearings, concluding that the input location of  $-30^\circ$  was the worst location for lubricant to be introduced. Strand (2005) investigated 3 different types of grease channel design; no groove, X groove (figure eight) and H groove (straight and circular), and their influence on wear. The H groove was found to perform the best, and unexpectedly the X grooved bush performed slightly worse, but similar to the bush with no groove.

Schuller et al. (1968) conducted comparative stability experiments between 3 types of herringbone designs. Herringbone or spiral grooves as they are sometimes know, have attracted much attention over the last few years for their applications in consumer items such as computer hard disk drives (Kawabata et al. 1989), due to the attractive properties of reduced noise, friction and extended lives (Muijderman 1979). However the spiral or herringbone design is only suitable for rotation in one direction (Muijderman 1979), hence Kawabata et al. (1989) proposed a new reversible design using a numerical approach. Hirayama et al. (2009) developed a methodology for optimising herringbone groove dimensions to improve repeatable run out characteristics of spindles. Sep et al. (2013) also investigated the effect of helical groove geometry, but in a sliding journal application with

regards to abrasive wear, and how to move wear debris and contaminants out of the loaded region, and touches on the potential of surface texturing for journal bearings.

Some work has been conducted on the effects of clearances, edge effects and surface texture. Applying a texture to a lubricated sliding surface was found to improve the tribological properties, by creating micro hydrodynamic bearings, therefore reducing friction (Ronen et al. 2001; Pettersson & Jacobson 2003). In the mixed lubrication regime, it was found that if dimpling was applied around the entire bore then COF could be improved, however worsened the performance if in the hydrodynamic regime (Lu & Khonsari 2007a). Sinanoğlu et al. (2005) applied a surface texture to the outer diameter of the shaft, and concluded that a trapezoidal profile on the shaft performs better than a saw tooth profile. Colbert et al. (2010) looked at edge effects, clearances and wear, and proved that a sharp edge should be avoided, and best performance could be obtained from a radiused bush rather than chamfered one. Strand (2007) conducted a Finite Element Model (FEM) to optimize journal bearing housing design looking at how to distribute the pressure across the pin without reducing the area. Prabhu (1997) looked at the horizontal misalignment effects of a hydro-dynamically lubricated journal bearing, by examining the coast down time of the bearing with regards to the angle of misalignment. Identifying the mixed lubrication regime, and that increasing misalignment causes an increase in the fluid film friction and hence an increase in the deceleration of the bearing.

### 2.3. Performance of the Pin Joint

Research into oscillatory journal bearings has been conducted in recent years. Glaeser & Dufrane (1976) conducted some early work on the performance of heavily loaded oscillatory journal bearings, using metallic bearings and a variety of different greases. Their results were based upon two bearing specimens; Beryllium Copper alloy and Aluminium Bronze, running against M-50 tool steel, and AISI 4340 steel. Although the Beryllium copper alloy is favoured as a bearing material for its higher load carrying capacity and low wear rates at high bearing pressures it was found to carry a health risk of Chronic Beryllium disease (Darby & Fishwick 2011). Glaeser and Dufrane (1976) highlight the sensitivity of both the Aluminium Bronze and Beryllium Copper alloys to the effects of grease starvation, and the potential advantages of plastic based materials.

Wear of Aluminium Bronze against tool steel under boundary lubrication conditions was conducted to prevent seizure of aircraft fuel pumps. Experimentation was conducted using

pin on disc testing, and protecting wear debris were found to be  $\text{Cu}_2\text{O}$  and that material was transferred from the Aluminium Bronze pin to the steel disc, with the transfer film being Aluminium rich. Transfer occurred during initial stages and then following that only at film breakdown (Sullivan & Wong 1985).

Zhu et al. (2010) investigated the pressure distribution and the frictional torque in the articulating pin joints, concluding that friction co-efficients were in the range 0.08 to 0.11 for grease lubricated contact. The pressure distribution was found to be approximately cosinusoidal over a range of  $\pm 60^\circ$  regardless of radial load. It was also shown that there was a difference between nominal and true friction torque on a pin joint. The true torque on a joint includes the components of pressure that do not support the normal load, and therefore gives a greater torque requirement than that normally calculated by  $\mu = PD/2$ .

Zhu et al. (2012) continued onto develop a model to determine the lubricant film formation and the frictional torque for a landing gear application. The model was validated with experimental data, both numerical and experimental approaches determined that the joint investigated was operating in the boundary regime with little effect from hydrodynamic lift. However prior knowledge is required for the model regarding the dry friction co-efficient value.

Strand (2005) studied grease lubricated heavily loaded oscillating bearings in construction machinery developing three finite element models. One to replace the pin to improve computational time, one to study the parameters governing the pressure distribution and a final one to model the wear.

The service life of grease was found to not be fully utilised by Ugryumov & Pedrik (1982) for a small amplitude oscillating joint. The friction co-efficient for Bronze against a steel shaft was found to be 0.18 for a contact lubricated with a lithium based grease. The re-lubrication interval was established to be 50 hours, 4 -5 times longer than established previously. The temperature of the joint was not monitored, but simply allowed to cool between tests.

Lu & McKellop (1997) considered the frictional heating effects in a hip joint simulation with UHMWPE after a run in period had been completed. Temperatures were found to rise to a steady state value between 40 and  $50^\circ\text{C}$ , measured 0.5 mm beneath the sliding surface.

Rezaei et al. (2011) conducted a numerical and experimental study of large scale polymeric composite journal bearings, oscillating the shaft using a lever arm set up. The numeric model

is shown to be accurate for the quasi-static condition but for the 2D dynamic condition was found to be time consuming.

Ligterink & de Gee (1996) use a circular equation approach for measuring wear in oscillating bearings, again based upon a displacement approach. However this displacement must be a measured or guessed value.

Gawarkiewicz & Wasilczuk (2007) investigated the effect of small amplitude oscillations on the wear of self-lubricating bearings, monitoring the wear by surface profilometry of a machined groove in the specimens, concluding that the real sliding distance is lower than the apparent one, due to the tangential elasticity of polymer based bearing materials which results in an over prediction of wear rates if stick-slip behaviour occurs.

## 2.4. Conformal Contact

The contact between conformal cylinders is a complicated phenomenon, especially when considered with respect to journal bearings. The problems of the cylindrical conformal geometry, small clearances and a finite length, all combine. How the load is distributed is of great interest when designing a journal bearing. Of special interest is the arc of contact.

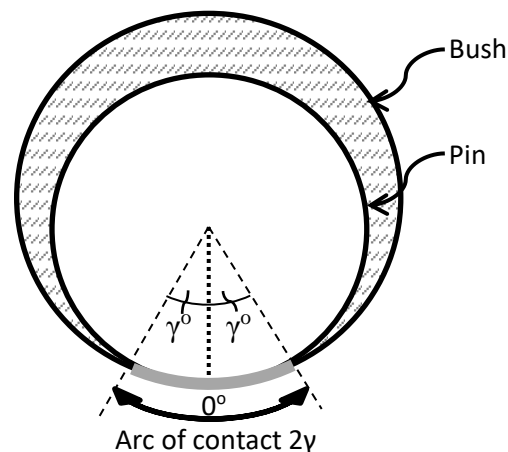


Figure 2.7: Definition of the arc of contact of a pin against a bush

The most commonly used pressure distribution model for a bearing, and often quoted by manufacturers is the projected area method, where the load is assumed to be distributed across the whole width of the bearing. This has the advantage that very few input parameters are required to determine the necessary bearing size. Unfortunately however consideration of the materials and clearance between the contacting bodies is not taken into account, making predictions for soft/hard material interfaces difficult.

The cosinusoidal method resolves the pressure distribution around the pin assuming 180° contact. It is still however limited as it does not consider the material parameters.

Heinrich Hertz developed a theory for spherical and cylindrical elastic bodies in contact in 1880, that has become a mainstay of Mechanical Engineering (Johnson 1982). Hertz theory mainly focused on external contact of bodies, and that it was a case of stress concentration so attention could be focused close to the point of contact (Johnson 1982). In certain circumstances, the theory can be extended for cylinders in conformal contact, such as cylindrical roller bearings, but must be applied correctly to avoid breaking one or more of the assumptions made by Hertz. One of the big advantages of the Hertzian contact model is that the material parameters are considered, through the reduced modulus term (equation 2.2).

$$\frac{1}{E^*} = \left( \frac{1 - \nu_1^2}{E_1} + \frac{1 - \nu_2^2}{E_2} \right) \quad (2.2)$$

Where  $E^*$  is the reduced modulus of elasticity,  $\nu_1$ ,  $E_1$ , and  $\nu_2$ ,  $E_2$  are the Poisson's ratio and modulus of elasticity for bodies 1 and 2 respectively. The width of contact for parallel cylinder in contact can be calculated using

$$a = \sqrt{\frac{4P'R'}{\pi E^*}} \quad (2.3)$$

Where  $P'$  is the load per unit length and  $R'$  is the reduced radius of the contact. Unfortunately however there are three main problems that can arise with the Hertzian contact (Johnson 1982; Pereira et al. 2011):

- Compliant elastic solids do not obey this
- Does not account for the energy dissipation unless quasi-static
- With conforming surfaces such as a pin and bush contact, the arc of contact can become large with comparison to the radius.

In the case of journal bearings, the contact area rapidly increases with load and becomes comparable to the radii of curvature of the contacting bodies, breaking one of the assumptions made by Hertz.

As a result, several researchers attempted to improve upon the Hertz theory with the addition of adhesive and separation components such as that of Bradley (1932), Johnson

Kendal Roberts (1971), Derjaguin Muller and Topolov (1975), Tabor (1977) and Maugis-Dugdale (1992) to increase the contact region calculated by Hertz (Johnson 1997).

Goodman & Keer (1964) removed the assumption that a small contact region is made to investigate the state of stress with identical materials, and identified that if the contacting bodies have a large difference in radii then the Hertz equation must be used.

Steuermann (1949) solved the problem in 2D for a disc in an infinite plate, using integrals and finite difference methods. The solution is only given for arcs of contact less than 60°, and assumed that the shear stresses vanish in the plate.

Persson (1964) developed an integro-differential equation for the pressure distribution and validated it with a pin loaded against an instrumented flat plate with a hole in. This solution however was only valid for identical contacting materials.

Ciavarella and Decuzzi developed a closed form of Persson's solution, for both cases of elastic similarity (2001a),

$$\frac{E_1^* \Delta R}{P'} = \frac{(\alpha - 1)(\log(b^2 + 1) + 2b^4) + 2}{\pi(1 - \alpha)(b^2 + 1)b^2} \quad (2.4)$$

and elastic dissimilarity (2001b).

$$\frac{E_1^* \Delta R}{P'} = \frac{(\alpha - 1)(\log(b^2 + 1) + 2b^4) + 2}{\pi(1 - \alpha)(b^2 + 1)b^2} - \frac{4\beta}{\pi(1 + \alpha)} \quad (2.5)$$

Where  $b = \tan\left(\frac{\gamma}{2}\right)$  with  $\gamma$  the arc of contact,  $\frac{E_1^* \Delta R}{P'}$  is the dimensionless load parameter and,  $\alpha$  and  $\beta$  are Dundur's material parameters

$$\alpha = \frac{((k_1+1)/n_1) - ((k_2+1)/n_2)}{((k_1+1)/n_1) + ((k_2+1)/n_2)} \quad \beta = \frac{((k_1-1)/n_1) - ((k_2-1)/n_2)}{((k_1+1)/n_1) + ((k_2+1)/n_2)} \quad (2.6 \& 2.7)$$

With  $n_i$  the shear modulus and  $k_i$  Kolosoff's constant.

$$n_i = \frac{E_i}{2(1+\nu_i)} \quad k_i = \frac{3-\nu_i}{1+\nu_i} \text{ (Plane stress)} \quad (2.8 \& 2.9)$$

Ciavarella and Decuzzi (2001a; 2001b) concluded that when the angle of contact is less than 30° the strength of the joint reduces to that predicted by Hertz. Noble & Hussain (1969) also obtained a solution for elastic dissimilarity but only for a zero clearance condition.

Chen & Marshek (1988) considered the contact of a 2D long cylinder and closely conforming cylindrical seat. By guessing instead of calculating a relative approach unlike Woodard, they were able to avoid a large scale linear system. They compared their result to Hertz and Persson theories and found good agreement with Persson, as the Hertzian theory underestimated the maximum contact pressure and overestimated the maximum angle of contact. At contacting angles of less than  $15^{\circ}$  they found all solutions to be in close agreement.

Zhu et al. (2010) conducted ultrasonic measurements of the contact pressure and arc of contact for a steel pin loaded against aluminium bronze bushes. The findings were compared with the Hertz and Persson models, concluding that the Hertzian contact theory could still be applied to estimate the contact of a journal bearing with a steel pin in aluminium bronze bushes, but was more accurate at higher loads. While the Persson method predicted higher pressures for the contact, especially at low radial loads.

Almost all of these methods assume elastic similarity, except for Ciavarella & Decuzzi, however this is a relatively heavy in terms of computational power using 21 equations to compute a relatively simple concept.

Deters et al. (2003) highlight a circular equation approach developed by Wenger (1964) for calculating the angle of contact for very elastically dissimilar materials, based upon the deformation and wear; however to determine the arc of contact these two parameters must be known in advance. This is acceptable if the load applied is static, and the bearing has been run in sufficiently so that the wear has reached a steady rate.

Ligterink & de Gee (1996) also applied the circular equation approach, however considered it only for the oscillating nature of the bearing, again once a known displacement had been recorded.

## 2.5. Material Selection for Pin Joints

Advanced bearing solutions are most likely to involve using a composite or polymer material, as suggested by McCarthy et al. (1994), in order to reduce operating costs by reducing weight, and therefore saving fuel. However care must be taken in order to select a material that performs well under impact loading conditions, as Zhang (1998) found that the PTFE wear mechanism is mainly plastic fracture, while Nylon 6 is more susceptible to erosion.

Both surface roughness and hardness of the mating surfaces are important tribological parameters to consider when working with self-lubricating bearing materials. It can be said that surface roughness is of great importance when dealing with plastic bearing materials as it is well documented that micro cutting will occur where hard asperities plastically plough through a softer mating one (Lancaster 1972a; Stuart 1998), and it is known that a metal and plastic interface will cause this phenomenon if the relative surface finishes differ greatly (Pinchbeck 1961). It is therefore recommended that the mating surface finish is between 0.2 and 0.4 microns (ESDU 87007 2010).

The hardness of the contacting materials generally defines which material will wear at a higher rate. For two rough contacting materials, it is the harder material that will typically plough through the softer one. When dealing with filled polymers and a very hard counter face material (>600 VHP) the abrasive effect of the filler becomes negligible, and correction factors may be applied to approximate those of unfilled polymers (ESDU 87007 2010).

The Archard wear model (Williams 2005) quickly shows the significance of the hardness of the mating components and its effect on the volume of debris removed, where  $V$  is the volume of wear debris produced,  $H$  is the hardness of the softest mating pair,  $F_N$  is the normal force applied to the contact,  $s$  is the sliding distance and  $K$  is the dimensionless wear coefficient constant. Hence a harder material results in a lower volume of wear debris.

$$V = K \frac{F_N}{H} s \quad (2.10)$$

### 2.5.1. Viscoelasticity

Viscoelasticity of materials in contact is by no means a simple phenomenon, and therefore only brief notes will be made about it here. For self-lubricating polymer bearings consideration also has to be given to the nature of the materials, and the configuration of the loading conditions.

For materials such as a steel pin, loaded against aluminium bronze bushes the Hertzian and Persson methods have been proven to be reasonably accurate (Zhu 2012), in predicting the nonlinear relationship between force and displacement (Johnson 1982; Johnson 1994), it can only be done under quasi-static conditions as there is no account for the energy dissipated. The aluminium bronze bush and steel pin, while elastically dissimilar are both much stiffer materials than self-lubricating polymer composites, and will therefore show less sensitivity to viscoelasticity.

To further complicate the problem aircraft landing gear joints, such as the one selected in this study are subjected to a dynamic motion, as the aircraft taxis along the runway. Therefore the problem suddenly becomes much more complex and consideration to the viscoelastic nature of the polymers needs to be given, as energy will be dissipated during the loading and unloading of the joint.

The Kelvin-Voigt model is a simple viscoelastic model that has been used to predict linear viscoelasticity. It is more commonly recognised as the classical parallel spring-dashpot model, however due to its simplicity it is generally inadequate to do so with polymer materials (Bentham et al. 1996).

Some of the energy dissipated can be accounted for through the addition of adhesive and separation components to the Hertzian models as mentioned earlier (section 2.4) (Johnson 1997). However energy can also be dissipated through wave propagation, friction and the work of plastic deformation (Lim & Stronge 1999).

Pereira et al. (2011) conduct a critical review of cylinder contact force models for the use in analysing the viscoelasticity, covering the Kelvin-Voigt model, and several adaptations of Hertzian contact (Pereira et al. 2011). The four models discussed are the Johnson Model (1994), Radzimovsky Model (1953), Goldsmith Model (1960) and Lankarani & Nikravesh Model (1994).

The Johnson, Radzimovsky and Goldsmith models are all based upon the Hertzian models and therefore encounter mathematical limitations, due to the use of the logarithmic function (Pereira et al. 2011).

The Lankarani & Nikravesh model differs in that the contact force can be expressed as an explicit function of indentation, and therefore reduces computational power. Given this and that the model also can handle the energy dissipation during the impact process, it is often selected by researchers for contact and impact problems. In the comparison made by Pereira

et al (2011) however, the term accounting for the energy dissipation is neglected in order to compare with the other models that are purely elastic. The solution is initially developed for spherical bodies, but is extended for cylindrical contact.

The Energy dissipated during contact is covered in more depth by Hunt & Crossley (1975) who further explain the limitations of the Kelvin-Voigt model. Mainly which indicates that there is a tensile component acting on the contacting bodies just before separation.

Mindlin & Deresiewicz (1953) show that the magnitude of the normal and tangential loads along with the history of the loads influences the friction between the contacting bodies. Lim & Stronge (1999) use a plane strain and time dependent approach to obtain the tangential force and the energy dissipated by friction. Again Hertz-like contact is assumed from the use of steel and aluminium half-spaces.

The contact of viscoelastic bodies brings with it the additional complication of the contact region varying with time and therefore requires the correct selection and application of boundary conditions (Lee & Radok 1960). Pereira et al. (2011) discuss in detail the validity domains of the contact models, including the significance of converging geometry. To conclude Pereira et al. (2011) identify the three main problems associated with the consideration of viscoelasticity in contact force models. The first problem is a numerical iterative technique is generally required. The second relates back to the problem of conformal geometries as many are derived with Hertzian analysis. Finally the third is the use of the logarithmic function which imposes mathematical constraints on the model.

Therefore given the additional complexities of a significantly viscoelastic material in converging contact, such as self-lubricating polymer composite bearings, this work does not attempt to include viscoelasticity more than highlighting its importance.

## 2.6. Conclusion

Grease lubrication is a topic that has been well studied over the years, including designs of lubrication channels and the effects of surface texture. Grease lubricated journal bearings in oscillatory motion has also been studied but to a much lesser extent, while the effect of the articulation angle has largely been neglected. Re-lubrication of pin joints has also very briefly been studied, however only at fixed articulation angles and the temperature of the joint was not controlled. A large amount of research was conducted on self-lubricating bearings in and around the 1970's, however more recent advances in materials has not been greatly

investigated. Self-lubricating bushes in an oscillating journal bearing application is an area that has recently been attracting more interest. Two models are commonly used for the contact of conformal cylinders, however little consideration has been given to the contact of significantly elastically dissimilar materials. Many of the works completed for analysing pin joint contact have considered the pin joint to be a hole in an infinite plate, or have neglected the dimension of the elastic body that is being indented. Investigation into the wear of a self-lubricating bush under dynamic loading of a pin joint has not been conducted.

[Blank Page]

# 3.

## Experimental Techniques

In this chapter the two servo-hydraulic test rigs used are described. One test rig simulates the radial loads applied to the pin joint as the aircraft is manoeuvred on the ground with the gear down locked. The second test rig simulates the extension retraction of the gear when the aircraft is airborne. The instrumentation used in the measurement and control of these two test rigs is described, along with operating conditions and sample results.

### 3.1. Loading of a Landing Gear Pin Joint

Joints in aircraft landing gear are typically subjected to two types of loading, one when the aircraft is on the ground where there is no rotation of the joint but the weight of the aircraft must be supported. The other is the rotation of the joint which occurs when airborne hence comparatively low radial loads as only the weight of the gear must be considered. Two bespoke test rigs were manufactured to simulate each type of loading. The pin joint radial load tester simulates the loading on the gear when performing ground manoeuvres, while the pin joint function tester simulates the rotation of the joint as the landing gear is extended and retracted.

### 3.2. Pin Joint Radial Load Tester

The joint selected for investigation is located on the locking stay of the Nose Landing Gear of a single aisle passenger aircraft. This joint does not hold the entire weight of the aircraft, but prevents the gear from deflecting laterally, and therefore the load requirement is relatively small. Some studies have already been undertaken by the aircraft manufacturer regarding this joint and therefore more information was available, such as the load history and magnitude of loads. Figure 3.1 shows a schematic of how loading on a typical pin joint develops from an uneven runway as the gear tries to deflect laterally.

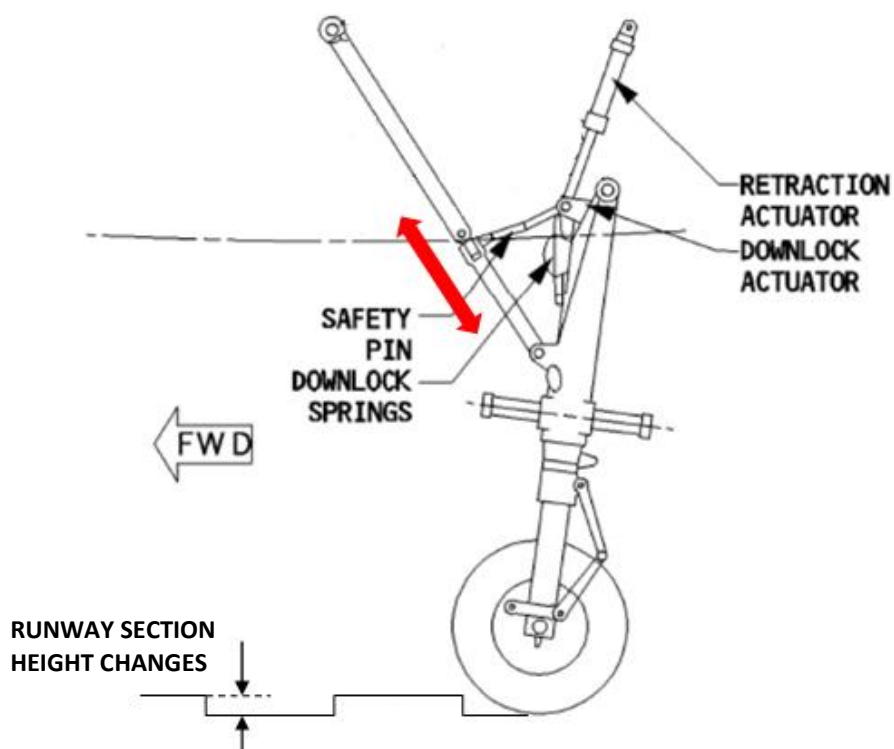


Figure 3.1: Development of loading on drag stay joint as a result from changes in runway height

The joint is subjected to tensile and compressive loading developed from the runway. Not only must consideration be given to the strength of the struts used, but also the pin, bearings and the clevis itself.

### 3.2.1. Loading Clevis

Simulation of the tension and compression loading on the pin in the radial direction when an aircraft taxis along the runway required a new test fixture to be commissioned. The fixture was designed to fit onto a servo-hydraulic load frame. Geometric similarity was maintained by using the same critical dimensions on the clevis as the actual aircraft part. The fixture was reduced in height compared to the original aircraft component to enable ease of manufacture and to reduce the risk of deflection occurring in the clevis joint at high loads.

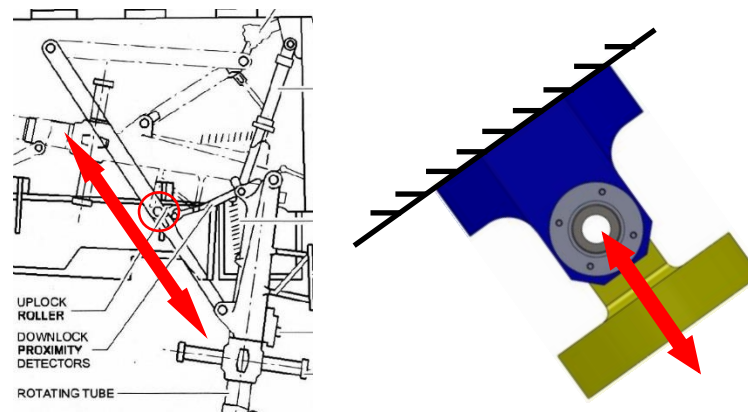


Figure 3.2: Design of radial load test rig to simulate tension compression loading

Figure 3.2 shows the joint in an aircraft schematic and outlines how it is loaded as a result of the changes in runway height and how this is replicated under laboratory conditions. It should be noted here that the CAD model of the test rig has been rotated to help understanding.

### 3.2.2. Single Axis Test Frame

The servo-hydraulic test frame is fitted with both a strain gauge based shear web load cell for measuring force, and an internal Linear Variable Differential Transformer (LVDT) (Dally, Riley, & McConnell, 1993) for measuring displacement. The test frame could be controlled in either Force or Position mode, using the feedback from the sensors, a PID control loop and servo-hydraulics. During this investigation Force mode was used to simulate a sinusoidal loading, and the displacement recorded. Displacement was recorded using the load frame's internal LVDT, as well as an external LVDT (Figure 3.3) which was located between each half of the clevis. The external LVDT was added to the test rig as it was observed during testing at higher loads that that load frame's LVDT was not only recording the displacement of the specimens but also the displacement of the load cell, and the deformation in the test clevis.

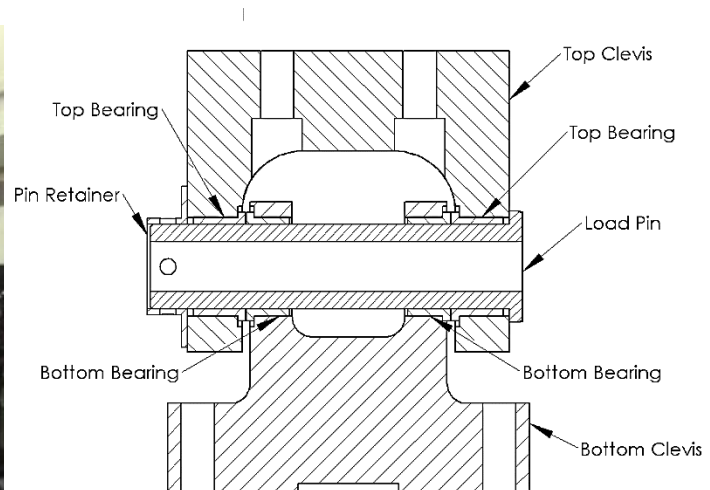


Figure 3.3: (left) Radial load test rig mounted on the servo-hydraulic test frame, (right) Cross section of the radial load test rig showing the location and orientation of the bearings under test

Figure 3.3 (right) shows a cross section of the test fixture, and how the bearing specimens are located and orientated. The top clevis was bolted to the load cell, whilst the bottom clevis was connected to the servo-hydraulic actuator.

### 3.2.3. Instrumentation

Control of the servo-hydraulic load frame was completed using a MOOG Smartest One portable test controller. This controller was also used to record the data at a rate approximately ten times greater than the frequency that the test was run. The data recorded by the controller is listed below:

- Current Cycle
- Force Commanded [kN]
- Force Feedback [kN]
- Position Feedback Internal LVDT [mm]
- Position Feedback External LVDT [mm]

#### 3.2.3.1. Load Cell- Structure and Configuration

Given the large loads that the joint was subjected to, a test frame with a 250 kN load cell was used. The displacements measured were comparable to those measured by the internally bonded strain gauges in the load cell Figure 3.4. Therefore it was important to isolate specimen deformation from that occurring in the load cell.

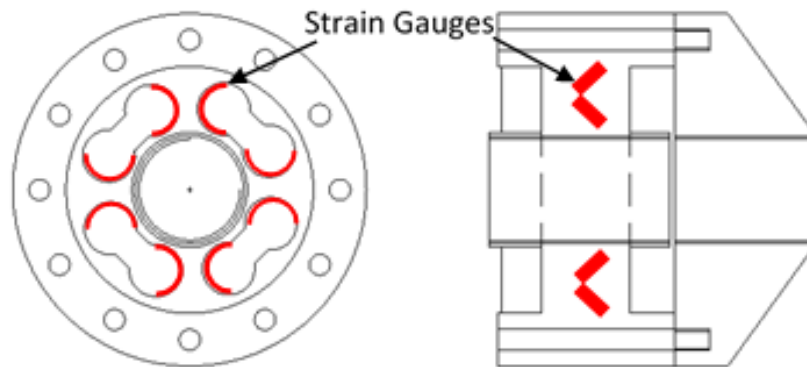


Figure 3.4: Location of strain gauges bonded in a pancake type load cell

Displacement of the test clevis must also be considered, which was completed using a single strain gauge bonded to each clevis lug at the location of the thinnest section, on the centre line of the bore (Figure 3.5). Neale (2013) shows an exaggerated example of how a clevis would deform under a compressive load, the outer lugs of the clevis spreading out, and the resultant pressure distribution on the pin Figure 3.6.

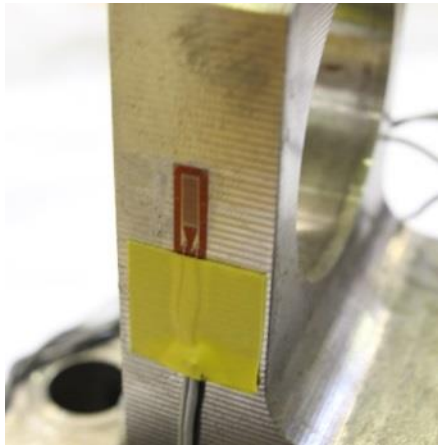


Figure 3.5: Single strain gauge bonded to the weakest part of the clevis lug

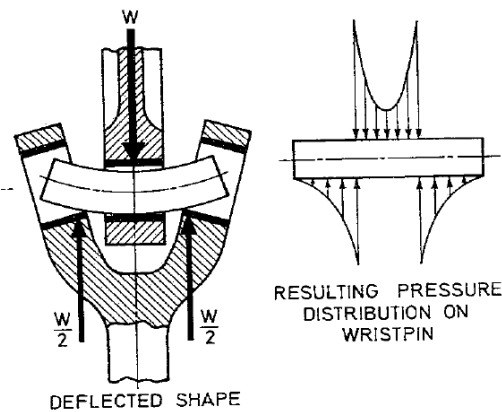


Figure 3.6: Deformation and pressure distribution in a loaded clevis

### 3.2.3.2. Instrumented Load Pin

Tests were also conducted with an instrumented load pin which was substituted for the standard aircraft pin, for a selection of load displacement tests. The load pin supplied by Strainstall was fitted internally with 4 full bridge strain gauges located at the points of highest shear between the bushes in both the x and y directions, 2 at the head end, and 2 at the far end. Where X1 and Y2 are located at the head end of the pin, and X3 and Y4 are at the far end of the pin.

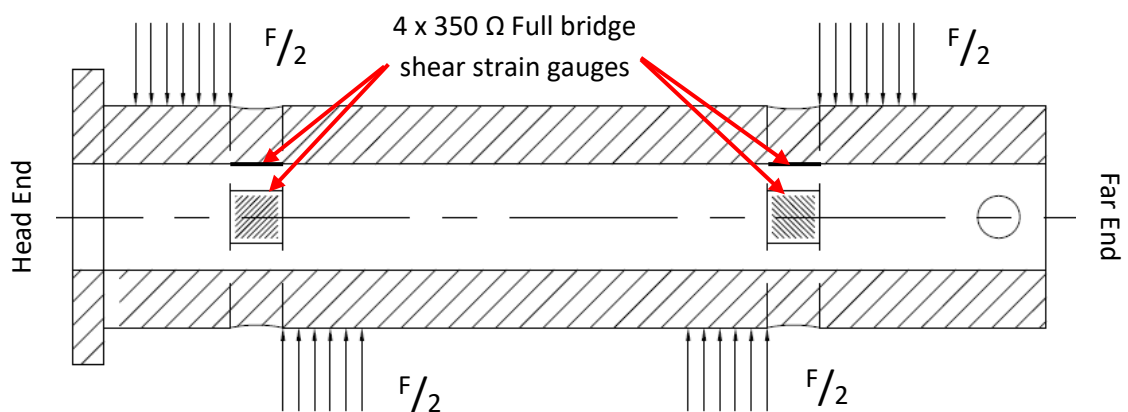


Figure 3.7: Instrumented load pin with 4 internally bonded full bridge shear gauges

The gauges were positioned to measure the pure shear force which was introduced into the pin through the machined grooves. The points of maximum shear force are indicated by the shear force diagram shown in Figure 3.8.

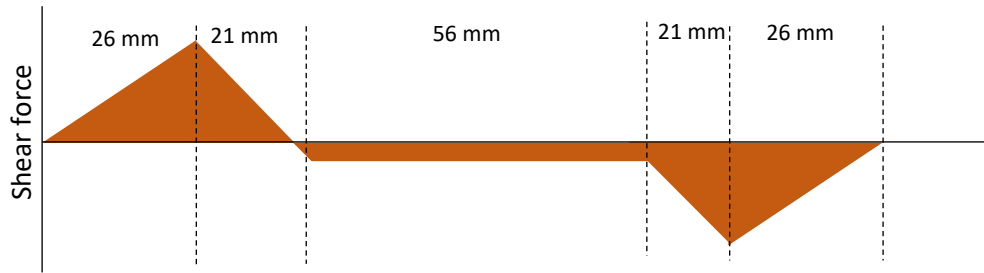


Figure 3.8: Representative shear force diagram showing the regions of maximum shear

Any change in length of strain gauges will cause a small change in resistance. By connecting several strain gauges into a balanced Wheatstone bridge this small change in resistance can be measured as a function of the excitation voltage.

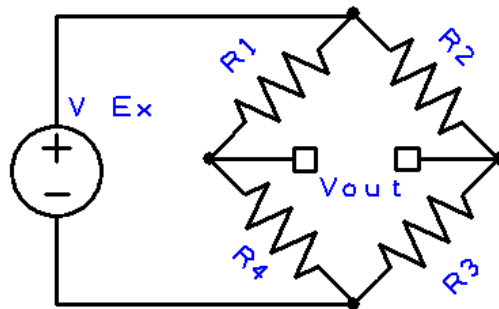


Figure 3.9: (left) Wheatstone bridge connections for strain gauge connection, (right) Vishay model P3 strain indicator and recorder

The load pin and load cell used a full bridge arrangement, where all four resistors are active arms in the bridge. Whereas measurement of the clevis deformation used only a single strain gauge and hence a single active arm (quarter bridge) therefore the bridge was completed using completion resistors. Using the gauge factor of the strain gauges and the excitation voltage, the output from the Wheatstone bridge (mV/V) may be converted into engineering units such as load kN or mm. For the test frame's load cell this conversion step was completed by the MOOG Smartest One controller, along with filtering and signal conditioning. For the strain gauges monitoring the clevis lugs, and the load pin a Vishay model P3 strain indicator was used.

For both the clevis strain gauges and the load pin mV/V outputs were recorded on each of the 4 channels. The bridges were always balanced before load was applied. mV/V outputs were chosen for recording as they are the raw output of the strain gauges before any scaling was applied. Calibration of the load pin was conducted by Strainstall up to 200 kN, and the best straight line fits for each of the 4 bridges was calculated and is displayed in Table 3.1.

Bridge	X1	Y2	X3	Y4
Output mV/V	2.7504	2.6995	2.755	2.6987

Table 3.1: Best straight line calibration values for each gauge in the load pin

In order to investigate the angle of contact between the bushes and the calibrated load pin. The load pin was fitted with a plate marked at 5° intervals, and positioned in the clevis with the y axis located at 0°. The clevis was loaded in compression only, to negate any effects of clevis extension as described above. Given that the minimum load observed in service was 15 kN, the clevis was loaded to this magnitude in a 25 kN electric test frame.

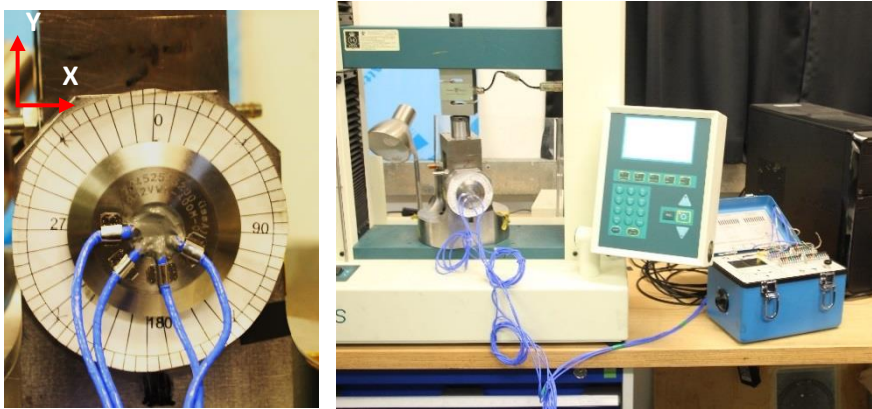


Figure 3.10: Instrumented load pin with marked plate and orientation of the gauges (left), load pin incremented around to obtain the strain distribution (right)

Figure 3.11 is for an applied load of 15 kN rotated through an angle of 360°, it can be seen that the load has been split almost equally by the two lugs of the clevis, as would be expected. Additionally it can be seen that the Y bridge measurements are approximately 90° behind the X bridges, again as expected from the location of the gauges in the load pin. It should be noted here that the X and Y directions marked on the pin were defined by the manufacturer such that, when orientated in the Y direction the maximum shear force will be observed. The same applies for the x direction. Therefore the maximum results of the Y bridges in Figure 3.11 at  $\Phi$  of 0° and 180° are as expected. Furthermore it can be seen that the bridges are symmetrical in both the positive and negative load directions, proving again that the magnitude of the load is the same on both halves of the clevis and also that all gauges are reading approximately the same in any orientation of the pin.

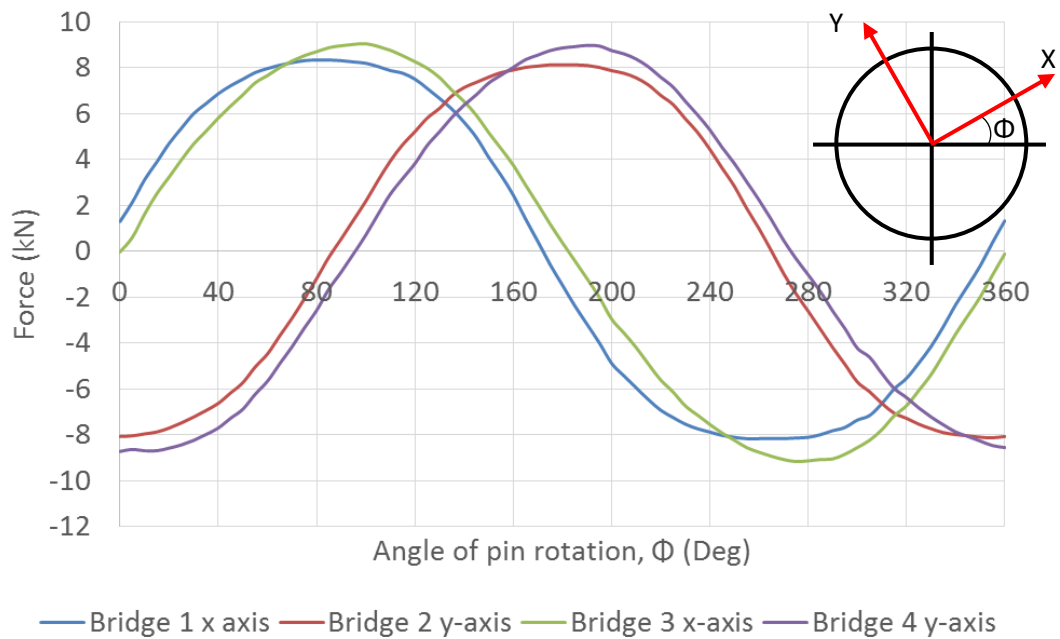


Figure 3.11: Load profile for 0-360° incremented at 5° for a constant load

The electric test frame was less sensitive to the feedback loop than a servo-hydraulic frame, due to the absence of fluctuations as a result from valves and pumps. Thus making it more suitable for use in quasi-static loading applications. Load was applied using a leadscrew, and therefore care must be taken with regards to backlash.



Figure 3.12: Small scale test clevis with externally mounted LVDT (Top), knurled pin to produce an imprint on the bore of the bush (Bottom)

A small scale test clevis was used to investigate the arc of contact for a steel pin loaded against a plastic bush. 12 mm diameter silver steel was used to manufacture the pins and a textured surface was applied to the pin by lightly knurling. The knurling process caused a slight increase of the nominal diameter, even when the rough edges were removed. The

texture was necessary to create an imprint of the shaft into the plastic bush. A single bush 16 mm long and 16 mm OD was used. The internal diameter was varied to account for different wall thicknesses of bushes, the standard bush ID used was 12.2 mm.

An external LVDT was used again in order to ensure that the machine stiffness and load cell deflection was accounted for as described earlier. The imprint left in the bush by the knurled pin could then be viewed once the joint was disassembled. To easily view the imprint the bush was cut into two halves, and could then be inspected under a microscope. Figure 3.13 shows a microscope image of the imprint. It should be noted here that due to the curved nature of the bush, the amount of the imprint in focus is as a result of the focal length of the microscope lens. Additionally it should be noted that the pattern appears tapered here due to misalignment of the test clevis. A self-aligning plate was added to the test setup to eliminate misalignment effects, and several measurements for the contact width taken and averaged to obtain a representative value.

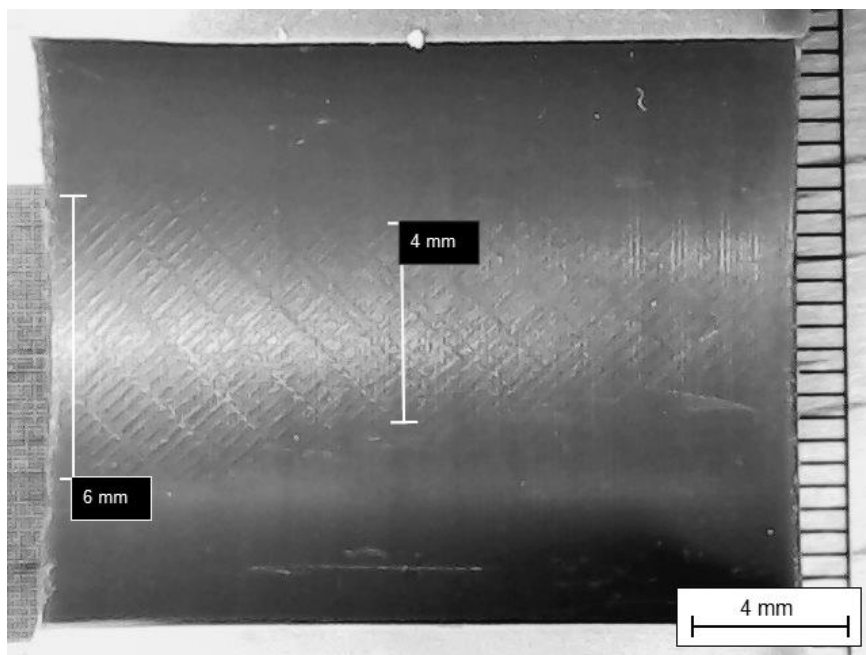


Figure 3.13: Microscope image showing the imprint left by the knurled pin, showing the contact area

In order to measure the width of contact, the imprint was located with an optical microscope, and photographed. The size of the contact measured and calibrated.

### 3.2.3.3. LVDT Structure and Configuration

The Linear Variable Differential Transformer (LVDT) was used to measure displacements and operates using inductance. This is achieved using 3 coils. The primary coil is the excitation source, while the other two coils are positioned both sides of the primary coil and are linked together to form a single secondary coil. The position of the core induces a varying voltage in the secondary coil.

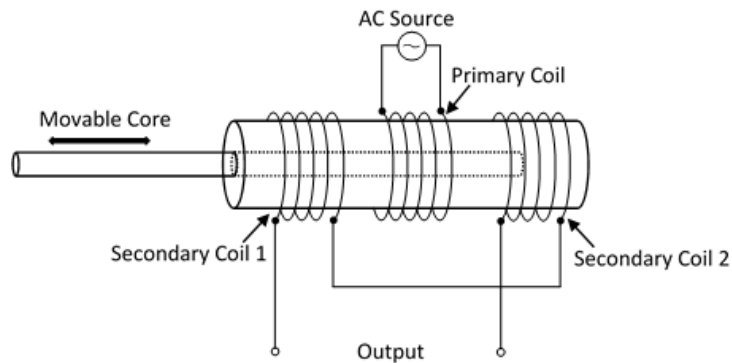


Figure 3.14: Schematic of an LVDT showing how displacement can be measured without wearing out the transducer

The LVDT requires signal conditioning to demodulate and filter the secondary coil output to produce an analogue signal. The test frame's LVDT signal was conditioned using the Smartest One controller, however given the issues addressed above, with regards to load cell deflection the external LVDT also required signal conditioning. This was completed using a D.C. LVDT which contained the necessary signal conditioning built into the body of the LVDT. Given that there was no mechanical contact in the transducer, and therefore no wear or friction, LVDTs are popular for wear and fatigue work.

The test frame's LVDT was  $\pm 50$  mm to allow for general purpose testing, and therefore was less suited to measuring relatively small displacements. The external LVDT however has a higher resolution as it was only  $\pm 2.5$  mm, and isolated the system under test.

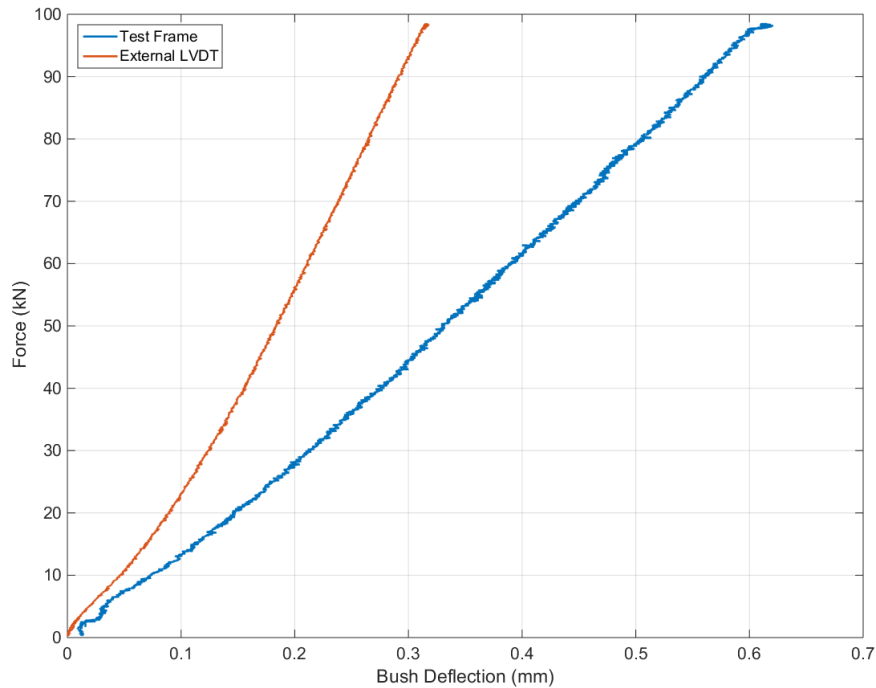


Figure 3.15: External LVDT measures only deflection of the Gar-Max bush specimen up to an applied load of 98 kN

Figure 3.15 shows the reasoning behind the use of an external LVDT to measure the deflection of the pin joint. The test frame's internal LVDT was reading nearly double the displacement actually occurring in the joint. The deflection of the load cell is the most significant contributing factor, as discussed previously.

### 3.2.4. Servo valves and PID control

Control of servo-hydraulic test frames typically use a closed loop system, using the feedback from either the force or position sensors fitted. The feedback signal was compared to the commanded signal input by the user. In order to minimise the deviation between the two, the PID (Proportional Integral and Derivative) control system was implemented (Parr, 2011), which then corrects the command signal to the Servo-Valve, controlling the fluid flow. (MOOG, 2014).

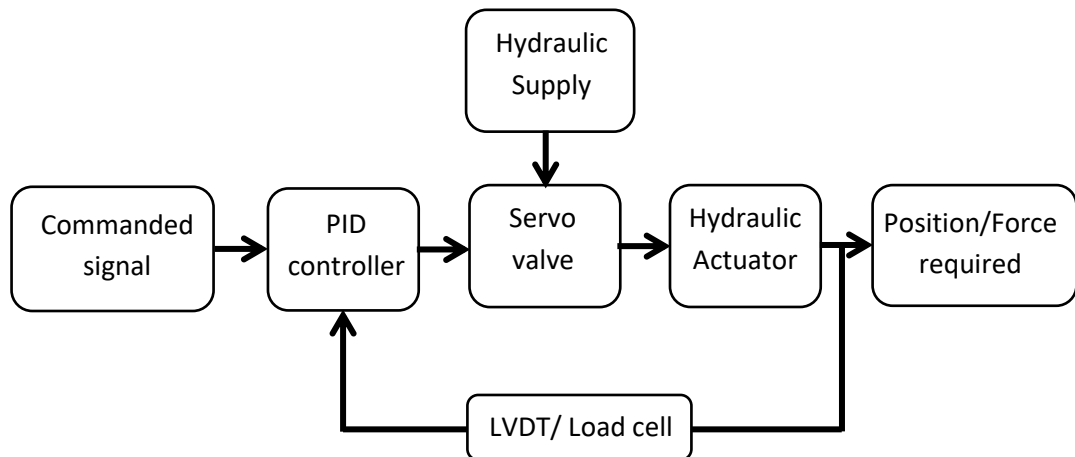


Figure 3.16: Flow chart for PID control of a hydraulic actuator

PID control was typically used for servo-hydraulic controllers as Proportional control alone cannot offer full control- described below.

An increased value increased the size of the control signal, therefore improves the speed of reference tracking, and performance of disturbance rejection. It also decreases, but cannot completely remove the output offset from the desired reference value, or the offset in the output due to constant load disturbance. Therefore an increasing value may become too large leading to saturation of the controller or limiting problems of actuators (Wilkie, Johnson, & Katebi, 2002).

Figure 3.17 is a good example for saturation of the control signal, as it shows a failed HDPE specimen which was the result of the proportional component of the PID tuning being set too high, resulting in instability of the system, and therefore extruding the HDPE out of the joint at 120 kN.



Figure 3.17: An example of poor PID tuning for HDPE bushes

Therefore it was necessary to add additional terms to the controller I and D. The addition of the I (integral) term was added to correct any steady and continuing offsets from the reference signal level (the main problems of proportional control) however it was typically one or the other, and more often it was the ability to maintain reference levels ensuring that the desired value was actually reached. This however had the disadvantage that slower response times were observed than with Proportional alone, and also some instability introduced (Wilkie et al., 2002).

Therefore the addition of the Derivative term was used, to improve the damping of the system, but will have no effects on the steady state error as the derivative of a constant error is zero. Hence by combining all three of these terms in the correct magnitudes a responsive closed loop system may be produced. (Wilkie et al., 2002).

Earlier in Figure 3.16 the basic control mechanism of a servo-hydraulic test frame was presented in the form of a block diagram. However it should briefly be mentioned here about the how the servo valve works and how its construction can affect the testing.

A servo valve enables the high frequency, and steady control of an oil flow. To fully understand how the control loop works and how the test rig behaves when operating requires some basic knowledge of the servo valve. The servo valve was controlled by applying a current to the torque motor (Armature, coil and flapper assembly in Figure 3.18) (MOOG, 2014). The amount of current applied, will determine how far the flapper will move. The amount that the flapper moves from the central position, will cause a restriction at the outlet of one of the nozzles, resulting in a pressure difference between each side of the servo valve spool, causing movement of the spool to equalise the pressure. There are some different designs of servo valves such as Jet pipe, and two stage, which have not been discussed here but operate in a similar manner (Parr, 2011).

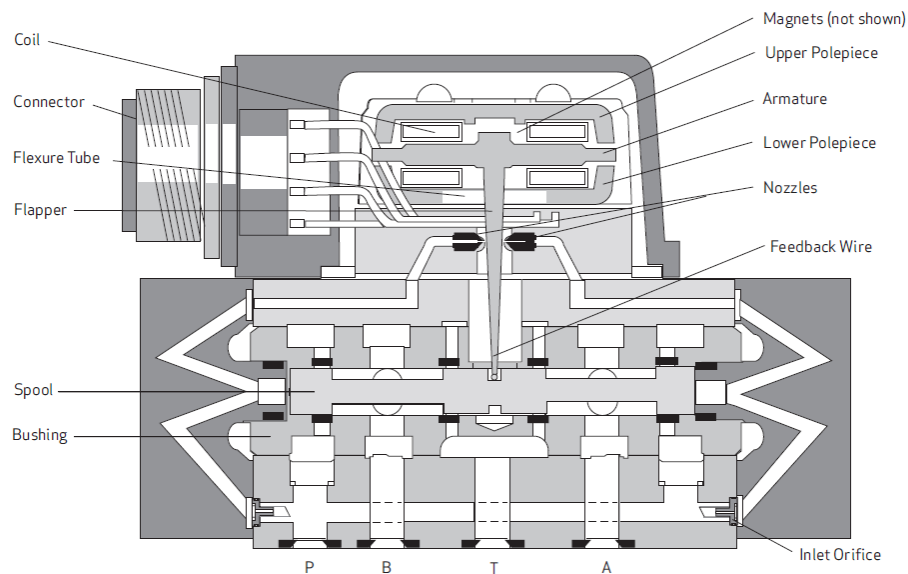


**Figure 3.18: Cross section of a servo valve which controls the flow to the actuator**

If the values for the PID tuning were not correct, the servo valve, and therefore test frame could not perform to optimum conditions. For example if the Proportional value was set too low, on a high load high cycle application, then the maximum loads demanded were not achieved, as the system was operating too slow, i.e. the spool in the servo valve was not moving fast enough in the given time to allow enough oil flow, before returning in the opposite direction. As explained above if only a step or ramp input was input then eventually the Integral term would bring the command and feedback signals to match.

A typical plot of the force command and the force feedback signals controlling the testing is shown in Figure 3.19, here the joint was oscillated between 0 and 57 kN. It can clearly be seen that there was a slight phase lag between the feedback and command signals, this was noted during testing but was known to be of little importance as the testing was based upon the number of cycles and the amplitude of oscillation. The amplitude of oscillation had to be closely monitored for different samples and loads, as the PID tuning occasionally required altering to ensure that the amplitude of the feedback signal was close to that of the command signal.

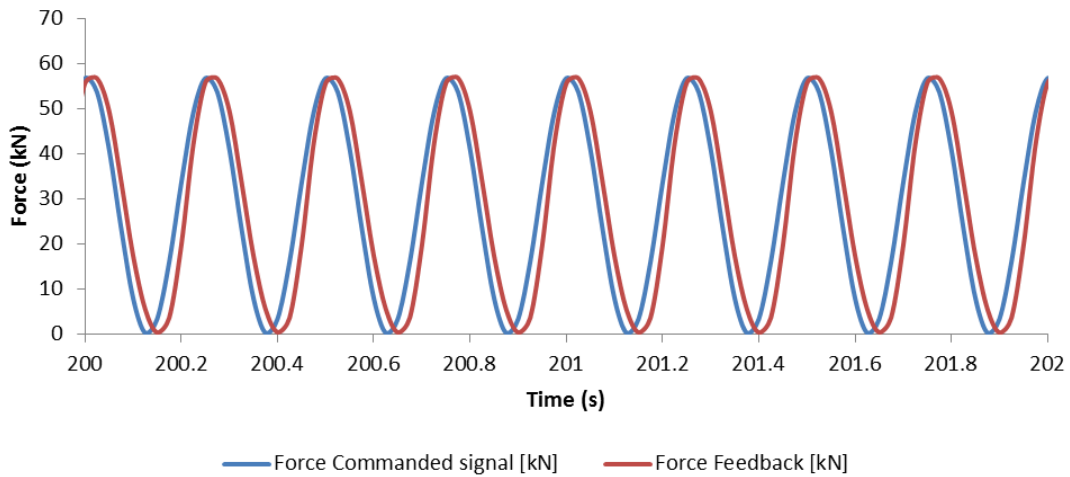


Figure 3.19: Accurate control of the radial load test rig in the Force control mode, amplitude of the commanded signal and feedback signal matches with little error for Gar-Max bushes between 0 – 57 kN

To ensure reliable repeatable testing each load case conducted was completed using the programming language Ruby and the scripting function on the controller. This not only had the advantage of repeatability, but also allowed for more efficient post processing with no unnecessary data being recorded after the stop cycle had been reached and also allowed data files to be saved with similar file names for ease of processing in Matlab. For some of the testing conducted, where no user intervention was necessary, a technique called sequencing was used allowing several scripts to be completed back to back, minimising the time required for testing.

### 3.2.5. Specimen Temperature and Humidity

Before any testing, specimens were conditioned according to a modified ASTM standard (ASTM, 2013) in an oven for 24 hrs at a temperature of 70°C and then 4 hours in between each test, to ensure that minimum moisture absorption could take place. Once tested the bushes were stored in a desiccator with silicon dioxide granules to ensure that the samples were as dry as possible.



Figure 3.20: Bushes stored in a desiccator while not being tested (a), monitoring of laboratory temperature and humidity (b)

Atmospheric temperature and humidity were also monitored during testing using a standalone temperature and humidity sensor. Control of the laboratory temperature and humidity was not possible. It was deemed unnecessary to measure the temperature of the bushes themselves during this testing as any modifications to the bushes for insertion of a thermocouple, would alter the load carrying capacity and may cause an initiation point for failure. Testing was conducted at room temperature and pressure conditions. In service loads are experienced continuously at ground level condition therefore there are no beneficial cooling aids from the atmosphere.

### 3.2.6. Fitting and Removal of Bearings

Fitting of the specimens was conducted using a custom made fitting mandrel manufactured from HDPE (High Density Polyethylene) to ensure that the bearings were not damaged during installation or removal. For both installation and removal processes, the bearings were pressed in or out using a threaded bar, and two nuts. If installation of the bearings seemed to require a large amount of force, the bushes were removed and examined.



Figure 3.21: Fitting mandrel to prevent damage to specimens upon fitting and removal

Specimens were marked in a distinctive pattern to ensure that the order and the orientation of each bush could be recorded and repositioned if required. The methodology of marking the specimens for radial load testing, is outlined below.

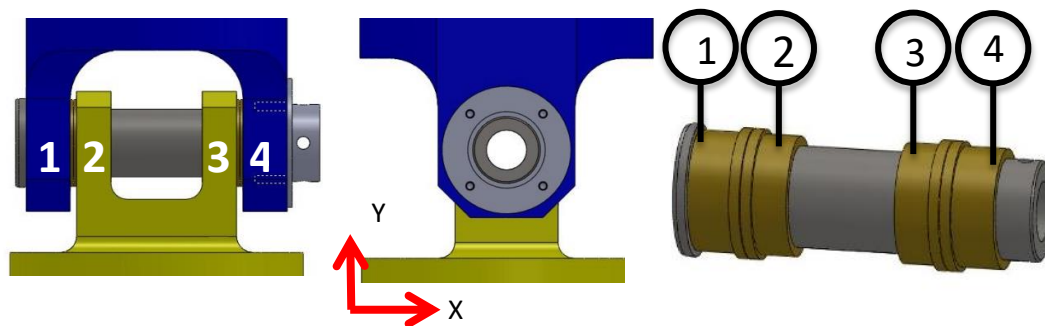


Figure 3.22: Bush notation and location in the radial load test rig

### 3.2.7. Loading Conditions

The self-lubricating polymer composite alternative bearing materials were required to be tested for 3 Aircraft lives, to minimise the risk of failure during service. Specimens that successfully complete the three aircraft lives will be tested further by the aircraft and landing gear manufacturers prior to fitting on aircraft for verification and validation purposes. A single aircraft life for a typical civil aircraft is approximately 20 years (Ruishen, 1989). Tests were conducted at realistic loading conditions from -144 kN to 167 kN with a specified number of cycles for each loading scenario. This data was intended to simulate the magnitude of the loads and the number of instances that occurred in that range, during the life of an aircraft. This data was obtained from in-flight recording and was kindly supplied by Airbus UK. Loading was not required to be continuous, such that 1 aircraft life must be completed in one test. However it was required to be conducted as an aircraft life i.e. 167 kN, 375 times, then 105 kN, 33750 times (not 167 kN, 1125 times) to avoid premature failure of the specimens by inducing low cycle fatigue.

Loads quoted below are for 1 Aircraft Life (LC), cycles are to be repeated 3 times with a sinusoidal load application at a frequency of 4 Hz.

Load (kN)	No Of Cycles	Time (Hours)
167	375	0.026
105	33750	2.344
98	3000	0.208
76	3000	0.208
70	33750	2.344
66	6000	0.417
57	3750	0.260
53	67500	4.688
47	35,600	2.472
38	143250	9.948
15	101250	7.031
-45	30000	2.083
-62	36750	2.552
-70	16875	1.172
-91	16875	1.172
-144	375	0.026
		36.951

Table 3.2: Loading conditions for the radial load test rig

A complete load cycle was from 0 to load i.e. 0 to -144 N, then back to 0. During the cyclic tests described in Table 3.2 the displacement from the external LVDT was continuously

recorded. As would be expected, this produced a sinusoidal wave as a result of the control system. In order to produce meaningful results from this data, it was necessary to calculate the maximum and minimum values of the LVDT per cycle (Figure 3.23). From there the displacement of the joint per cycle could be determined, by calculating the range of travel of the external LVDT (Figure 3.24), and any trends identified for each test case conducted. The mean and standard deviation were calculated for each test case to minimise the influence of noise. It can be seen for the example given in Figure 3.23 and Figure 3.24 using Gar-Max, there is a slight initial period of change in the first 400 cycles as running in wear occurs, and the effects of creep from the previous test are removed.

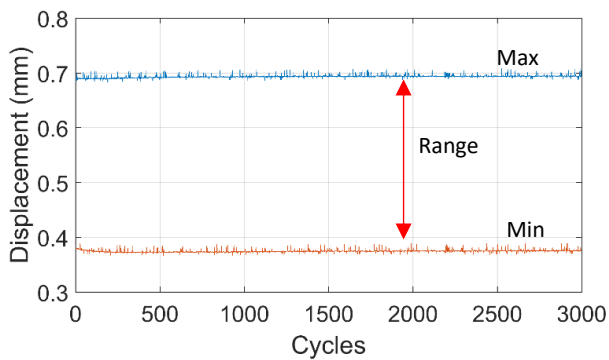


Figure 3.23: Maximum and minimum displacement per cycle

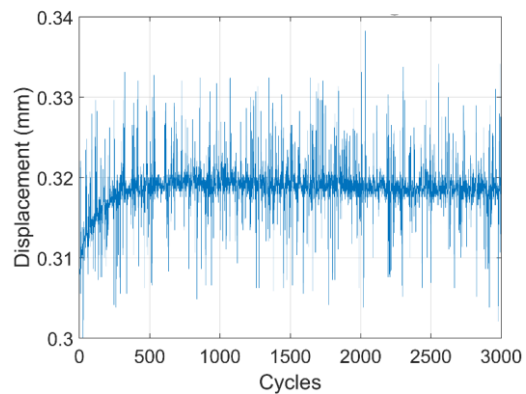


Figure 3.24: Average range of travel per cycle

### 3.3. Pin Joint Function Tester

Holding the weight of the aircraft when it is on the ground and enabling ground manoeuvres is only part of the requirement for aircraft landing gear. The other main requirement of the landing gear is to be able to extend and retract, so that it causes minimum disturbance to airflow as the aircraft is flying. Therefore the joint must be able to rotate through a limited motion only. Figure 3.25 shows the location of the joint being investigated, and how the joint must articulate, as the gear is extended and retracted.

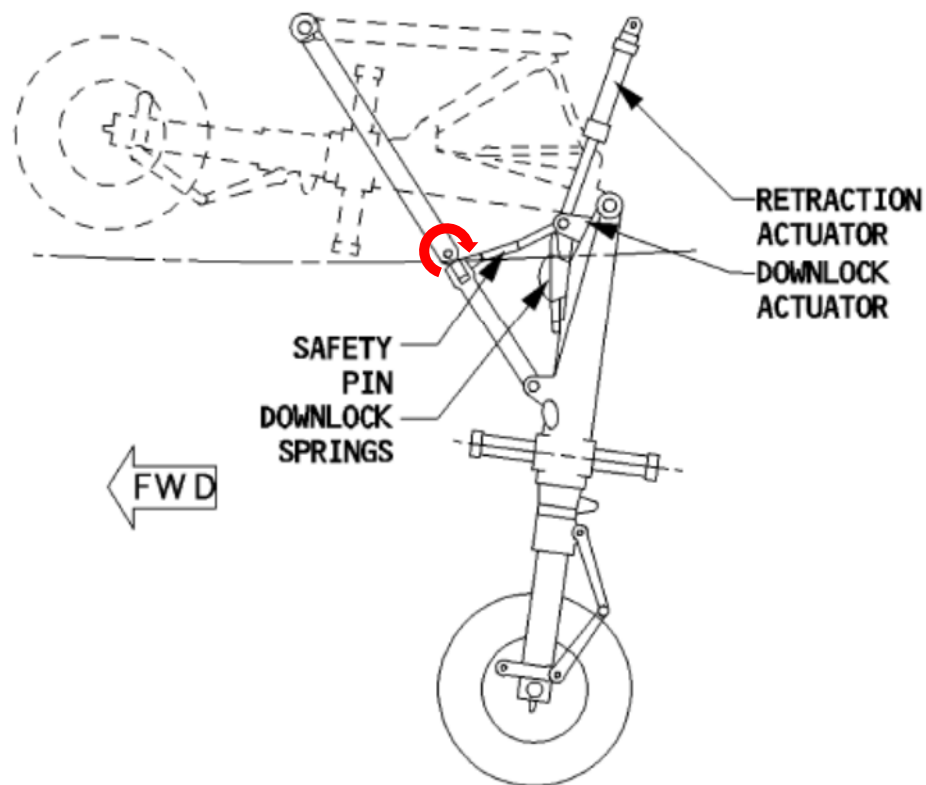


Figure 3.25: Development of loading on the drag stay joint from the extension and retraction of the gear

### 3.3.1. Loading Clevis

In order to simulate the reciprocating articulating motion of aircraft landing gear joints, a bespoke test head was manufactured. This bespoke test head was able to accept two different pin geometries, one from a main landing gear side brace and the other the nose landing gear dray stay joint. Both grease lubricated and dry tests could be conducted. The test head was fitted to a Tension Torsion servo-hydraulic test frame.

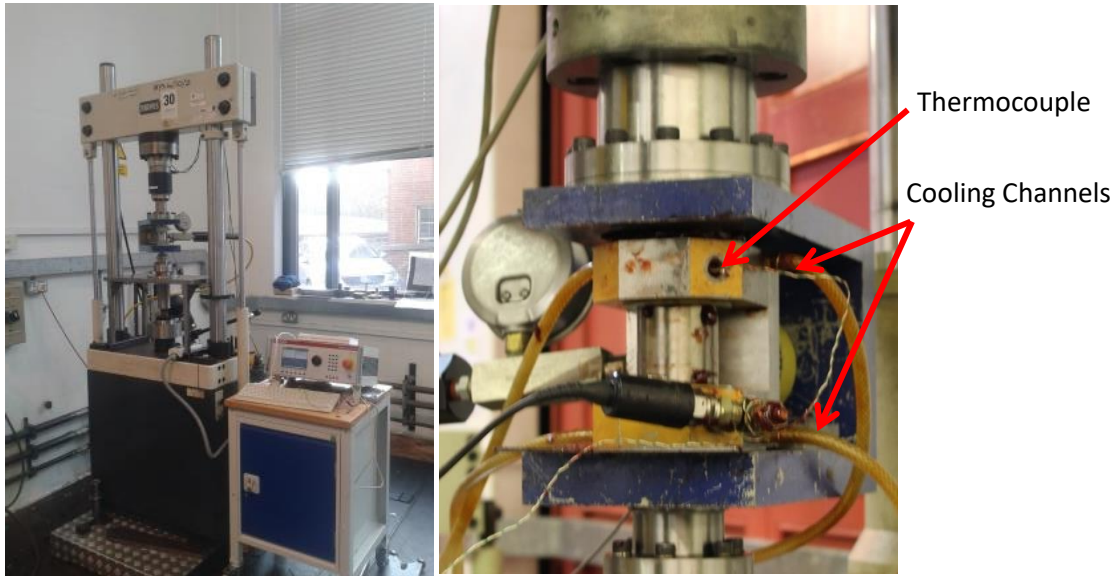


Figure 3.26: Pin joint function tester mounted to the test frame (left), the bespoke test head (right)

The outer clevis contained a pair of cylindrical roller bearings to support the pin and allow free rotation, and was mounted to the load cell so that when the radial load was applied, the torque required to rotate the pin to the position commanded could be recorded. The radial load was applied using an Enerpac hydraulic actuator between the outer clevis and the inner clevis (Figure 3.27).

The inner clevis holds the test bushes, and has cooling channels machined in to enable coolant to be circulated through the clevis to maintain a constant operating temperature for long duration testing. The load from the hydraulic actuator creates the contact pressure between the pin and bush as the outer and inner forks are pushed apart.

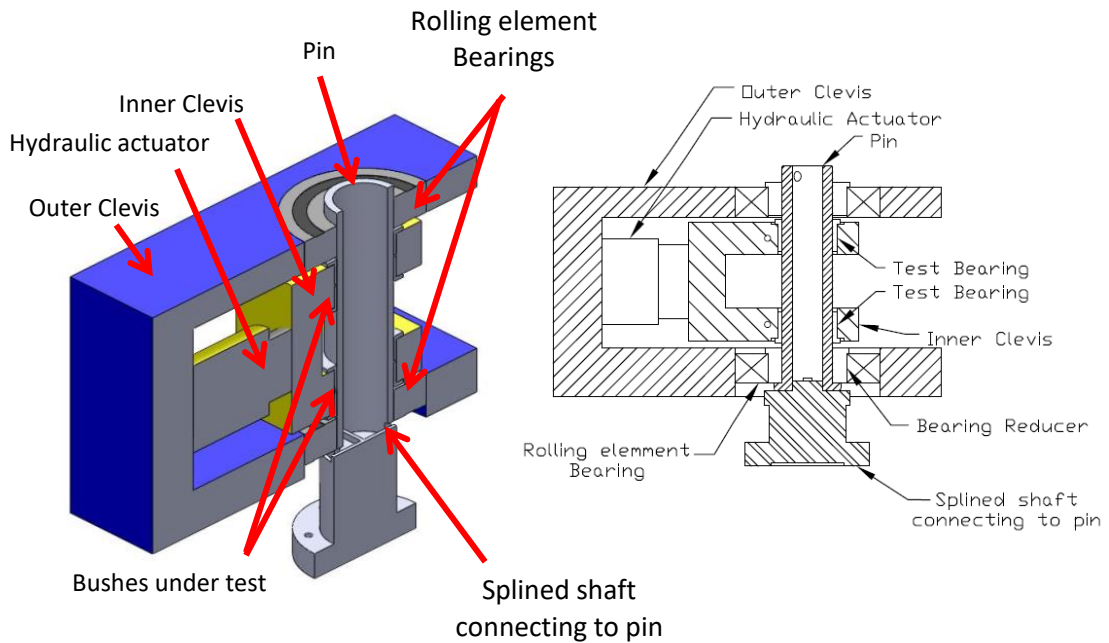


Figure 3.27: Cross section of the bespoke test head developed for testing of oscillating bearings

The pin was oscillated through the use of splined drive shafts, one of which transmits the drive to the pin, and the other eliminates any tensile loading from taking place (not shown) Figure 3.27.

### 3.3.2. Bi-axial Test Frame

The Bi-axial test frame operates in a similar manner to the single axis tension compression test frame described above, however has the addition of a second torsional actuator, servo valve and control channel on the MOOG Smartest one portable test controller. This enables bi-axial operation of the test frame. In the simulation of the extension and retraction of the landing gear, only the torsional axis was required. The actuator could rotate  $\pm 40^\circ$  per cycle.

Measurement of the rotational displacement was conducted using a Rotational Variable Differential Transformer (RVDT), which was of similar construction to the LVDT described above, however the coils are in a circular arrangement.

Similar to the load frame described above in section 3.2.2, a strain gauge based load cell was located at the top of the test frame, however due to the additional actuator the load cell was a biaxial load cell, combining a torque transducer, which was used to record the torque feedback.

### 3.3.3. Instrumentation

This method recorded the torque required to turn the pin and the position at which that torque was achieved. This however measured the torque in both the test bushes, and the two support roller bearings. The torque in the roller bearings was measured in situ on the test rig by oscillating the actuator, with no radial load applied to the joint through the bush pin interface and was found to be within the noise range of the transducer (Zhu, 2012). A typical friction co-efficient for the roller bearings used was  $\mu=0.0011$  (Schaeffler Group, 2006), which is well below the range of friction co-efficients measured in this investigation.

The radial load was measured using a diaphragm voltage based pressure transducer, calibration and data acquisition was completed using the controller and the cross sectional area of the cylinder. A Pseudo channel was set up and configured on the MOOG controller to calculate COF (Co-efficient Of Friction). This was done using the live feed from pressure transducer and the torque feedback. There were two main advantages of this Pseudo channel being configured:

- to ensure that the time stamp of the pressure transducer, and the torque cell were the same
- so that COF could be calculated as the test was running, therefore saving valuable post processing time

The temperature of the bush was recorded using a k type thermocouple, and a Cold Junction Compensator (CJC) and amplifier was used to amplify the signal to 0-10V, and was recorded by the MOOG. For lubricated bearing testing the temperature of the grease was recorded using a thermocouple, inserted into a lubrication channel. A second pressure transducer was fitted in the grease supply line for the other bearing. The purpose of this pressure transducer was to establish how easily the greases could be replenished after a test had been conducted.

Additional LVDTs were added to the test for self-lubricating polymer bushes due to the possibility of extrusion and permanent deformation at much lower bearing pressures than Aluminium Bronze. One LVDT was set up to monitor the displacement of the clevis, as it could not be distinguished if a decrease in the Enerpac pressure was as a result of the bearings wearing or hydraulic leakage back through the valves holding the radial load.

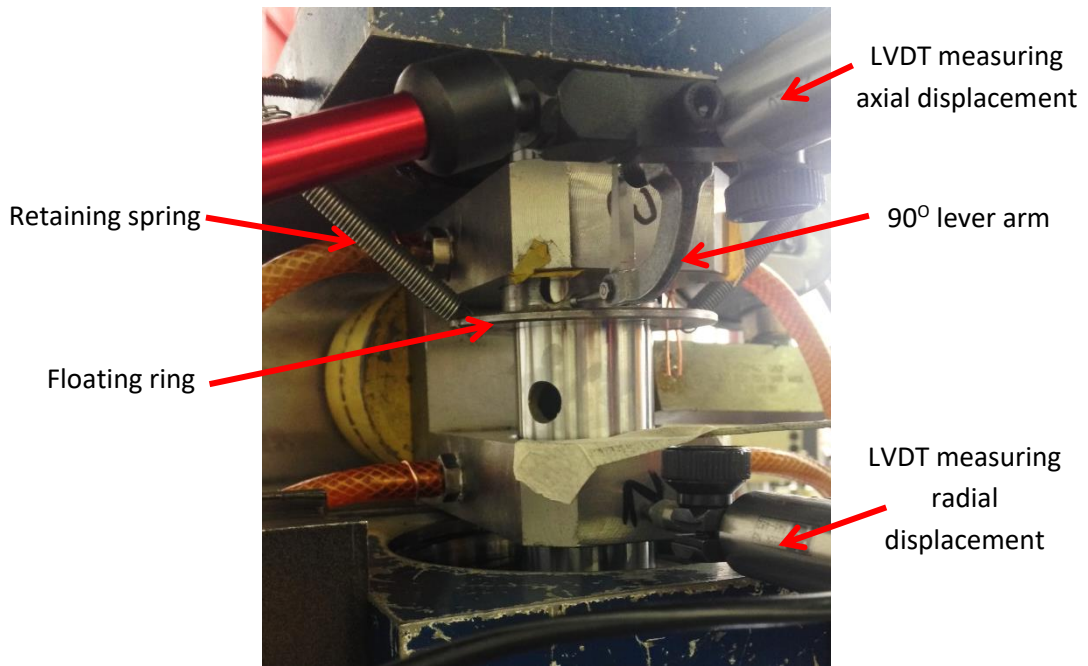


Figure 3.28: Additional LVDTs measuring movement of the clevis and bush extrusion

A second LVDT was positioned to monitor any displacement of the bearing in the axial direction, along the pin. The addition of a floating ring with a flange and 90° lever arm on the LVDT was used to monitor any change in the displacement. Clearance between the ring and pin was great enough to not come into contact, hence it was able to float along the length of the pin. Two springs with low spring constants were attached to the floating ring and to the top half of the outer clevis, ensuring that the bearing and floating ring were in contact at all times. One LVDT of each type was located on each clevis lug, as it was believed that symmetrical behaviour would occur and also due to space and instrumentation constraints.

The data recorded by the controller is listed below:

- Current Cycle
- Position Commanded [Deg]
- Position Feedback RVDT [Deg]
- Force Feedback [Nm]
- Radial Load applied [kN]
- COF
- Temperature [°C]
- Pressure of grease injected [Bar]
- Radial displacement of the clevis [mm]
- Axial extrusion of bushes [mm]

### 3.3.4. Sample Raw Results

As the pin was articulated under position control the resultant torque was recorded (Figure 3.29). The Pseudo channel on the MOOG Smartest One controller was configured to calculate the non-dimensional group  $\frac{T}{FR_p}$ . Where  $T$  is the required torque,  $F$  is the applied normal load calculated from the cross sectional area of the Enerpac and the measured pressure, and  $R_p$  is the Radius of the pin. The output as given by the controller is shown in Figure 3.30 (left).

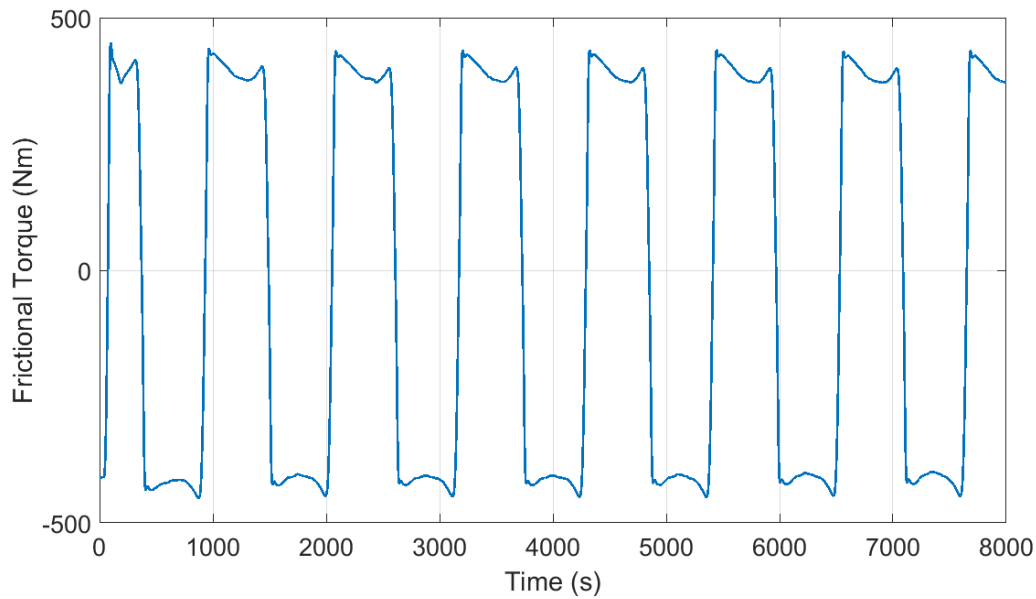


Figure 3.29: frictional torque required to turn the pin

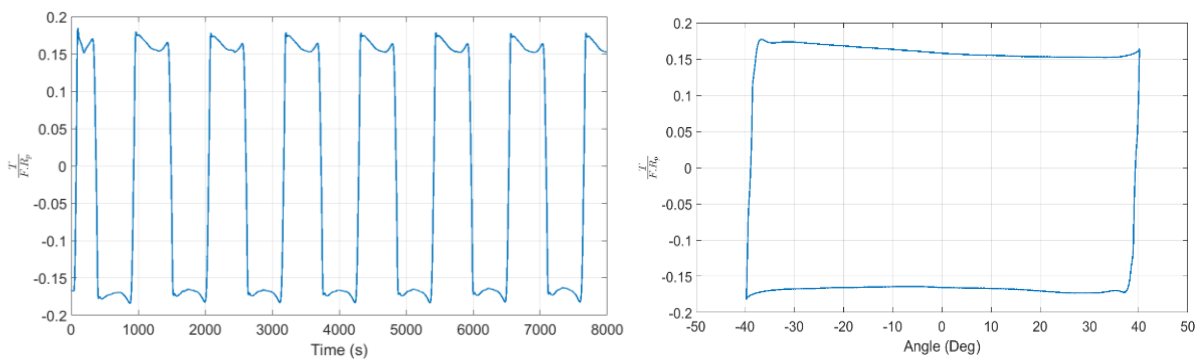


Figure 3.30: Non-dimensional group against time (left), Non-dimensional group single cycle against articulation angle (right)

Plotting the non-dimensional group against the articulation angle (Figure 3.30 right), enables the isolation of a cycle and therefore simplifies the averaging of multiple cycles. The vertical lines show where the joint is stationary as the direction of oscillation is reversed. The stick slip behaviour can be seen more easily on the horizontal lines in Figure 3.30 (right) as the grease is entrained into the contact with an increasing articulation angle by the steady decrease in the non-dimensional group. A sharp increase is then observed at the end of the articulation angle as a result of the decreasing velocity of the joint before reversing direction. The reduction in velocity causes the film to breakdown, stick behaviour to dominate and hence a sharp rise. This behaviour can be observed for the opposite direction, resulting in negative values.

Taking an average from this single cycle to obtain a value for the COF would return a result of approximately 0 which is not possible, given the positive and negative values, therefore the absolute values are taken (Figure 3.31). The change in direction is still evident where the non-dimensional group tends to 0. Inclusion of these data points in the averaging would result in a lower COF than is actually obtained, and therefore these stationary points are excluded from the averaged values by calculating the average absolute COF 2 degrees less than the extremities. An average COF value can be calculated by using the absolute values of the wave, and taking a mean value of when the joint was in motion.

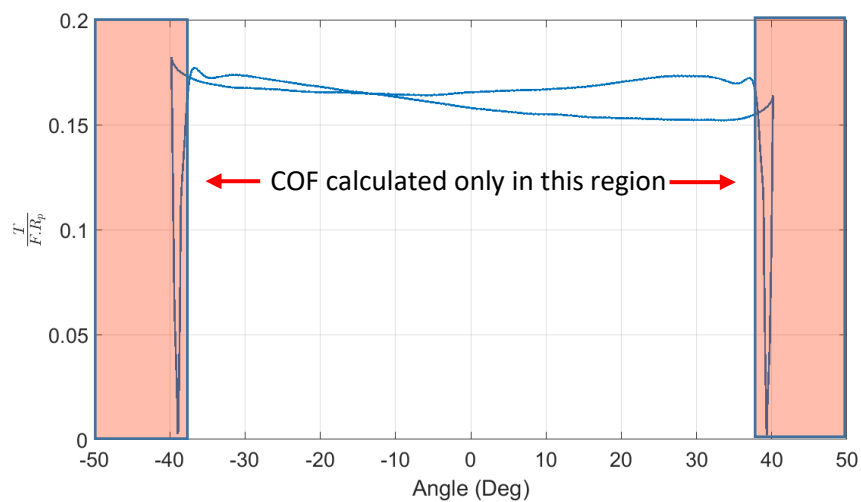


Figure 3.31: Absolute value of the recorded COF averaged between the marked positions

### 3.3.5. Loading Conditions

The radial loads applied to the aircraft joint during articulation are low in comparison to the radial loads experienced during ground handling, due to the absence of the aircraft weight. Radial loading during articulation is due to self-weight of the landing gear and air resistance only.

Test Sequence	Bearing Pressure (MPa)	Angle of Articulation (Degrees)	Surface sliding Velocity (m/s)	Lubrication
Effect of Lubricant	1.25 5 10 15	±40	0.0373 0.0747 0.145 0.299 0.373	Mobil 28 Aeroshell 22
Articulation angle	10 20	±20 ±30 ±33 ±35 ±40	0.02 0.04 0.06 0.08 0.10 0.12 0.14 0.16	Mobil 28 Shell Alvania HDPE
Lubricant life	10	±40	0.373	Mobil 28
Lubricated vs Unlubricated	10	±40	0.373	HDPE Aeroshell 22
Maintenance free	4.5 7.5 15 30 45	±20 ±30 ±33 ±35 ±40	0.02 0.04 0.06 0.08 0.10 0.12 0.14 0.16	4 self-lubricating bearings

Table 3.3: Loading conditions for the pin joint function tester

### 3.3.6. Test Specimens

A combination of grease lubricated and self-lubricating bushes were tested. For grease lubricated testing the bushes, pin and clevis were cleaned with acetone when changing greases and grease channels were primed with the new grease, prior to fitting bushes. Separate grease guns were also used to minimise the risk of cross contamination. For the self-lubricating bushes, the pin and clevis was cleaned with acetone between each specimen to remove any wear debris that may have been deposited during the testing.

### 3.3.7. Procedure

Bushes were fitted and removed from the clevis in the same manner as described in section 3.2.6. The same identification system for the bushes was used. Given that the test clevis contains two rolling element bearings to react the load with minimal friction, a pair of bushes was not used. Bushes 1&4 were substituted for bearing reducers to allow direct contact between the rolling element bearings and the pin. Bushes 2&3 were fitted into the clevis as normal, and hence for continuity the same notation has been used. Bush 2 which was located closest to the head end of the pin in the lower clevis, was again located closest to the head end of the pin in this test rig, hence bush 2 was located in the lower lug of the loading clevis. Again specimens were aligned in the Y direction (Figure 3.32) with a mark on the specimen so that wear marks were obvious and that specimens could be re inserted if required.

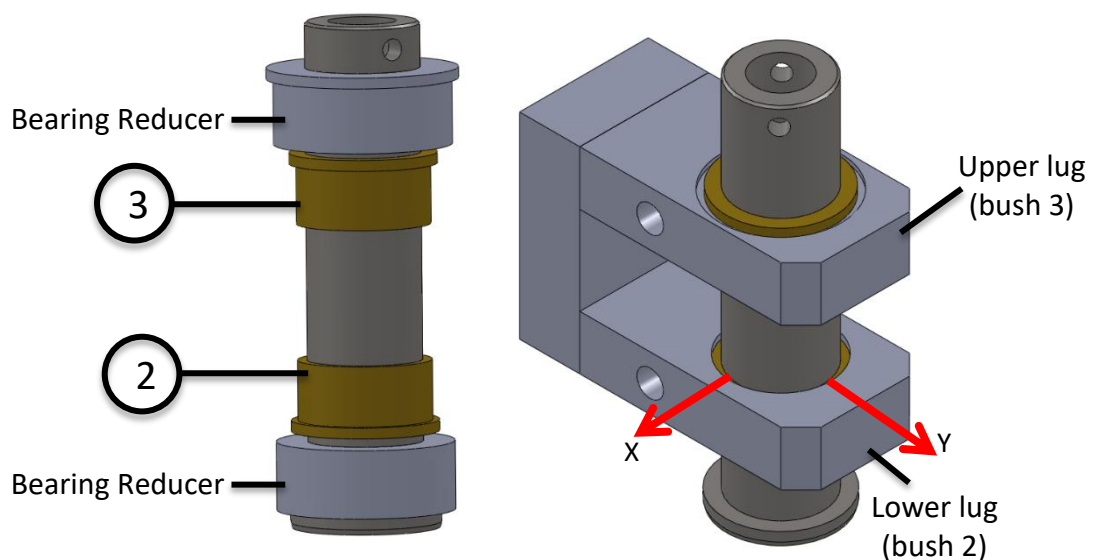


Figure 3.32: Bush Identification and bearing reducers (left), Bush orientation (right)

### 3.4. Conclusion

Two bespoke test heads were manufactured for laboratory simulation of an aircraft landing gear pin joint. The radial load test rig simulating the tensile and compressive loads applied to the joint was shown to reproduce field loading accurately and displacement of the joint was shown to benefit from the addition of a secondary external LVDT to eliminate the deflection of the servo-hydraulic test machines load cell. The pin joint function test rig was commissioned to measure the COF of dry bearings and the effects of lubricants under both field conditions and more severe loadings than would be observed during the extension and retraction of the landing gear. A clevis of reduced size and complexity was also used with a knurled shaft to determine the width of contact.

# 4.

## Characterisation of Specimens

Five maintenance free bushing materials were selected for evaluation, for use in aircraft landing gear. Four of these materials were supplied by the manufacturers as an alternative solution. The fifth specimen was manufactured in house from HDPE in order to determine how a readily available plastic bearing performed in comparison.

## 4.1. Specimens

Five low maintenance bushing materials were selected for evaluation, from a variety of bearing manufacturers. Each of the materials was of a different composition to evaluate a selection of on the market solutions. Materials were primarily selected for their performance as low maintenance bushing materials and secondly selected for their reduced weight. The bearings were supplied in two lengths to be a direct replacement for the lubricated aluminium bronze bearings currently used.

KAron B was liner consisting of a blend of powdered PTFE and other fillers bound in epoxy, bonded to a stainless steel backing, offering thermal resistance of up to 232°C. Other substrate materials were available however the steel backing was selected to ensure the performance of the liner was assessed rather than the substrate (Kamatics 2010).

Meldin 5330 was based on Polyaryetherketone (PAEK) and polyetheretherketone (PEEK) to provide good chemical resistance and strong mechanical properties, while also offering thermal resistance up to 300°C (Saint-Gobain 2014).

Gar-Max consists of a PTFE surface liner and high strength fibres twisted together encapsulated with an epoxy resin enhanced with a self-lubricating additive. Temperatures up to 163°C are quoted (GGB 2009).

Vespel SP 21, a polyimide produced from pyromellitic dianhydride (PMDA) and diamino diphenyl ether (ODA), enhanced with 15% graphite. Thermal resistance in excess of 400°C. is quoted (DuPont 2002).

Many of the commercial bearing solutions contain either PTFE or graphite in the bushes due to the benefits offered in terms of a low COF. However given the poor wear performance of pure PTFE it is often blended with additional polymers for increased wear resistance and mechanical strength along with improved performance at extreme temperatures. Thermoplastic materials such as PEEK and PAEK offer the advantages of resistance to high temperatures and improved mechanical strength as well as chemical resistance, and are therefore often selected for this purpose.

The commercial bearings supplied are already approved for aerospace applications which was a considerable factor when selecting materials for testing. The design of the bushes was completed by the manufacturers to ensure the best possible performance from the materials with regards to optimum clearances and fits. It should be noted here that the dimensions

supplied by DuPont for Vespel SP 21, were adjusted following a fitting attempt. The ID of the bush reduced significantly when fitted in the housing, as a result of the large interference fit between the OD of the bush and the housing, preventing the pin from being inserted. Flanges are present on all designs to constrain the bushes to the housing once the joint is assembled as a result of the back to back orientation of the flanges. While bush to bush contact should not occur in service it is one area that should be taken into consideration. For some materials such as Vespel 21 problems can arise as the lubricating mechanism of the bushes relies on contact with a hard smooth surface rather than the material itself. For materials such as KAron B, the liner has also been bonded to the flange of the shorter lower clevis bush in the case of contact.

HDPE was selected to enable performance comparisons of a readily available cheap light weight plastic to the current grease lubricated technology, and the high performance aerospace grade greases and polymers.

Small PVC bushes were used for the experimental validation of a contact model developed in section 5. The bushes are not characterised here as they were not manufactured and tested with the representative aircraft geometry. The design of these bushes was such that there was no flange, and only a single bushing was used in the joint to simplify and verify the loading taking place.

	Picture	E (GPa)	Composition	ID	OD
Kamatics KARON B		Substrate dependent  Liner 4.8	Steel Substrate with a liner	42.00- 42.025	49.04- 49.027  Liner 0.3 thick
Saint Gobain Meldin 5330		19	PAEK &  PEEK	42.09	49.05
GGB GAR-MAX		10 -14	Wound PTFE	42.10- 42.20	49.07- 49.02
DuPont VespeI 21		3	PDMA & ODA  15% Graphite	42.00- 42.19 <sup>1</sup>	49.25 <sup>2</sup>
HDPE		1	High Density Polyethylene	42.08- 42.19	49.04- 49.03

Table 4.1: Summary of material properties, composition and dimensions

The manufacturer's data sheets for each of the materials can be found in Appendix A. It should be noted here that due to the commercial sensitivity of the project only limited data is publicly available.

<sup>1</sup> Manufacturers' recommendation 42.39±0.02

<sup>2</sup> Manufacturers' recommendation 49.30±0.02

## 4.2. Surface Roughness of Bushes

Measurements for surface roughness were taken in the bore using a linear profilometer. Ra and Rq values were recorded for each of the bushes and in both the x and y directions, as described in section 3.7 and the values averaged. The results are displayed in Figure 4.1.

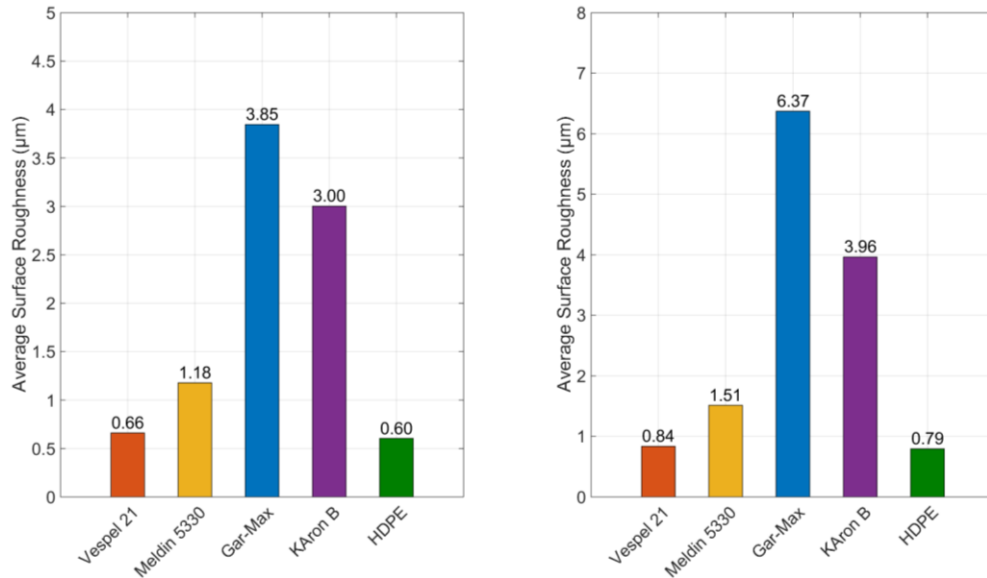


Figure 4.1: Average surface roughness values of the flanges for each material (left Ra, Right Rq)

In addition the skewness  $S_k$  was also measured and averaged for each of the bearing materials, and was found to be -0.57, -0.34, -2.55, -0.625 and -0.38 for Vespeal 21, Meldin 5330, Gar-Max, KAron B and HDPE respectively. Negative skewness values indicate that the surface contains many valleys, which is important for the storage of lubricant and wear debris within the lubrication process.

Surface roughness measurements were also taken from the flanges of all of the specimens using an optical profilometer. Measurements were taken from the flange to give an overview of materials. Optical microscopy could not be performed on the bore of the bush without sectioning, and therefore destroying a specimen. Table 4.2 shows the flange surface, along with the profile in the x direction and y direction. The arithmetic mean height ( $S_a$ ), and the root mean squared height ( $S_q$ ) of the surface was recorded along with the skewness ( $S_{sk}$ ). The results are displayed in Table 4.3.

Surface roughness of both Karon B and Gar-Max were expected to display high values given the nature of the materials. The roughness results from the flange, also confirmed the higher results and the optical image quickly shows this by the greater number of asperities visible.

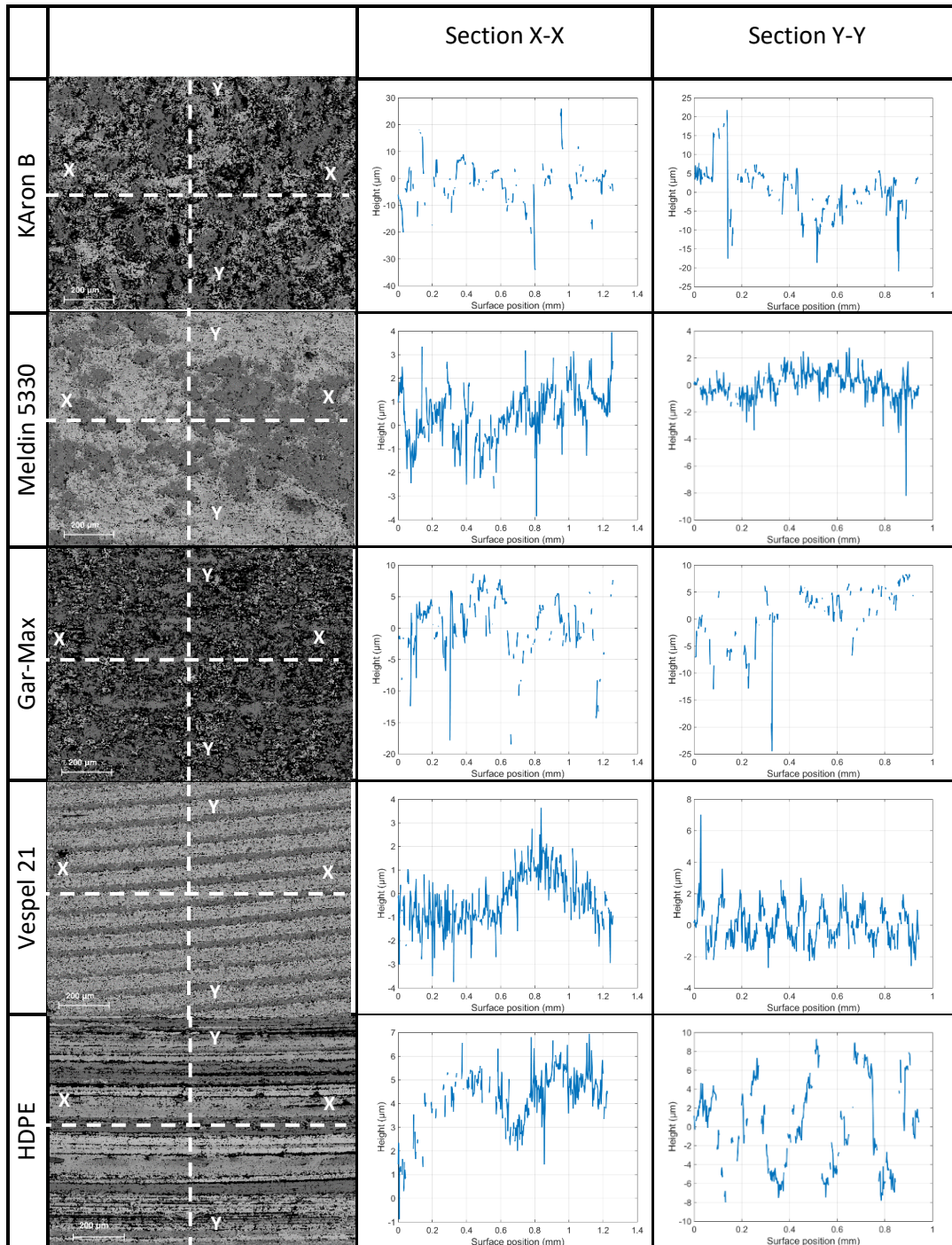


Table 4.2: Optical surface profiles and sections in X and Y directions

	Sa ( $\mu\text{m}$ )	Sq ( $\mu\text{m}$ )	Ssk
KAron B	5.283	7.238	-0.822
Meldin 5330	1.026	1.37	-1.581
Gar-Max	3.892	5.05	-1.237
Vespel 21	0.924	1.13	0.119
HDPE	3.985	4.728	0.062

Table 4.3: Summary of the Surface arithmetic mean height (Sa), surface root mean squared height (Sq), Skewness of the surface (Ssk).

For Gar-Max a filament wound bearing the fibres can clearly be observed in the surface by eye. KAron B is also of a fibrous nature and therefore relies on a similar mechanism where material is transferred from the random fibre orientation of Teflon and other fillers in the liner material to the mating counterpart which generates a thin film on the mating counterpart and reduces the COF.

#### 4.2.1. Pin Characteristics

The surface roughness of the counter face material was measured and recorded, as noted in section 2 the hardest and roughest surface will determine the wear characteristics of a system. Two designs of pin have been considered, the first was the current standard aircraft pin, used in service. The second pin was a bespoke load sensing pin, used for testing purposes. It should be noted here that no cyclic loading in the radial load test rig was completed, with the load sensing pin only static load testing was conducted. The load sensing pin was not used in the pin joint function tester. Therefore the increased surface roughness of the pin would have a negligible impact on the acceleration of wear of the bushes.



Figure 4.2 Standard aircraft load pin left, load sensing aircraft pin right

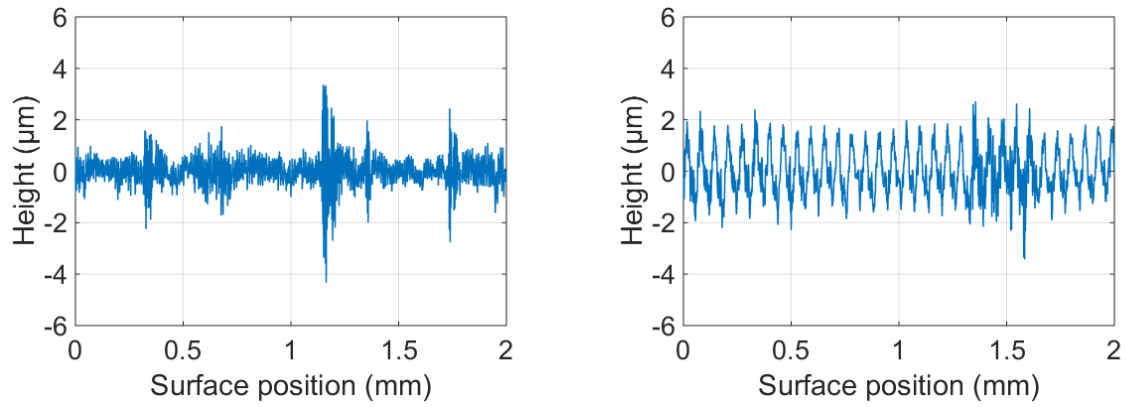


Figure 4.3: Surface roughness plots of standard aircraft pin (left), and load sensing pin (right)

The Ra values of the two pins was found to be  $0.14 \mu\text{m}$  and  $0.632 \mu\text{m}$  respectively and Rq values were found to be  $0.24 \mu\text{m}$  and  $0.733 \mu\text{m}$ . The rougher surface of the load sensing pin was attributed to the turning process. The machining marks can clearly be seen in Figure 4.3.

Given that the wear is also governed by the hardness of the asperities as discussed in section 2. The hardness was also measured. The standard pin was found to have a hardness value of 48 Rockwell C, while the load sensing pin had a value of 47 Rockwell C.

### 4.3. Mass of Bushes

Comparisons between the specimens in terms of mass were made. A complete set of 4 bearings (2 for the upper clevis and 2 for the lower clevis) were weighed to compare potential weight savings if installed in aircraft landing gear. Figure 4.4 shows the lowest joint mass to be HDPE, however out of the commercial solutions Meldin 5330 and Vespel 21 are the lightest. KAron B unsurprisingly was the heaviest following the Aluminium Bronze, as a result of the stainless steel backing. Measurements were taken using a Sartorius Electronic Analytical Balance Basic Plus BP210D with a readability of 0.01 mg. It should be noted here that potential weight savings could be higher still as the mass saving from the removal of lubricants has not been considered here.

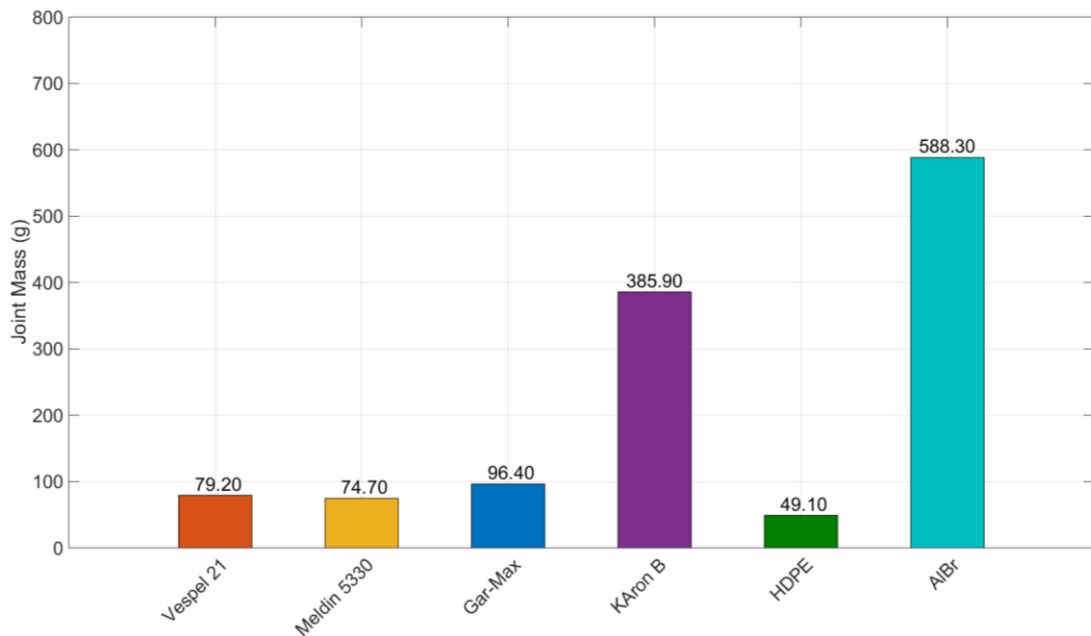


Figure 4.4: Comparison of bush mass for all the bushes in a joint

#### 4.4. Deviation from Roundness Plots

The deviation from roundness was measured on an upgraded Taylor-Hobson Talyrond 100, with a LabView interface programme. LabView interfaces with the Talyrond using the existing Talyrond stylus for the out of roundness measurement, and a newly fitted rotary encoder complete with a Digital to Analogue Converter (DAC) for the rotational position. This generates a 0-360° linear slope for each revolution, building up a saw-tooth wave for multiple revolutions.

A digital scale unit was included to measure the height of the probe. For all measurements taken a 6 mm diameter ball type probe was used to ensure that surface roughness was not significantly influencing the roundness measurements.

Table level was measured through a ball ended LVDT, running on a machined plate. The ball ended LVDT was used to minimise friction between the machined plate, and the LVDT point of contact. A bespoke securing collar was produced to clamp the bush to the table using the flange.

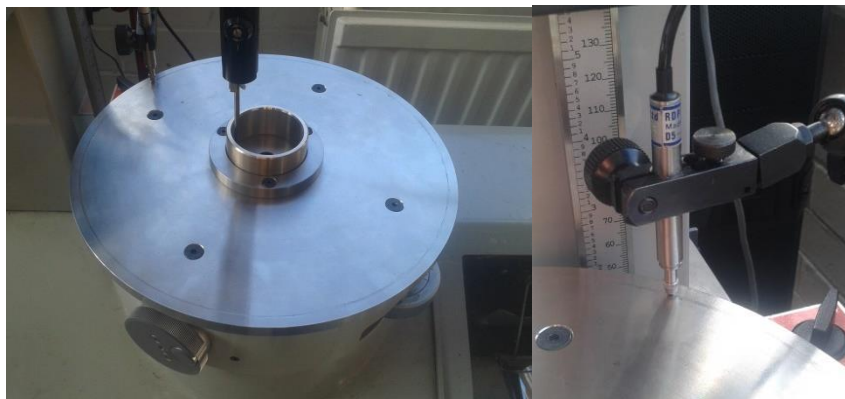


Figure 4.5: Talyrond clamping plate and LVDT measuring table level

Figure 4.6 shows a schematic of the complete Talyrond measurement system, and the signal conditioning required before the data is simultaneously logged. The stylus was calibrated to  $10\ \mu\text{m} \pm 5\ \mu\text{m}$ .

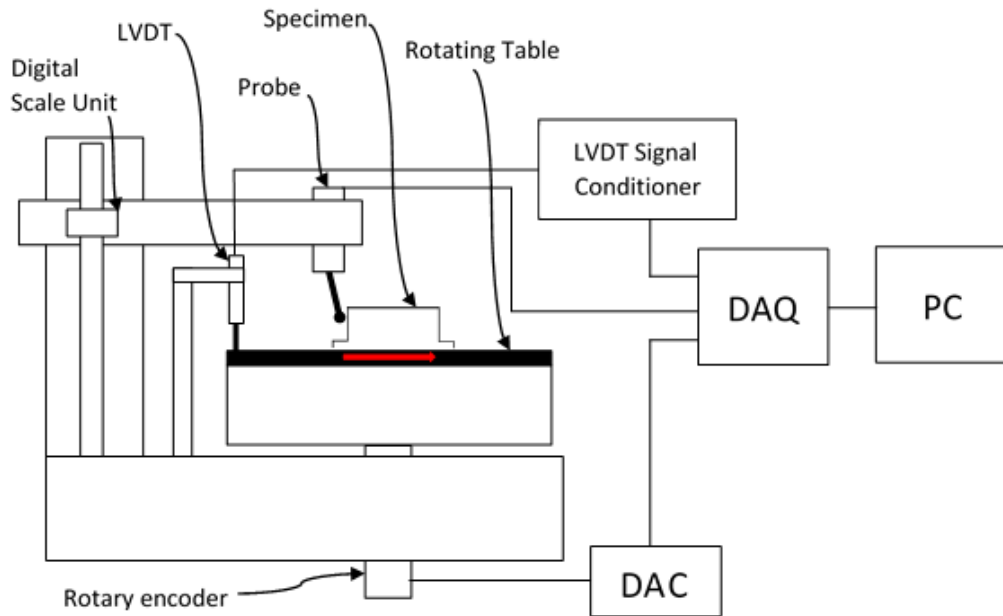


Figure 4.6: Schematic of the bespoke Talyrond data acquisition

The bushes were measured at several heights throughout the course of the testing programme. The measurement heights for the two types of bush are shown in Figure 4.7 for the internal diameter. The external measurement heights were reduced, due to the clamping collar Figure 4.8.

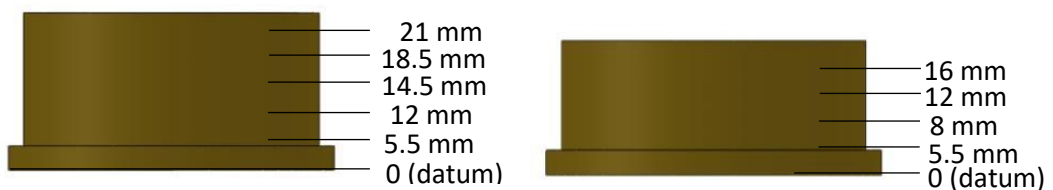


Figure 4.7: Bearing measurement locations for ID measurements

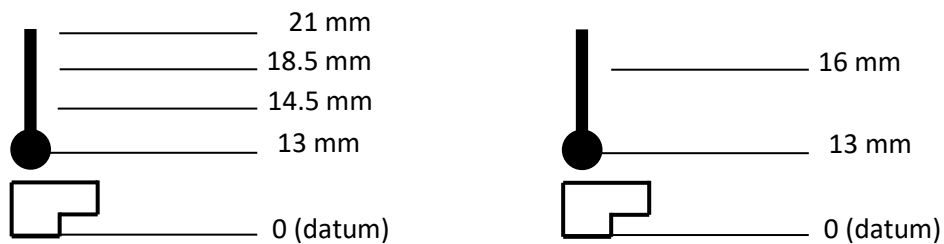


Figure 4.8: Bearing measurement locations for OD measurements

For the radial load test rig (section 3.1) bushes were measured before any testing was conducted, and then after the first life cycle had been completed. For the second life cycle, bushes were measured after each load case in the life cycle (table 3.6.1 section 3.6), and finally after the third life cycle. For the pin joint function test rig (section 3.9) bushes were measured only before and after testing. To ensure that the data was reliable, 6 revolutions for each measurement were recorded.

## 4.5. Conclusion

Five maintenance free bearings were selected and characterised. Optical surface roughness measurements of the flanges, identified KAron B to be the roughest material with an Sa value of 5.283  $\mu\text{m}$  and Vespel 21 to be the smoothest with an Sa of 0.924  $\mu\text{m}$ . This trend was observed for both arithmetic mean height and RMS height of the surface.

Surface roughness of the bore was measured using a linear profilometer, identifying Gar-Max to be the roughest material with an Ra of 3.85  $\mu\text{m}$  and again Vespel 21 to be the smoothest with an Ra 0.84  $\mu\text{m}$ . Again for both Ra and Rq values.

Surface roughness heights from both the bore and the flange showed Vespel 21 to be the smoothest out of all the commercially available solutions, followed by Meldin 5330, KAron B and Gar-Max.

The mating surfaces of the bearings were also measured for surface roughness. The standard specification aircraft pin was found to have an Ra value of 0.14  $\mu\text{m}$  and the bespoke load sensing pin was 0.632  $\mu\text{m}$ . The higher value was attributed to the turning marks left from the manufacture of the pin. The hardness was also measured to be 48 and 47 on the Rockwell C scale. The hardness of the pins in comparison to all of the bearing materials shows that wear is more likely to occur in the bore of the bushing than the pin.

Bearings were weighed as a complete set and compared to assess potential weight savings on the aircraft landing gear. Meldin 5330 was found to be the lightest material and KAron B was the heaviest due to the stainless steel backing that the liner material was bonded to.

Roundness of the specimens was characterised using an upgraded Taylor Hobson Talylond 100. A rotary encoder, digital scale unit and an LVDT were added to the unit, and recorded through a custom data acquisition system. The upgraded measurement system showed good repeatability for 6 revolutions per measurement.

# 5.

## Static Deformation of a Radially Loaded Pin Joint

In this chapter static loading of a pin joint is completed. A model to predict the displacement of a polymer composite bush of a finite thickness under an applied load is developed. The model was experimentally validated initially with small PVC specimens and later for the materials identified in the previous chapter.

## 5.1. Theoretical Modelling of Displacement

It is proposed in this work, that the contact of a pin loaded against polymer composite bushes progresses through a number of different stages as the load is applied. Stage (i) typically occurs at low loads, depending on the Young's modulus of the bearing material, and is when the main non-linear displacement occurs as the arc of contact and hence area increases with increasing load. Stage (ii) occurs when the contact is fully "saturated", the arc of contact has increased to approximately  $180^\circ$ , and the joint stiffness remains constant, therefore all deformation is elastic deformation of the bearings. Stage (iii) and (iv) is the non Hookean behaviour of the polymers at higher loads, leading to the plastic deformation of the bearings through extrusion.

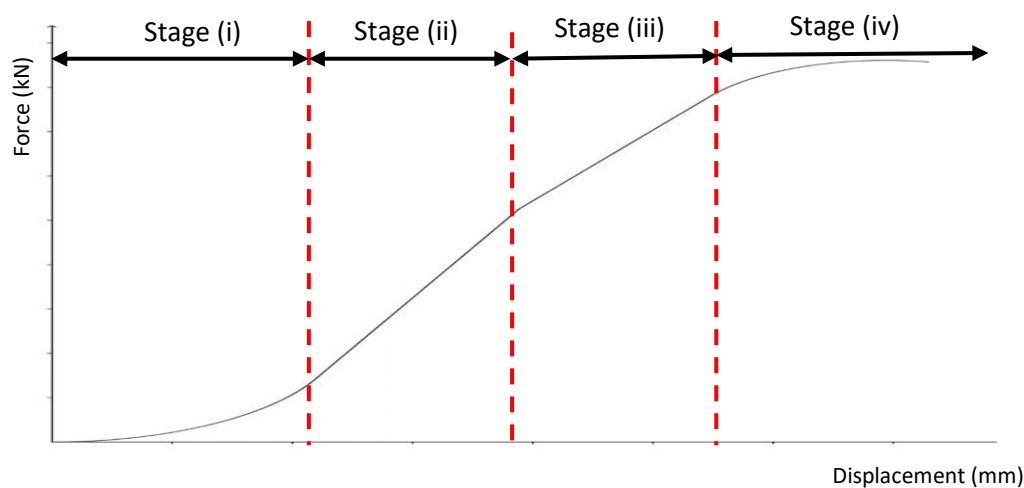


Figure 5.1: Proposed stages of pin joint contact for polymer bushes

The main focus of this research is to evaluate the non-linear contact occurring in stage (i) for the polymer composite bearing materials. For these materials it is expected that the largest wear rates will occur during this period, for a non-rotating joint such as that in an aircraft landing gear when down locked in position. The application and removal of load would result in the largest amount of counterface sliding. Depending on the number of cycles that this type of joint would be subjected to would be one of the main causes of failure. Stage (ii) would be linked to the fatigue limits of the material, as the arc of contact is not changing further upon the application and removal of load within this region, all deformation is due to the material properties. Typical S-N curves of the material would provide the relevant information for cyclic loading.

The widely accepted method of evaluating non-conforming circular geometries in contact is the use of Hertzian contact theory as detailed earlier in section 2.4. Hertzian contact is used

for point and line contact, where the area of contact is small with respect to the size of the contacting bodies. Contact between diverging and in certain circumstances conforming cylinders, if the outer radius is large enough, results in line contact. If the clearance between the two cylinders is too small, or the difference in moduli is too large then the assumption of the contact area being small in comparison to the size of the contacting bodies is violated. For the application here the contact area is large due to the significant difference in moduli and therefore the theory cannot be used.

Therefore a method for calculating the displacement of a plastic journal bearing of finite length has been developed based upon the work conducted by Wenger (1964), using the circular equation approach. Ligterink & de Gee (1996) used a similar approach for the calculation of wear in oscillating bearings, however displacement had to be measured. This displacement therefore was either determined from wear testing or was a guessed value.

Wenger's approach assumes that the shaft is not subjected to any deformation, which is a reasonable assumption when dealing with metal shafts in polymer bushes, as the majority of deformation will occur in the bush. The model also assumes a bush with no initial wear, and therefore can be extended to determine the running in wear occurring as a result of the loading and unloading of the bushes.

Being able to predict accurately the displacement of a bearing due to applied load before testing, eliminates the guess work in either having to predict the combination of wear and displacement, or by conducting expensive full scale testing only to discover that the bearing is unsuitable.

Therefore the model has been set up to require only the inputs of Force ( $F$ ), shaft radius ( $R_p$ ), internal bush radius ( $R_b$ ), bush wall thickness ( $bt$ ), total bush length ( $bl$ ), and the material properties of the contacting bodies  $E$  (modulus of elasticity) and  $\nu$  (Poisson's ratio). From these parameters, it can be seen that the model is capable of handling 3-dimensional problems, rather than just the 2d case considered by Wenger (1964) and Ligterink & de Gee (1996).

It should be noted here that when considering a system with multiple bushes, a simplification is made that lengths of the bushes in contact with the pin can be summed together to obtain the total length of the bush i.e.  $bl = L1 + L2 + L3 + L4$  (Figure 5.2)

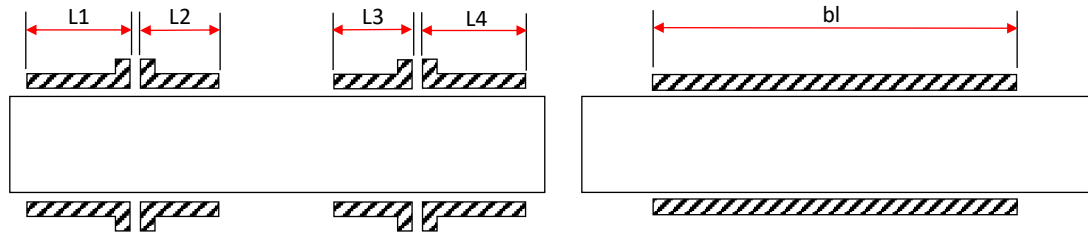


Figure 5.2: Bush lengths can be summed together

The contact area is directly proportional to the displacement, and therefore force applied, hence as the force is increased, so will the area of contact. However this will lead to a decreasing rate of displacement, as more of the polymer composite is resisting the applied load.

The assumptions made are:

- The bushing material has a much lower modulus of elasticity than that of the shaft material, hence negligible deformation of the shaft will occur (in accordance with Wenger)
- No deformation of the housing occurs
- In the centreline of loading, the equation  $E = \sigma/\epsilon$  remains valid, where  $E$  is the modulus of elasticity, and  $\sigma$  and  $\epsilon$  are the stress and strain in the bush respectively
- No tensile components act upon the bush
- The datum for total displacement measurement is from the centre point of the bushing ( $C$ )
- Upon initial contact line contact will occur when considered in 3D, and point contact in 2D.
- Loading is considered to be parallel
- As the area of contact increases, only the width of contact increases, therefore the material resisting the applied load increases.
- For simplicity the area of contact is considered to be rectangular, with the maximum equal to the projected area
- Only vertical deflection of the bush is considered, axial deformation of the bush is not considered
- The maximum displacement of the bush occurs in the centre line of loading.
- The model is operating in the elastic region only
- Both bush and shaft are perfectly round and concentric and can be represented by the equation for a circle at any point along the length

To develop the model it must first be assumed that the bush is loaded parallel, such that line contact occurs initially, and also that the radii of the outer and inner surfaces of the bush are great enough to be considered infinite, such that they are parallel. The distance between the outer and inner surfaces is  $bt$ , the thickness of the bush.

Consider then an element of width  $(2.\delta x)$ , which is a thin slice of the bush about the centreline of the loading direction, sufficiently thin that the line load can be considered to be evenly distributed across the width of the element.

Assume that the element is in equilibrium in the radial direction due to the equal and opposite loading from the remainder of the bush. Deformation of the bush in the axial direction is considered to be negligible compared to that in the vertical direction when in the elastic region. Then it can be seen that the application of a compressive load would then result in a reduction in the height of the element, developing both a stress and strain within the material. This change in displacement can then be denoted  $\delta$ , which conventionally can be calculated by re-arranging the expanded form of Young's Modulus (Equation 5.1)

$$E = \frac{Fl_o}{A\delta} \quad (5.1)$$

Where  $F$  is the applied load,  $l_o$  is the original length of a generic specimen,  $\delta$  is the change in length,  $A$  is the cross sectional area of the specimen and  $E$  is the modulus of elasticity. Applying Equation 5.1 to the element considered above of height  $bt$ , the original length of a generic specimen can be redefined as the bush wall thickness for simplicity. The cross sectional area ( $A$ ) can be redefined as  $2.\delta x$  multiplied by the length of the bearing in the axial direction  $bl$ . Therefore Equation 5.1 can be re-written as

$$E = \frac{F.bt}{2.\delta x.bl.\delta} \quad (5.2)$$

Given the modulus of Elasticity for the bush is known, and the cross sectional area of the element is the width of contact multiplied by the length of the bearing  $bl$ , the change from original height (or length if the typical notation of Young's Modulus is used)  $\delta$ , can be calculated for a given applied load.

For the assumptions made earlier, the width of contact is infinitely small and does not change in size. However given the geometry of the pin joint, it is clear that the area of contact will increase for an applied load, additionally the contact along the axial length of the bush is already at the maximum, the only dimension to increase in size is the width of contact.

Therefore it can be said that for the polymer composite pin joint loaded with a steel shaft the width of contact and hence area of contact will be a function of  $\delta$ .

An important simplification is made here that the cross sectional area in Equation 5.1, used to calculate the modulus of elasticity, is the same as the assumed rectangular area of contact of a bearing. By making this simplification an increase in load applied to the bearing/shaft interface, will generate a larger area of contact. This larger area of contact, will then increasingly resist the applied load, through material properties, as explained by Equation 5.1.

To obtain an expression for the change in area in terms of  $\delta$ , consider only the geometry of a pin loaded against a bush, at an exaggerated clearance (Figure 5.3), where  $R_b$  and  $R_p$  are the internal radii of the bush and external radii of the pin respectively. If reference is taken from the centre of the bush ( $C$ ), then the eccentricity  $e$  is the sum of the radial clearance and the deformation of the bush  $\delta$ .

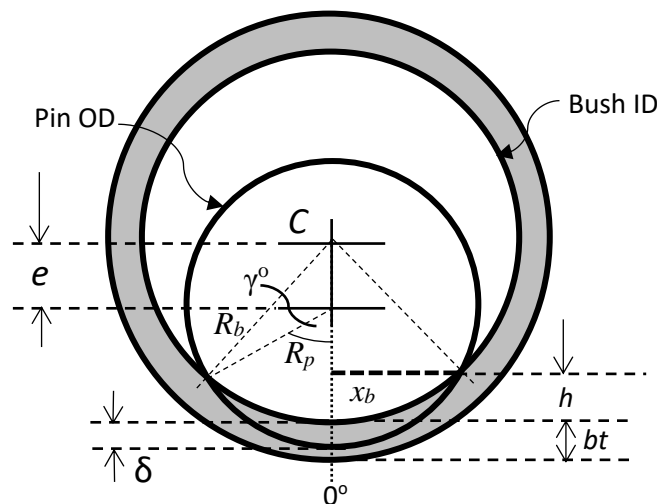


Figure 5.3: Schematic of the circular equation approach, where  $C$  is the centre point of the bush,  $e$  is the eccentricity of the pin bush relationship,  $h$  is the height of the arced section,  $x_b$  is half chord length,  $\gamma$  is half the arc of contact and  $\delta$  the displacement of the pin into the bush

Therefore the circular equation approach states that circle representing the bush has the equation

$$x_b^2 + y_b^2 = R_b^2 \quad (5.3)$$

where  $x_b$  and  $y_b$  are the horizontal and vertical components of the bush about the centre point  $C$  and the circle representing the pin has the equation

$$x_p^2 + (y_p - e)^2 = R_p^2 \quad (5.4)$$

Similarly with  $x_p$  and  $y_p$  being the horizontal and vertical components of the pin about the centre point C, with the addition of the term  $e$  to allow for the offset. Given that it has been assumed that only vertical movement of the pin occurs when loaded, the intersection of the circles will have the same value for the horizontal components  $x_b$  and  $x_p$ . Therefore where the equations intersect a simultaneous equation is developed by equating  $x_b$  and  $x_p$ .

Using the same circular equation approach as Wenger (1964), Ligterink & de Gee (1996) and Deters et al. (2003), the  $y$  component can be written in terms of displacement and the radii of the surfaces, since  $x_b=x_p$

$$y_b = \frac{R_b^2 - R_p^2 + \delta^2}{2\delta} \quad (5.5)$$

Substituting  $y_b$  (Equation 5.5) into Equation (5.3),  $x$  can be expressed entirely in terms of the displacement and the radii of the bodies. This would then be considered the half width of contact.

$$x_b = \sqrt{R_b^2 - \left(\frac{R_b^2 - R_p^2 + \delta^2}{2\delta}\right)^2} \quad (5.6)$$

Returning to the element considered above under the application of a load, the assumption of line contact will no longer be valid, as the width of contact will increase, therefore  $\delta x$  will become  $x_b$ . Re-arranging equation 5.2 to become

$$x_b = \frac{F \cdot bt}{2 \cdot bl \cdot \delta \cdot E} \quad (5.7)$$

Enables easy substitution of Equation 5.6 for  $x$  the half contact width in place of the half width of the element, which gives.

$$\frac{F \cdot bt}{2 \cdot bl \cdot \delta \cdot E} = \sqrt{R_b^2 - \left(\frac{R_b^2 - R_p^2 + \delta^2}{2\delta}\right)^2} \quad (5.8)$$

Which is an expression with only geometrical material and displacement parameters. Expanding and simplifying, an expression for the displacement can be written as

$$\delta^4 - 2\delta^3 R_p - \frac{F^2 bt^2}{4E^2 bl^2} = 0 \quad (5.9)$$

Which is a quartic function, and can be solved using Ferrari and Cardano's (Merzbach & Boyer, 2011) solution for the 3<sup>rd</sup> and 4<sup>th</sup> root,

$$\delta = -\left(\frac{b}{4a}\right) + S - \frac{1}{2}\sqrt{-4S^2 - 2p - \frac{q}{S}} \quad (5.10)$$

where

$$p = \frac{(8ac - 3b^2)}{8a^2} \quad (5.11)$$

$$q = \frac{b^3 - 4abc + 8a^2d}{8a^3} \quad (5.12)$$

$$S = \frac{1}{2}\sqrt{\left(-\frac{2}{3}p\right) + \frac{1}{3a}\left(\frac{Q + \Delta_0}{Q}\right)} \quad (5.13)$$

And

$$Q = \sqrt[3]{\frac{\Delta_1 + \sqrt{\Delta_1^2 - 4\Delta_0^3}}{2}} \quad (5.14)$$

with

$$\Delta_0 = c^2 - 3bd + 12ae \quad (5.15)$$

$$\Delta_1 = 2c^3 - 9bcd + 27b^2e + 27d^2a - 72ace \quad (5.16)$$

And a, b, c, d and e are the co-efficients relating to Equation (5.8)

$$a = 1, \quad b = -2(R_p), \quad c = 0, \quad d = 0, \quad e = \frac{(F^2(bt^2))}{E^2bl^2}$$

Therefore the total displacement can then be calculated using Equation (5.10), for the third negative root.

For all the current conformal contact models the bush wall thickness has always been neglected, with the contact normally evaluated as a hole in a flat plate. For the case of a heavily loaded polymer journal bearing this assumption is no longer valid especially if loaded between a steel shaft and steel housing. Hence it is important that the thickness of the bearing itself must be considered in the calculation of the contact area.

Figure 5.4 shows the shape of the load displacement curve generated using the model (Equation 5.8). The model has been run 10 times with only the OD of the bearing changed, to show the effects the calculated wall thickness of the bush has on the deflection of the bushing material. The wall thickness has largely been neglected in previous attempts to solve

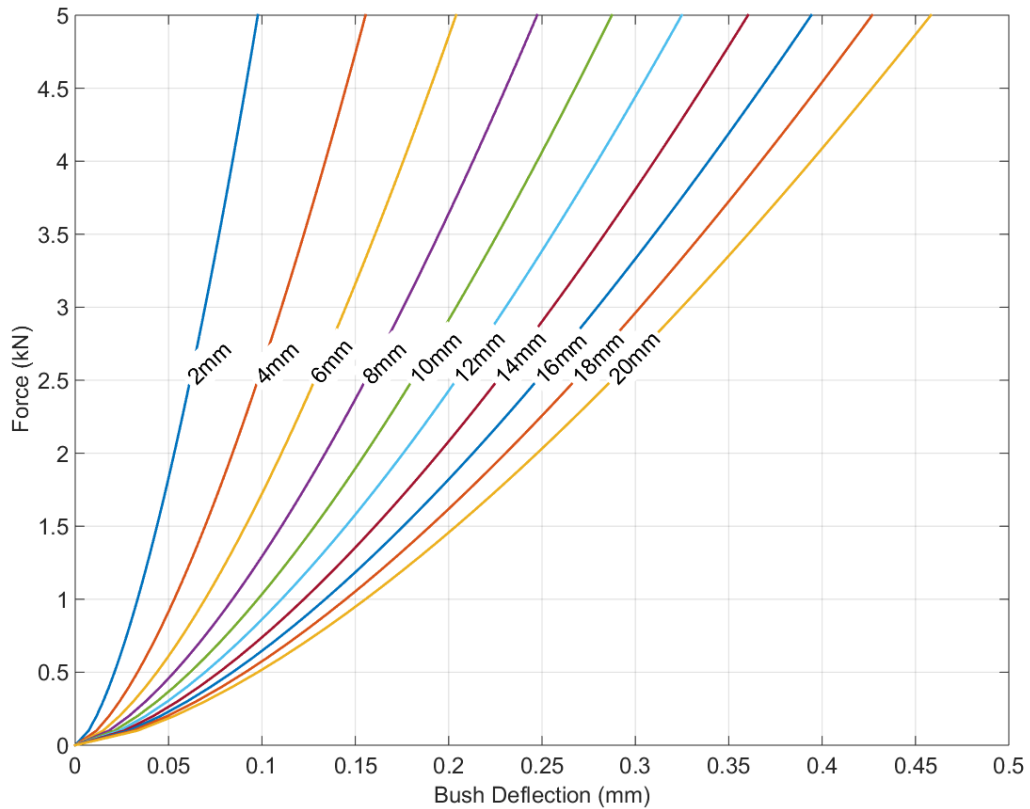


Figure 5.4: Predictions of force and displacement, with varying OD to show the effect of bush thickness increasing from 2mm to 20mm

the contact of elastically dissimilar conforming bodies. ESDU 87007 (2010) explains the importance of the wall thickness of the self-lubricating bearing, in terms of the load carrying capacity, and the heat dissipation, where a thin wall improves both. The figure generated here shows the higher load carrying capacity at lower wall thicknesses. Additionally it shows that for thicker bearings there is little difference as would be expected for a hole in an infinite flat plate.

The model developed above was expanded to enable calculation of the arc of contact. The calculated displacement of the shaft required modification using the relationship (Equation 5.17) given by Deters et al. (2003), to give the height of the arced portion ( $h$ ) (Figure 5.3) from the Diameter of the bush ( $D_b$ ), for the calculation of the actual contact width ( $x_{bm}$ )

$$h = \frac{\delta D_b}{2} \tag{5.17}$$

$$x_{bm} = 2\sqrt{h(2R_p - h)} \quad (5.18)$$

The subtle difference between Equation (5.6) and Equation (5.18) for the calculation of the contact width is that the model has been constructed using the origin of the bush, however to accurately calculate the arc of contact the radius of the pin must be used. Once the modified value for  $x_{bm}$  has been calculated, the arc of contact can be determined through trigonometry.

As would be expected, there are some limitations of the model such as consideration is only given to the bush in the elastic region of the bush material. As the bush is loaded into the plastic region, consideration needs to be given to the fact that the equilibrium in the axial direction will no longer be maintained as it is the only unconstrained dimension of the bush when loaded against two steel components; the shaft and the housing. This will most likely result in extrusion of the bush if the material is homogeneous in its composition.

The model is only valid if the materials are significantly elastically dissimilar. An Aluminium Bronze bush fitted into a steel housing and loaded with a steel pin, will not be accurately represented by this model.

Furthermore there is no boundary condition limiting the displacement of the pin loaded against the bush, hence care must be taken when applying the model to ensure that  $\delta < bt$ .

Consideration to the near fit condition (zero clearance), or interference fits is not attempted with this model, given the negative pressures that result. Care must also be exercised when applying the model to bushes with a very thin wall thickness.

The area of contact is assumed to be rectangular, based upon the chord length between the points of intersection of the pin and bush circles and the load transmitted in the vertical direction only through this region.

## 5.2. Static deformation

Load displacement plots were generated using the load frame and instrumentation described in section 3.2. A steel pin was loaded against a single PVC bush at a range of loads, to validate the model developed, for a plastic bush loaded against a rigid shaft. Bearing pressures of 26, 52, 78 and 104 MPa were used, which greatly exceeded the maximum 42 MPa (167 kN table 3.2 section 3) pressure experienced by the aircraft joint. The hysteresis was more obviously observed at the higher loads, and it can be seen that the joint is entering stages (iii) and (iv) from 52 MPa. All loads showed a degree of hysteresis.

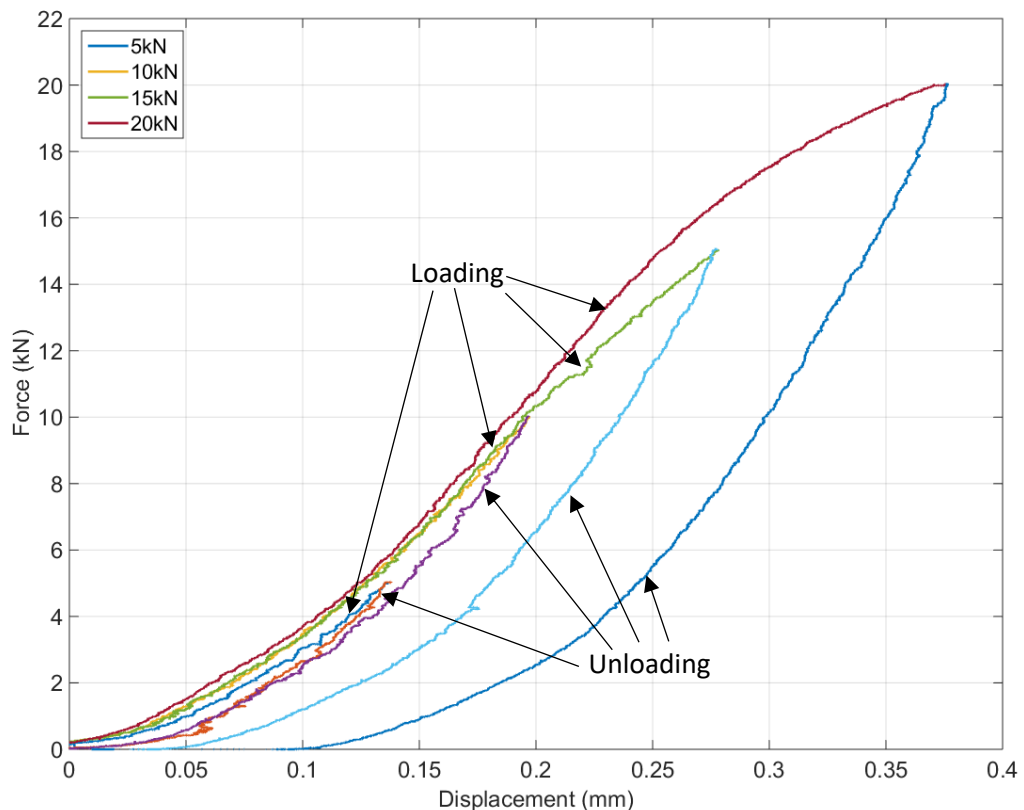


Figure 5.5: A steel pin 11.98mm OD loaded against PVC bushes 12 mm ID for a range of loads, showing the non-linear behaviour of the joint

For the conformal contact of a rigid shaft against a softer elastic bush, there will not only be the materials behaviour itself upon the application of a load, but also the growth of the contact area. For polymer materials, this contact area will be much greater than that of the aluminium bronze equivalents, and will therefore require a much lower load to achieve a saturated contact, where the arc of contact is at its greatest.

### 5.3. Experimental Validation

The displacement theory outlined above was validated using a single PVC bush nominal ID 12 mm, loaded against a pin of OD of 11.98 mm. The test was repeated 4 times with new bushes for each test. The experimental force displacement plots are compared with an envelope of the calculated results in Figure 5.6. For the model, an envelope of results was calculated given that there is a range of values for the elastic modulus. The calculations were conducted with a minimum value of 2.4, and a maximum value of 3 GPa. It can be observed from Figure 5.6 that tests 1 and 2 were repeatable with respect to each other, but fall slightly short of the minimum displacement limit calculated and show a much sharper curve at the start of the test. Test 3 falls close to the higher E value envelope limit, and test 4 crosses the envelope limits a couple of times.

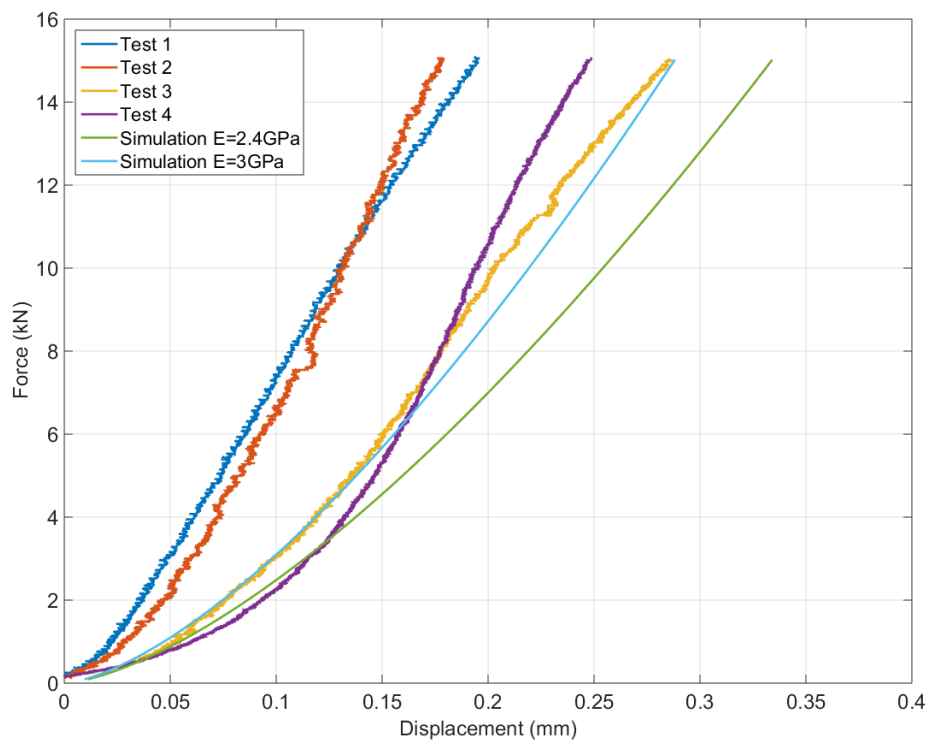


Figure 5.6: Load displacement plots of PVC bush thickness 2 mm, 12 mm ID, steel pin 11.98 mm OD compared against simulation using maximum and minimum values of E

The test was repeated using a larger bush ID of 13 mm (Figure 5.7), along with the same diameter pin in order to investigate the effects of different bush wall thicknesses and hence clearances. Tests were repeated 3 times. The first test was again slightly offset, but of a similar profile to the envelope. The second test was much more linear and shows an error of an increase in force with no increase in displacement. Again test 3 falls within the envelope well.

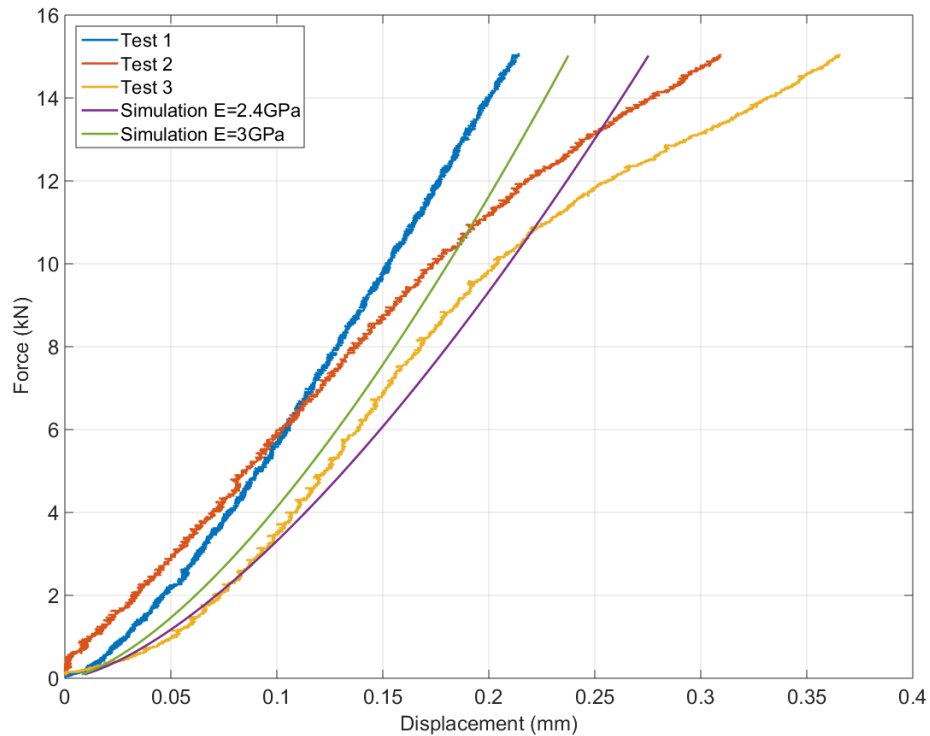


Figure 5.7: Load displacement plots of PVC bush thickness 1.5 mm, 13 mm ID, steel pin 11.98 mm OD compared against simulation using maximum and minimum values of E

For the thinner walled bush, it can be observed for tests 2 and 3 that stages (iii & iv) described in section 5.1 are beginning, showing the non Hookean behaviour of the material. It can be seen for the two wall thicknesses tested, there is some discrepancy between the repeats. This is not surprising given that greater machining tolerances must be accepted for polymer materials, due to deformation during machining, where a reduced clearance results in a more linear response. In addition differences in the material properties for the different batches used for the manufacture of the bushes was not accounted for with a sample taken and experimental determination of material properties.

It should be noted here that excessive noise was observed on the LVDT signal as a result of oversampling during data acquisition, therefore Savitzky-Golay filtering of the signal has been applied to reduce the noise on the signal, without distortion (Gander & Hrebicek, 2012).

The experimental results for PVC at 2 different wall thicknesses (2 & 1.5 mm) were in shown to be in general agreement with the model developed. Consideration should be given to the challenges of machining polymers with a thin wall, as the centre of the raw stock is removed by drilling the rigidity of the bush walls decreases. This increases the likelihood that the walls of the ID and OD may no longer be parallel.

### 5.3.1. Aircraft geometry

The aircraft joint is a real engineering joint and therefore is not as simple as the theory that was developed above. The aircraft joint is made up of four bushes; two in the lower clevis and two in the upper clevis. With the application of load all of these bushes will deform, but not necessarily in a uniform manner, the bushes will see oppositely applied loads in order to maintain equilibrium. The upper clevis bushes are of a longer design than the lower clevis bushes, therefore have a greater projected area and would result in lower bearing pressures. Given the relationship between contact area and displacement developed in the model above, a larger contact area would result in a smaller displacement. Hence for the two sizes of bushes used in the aircraft joint, un-equal amounts of displacement will occur in each half.

Therefore by applying the theory once for the upper clevis with the longer bushes and then again for the lower clevis with the shorter bushes, only considering  $L_1+L_4$ , and  $L_2+L_3$  respectively for the contact length. The calculated displacements can be summed together to give the total displacement of the joint.

The four commercially available specimens described in section 4 were loaded in the radial load test frame (section 3.2) with the standard aircraft pin and were varied with load. Figure 5.8 shows the total calculated displacement and the experimental displacement of the joint for each of the materials. From this figure, it can be seen that the simulated displacement up to 98 kN is in excellent agreement for both Gar-Max and Meldin 5330.

For Vespel 21 the simulation greatly overestimates the bush deflection. This is likely to be a result of anisotropy of the material introduced during the manufacturing process. The Vespel designers handbook (DuPont, 2002), explains that properties are different depending on the direction of force applied during manufacture, and that highest strength is found in the perpendicular direction. However exceptions to this rule are stated explicitly for some of the data presented in the designers handbook such as for the compressive and thermal properties quoted.

Given that Gar-Max and Meldin 5330 produced similar experimental data to Vespel and are in the 10-20 GPa range, with the remaining input parameters being similar, it is highly likely that the low value for  $E$  at 3 GPa has been determined in the opposite direction to which the bushes were loaded, resulting in a large over prediction of the simulated data.

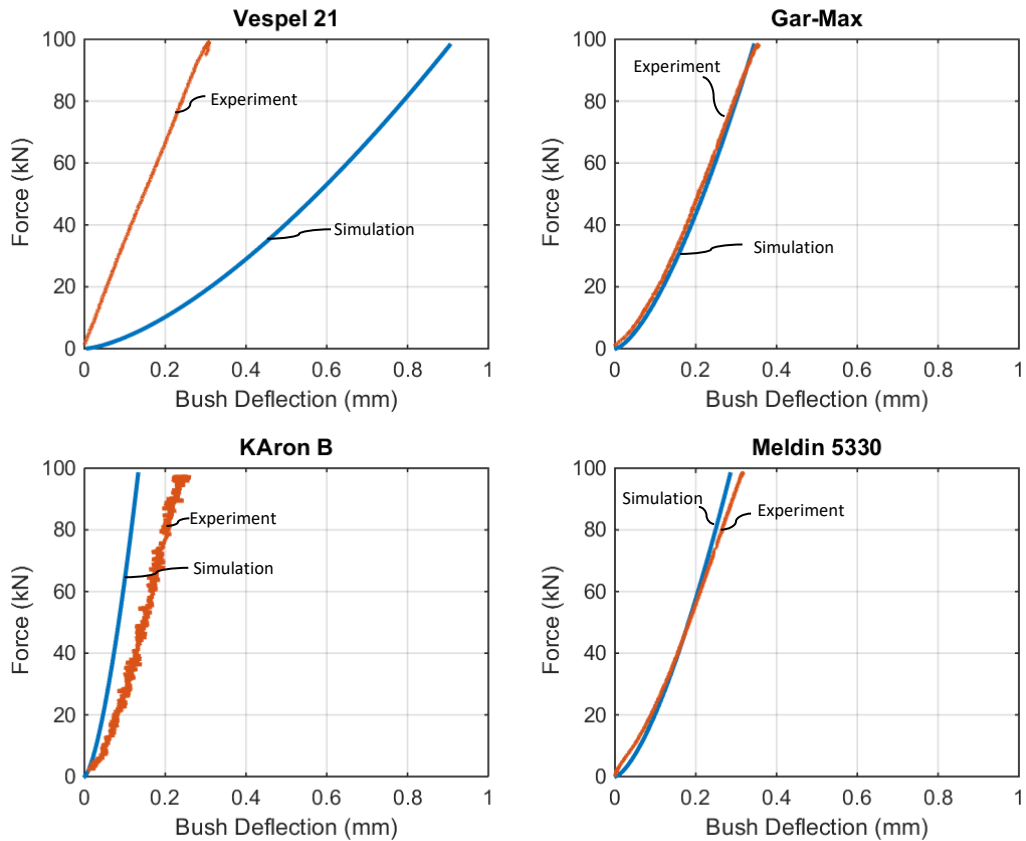


Figure 5.8: Validation of simulation with a real engineering joint for four potential bushings

KArOn B is under predicted by the simulation, however this is not a surprising result given the composition of the bearing, a liner bonded to a steel backing. For the simulation, the thickness of the bush was set to be the thickness of the liner only, hence no consideration was given to the steel backing. It should also be considered that the KArOn B solution is a much stiffer joint and therefore consideration should be given to the validity of the assumption that there is no deflection of the pin.

Running the model with an increasing modulus of elasticity, it can be seen from Figure 5.9 that a value of 15-18 GPa more accurately predicts the displacement of Vespel 21 than the value of 3 GPa provided by the manufacturers. Therefore given the similarity between the experimental results in Figure 5.8, for the materials with a modulus of elasticity in the region of 10-19 GPa and the improved agreement of the model developed also in this range concludes that a larger value for the modulus of elasticity both experimentally and theoretically predicts the displacement more accurately.

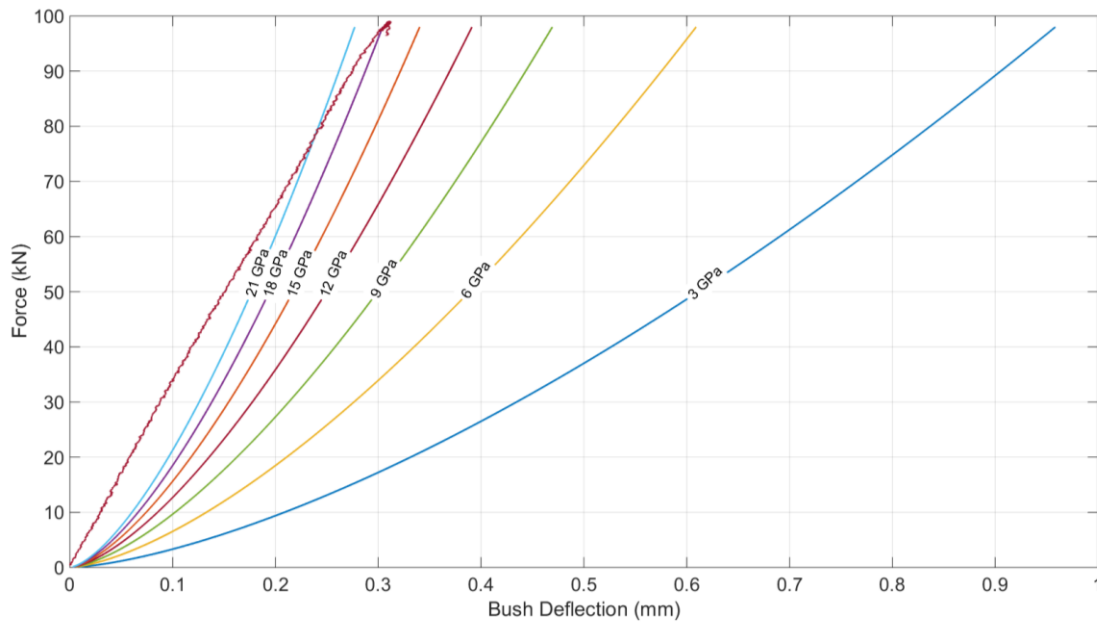


Figure 5.9: Simulation showing the sensitivity to the Modulus of Elasticity and Vespel 21  
Experimental result

While an increase in the modulus of elasticity to a similar size of the other polymer composite materials results in a stiffer joint, it can still be observed that the simulated result contains a non-linear region, while the experimental result displays a much more linear response. This is due to the difference in the fits of the bearings. Table 4.1 (section 4.1) highlights that the OD of Vespel 21 is approximately 0.2 mm greater than all the other materials, and the ID is within the same range as the other materials. Calculation of the volumetric change of the Vespel 21 bush between the free state and when it is fitted into the steel housing, shows that it becomes a neat or zero fit condition which falls outside of the capability of the model developed. However the neat fit condition does explain the more linear experimental response, as the arc of contact is “saturated” much earlier if not by the fit alone.

The model was shown to successfully predict the bush displacement of two different wall thicknesses for PVC using only geometrical and material parameters. Further verification was provided by the successful prediction of two commercially manufactured bearing solutions, of different materials and geometry to the PVC.

### 5.3.1.1. Maximum static displacements

The results of the maximum static displacement were recorded for each of the test cases described in section 3.2.7. The static measurements were recorded before each test case of the dynamic loading was conducted. The results are displayed and compared below (Figure 5.10). It can be seen from here that the general trend as expected is an increase in bush deflection with an increase in load. It should be noted here that the negative loading conditions have been displayed as absolute for the sake of clarity. This is the convention used throughout. KAron B shows the highest joint stiffness, identified by the smallest amount of displacement out of the four materials tested, while Gar-Max shows the highest.

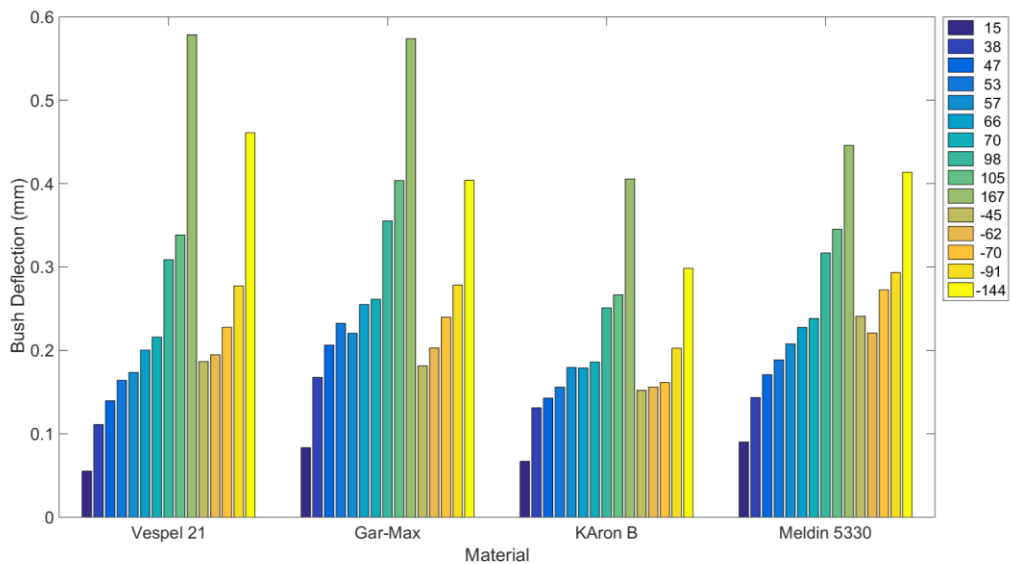


Figure 5.10: Maximum static displacement for each load and each material

## 5.4. Conclusion

A load displacement model was developed, simulating the displacement of a self-lubricating joint under an applied force. Development of the model was based on the intersection of circles and considered the thickness of the bush wall. Experimentation with a single PVC bush was conducted to verify the model, and good agreement was found for the lower contact loads. Further experimentation was conducted using four commercial bearing solutions with a double bush arrangement. Using the model twice, once for the upper clevis and once for the lower clevis, again showed good agreement for Gar-Max and Meldin 5330. KAron B did not follow the theory due to the steel backing of the liner. Whereas Vespel 21 experimentally produced similar results to Gar-Max and Meldin 5330, however a much lower modulus of elasticity was quoted in comparison to these materials.

[Blank Page]

# 6.

## Wear of a Radially Loaded Pin Joint

Representative cyclic loading of an aircraft landing gear joint was completed for four self-lubricating bearings identified in section four, and measurements of wear and deformation were taken throughout.

## 6.1. Dynamic Load Testing and Wear

Dynamic load testing was conducted on each of the four specimens for a complete aircraft life cycle as described in section 3.2.7. The signal from the LVDT was recorded during dynamic testing, this provided information for the displacement per cycle. Calculating the maximum and minimum values per cycle, enabled the range of the LVDT to be calculated per cycle as described in section 3.2.7. A mean value was taken from the range of all the cycles for each test case, as given the dynamic nature of testing it is difficult to accurately determine the true maximum and minimum values. A 95% confidence interval was applied to the data to minimise the influence of noise, represented by the error bars in Figure 6.1. The results are displayed and compared below in Figure 6.1.

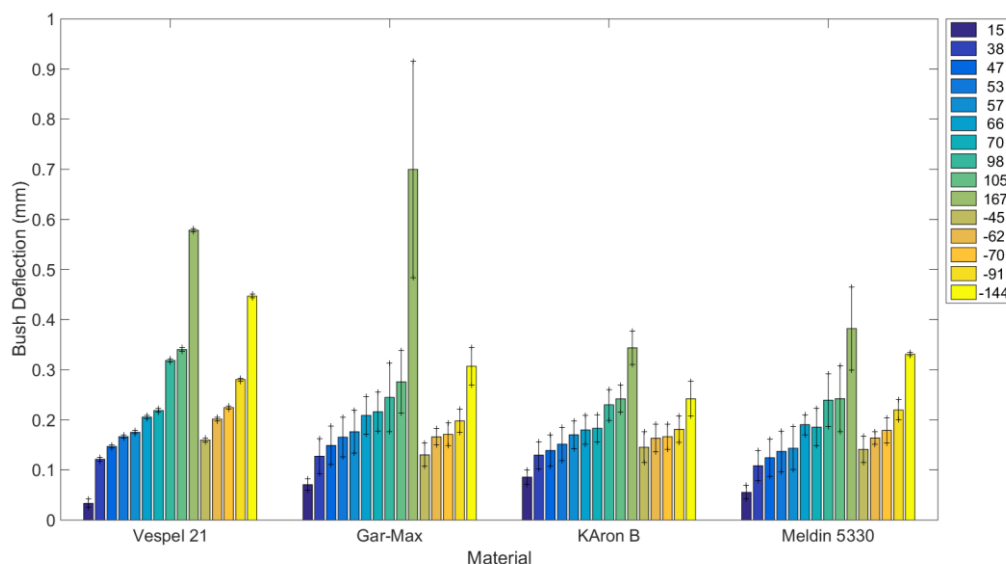


Figure 6.1: Maximum dynamic displacement for each load and material LC1

As would be expected, from Hooke's Law and Figure 5.10 for higher loads, a higher displacement is observed. This however makes it difficult to separate the elastic deformation and permanent deformation, such as plastic deformation or wear.

Therefore by subtracting the maximum static displacement Figure 5.10 from the dynamic displacement calculated in Figure 6.1, the permanent damage sustained by each test case can be estimated as shown in Figure 6.2. It is assumed here that any permanent deformation occurring upon the application of the load would be identified during the static testing conducted (e.g. Figure 5.10), any progressive plastic deformation would be observed during the cyclic loading. Only the amount of permanent damage can be determined here, without additional measurements no conclusion can be drawn as to the root cause of the deformation, as it could be a result of either creep, wear or plastic deformation. It can

however be seen from Figure 6.2 that permanent change is negligible in comparison to the error from measurement. It can be seen that Vespel 21 returned a maximum change of  $-27 \mu\text{m}$  at  $-45 \text{ kN}$ , Gar-Max  $-127 \mu\text{m}$  at  $105 \text{ kN}$ , Karon B  $-62 \mu\text{m}$  at  $167 \text{ kN}$ , and Meldin 5330  $-103 \mu\text{m}$  at  $105 \text{ kN}$ .

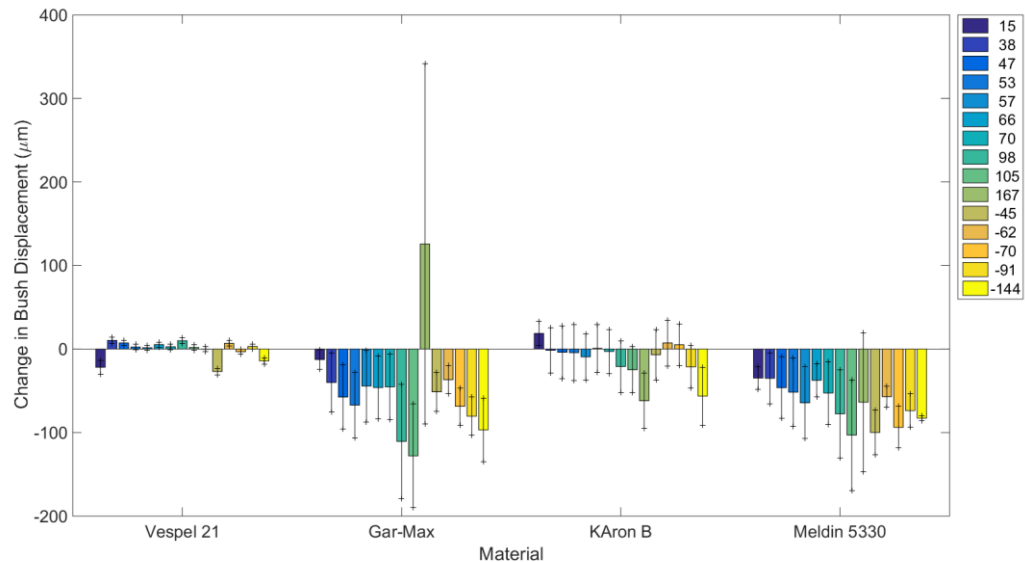


Figure 6.2: Wear+creep+plastic deformation for each load and materials after LC1

The joint was retested for a second aircraft life cycle, and the same procedure followed. There was a slight difference in the testing regime that the joint was dis-assembled after each loading condition to enable a roundness measurement to be taken. The joint was then re-assembled and the next test case completed. This inevitably introduced additional errors into the measurement, from removal and refitting, but enabled more in-depth analysis of the joint as testing progressed. The dynamic measurement of the second aircraft life is shown in Figure 6.3 before the subtraction of the elastic component. It can be seen that there is a general increase in the deflection of all materials, but little else. Gar-Max shows a small anomaly for the  $53 \text{ kN}$  test case, where deflection is greater than the  $57 \text{ kN}$  and  $66 \text{ kN}$  case.

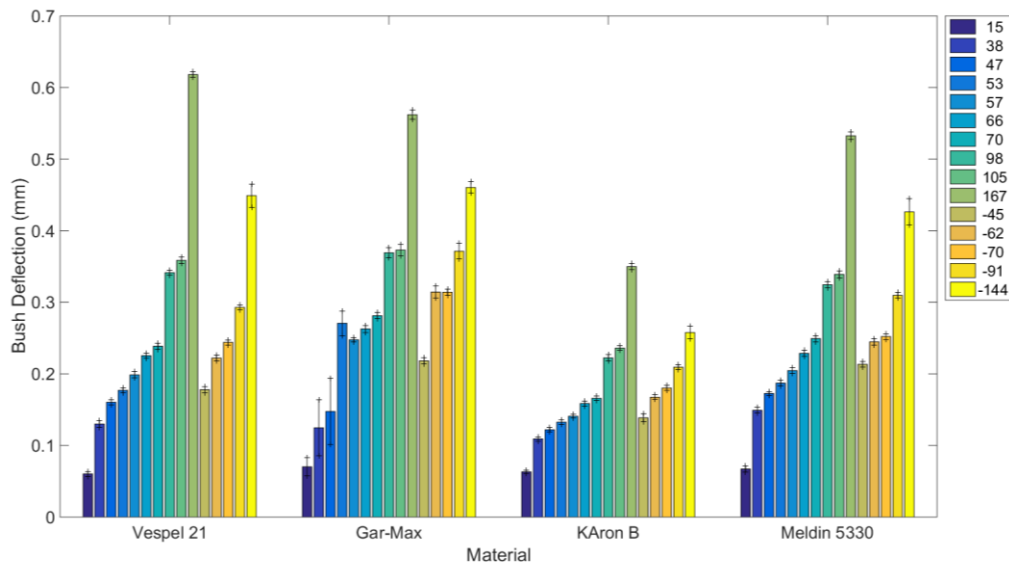


Figure 6.3: Maximum dynamic displacement for each load and material LC2

Figure 6.4 shows the analysis of the LVDT from the second life cycle following the subtraction of the elastic component. Vespel 21 returned a maximum change of 40  $\mu\text{m}$  at 167 kN, Gar-Max 111  $\mu\text{m}$  at -62kN, Karon B -55  $\mu\text{m}$  at 167 kN, and Meldin 5330 87  $\mu\text{m}$  at 167 kN.

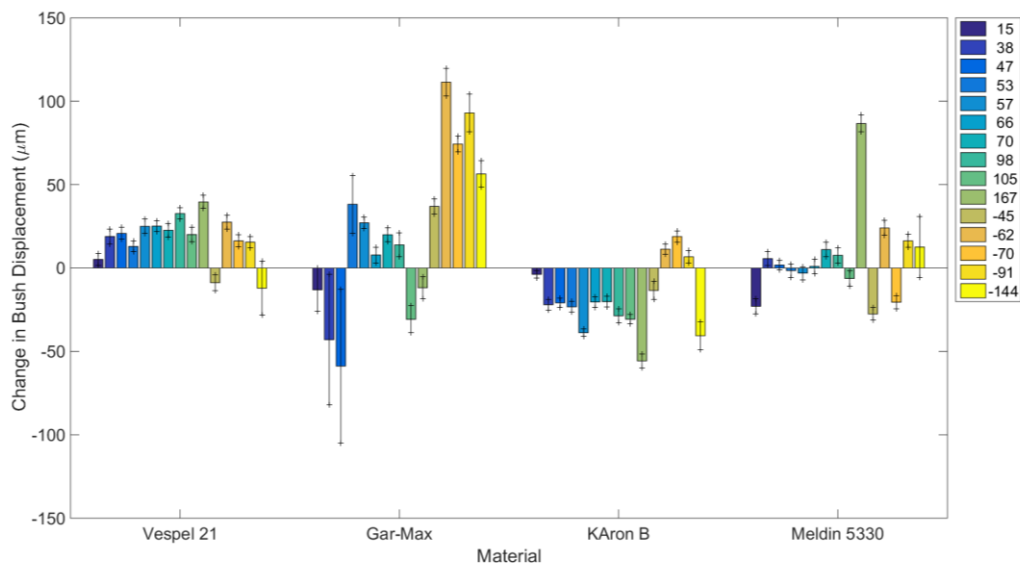


Figure 6.4: Wear+creep+plastic deformation for each load and materials after LC2

The joint was then tested for a third time, in which the test procedure was conducted in the same manner as the first life cycle. The results are presented below in Figure 6.5 for the permanent change, showing that Vespel 21 had a maximum of 45  $\mu\text{m}$  at 38 kN, Gar-Max had a maximum of -64  $\mu\text{m}$  at 105 kN, Karon -40  $\mu\text{m}$  at 167 kN and Meldin 5330 -61  $\mu\text{m}$  at -45 kN.

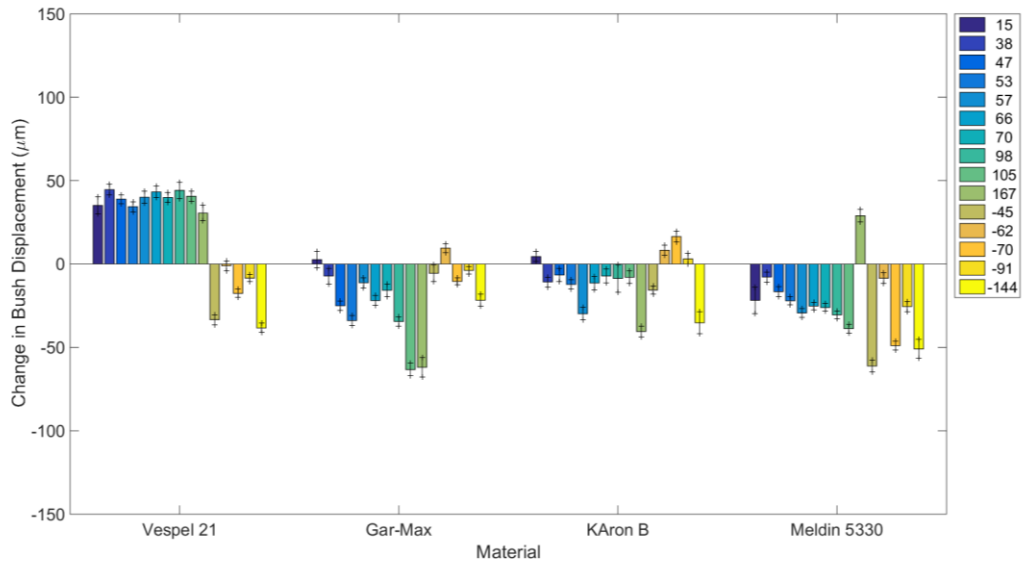


Figure 6.5 Wear+creep+plastic deformation for each load and materials after LC3

For the subtraction of the elastic component the load displacement values taken before the first aircraft life cycle have been used throughout the analysis to ensure consistency. Therefore considering the lower deformation in the final life cycle it can be concluded that the bearings have run themselves in. It should be noted that for change in bush displacement some of the maximum values are in fact negative. Given that this occurs in different life cycles, and the magnitude of the values are similar throughout. Coupled with the fact that extreme care was taken to ensure the bushes were always re-fitted into the same orientation, the conclusion can be drawn that the permanent deformation sustained by the bushes during this testing is of comparable magnitude to the error in the control loop of the servo-hydraulic system.

## 6.2. Talyrond Roundness

Roundness measurements were taken for each set of bushes before testing commenced, and throughout the test programme. Measurements were taken extensively throughout the second life cycle. The maximum deviation from round values for Vespel 21 for each test case at a measurement height of 5.5 mm for each bush is given in Figure 6.6. The direction of loading can be observed as there is a general increase in peak deviation for the positive loading of Vespel 21, bush 1, 0-180°, while the negative loads decrease slightly. However this effect is seen reversed for the opposite side of the bush (180°-360°) where the peak deviation of the negative loads increases, while for the positive loads it decreases and becomes more constant, indicating that the opposite side of the bush has been loaded.

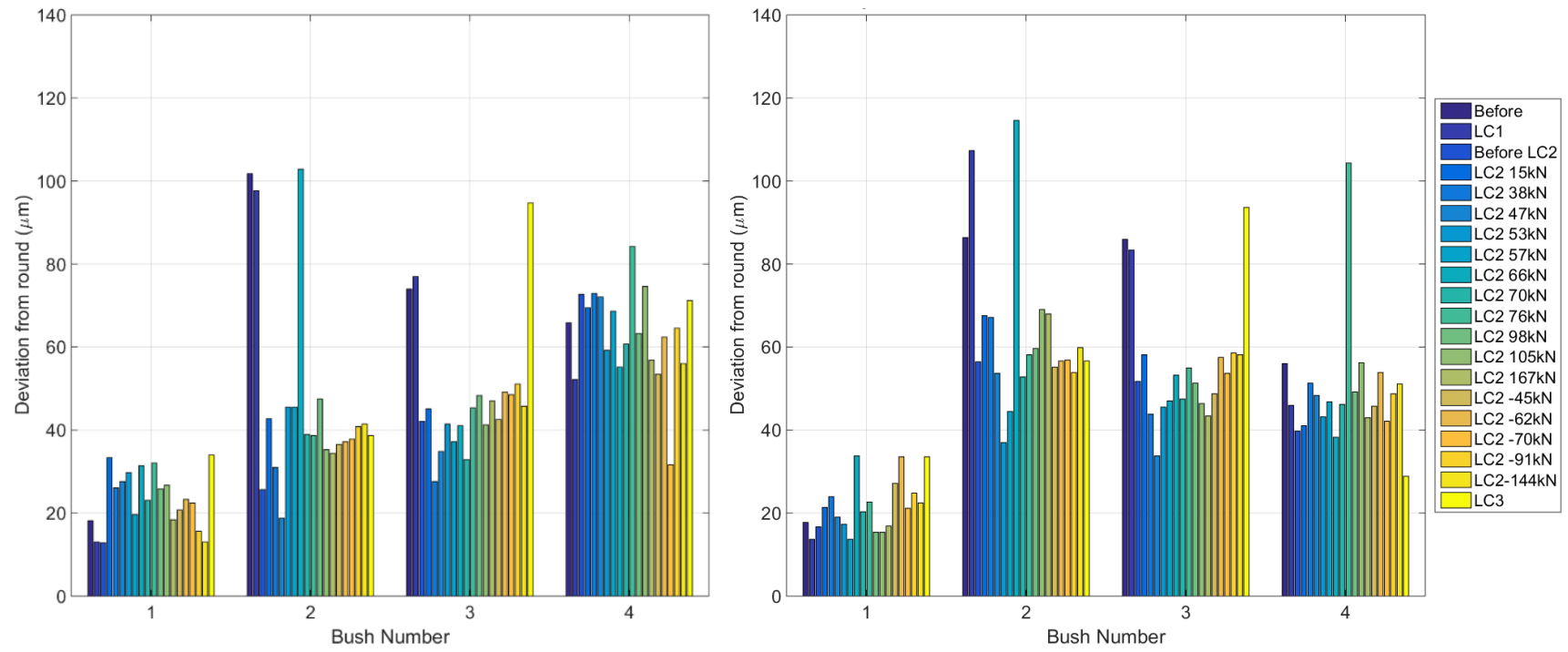


Figure 6.6: Peak deviation from round for the entire test programme for each half of each bush Vespel 21 at 5.5mm measurement height (left) 0-180°, (right) 180°-360°

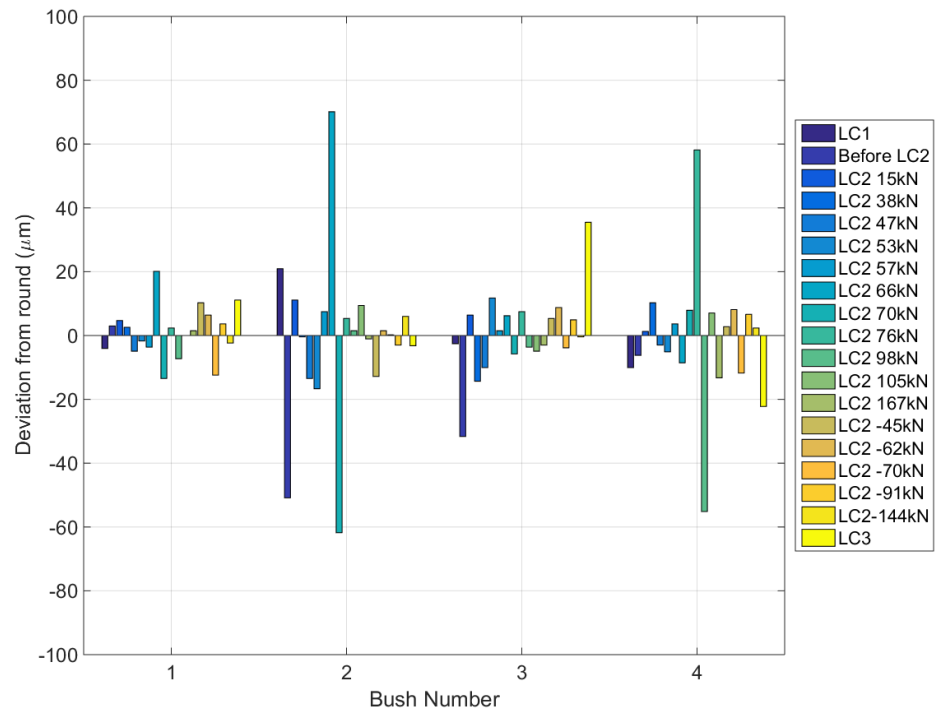
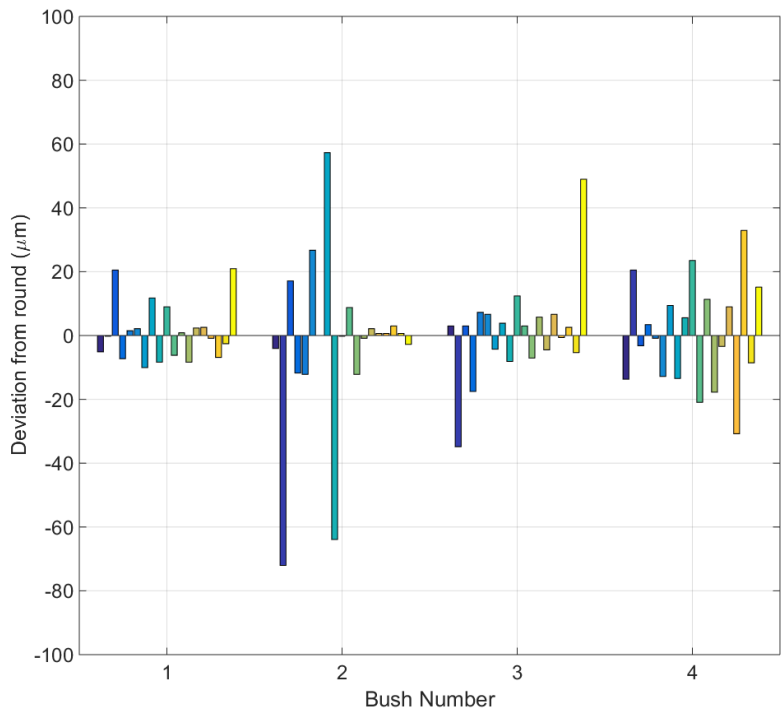


Figure 6.7: Change in peak deviation from round for the entire test programme for each half of each bush Vespel 21 at 5.5mm measurement height (left) 0-180°, (right) 180°-360°

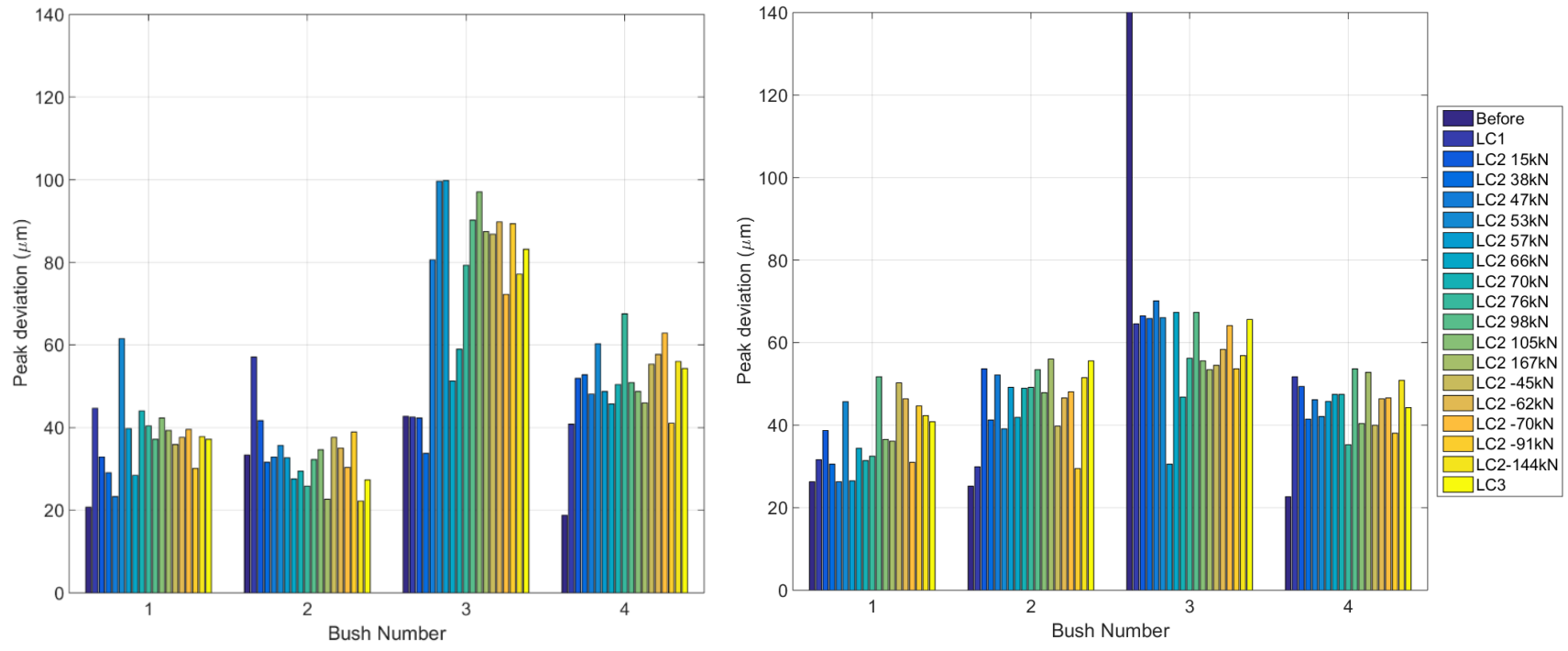


Figure 6.8: Peak deviation from round for the entire test programme for each half of each bush Gar-Max at 5.5mm measurement height (left) 0-180°, (right) 180°-360°

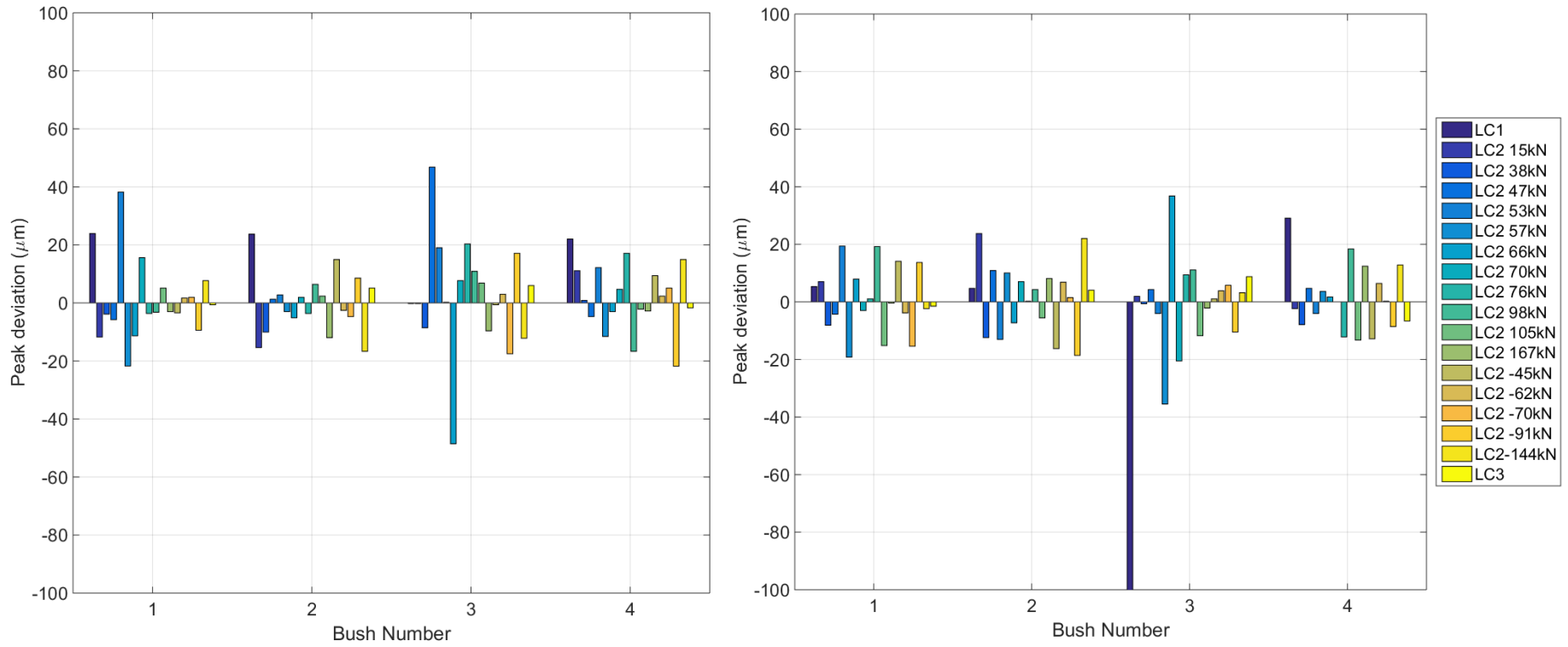


Figure 6.9: Change in peak deviation from round for the entire test programme for each half of each bush Gar-Max at 5.5mm measurement height (left) 0-180°, (right) 180°-360°

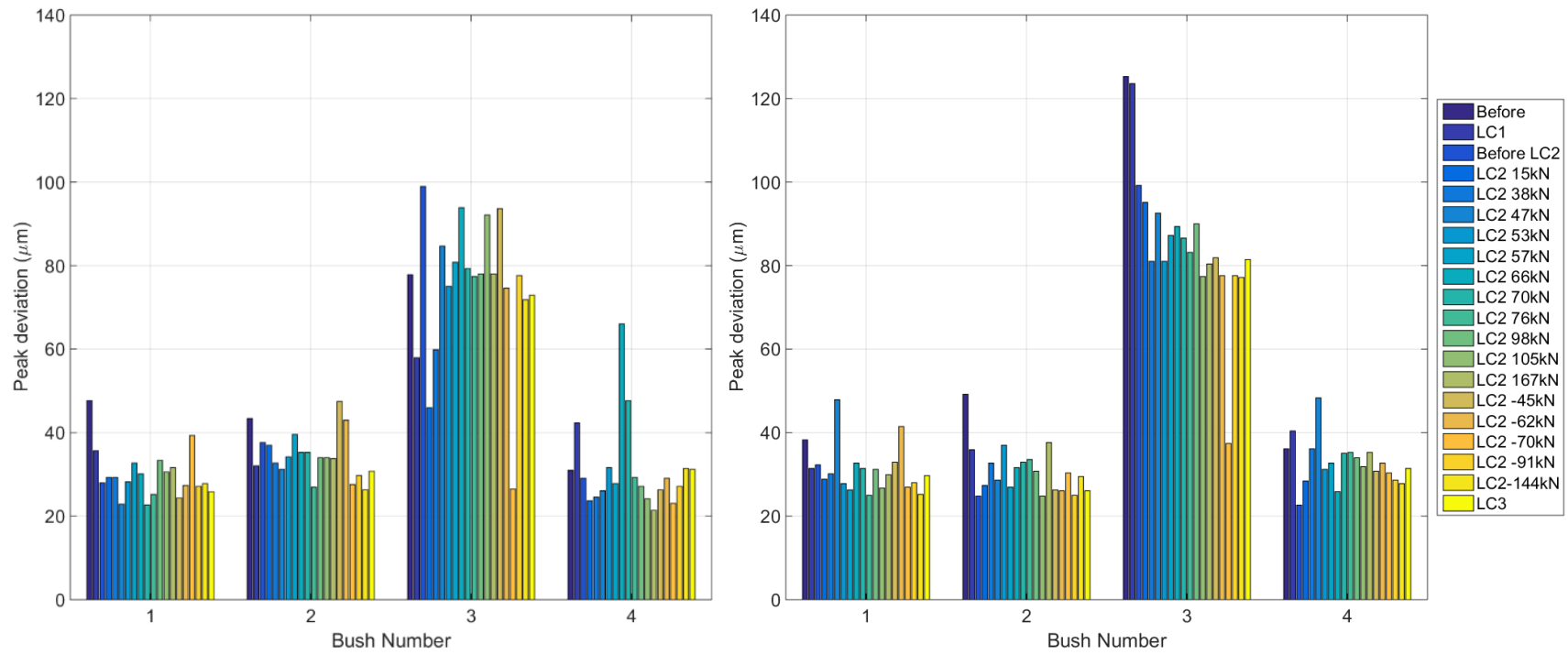


Figure 6.10: Peak deviation from round for the entire test programme for each half of each bush Meldin 5330 at 5.5mm measurement height (left) 0-180°, (right) 180°-360°

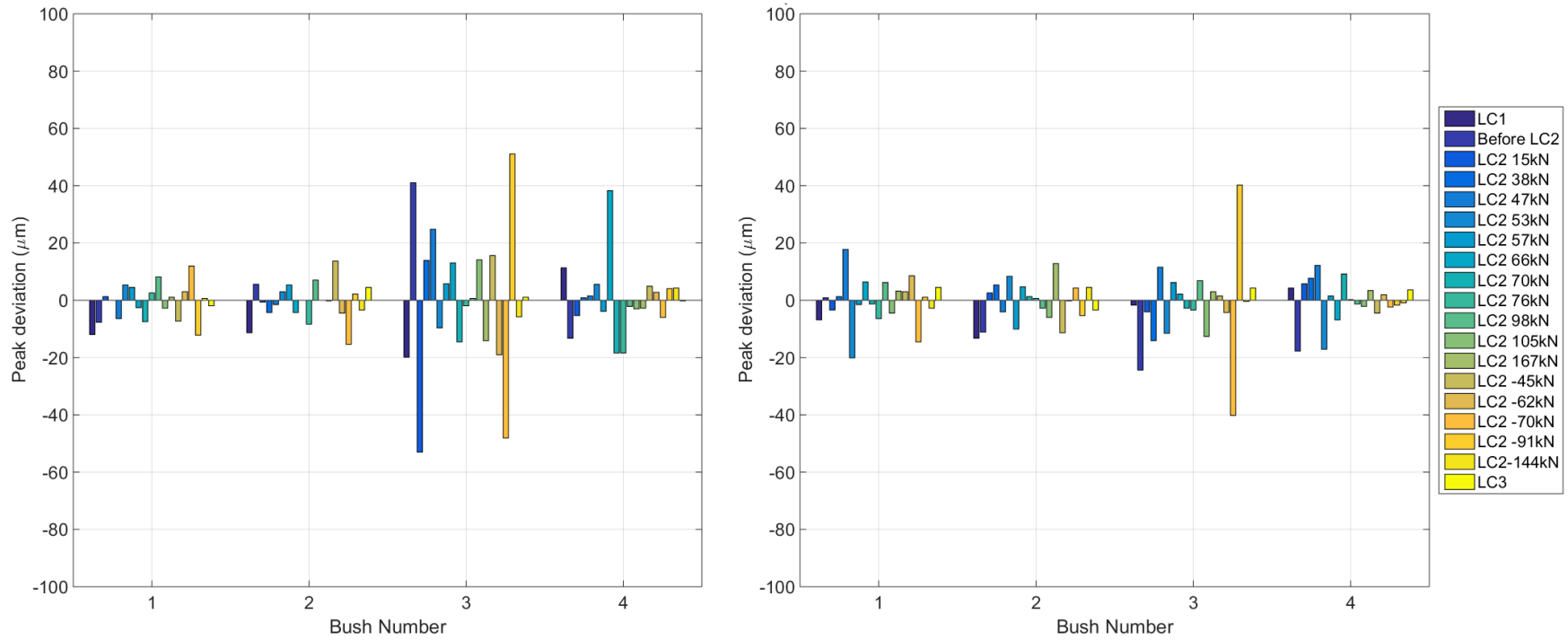


Figure 6.11: Change in peak deviation from round for the entire test programme for each half of each bush Meldin 5330 at 5.5mm measurement height (left) 0-180°, (right) 180°-360°

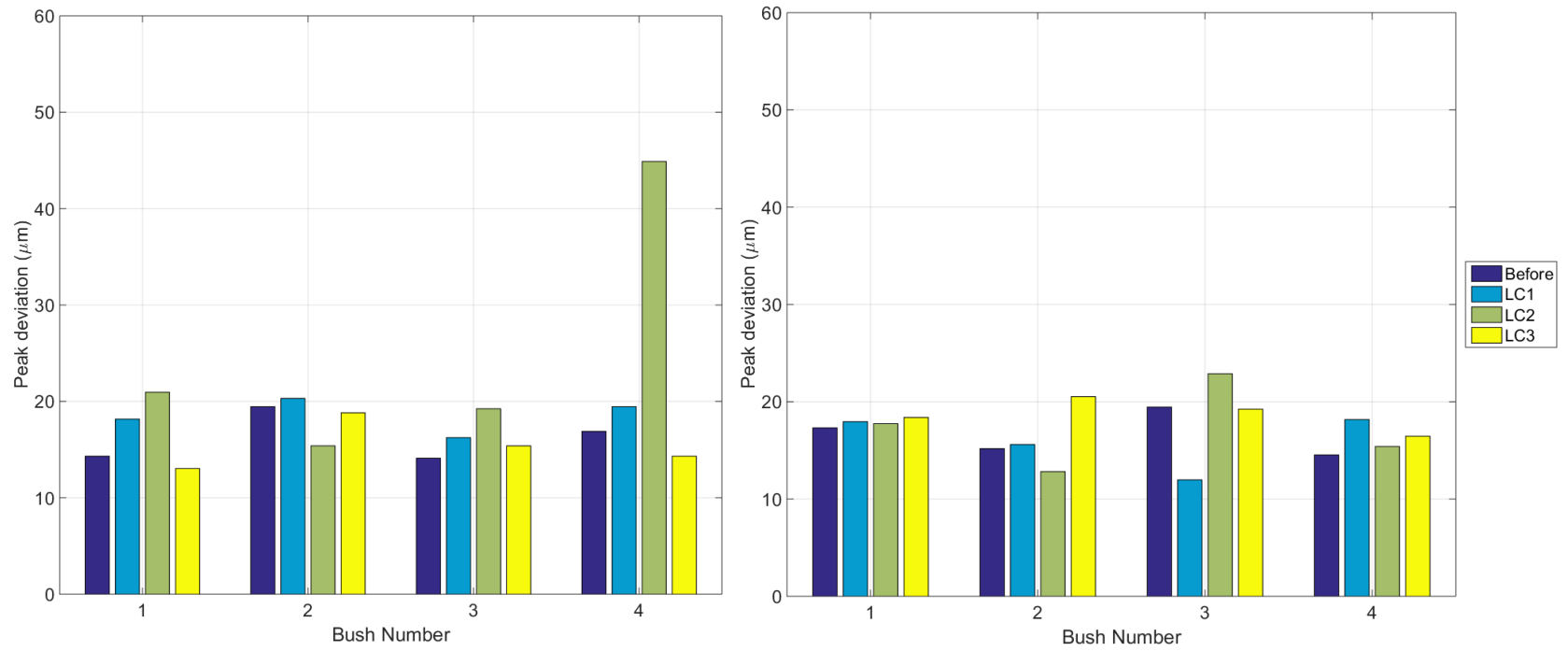


Figure 6.12: Peak deviation from round for the Before testing, after life cycle 1, life cycle 2 and after the third life cycle for each half of each bush Karon B at 5.5mm measurement height (left) 0-180°, (right) 180°-360°

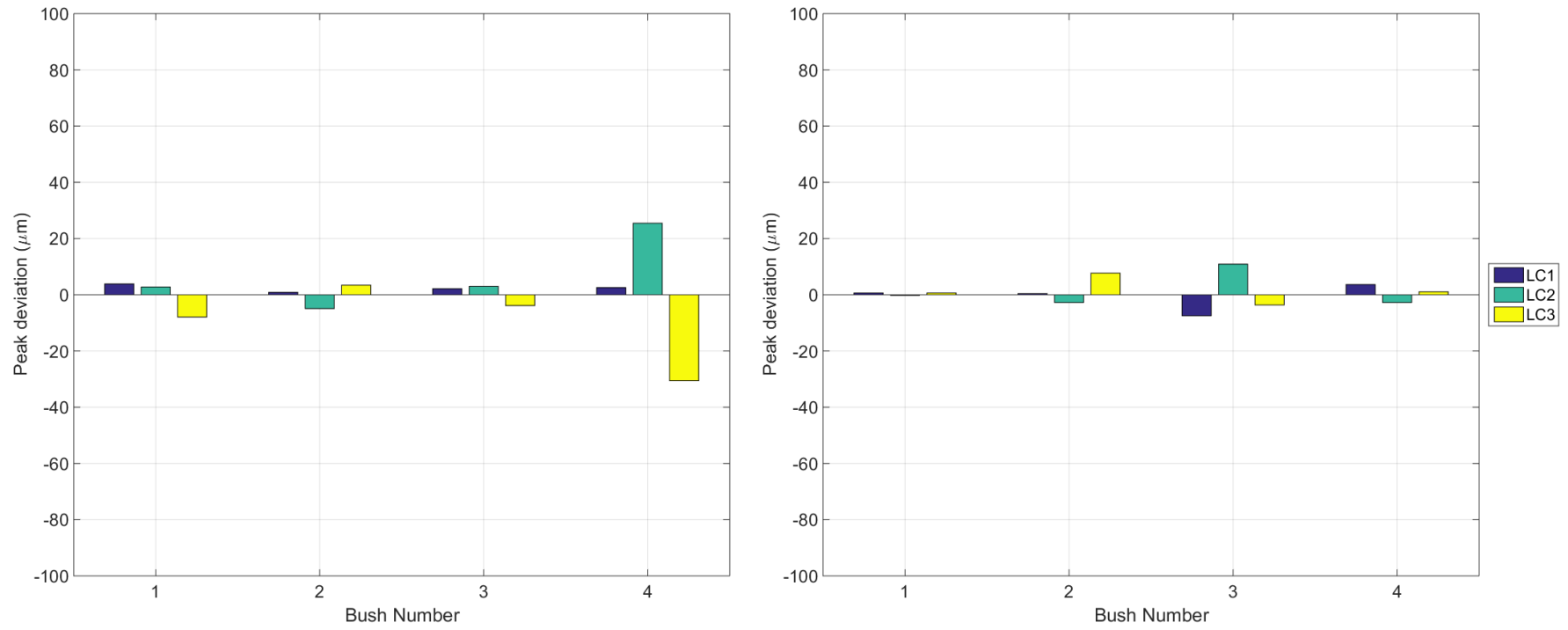


Figure 6.13: Change in peak deviation from round for the Before testing, after life cycle 1, life cycle 2 and after the third life cycle for each half of each bush KAron B at 5.5mm measurement height (left) 0-180°, (right) 180°-360°

It can be seen from Figure 6.6 that the amount of permanent damage fluctuates for each measurement. To enable this to be compared more easily, the previous measured value is subtracted from the newly measured one. The change in maximum deviations is then displayed in Figure 6.7 for Vespel 21. From this figure it can be seen that the change in roundness, rarely exceeds a magnitude of 20  $\mu\text{m}$  and that for some of the measurements taken the peak deviation is less than the test case completed before. This is due to the material recovering from the applied loading, highlighting that an element of creep is occurring in the bushes. For example 66 kN test case produces a large change, however it is followed by another large change in the opposite direction, returning the changes in magnitude to less than 20  $\mu\text{m}$ . Figure 6.8 to Figure 6.13 repeat the process described above for the other materials tested.

For all materials it can be seen that the measureable change from one test case to the next is in the region of microns, and the change from the start of testing to the end of life cycle 3 is in the order of 20  $\mu\text{m}$ . Measurements below this value would be unreliable due to the human error in setting up the bush to be concentric, and the error of the Talyrond.

Gar-Max bush 3 shows an obvious anomaly in the before measurement which is a result of one of the fibres not correctly bonded. It can also be seen that for Meldin 5330 and Vespel 21, an additional measurement Before LC2 was conducted. It would be expected to observe no change in the material, given that no testing has occurred. However given that the specimens were re-measured following a technical issue with the Talyrond at this point and also that the complete first life cycle for the other specimens was occurring, it is not surprising to see the time dependent phenomenon of creep occurring for materials that had been tested and were awaiting further testing to show a significant difference.

Linear interpolation has been used to generate a 3D figure from each of the measurement heights described in section 4.4 for each of the bushes showing the initial out of round and the progressive damage after the first and second aircraft lives. The figures for each of the materials, are displayed in Table 6.1 to Table 6.4.

It can be seen that for Vespel 21 little change has occurred from before dynamic testing was conducted to after the completion of the second life cycle. Bush 1 shows no measureable change for the three measurements, and appears to be perfectly round. Bushes 2 & 3 show initial out of roundness in 3 locations which was a result from the manufacturing process as the bush was held in a three jaw chuck. The initial out of round progressively improved after each life cycle as the bearing wore in as a result of the micro slip between the pin and bush

occurring as the joint was loaded and unloaded. Bush 4 again shows little to no change, however the effect of misalignment can be observed when measuring on the Talyrond.

Gar-Max at first glance appears to show the greatest amount of damage, but again comparing to the initial out of round indicates that no significant change has occurred. Gar-Max being a filament wound bearing has not been machined and therefore some initial deviation from round would be expected.

Meldin 5330 shows little change again for all the bushes, given that these bushes were machined from raw stock like Vespel 21, it is not surprising to see faint evidence of where the 3 jaw chuck held bush 3. It can be seen that there is significant damage for bush 4 after life cycle 2, however the opposite phenomenon occurring on the opposite side of the bush shows that this is purely due to an error in centring the measurement.

KAron B showed no measureable deformation for any of the bushes either from the manufacturing process or as a result of the testing. This is due to the increased stiffness of the joint as a result of the steel substrate. Therefore deformation from the 3 jaw chuck in the machining process is minimised, and with the liner being machinable, any deviations from roundness during the application of the liner can be machined back. The displacement during the static loading of the joint is also less, resulting in less counterface sliding.

The 3-dimensional linear interpolation provided a more informative and representative image of how the bushes deformed, due to the inclusion of the roundness measurements taken at different heights, as described in section 4.4. Concentricity was maintained by moving only the probe up, without altering any other settings, which provided additional information to that given above, as it could be determined if the bore had become tapered at any point during the testing. Localised peak deformations could also be identified and omitted when required.

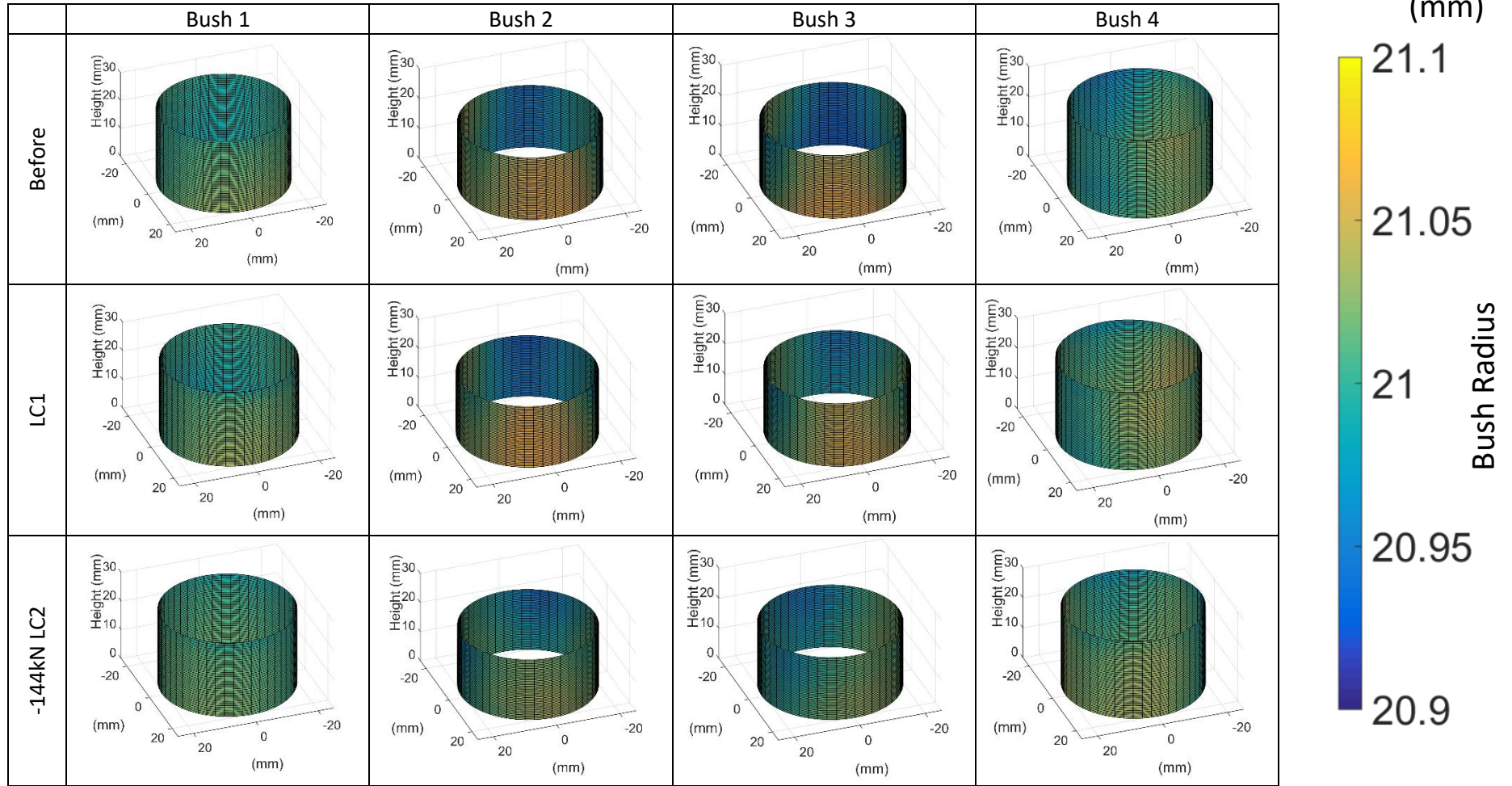


Table 6.1: 3D plots for all measurement heights before and after life cycle 1 & 2 Vespel 21

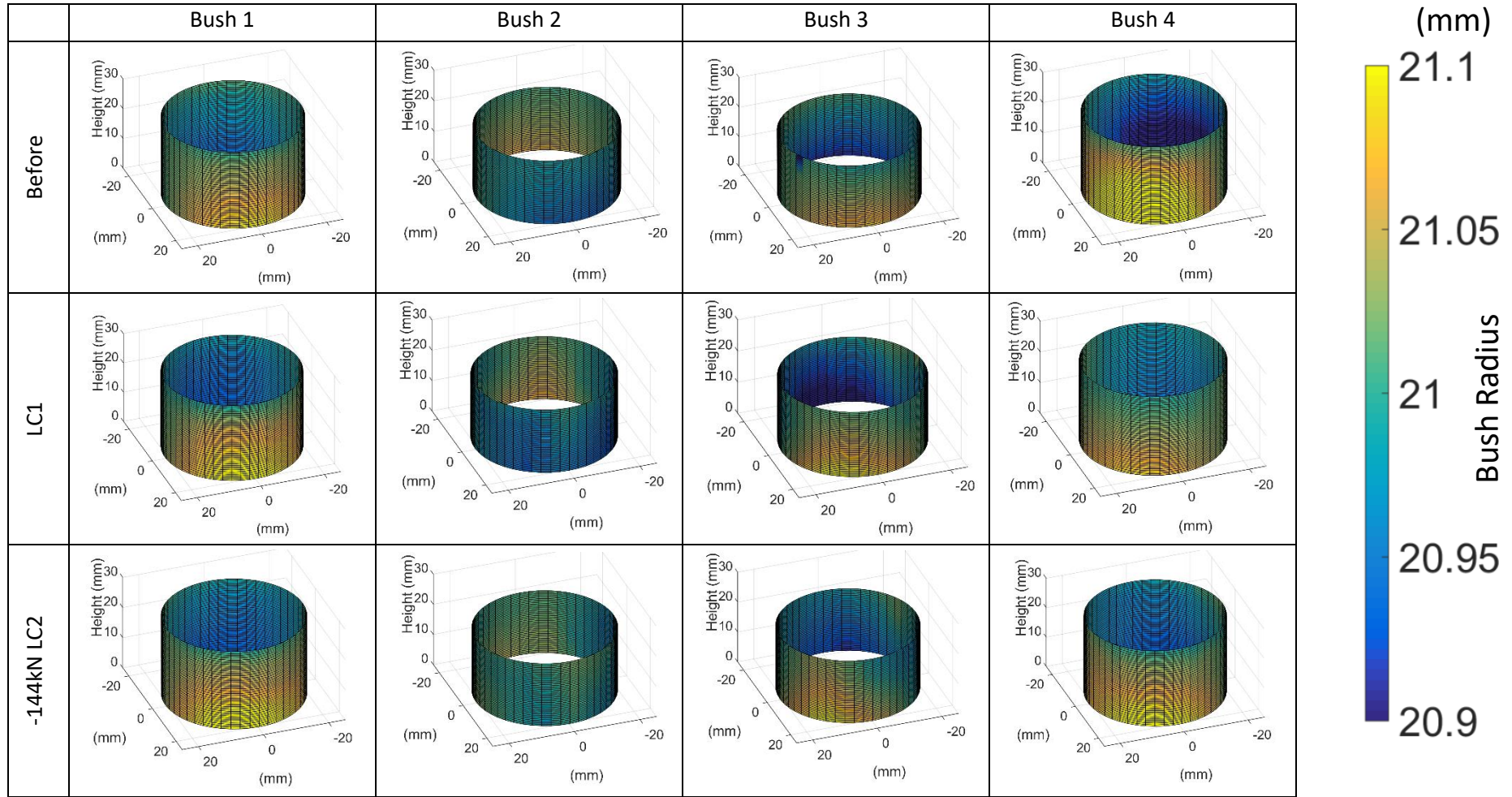


Table 6.2: 3D plots for all measurement heights before and after life cycle 1 & 2 Gar-Max

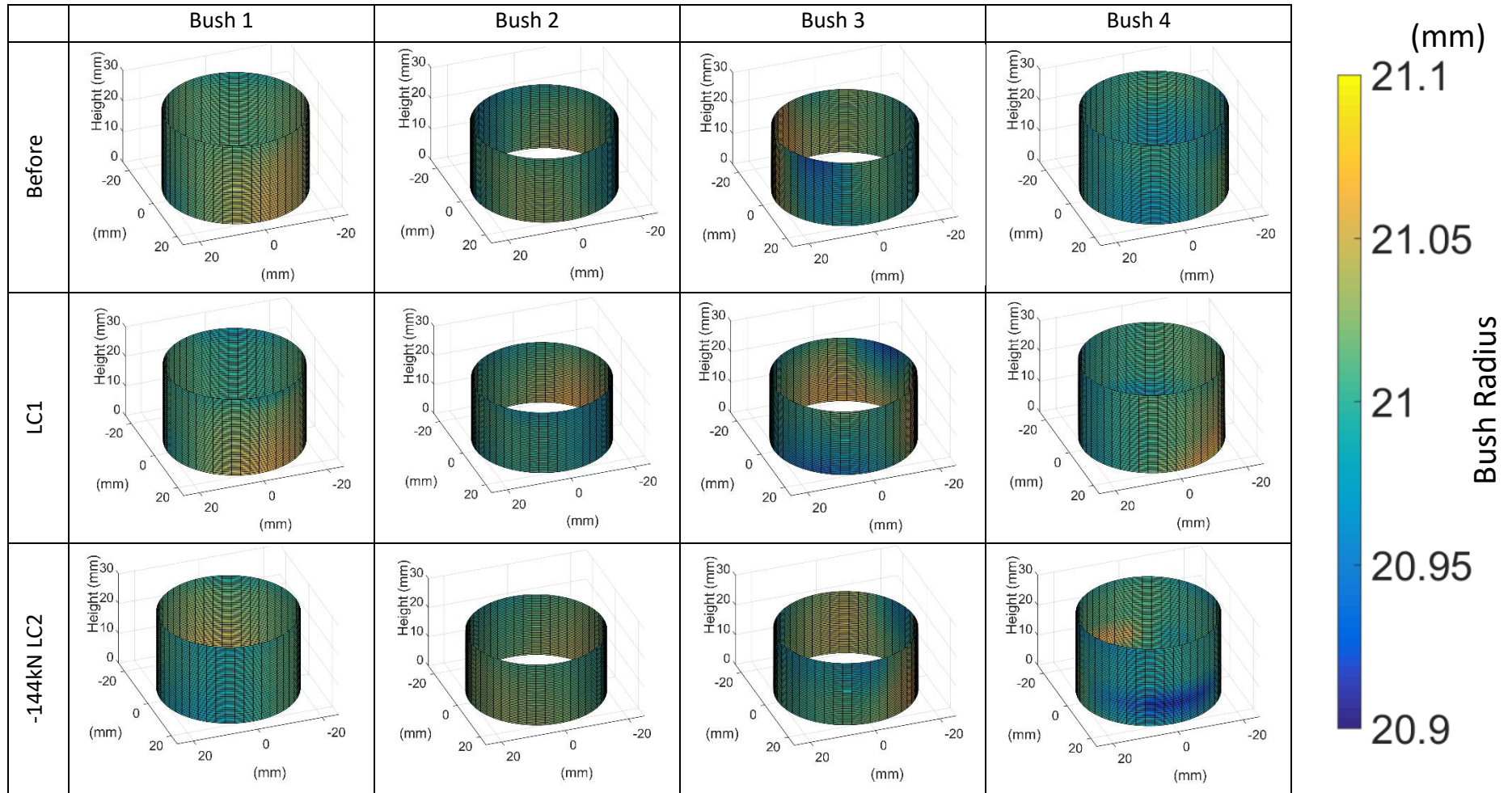


Table 6.3: 3D plots for all measurement heights before and after life cycle 1 & 2 Meldin 5330

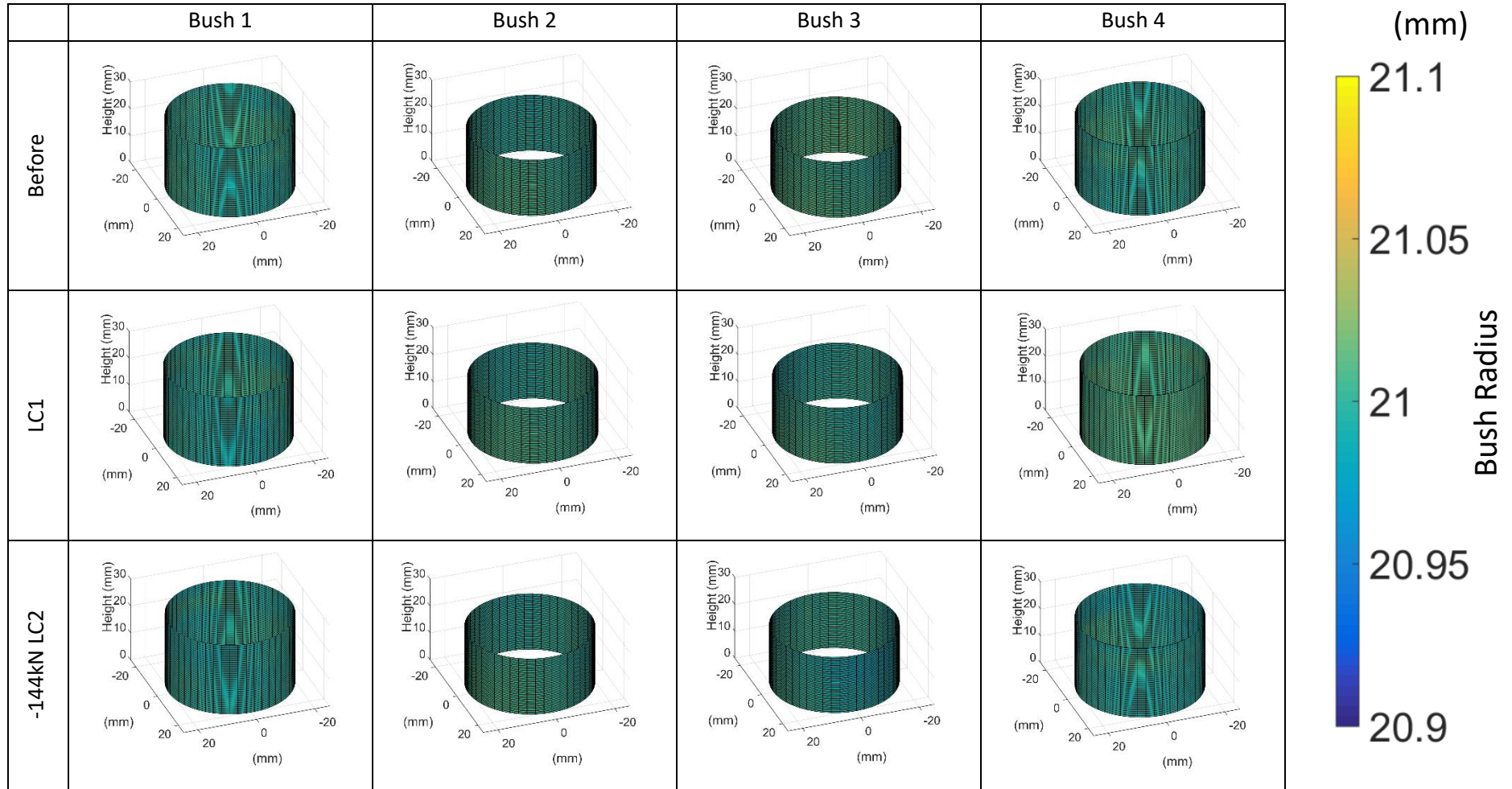


Table 6.4: 3D plots for all measurement heights before and after life cycle 1 & 2 KAron B

### 6.3. Visual Inspection

KAron B showed evidence of fretting on the OD, which resulted in seizure of the steel backing into the test clevis. It can be seen from Figure 6.14 that there are regions where the asperities have locally welded together and upon removal of the bearing has resulted in scarring of the OD, as the welded junction ploughed through the stainless steel, until the junction separated.



Figure 6.14: Fretting damage and localised asperity welding of the Stainless steel OD on KAron B to the clevis ID

On the OD of Gar-Max traces of a reddish brown coating indicated that an oxide had been formed. This is thought to have occurred from a very thin layer of rust developing in the bore of the test clevis in between tests. The rust being transferred from the clevis to the test bushings during the micro oscillation between the clevis and test bushing, as a result of the cyclic loading.

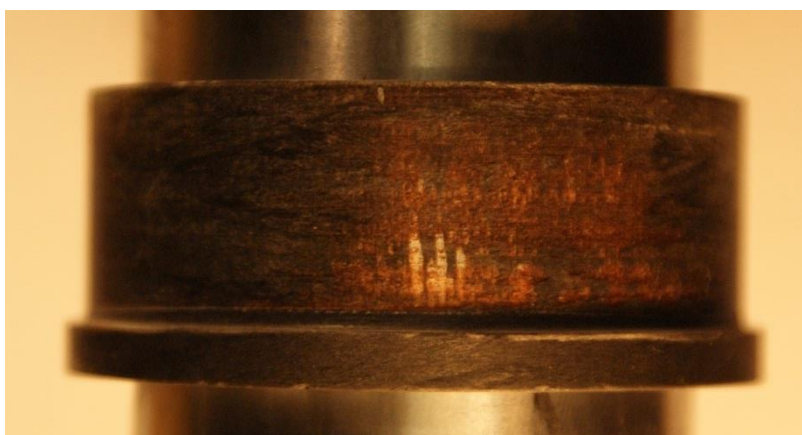


Figure 6.15: Transfer of oxidation from the test clevis to Gar-Max

Following the completion of life cycle 1 for four materials, the results from the visual inspections are displayed in Table 6.5.

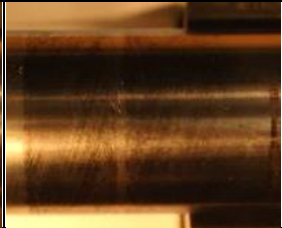
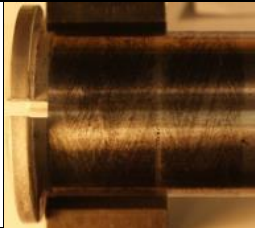
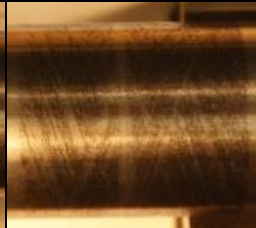
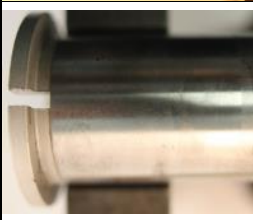
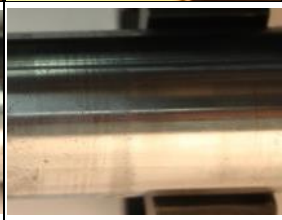
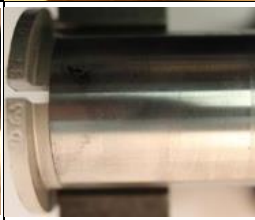
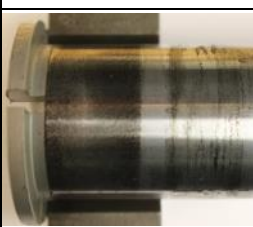
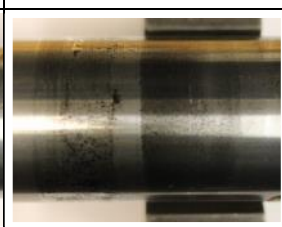
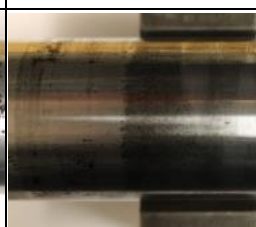
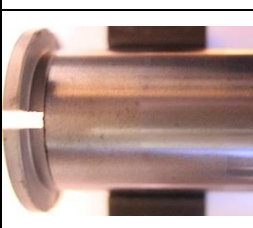
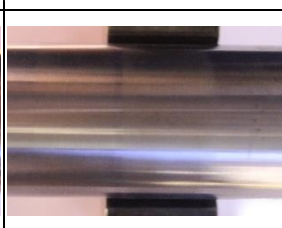
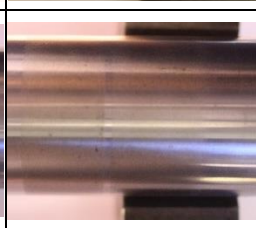
	Top		Bottom	
Gar-Max				
Meldin 5330				
Vespel 21				
KAron B				

Table 6.5: Summary of material transfer to pins after 1 aircraft life cycle

It can be seen from Table 6.5 that for Gar-Max and Vespel 21 there was some material transfer occurring. For Gar-Max the PTFE has transferred from the fibers to the pin, which was evident through the pattern produced in the contact region for all of the bushes. An even distribution between the two halves of the clevis, indicates even loading. Vespel 21 showed obvious evidence of material transfer, as the graphite has transferred to develop a lubricating film. It was more evenly distributed for the upper clevis than the lower, showing more relative motion between the pin and upper clevis bushes than the lower, which indicates a reduced clearance for the lower clevis. For both materials there appears to be a greater transfer at the head end than the far end of the pin, a result of unequal loading across all of the bushes. Meldin 5330 appeared to have polished the pin rather than transferred any material, while faint traces of material transfer were observed for KAron B for both the upper and lower clevis with an even distribution across all of the bushes. Microscopic inspection was required.

Vespel 21			
TOP		BOTTOM	

Table 6.6: Microscopic inspection of Vespel 21 in each bush location for both the top and bottom of the pin

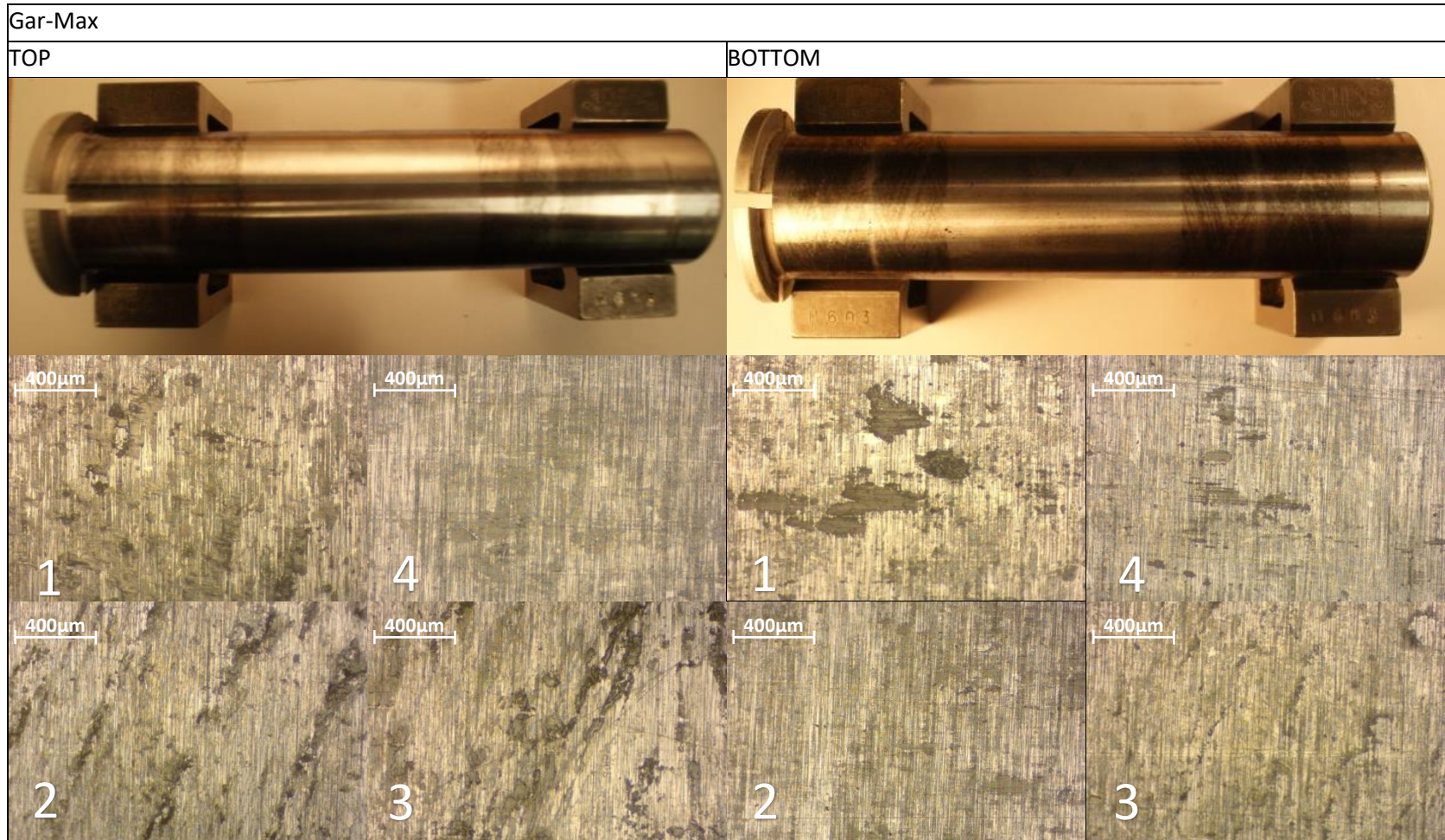


Table 6.7: Microscopic inspection of Gar-Max in each bush location for both the top and bottom of the pin

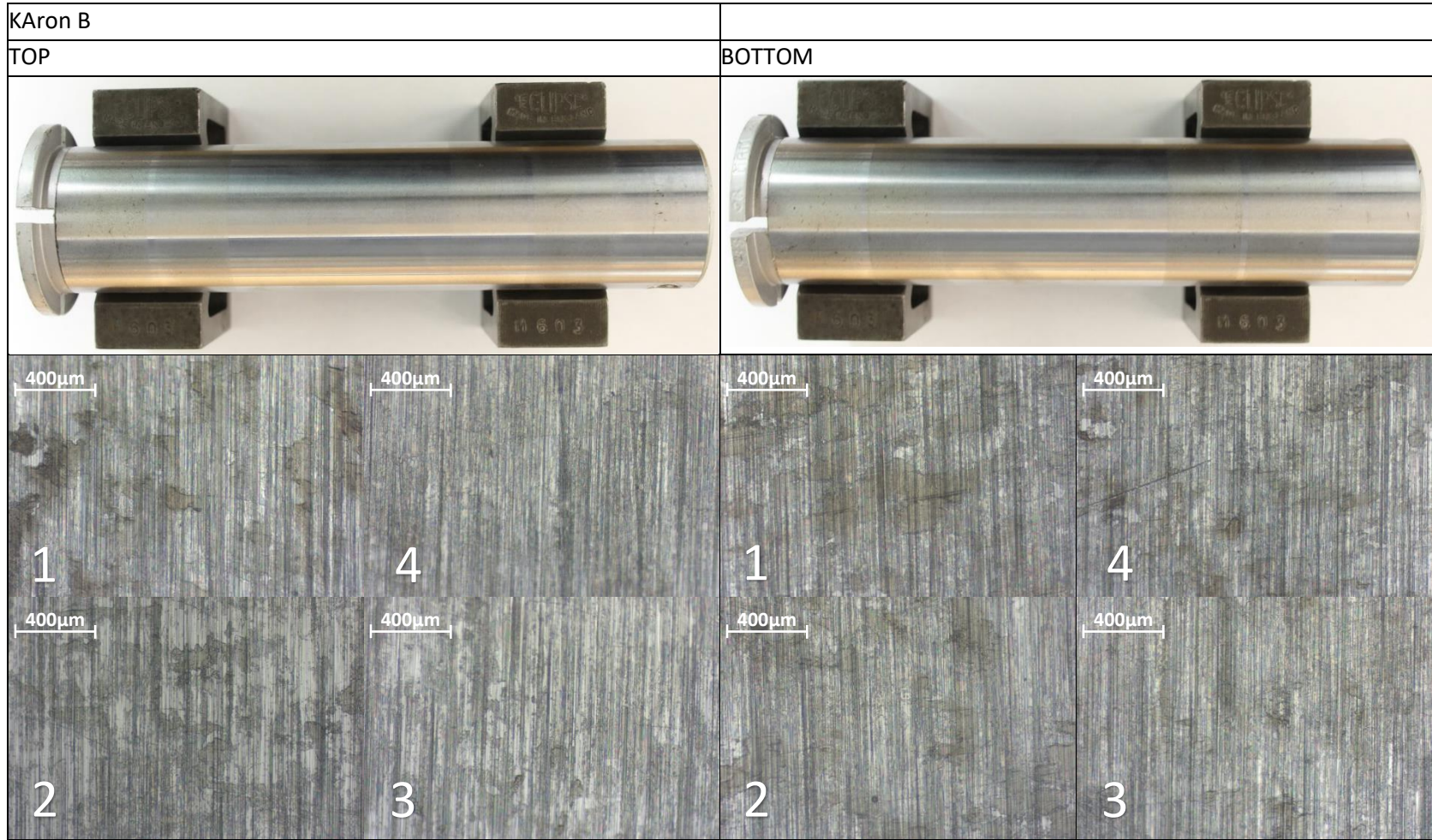


Table 6.8: Microscopic inspection of KArOn B in each bush location for both the top and bottom of the pin

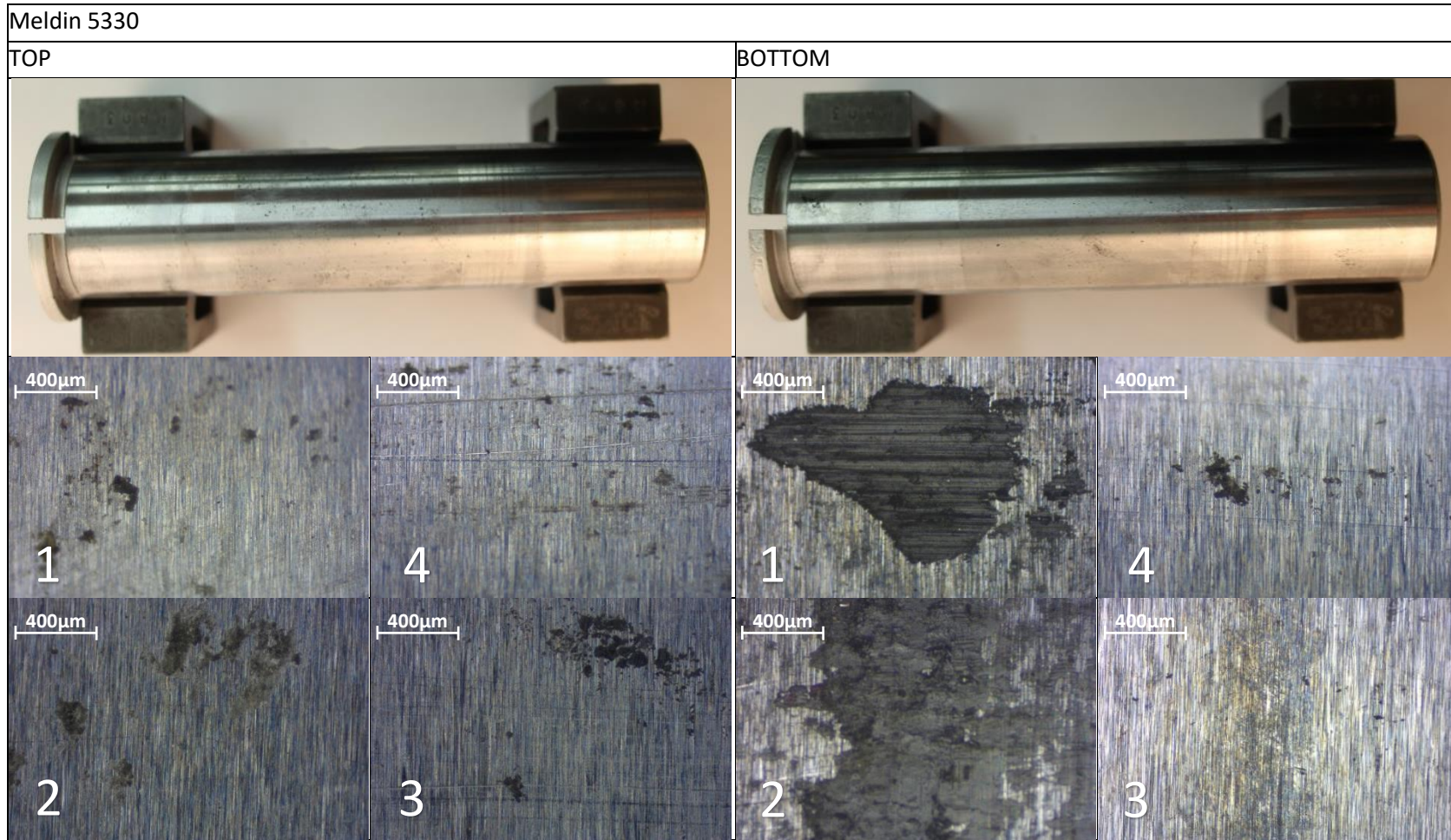


Table 6.9: Microscopic inspection of Meldin 5330 in each bush location for both the top and bottom of the pin

Microscopic inspection of the pins confirmed that Vespel 21 had transferred an even layer of graphite particles to the pin more prominently for the upper clevis bushes. Material transfer was however located in the regions of the lower clevis, but was found to be in lines radially around the pin with the greatest amount located at the edges of the bushes rather than an even transfer. It is proposed that the greater bearing pressure is resulting in a larger deflection of the bushes in the axial direction of the pin, slowly moving the wear debris out of the contact, and therefore reducing the benefit of lubrication that the particles bring to the contact. The size of the particles transferred to the pin was shown to be in the region of 100 – 200  $\mu\text{m}$ , typically the size of graphite particles included in bearings to improve dry lubrication performance. This is confirmed by the manufacturers information detailing that Vespel 21 includes 15% wt graphite.

It was more easily identified on a microscopic scale for Gar-Max that material had been deposited from the high asperities of the bush, the re-enforcing fibres. This is evident from a pattern left on the pin, rather than a coherent film, with spacing between the clearly defined lines in the order of 500  $\mu\text{m}$ , similar to the spacing between the fibres. In addition, the angle at which the material has been deposited on the pin at 18 – 19 $^{\circ}$  (Figure 6.16a) is comparable to that of the winding angle of the fibres in the bush at 14-16 $^{\circ}$  (Figure 6.16b) used during manufacture. Figure 6.16b is the inside of Bush 1 in the same orientation as the pin in Figure 6.16a.

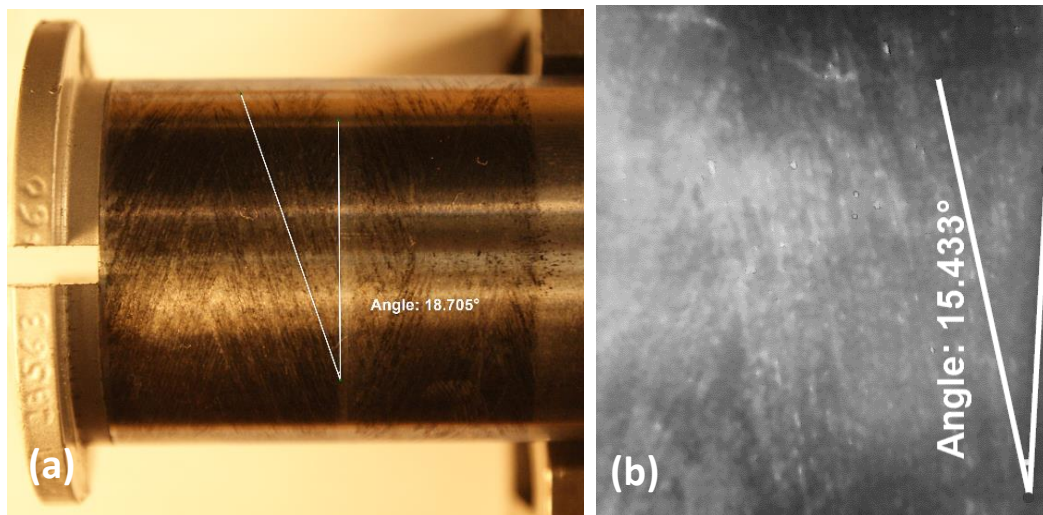


Figure 6.16: Angle of material transferred to the pin (a), Angle of fibre lay in Gar-Max resulting from the Manufacturing process (b)

The datum for the measurement of the angle for both Figure 6.16a & 6.16b is taken as the flange of the bush, hence a slight discrepancy is to be expected for these measurements given the reference of the measurement is a curved surface. The top of the bush can be identified in Figure 6.16b from a faint scratch along the top of the figure, which was caused during the fitting and removal process. It can therefore be concluded that the PTFE transferred to the pin from the sliding layer is used to generate a lubricating film from the larger asperities, as it was noted that after testing the bore of the bush was visibly smoother.

Microscopic inspection of KAron B revealed that platelets had been transferred to the pin, to develop a thin even layer of PTFE for all the bushes. The resulting transfer film can be seen to be uniform, where platelets had merged, rather than distributed individual platelets. The size of individual platelets that could be located was in the region of 200  $\mu\text{m}$ , comparable to the size of the larger asperities identified by the optical surface profile (Table 4.2 Section 4.2). Therefore it can be seen that the platelets, once transferred merged to generate a uniform film.

Meldin 5330 had transferred some material but did not appear to be forming a transfer film. The absence of wear debris and the presence of a shiny region for the macroscopic inspection indicate that polishing was occurring. Under microscopic inspection it was confirmed that little wear debris was present, and what appeared to be a reduced distance between valleys on the pin surface in the bush locations suggests wear of the asperities on the pin as polishing has occurred. Therefore both macroscopic and microscopic inspection indicate that the bushes were polishing the pin, rather than transferring material to build up a lubricating film. It should be noted here that all pins were standard aircraft landing gear pins, supplied by the aircraft manufacturer and therefore subject to strict MIL-SPEC and quality assurance standards to ensure that there is little difference between the surface roughness of the pins supplied.

For the bottom of the pin bushes 1 & 2 show a more significant amount of material transferred. However it should be noted that for bush one this was only a single large flake that had been removed and therefore was the only region of interest. It can also be observed from the axial ridges in this flake where the pin was removed, that the flake was also relatively thick.

Bush 2 appeared to show a more uniform transfer of material, however this was located in a line at the edge of the bushing indicating that wear debris were being moved out of the

contact, therefore offering little tribological benefit. Scratches can be observed in the axial direction of the pin as a result of fitting and removal. For the bottom of the pin, Bush 3 shows some clear radial marks in the macroscopic image. One of the striations was investigated microscopically to identify if it was due to material transfer and if the wear debris were being out of the contact. The discolouration of the ring on a microscopic scale, indicated that it was not due to material transfer but due to contamination. While every effort was made to minimise the risk of contamination from oil or grease during the whole test programme through thorough cleaning of the pins with acetone prior to fitting, it must be accepted given the servo-hydraulic test lab that a small amount of contamination may have occurred. Furthermore the striations are limited to only bush 3 implying that the cause of these striations was limited to only the one bush, and therefore it is likely to be due to a contaminant. The contamination was however thought to have had little impact on the outcome of the test results, as any materials likely to be fitted to an aircraft landing gear application are subjected to strict contamination testing as contaminants such as hydraulic fluid, grease, de-greasing compounds, dust and dirt are all common on aircraft landing gear. In addition, Meldin 5330 is resistant to many chemical compounds, such as Gasoline, Motor and mineral oil therefore having a minimal negative impact on the material performance.

Comparing the average size of the material transferred to the size of the high points on the optical surface profiles (section 4.2) showed good agreement for Vespel 21 and Karon B as they were of comparable size, indicating that the asperities adhered to the pin and were plucked from the surface of the bush. Gar-Max differed from this trend slightly due to the direction of fibre lay and the location in which the optical profile was taken, however it was clear that material had been transferred only in the regions where the fibres contacted the pin.

Inspection of the pin outside of the contact zone for the bushes indicated that mild fretting had occurred between the pin and the retaining collar for the polymer composite materials (Figure 6.17). It was observed that the same phenomenon did not occur for Karon B.



Figure 6.17: Evidence of fretting between the retaining collar and the pin for the 3 polymer composite materials

Therefore it was proposed that the rigidly mounted retaining collar on the upper clevis prevented equal amounts of deflection at the head end and far end of the pin for the materials with a lower joint stiffness. The unequal deflection produced motion in the axial direction, as the pin pivoted about the retaining bolt (Figure 6.18).

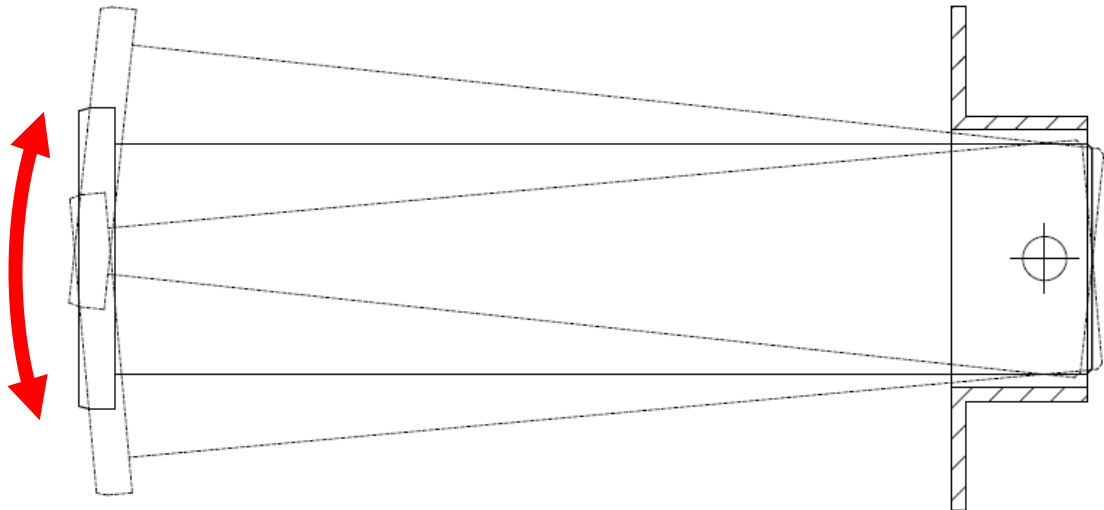


Figure 6.18: Pivoting of the pin about the retaining bolt, inducing an unequal load distribution between the head and far end of the pin

Results from the instrumented load pin described in section 3.2.3.2 further confirmed this. Measurements were taken every  $5^\circ$  for  $0-180^\circ$  at an applied load of 15 kN. Both the retaining pin and collar had been removed for the test to enable the pin to be rotated. The loads recorded by each of the gauges for each of the materials are shown in Figure 6.19. It should be noted here that bridges 2 and 4 have been plotted to show the maximum loads in the same locations as bridges 1 and 3 due to the perpendicular position of the gauges in the load pin. Therefore a sharp fluctuation in load can be observed in Figure 6.19 for these bridges, where the data has been joined, as a result of a slight misalignment of the gauges during manufacture of the load pin.

Figure 6.19 also showed that there was close correlation between the phase shifted bridges and the non-phase shifted. Additionally it can be said that the gauges located at the head end of the pin have consistently recorded a lower load than those at the far end, the only exception being KAron B. The lower load recorded at the head end is a result of a greater amount of plastic deformation or wear having taken place at this location. When each half of the clevis was loaded parallel to the other the far end carried a greater amount of load as

a result of the smaller clearance. Karon B shows exception to the trend, given the higher joint stiffness.

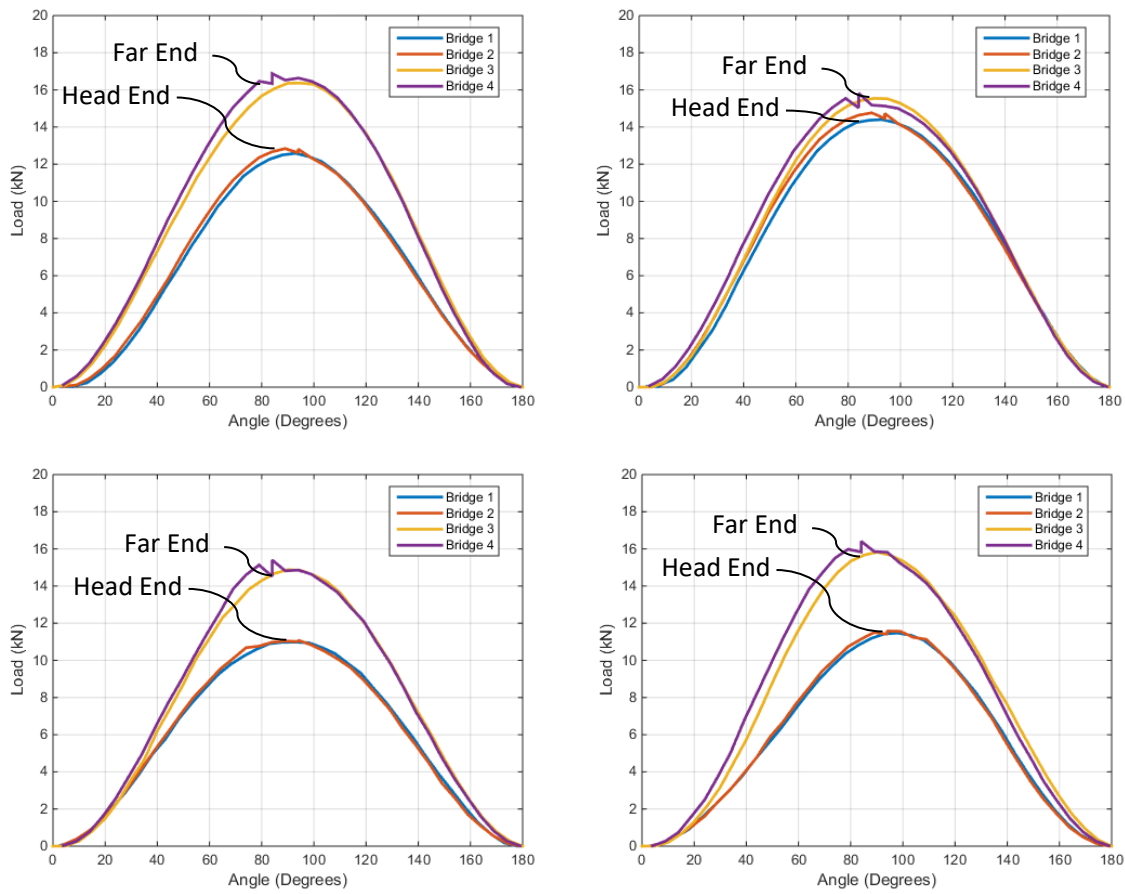


Figure 6.19: Load distributions for each bridge in the load pin for each of the materials. Clockwise from top left, VespeL 21, Karon B, Meldin 5330 and Gar-Max

Further evidence of the greater amount of wear or deformation at the head end can be observed from the visual inspections performed above in Table 6.5, where there has been more material transfer to the pin at the head end rather than the far end.

### 6.3.1. Failure of Vespel 21 Flange

Upon assembly of the joint in preparation of LC3 for Vespel 21, the flange on bush number 3 fractured when the bush was pressed fully home with the mandrel fitting tool. No abnormal forces or methods were used, and the bush was properly seated in the housing. Therefore the bush was removed from the clevis and inspected to determine what had caused the failure. Macroscopic inspection was conducted for four regions of interest, these are identified in Figure 6.20.

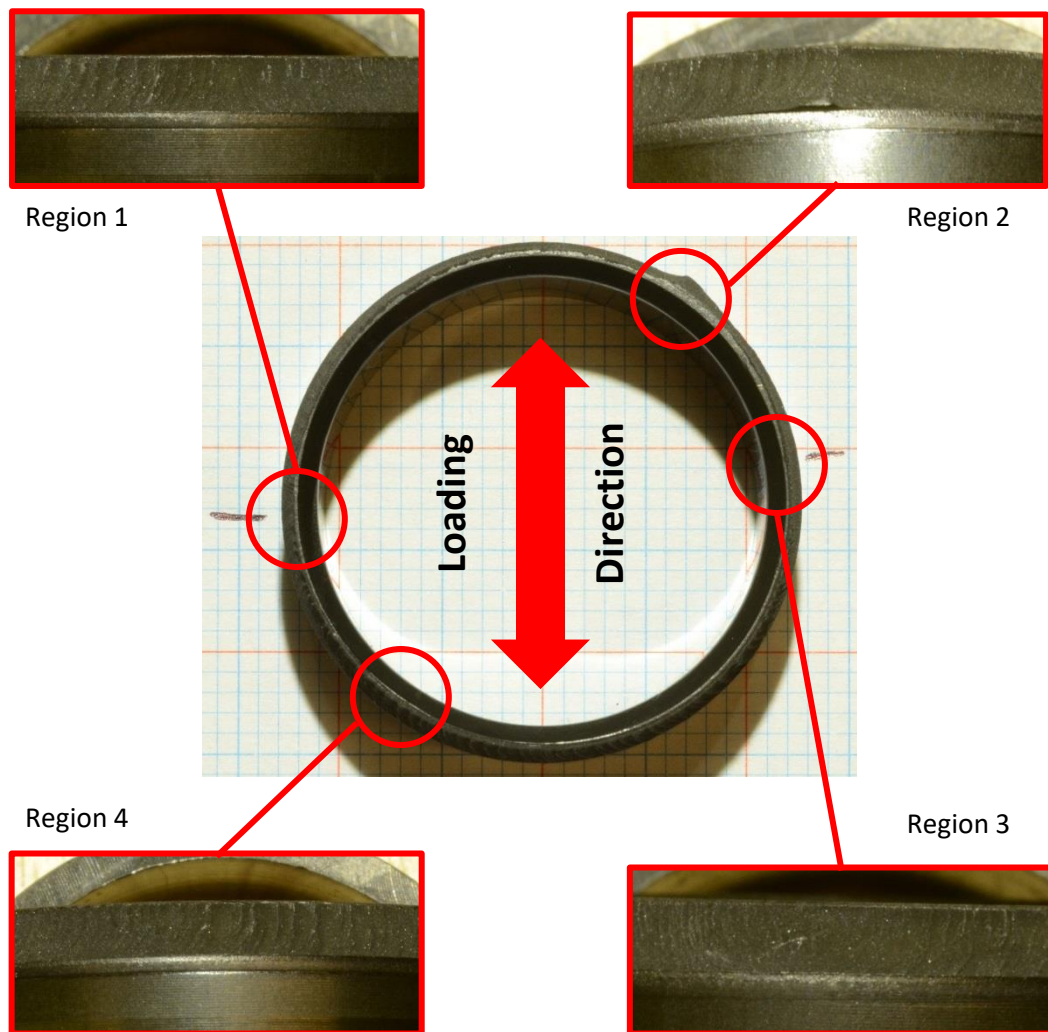


Figure 6.20: Regions of interest from the failed flange

Region 1 located perpendicular to the axis of loading shows the ridges on the fracture face changing direction. This was chosen as it was considered to be a potential source of crack initiation that resulted in the failure.

Region 2 was selected for further inspection due to the raised peak on the fracture face, indicating that fast fracture may have occurred in this location at the end of the fracture, resulting in the quick removal of material.

Region 3 again approximately perpendicular to the axis of loading shows another region where the ridges on the fracture face change direction. This region is also of a greater area than that of region 1 and shows a more porous texture between the ridges.

Region 4 is a representative image of the fracture face. The ridges can clearly be seen in this location to be travelling in the same direction, curving towards the high stress region of the flange corner, where the crack propagated.

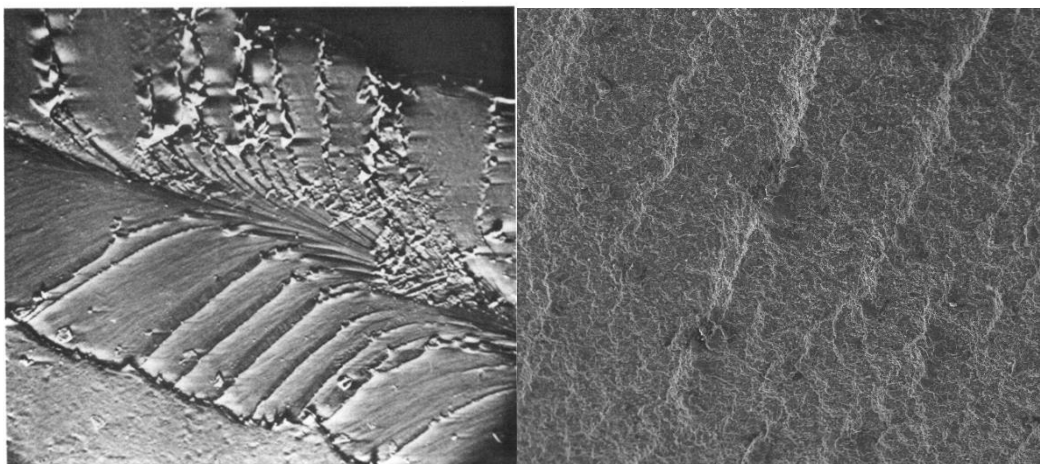


Figure 6.21: Fracture face (left) ASM handbook (ASM 1987) polyimide x120, (right) fracture face Vespel 21 x250

Comparison of the fracture face with that of a polyimide in the ASM fractography handbook (ASM 1987) shows an almost identical fracture face, of crack propagation. For the ASM case, the crack initiation was traced to a design deficiency, in the case of the polyimide bush, this was believed to be the fatigue.

Given the circumstances of the failure it is difficult to determine the cause of failure however it is predicted that this was a fatigue induced failure which initiated in two points, region 1 and region 3. The crack initiation was generated by the continuous growth and reduction of the contact area. The crack then travelled around the bush at the flange due to geometrical effects increasing the stress concentration until the two cracks met at region 2 the location of the fast fracture.

A replacement bush was manufactured and the testing of LC3 continued in an attempt to initiate another failure in bush number 2. Failure did not occur in bush 2 during LC3.

#### 6.4. Size of Contact

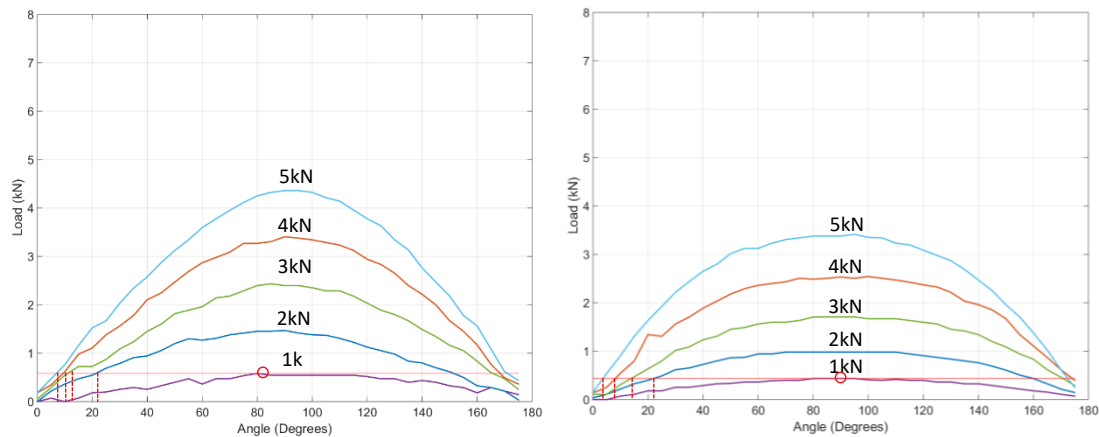
Following the successful completion of LC2 the pins were re-examined. For the three polymer composite materials it was observed that the region of contact was large and as expected could not be likened to Hertzian contact. Using the extended model developed in section 5.1 for calculating the arc of contact, the load at which the contact became “saturated” was determined. For Gar-Max the maximum load required to achieve saturation was 31 kN, while for Meldin 5330 it was 41 kN. The arc of contact was not calculated for Vespel 21 and Karon B as it was shown in section 5.3.1 that the simulation did not accurately predict the displacement, and therefore would not accurately predict the arc of contact.



Figure 6.22: Regions of non-contact observed at 90° to the loading direction

Large amounts of wear debris are observed along the length of the pin, outside the regions of contact, as a result of the removal and re fitting of the pin during the testing of LC2 disturbing the region of contact. However it can be seen that at 90° to the loading direction the region of contact did not spread over the full 180° but instead left a region for wear debris to build up in for Vespel 21, and a region of no contact for Meldin 5330.

Therefore further investigations into the arc of contact were conducted. A range of loads between 1 and 5 kN were used to investigate the development of the arc of contact by indexing the instrumented load pin by  $5^\circ$ . It should be noted here that these tests were conducted in compression only, to avoid any component of the clevis extension influencing the results.



**Figure 6.23: Change in the arc of contact from the load distribution plot, recorded with the load pin for Meldin 5330 (left) and Gar-Max (right)**

The load profile indicates that the arc of contact is  $180^\circ$  however given that the load pin measures shear force in the pin at a single location, the load profile generated cannot directly give the arc of contact. When the gauges are not orientated either perpendicular or in line with the applied load, a resultant force is recorded due to the internal stresses in the pin itself. Hence the forces cannot simply be resolved to determine the load profile and arc of contact. Therefore an approach to investigate the change in angle of the load profile to obtain the same resultant force for a range of load profiles was adopted. The lowest load profile was generated using an applied load of 1 kN and was indexed around by  $5^\circ$ , the maximum point of this load profile was located.

A line of constant load was positioned at that value, and the remaining load profiles completed. Nearest point intersection between the line of constant load and the remaining load profiles was conducted and the corresponding angular position found. The angular difference between these values was then calculated. Meldin 5330 showed a change in angle of  $60^\circ$ ,  $5^\circ$ ,  $5^\circ$  and  $0^\circ$  While Gar-Max showed changes of  $60^\circ$ ,  $10^\circ$ ,  $5^\circ$  and  $0^\circ$ .

It can be observed from Figure 6.23 that for Gar-Max the measured load was less than the applied load. For example an applied load of 5 kN by the test frame resulted in a measured load of only 3.5 kN by the load pin, this was caused by the flanges on the bushes being in contact, hence carrying a proportion of the load.

The calculated angular difference using the simulation was found to be 2.9°, 2.4°, 2.2° and 2.0° for Meldin 5330, and 3.5°, 3°, 2.7° and 2.5° for Gar-Max. Comparison of Vespel 21 and KAron B was not performed<sup>3</sup>, as it was evident that the change in angle technique was not a suitable method to verify the arc of contact, and it was shown in section 5.3.1 that the displacement model was not as accurate for these materials.

Results from the load pin could only be used to show if the change in the arc of contact with increasing loads was comparable to the calculated change in angle, rather than the complete arc of contact. Therefore PVC bushes were loaded as described in section 5.2, however a lightly knurled pin Figure 3.12 was used for loading. The bushes were sectioned and examined under an optical microscope, and measurements taken from the hatched pattern, left on the bush. Once the beginning and the end of the imprinted pattern had been identified, a measurement between the two positions was taken across the bush to determine the contact width. Several measurements were taken along the length of the bush, and 2 repeats conducted. The contact width then averaged and trigonometry used to calculate the half angle of contact. Table 6.10 shows the experimental results.

Load (kN)	2	4	6	8	10
Measured contact width (mm)	3.2	7.4	6.5	7.2	8.2
Half arc of contact (deg)	15.3	21.4	33.0	36.7	43.0

Table 6.10: Experimentally determined contact width and calculated half angle of contact

To ensure validity of the beginning and end of the contact regions described above, the knurled pin was loaded against a flat cylindrical surface at loads of 125 N, 250 N and 500 N. Hatchings of 0.3 mm, 0.5 mm and 0.7 mm respectively can still be seen at these loads (Figure 6.24).

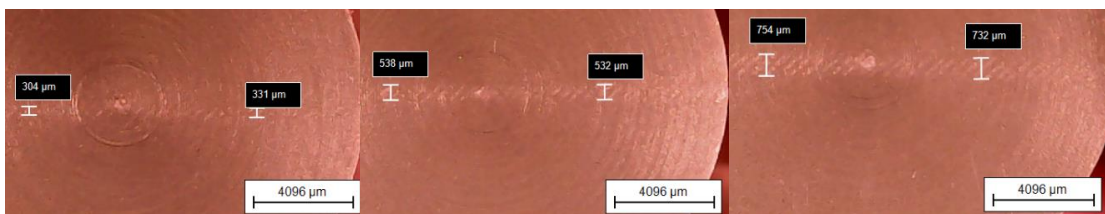


Figure 6.24: Evidence that a pattern is still left on the bush at low loads of 125N, 250N and 500N (left to right)

<sup>3</sup> Experimental results are detailed in Appendix B

Therefore if contact occurred and no imprint was produced, the load was less than 125 N which is 6.25% of the minimum applied load, and therefore could be neglected especially for the higher loads.

The dimensionless load parameter  $\frac{E_1^* \Delta R}{P'}$  was used to enable comparison of the experimental results, simulation results and the solution to Persson's equations for elastic dissimilarity (Ciavarella & Decuzzi 2001b). The non-dimensional load parameter was first calculated for the experimental and simulation results and for Ciavarella & Decuzzi's solution it was calculated using (equation 2.5).

Values for the non-dimensional load parameter corresponding to the values calculated for the experimental and simulation data were found, and therefore the corresponding half arc of contact  $\gamma$ . The results comparing the half arc of contact at the same non-dimensional load parameters are shown in Figure 6.25.

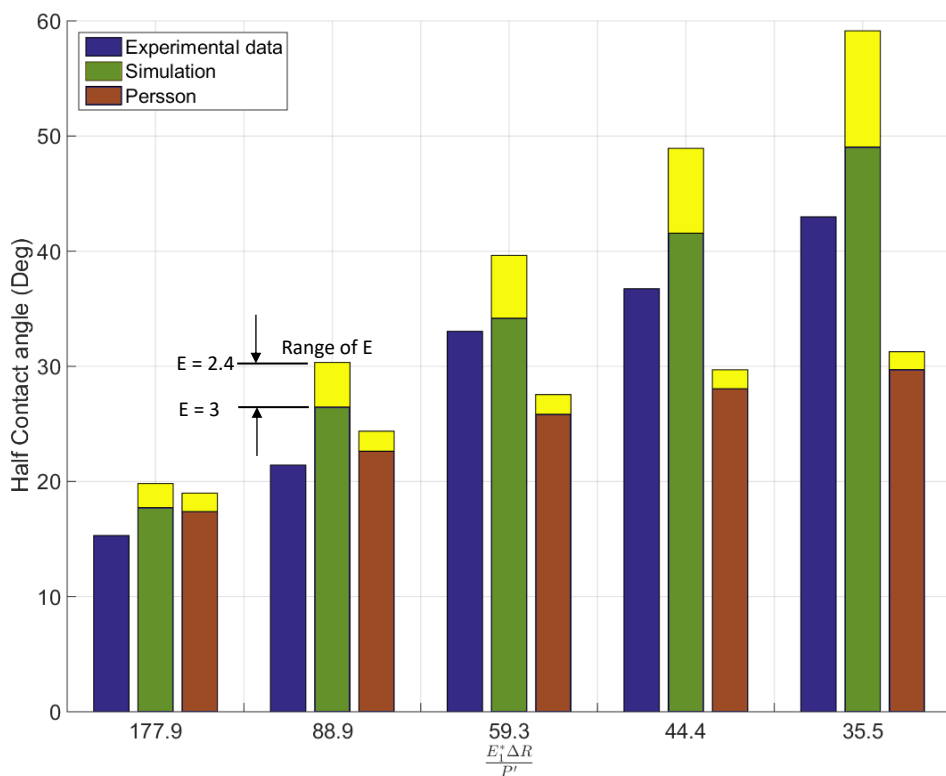


Figure 6.25: Comparison of the half the arc of contact for the experimental data, simulated data and the modified Persson solution at the same values of dimensionless load

The angle of contact is shown to be more accurately predicted when calculated by Persson for low loads than the simulation developed here. However as the load increases the

opposite is true, Persson's solution begins to plateau, while both the experimental result and the simulation continue to increase.

The two calculated data sets, have a region at the top of the bars to show the influence of the modulus of elasticity on the calculated result. The upper limit represents the lower modulus of 2.4 GPa, while the lower limit represents the higher modulus of 3 GPa. The modulus can be seen to have a greater influence on the simulation result, than on the calculations of Persson. A higher modulus would result in a consistently more accurate prediction of the arc of contact for the simulated result for all loads, and would also improve the accuracy of Persson's solution for the low load case.

The experimental method of measuring the width of contact, and then calculating the arc of contact, obviously carries with it some error. Given that the lowest material stresses will occur at the edges of the contact and the measurement was taken based upon the permanent deformation that occurred as the result of the knurled pin, it is highly likely that there was contact occurring that didn't result in permanent deformation. While attempts have been made to investigate the minimum force required to result in permanent deformation, through the use of the flat cylindrical surfaces, it was shown that loads as low as 125 N still resulted in a plastic deformation of 0.3 mm contact width. Therefore it is clear that there will still be significant amounts of contact in the elastic region increasing the width of contact and also the arc of contact, beyond what is currently being measured. The error introduced as a result of this increased width and arc of contact will be more significant at low loads, improving the agreement between the experimental results and those of the model developed here.

The Persson method plateaus due to the assumption of Hertzian contact, and therefore breaks the assumption that there is a small region of contact. In addition the person solution which works for elastically dissimilar materials, does not account for significantly elastically dissimilar materials such as a steel shaft loaded against a polymer bush. Furthermore the thickness of the bush is not considered.

There are of course some limitations of model developed in this work too, such as the assumption that there is no deformation of the shaft. While this may be a valid assumption at low loads and with materials that have a much lower modulus of elasticity than that of the pin. Care must be taken when applying the model to simulate high loads for materials such as Karon B, where the majority of the bush is steel, resulting in a much stiffer joint, and therefore less deformation of the bush.

One of the limitations mentioned in section 5.1 is that there is no limiting condition for the amount of displacement. If care is not taken, the displacement predicted by the model can exceed the bush wall thickness, resulting in a breakdown of the model as the element considered initially during the construction of the model ceases to exist, and the shaft would then contact the housing. In this situation, not only would the stiffness of the joint increase, the contact would be more similar to that covered by the Hertzian model. From purely a geometrical point of view with an increasing force in this case would result in a decreasing arc of contact, as the contact width would have reached the maximum value, that of the pin diameter, and then would begin to decrease as the chord length would be occurring on the opposite side of the contact, which is of course not possible with the materials and geometry considered here.

Additionally there is no limitation governing the change of Stage (i) to Stage (ii) from section 5.1, and can be seen in section 5.2 for the PVC bushes, where the non-linear contact changes to be linear for a constant arc of contact, and then enters the plastic deformation region. This plastic region is also one that has not been considered by the model developed. Further work focusing on the elastic plastic transition would result in a much more refined model. A model that can account for the transition between Stage (ii) and Stage (iii) would also include necessary components to represent the deformation occurring in the axial direction along the length of the pin, as the stresses within the bush material could no longer be neglected. There is also the limitation that the interference fits of the bushes are not considered, which of course results in a reduced clearance and in some situations can result in a neat or zero clearance condition.

## 6.5. Conclusion

Dynamic testing was conducted for the four commercial bearing solutions for a total of three aircraft lives. Cyclic displacement of the joint was recorded using an LVDT, and the static displacement subtracted from it to give the deformation of the joint per test case. The roundness of the bushes was also measured at specific intervals and the maximum deviation from round recorded. Comparisons between the deformation of the joint using the LVDT and the maximum out of round were in close agreement with each other, showing total permanent deformation to be in the region of 20  $\mu\text{m}$  or less, a similar value to that of the error in the measurement. It is recommended that in order to reduce the measurement error that a new bespoke measurement system is developed for measuring the roundness of the bushes in situ.

The load displacement model was extended to predict the arc of contact, and therefore investigation into the arc of contact was made based upon the visual inspection of the pins. An instrumented load pin was inserted into the joint, and indexed round with a constant load. This was repeated for five low loads, and the change in angular position of a load determined from the load profile generated. These results were compared to the modified load displacement model, and were found to be significantly different, showing changes of  $10^{\circ}$  and  $2.4^{\circ}$ . Experimentation was conducted using a lightly knurled pin loaded against the single PVC bush. Sectioning the bush following the application of a load revealed an imprint to be left on the bush which was measured, and the arc of contact calculated using trigonometry. The results from the model showed improved accuracy over that of the modified Persson solution at higher loads. The importance of selecting the correct value for the modulus of elasticity for the bush was highlighted, indicating that an increased value for E would result in a more accurate application of the model developed. It was therefore concluded that indexing the load pin, and calculating a change in the arc of contact was not an accurate method for verifying the arc of contact.

It was shown that careful consideration should be given to the pin retention technique when using polymer composite bushes at high loads. The retention technique used in this research showed that unequal loading of the bushes was occurring due to the pivoting of the pin on the retaining collar. This not only accelerated the wear of the bushes at the head end, which could be observed both from the material transfer to the pin and also the lower recorded loads with the load pin at these locations, but also resulted in fretting between the pin and the retaining collar.

Fracture of the flange occurred during fitting of Vespel 21 of the third bush prior to testing life cycle 3. Two initiation points were identified, located at  $90^{\circ}$  to the loading direction, on opposite sides of the bush. A replacement bush was manufactured for the completion of the test programme, with the expectation that bush 2 would fail shortly afterwards, which did not occur.

[Blank Page]

# 7.

## Articulation of a pin joint

In this chapter the effect of aviation grease and general purpose grease are evaluated for use in an oscillating pin joint. The regime in which the joint operates was experimentally determined. The angle of articulation was varied to investigate the effect on the life of the lubricant. The suitability of self-lubricating journal bearings in an oscillating application was examined.

### 7.1. Lubrication performance in an oscillating journal bearing

Inadequate lubrication between sliding surfaces will result in either seizure of a joint, or in unacceptable excessive amounts of wear. For aircraft landing gear the worst case scenario is seizure of the landing gear in the up-locked position, preventing emergency free fall of the gear. The oscillatory motion and the low sliding velocity of 0.07 m/s indicates that the joint would be operating in either the boundary or mixed lubrication regime (Zhu et al., 2012). Inadequate lubrication of the landing gear may occur as a result of missed service intervals, incorrect lubricant or thermal degradation for example.

Specially designed aerospace greases have been developed to lubricate the joints and minimise these problems. These are typically two phase systems consisting of a lithium soap thickener, and a mineral oil or synthetic base oil. The thickener acts as a reservoir, which upon shearing releases a base oil for lubrication of the contact (Booser & Wilcock, 1953). The thickener can also have a dramatic effect on lubrication performance through two main mechanisms; 'direct' where the grease thickener augments the oil film and the 'indirect' where the thickener releases the base oil through shearing (Bushan, 2001).

### 7.2. Dry Contact

Initial testing was conducted using the pin joint function tester described in section 3.3 to determine the COF value between a set of unlubricated aluminium bronze bushing and a steel aircraft landing gear pin, in oscillatory motion to provide a benchmark for comparisons. The aluminium bronze bushes and the steel aircraft landing gear pin were supplied by the aircraft manufacturer as a replica of the current aircraft technology. A variety of surface sliding velocities were investigated around the 0.07 m/s region which is typical of where the joint operates. A small number of cycles were run with a fixed articulation angle of  $\pm 40^\circ$  to determine the COF of the contact, without significant heating of the joint. Figure 7.1 shows the results of this testing.

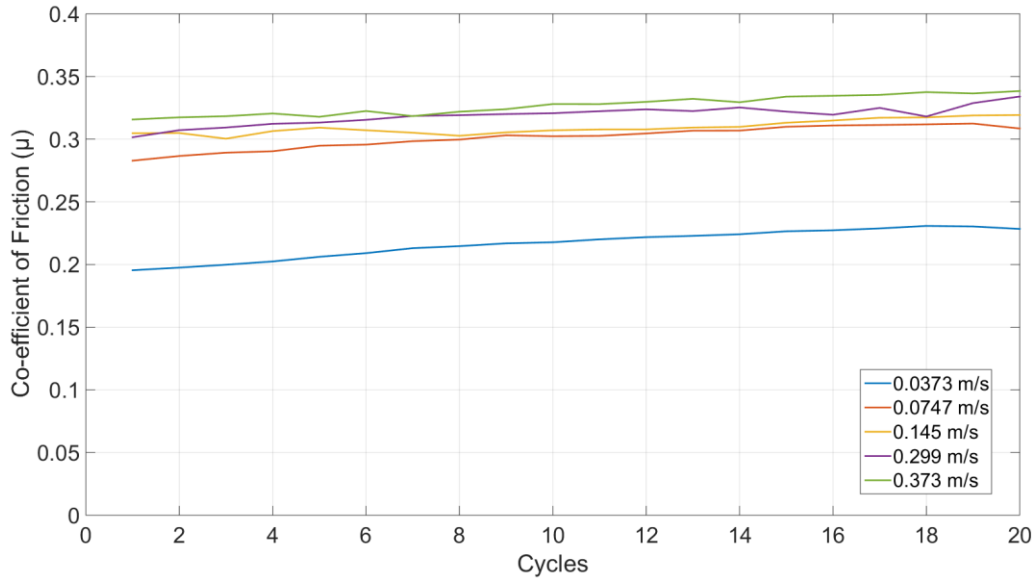


Figure 7.1: COF dry contact 10 MPa,  $\pm 40^\circ$  at a range of surface sliding velocities

The COF for the lowest sliding velocity was found to be significantly lower than all of the other tests conducted. The lower COF value has occurred, due to a lower rate of heat generation than the higher sliding velocities. At a low sliding velocity the system has time to dissipate the heat to the clevis and pin, moving it away from the contact. For the higher velocities however the rate of heat generation was greater than that at which it could be conducted away. Resulting in heating of the pin and bush, reducing the clearance between the two and therefore increasing the COF, hence the similarity between the higher velocities.

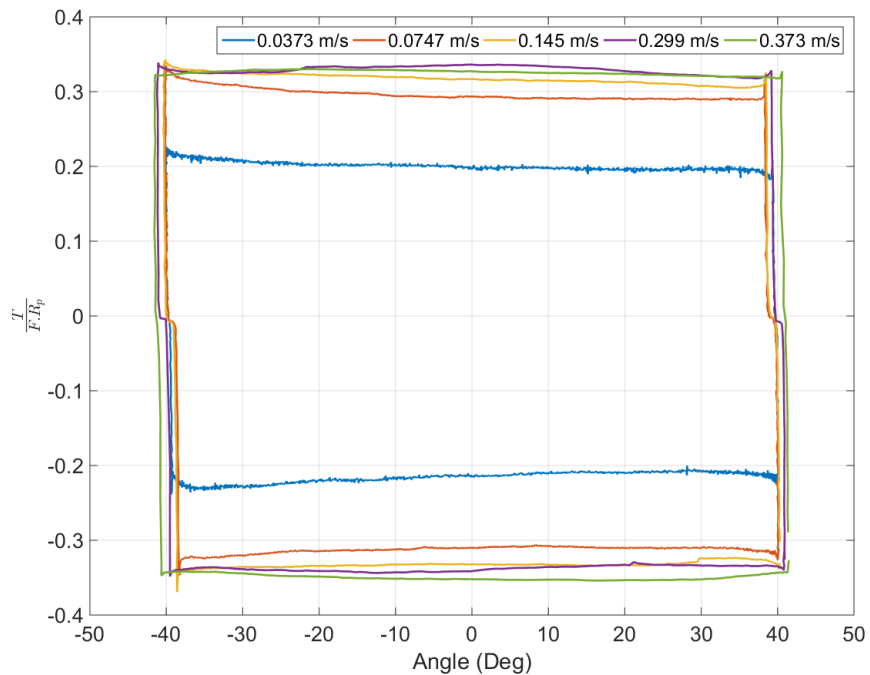


Figure 7.2: A typical cycle from each Velocity case at a bearing pressure of 10 MPa and an articulation angle of  $\pm 40^\circ$

Figure 7.2 shows a typical single cycle recorded from the articulating joint at each velocity tested. From this it can be seen that there was minimal stick slip behaviour from the joint for all velocities, as there is no significant peak in the corners. Additionally as expected there was no reduction in COF when the pin passes through the  $0^\circ$  position, the maximum speed, due to the absence of a hydrodynamic film. The analysis of the single cycle also confirms that the low velocity case is correct as the plot is uniform and evidently lower than the higher velocities.

### 7.3. Lubricated Contact

Testing progressed to evaluate the performance of grease. Surface sliding velocity was again fixed, along with the angle of articulation, and the load applied to the bearing. Two lubricants were injected into the contact, through the circumferential H shaped grooves, machined into the internal diameter of the aluminium bronze bushes. Grease was transferred from the grease gun to the bearing grooves through a grease point on the outside of the clevis, and then by a distribution channel. The two lubricants Mobil 28 and Aeroshell 22, are both Aerospace grade greases, typically used for lubricating landing gear. The COF for the lubricants was recorded and the performance compared to that of the dry case.

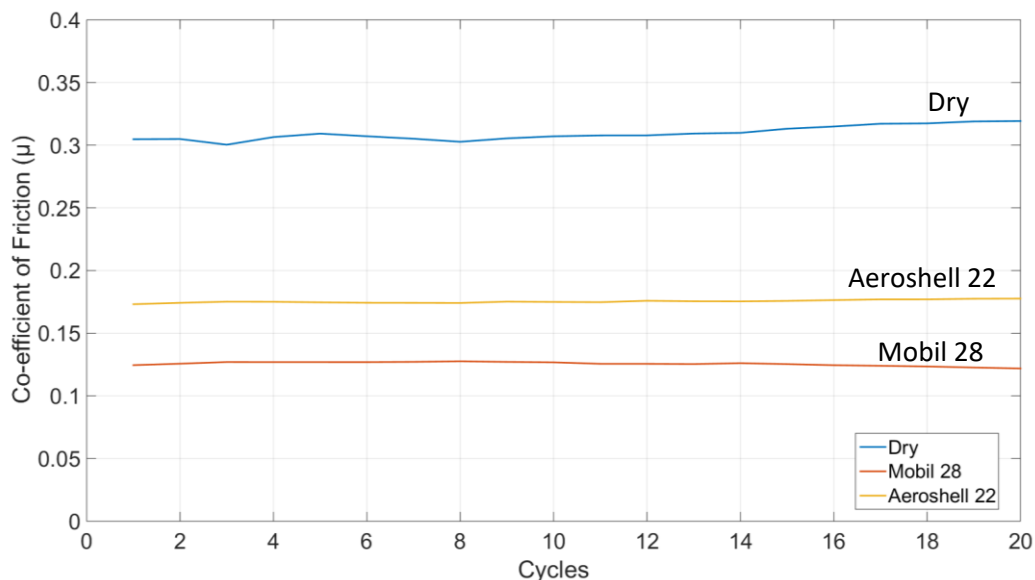


Figure 7.3: Effect of two aerospace grade greases Aeroshell 22 and Mobil 28 on the COF at 10 MPa and 0.145 m/s with an articulation angle of  $\pm 40^\circ$

Figure 7.3 immediately shows the frictional performance of each of these conditions. As would be expected, the dry case has a much higher co-efficient of friction of 0.33 than that of the lubricated cases, 0.19 and 0.14 for Aeroshell 22 and Mobil 28 respectively. Here it can

be seen that the joint has just entered the mixed lubrication regime given that both of these COF values are quite high, which is typical of boundary to mixed lubrication. Therefore it can be said that the lubricant is only just being entrained into the contact. This can be confirmed by inspecting Figure 7.4 showing a typical single cycle for each of the test cases. It can be seen that there was little evidence of stick slip behaviour and a decrease in COF for the maximum speed of the joint was also difficult to distinguish. There was however a slight reduction in COF that can be observed for Mobil 28 but not an amount significant enough to say that the joint is hydro-dynamically lubricated. Mobil 28 shows the lowest COF at the test velocity and pressure. The most likely reason for this improved performance is the use of a clay thickener for Mobil 28, rather than the microgel used in Aeroshell 22. Continually missed service intervals or joints will eventually lead to a rise in co-efficient of friction as the boundary lubrication regime begins to dominate.

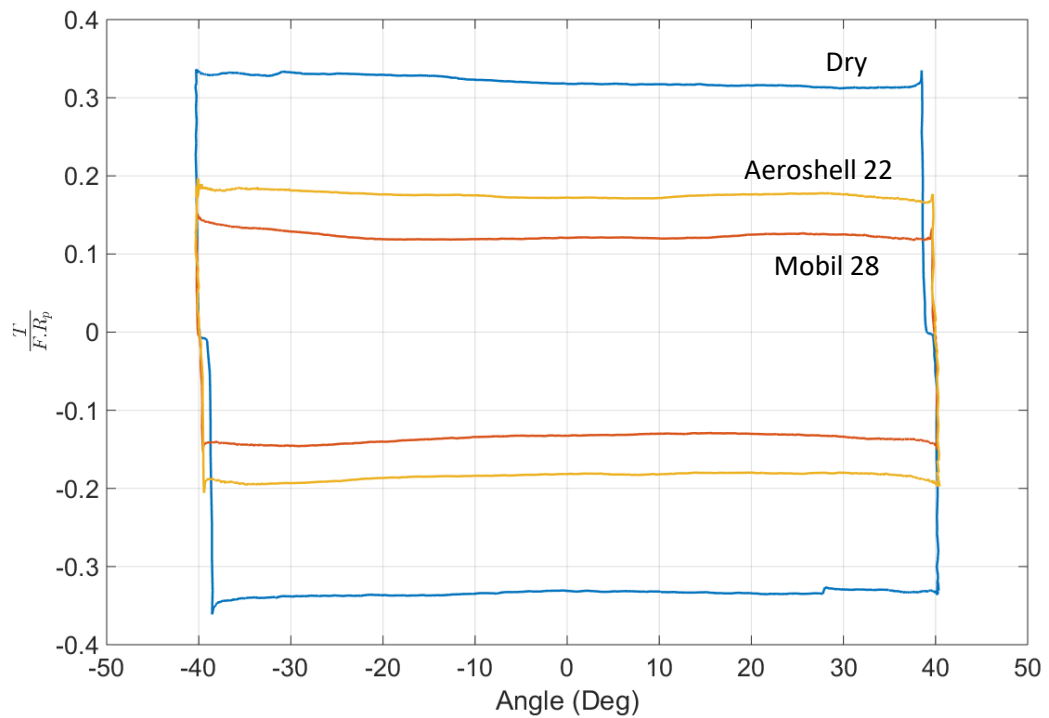


Figure 7.4: An isolated cycle from each lubrication case at a 10 MPa, 0.145 m/s, with an articulation angle of  $\pm 40^\circ$

## 7.4. Effect of lubricants on the contact

The two lubricants tested were subjected to a range of loads and sliding velocities, to determine which regime the joint was operating in. The sliding velocities used in section 7.2 for dry contact, were again used to enable direct comparisons to be made. The bearing pressures were 1.25 MPa, 5 MPa, 10 MPa and 15 MPa. The resultant co-efficient of friction can be displayed on the Hersey-Stribeck curve, using the Hersey equation

$$H \equiv \frac{\eta\omega}{p} \quad (7.1)$$

Where  $P$  is the mean contact pressure,  $\omega$  is the angular velocity of the pin, and  $\eta$  is the lubricant viscosity. The kinematic viscosity of the base oil was 29.3 mm<sup>2</sup>/s and 30.5 mm<sup>2</sup>/s for Mobil 28 and Aeroshell 22 respectively. The surface velocity stated is the mean value calculated using the radius of the pin and the reciprocal frequency. Figures 7.5 and 7.6 show the generated Hersey-Stribeck curves for Mobil 28 and Aeroshell 22 respectively.

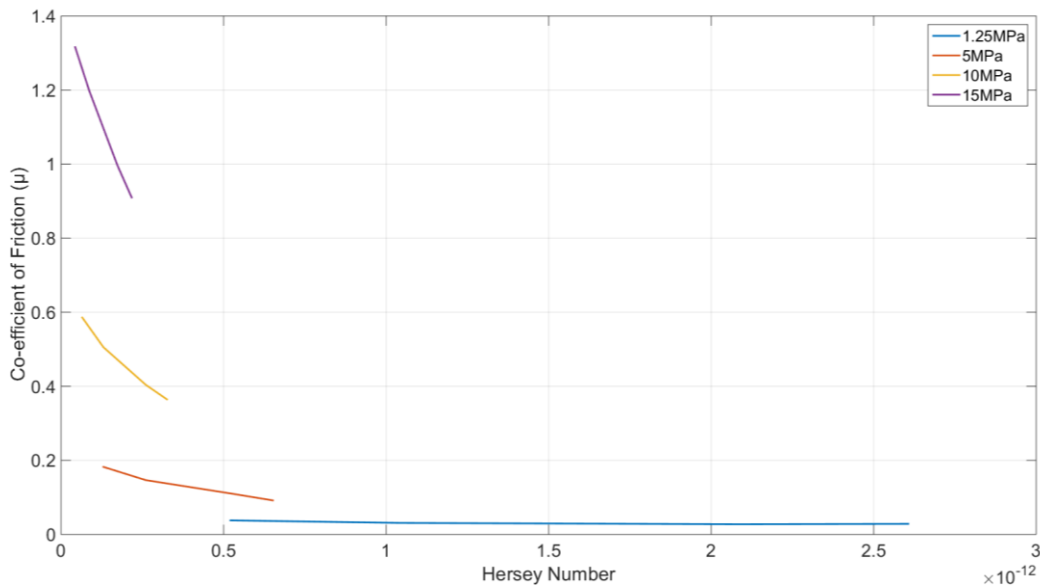


Figure 7.5: Stribeck curve generated for Mobil 28 using an articulation angle of ±40°

Given that the joint had a bearing pressure of 5 MPa and angular velocity of 12 deg/sec, the Hersey number is approximately 0.5x10<sup>-12</sup> for both greases (Mobil 28 and Aeroshell 22). This therefore places the joint in the boundary to mixed regime.

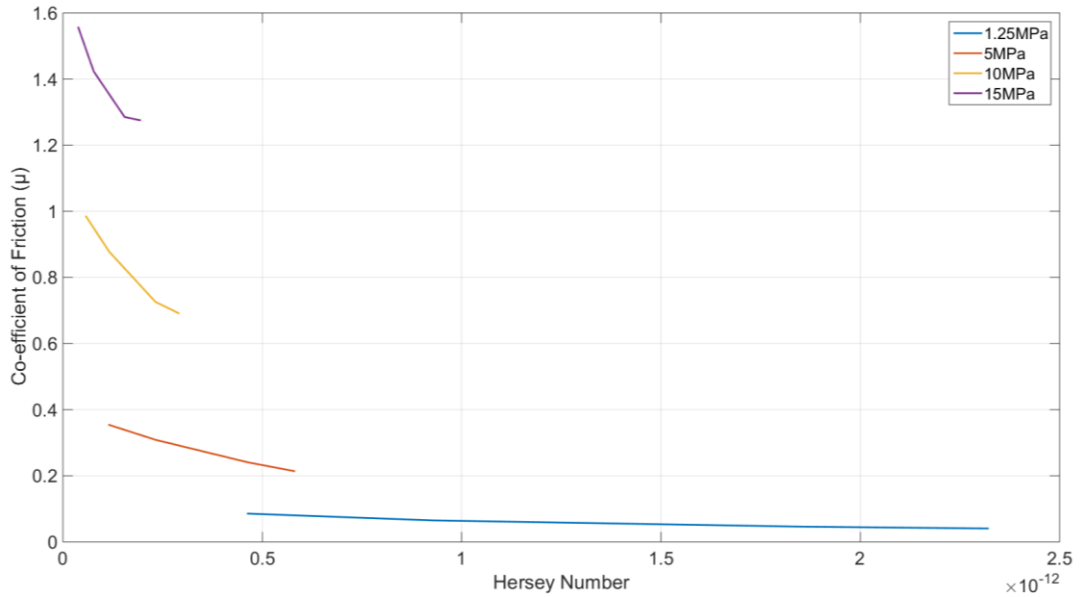


Figure 7.6: Stribeck curve generated for Aeroshell 22 using an articulation angle of  $\pm 40^\circ$

A typical Hersey-Stribeck plot is a continuous curve, however given the four bearing pressure cases tested four distinct curves for both lubricants can be seen (Figure 7.5 and Figure 7.6). For both lubricants tested the curves can be seen to overlap each other in terms of the Hersey number. From equation 7.1 it can quickly be realised that the same Hersey number can be achieved by adjusting either the sliding velocity or the pressure, hence at the higher velocities an overlap is achieved with the lower bearing pressure. The difference in the COF can then also be explained, as the higher velocity and the conformal geometry of the contact entrains more grease and results in a lower COF due to the faster generation of a hydrodynamic film.

### 7.5. Effect of articulation angle on re-lubrication interval.

A continuously rotating lubricated journal bearing shows little wear and a low COF when operating under normal conditions. During start-up however both COF and wear are high due to insufficient fluid separating the surfaces. As rotation continues and or the speed increases lubricant is pulled into the contact and the surfaces begin to separate. In the case of the oscillating lubricated journal bearing however the steady state of low wear and COF is not always achieved due to the decrease in velocity required to change the direction of motion, and hence the breakdown of the film.

### 7.5.1. Aerospace grade grease

The angle of articulation was investigated to determine if oscillating the joint by an amount greater than that of the arc of contact extended the life of the lubricant by entraining fresh grease into the contact. A range of velocities was used to obtain a Stribeck curve. Given the relationships  $\omega = 2\pi f\theta$  and  $\omega = \frac{U}{r}$  the reciprocating frequency of the joint was adjusted to ensure that the same mean sliding velocity  $U$  at the pin bush interface was maintained for the different angles of articulation  $\theta$  tested.

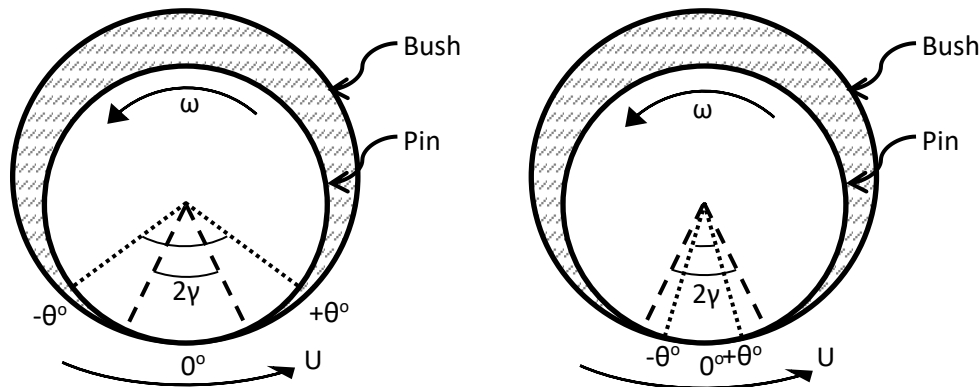


Figure 7.7: Schematic representing the angle of articulation

The first batch of tests conducted used a contact pressure of 20 MPa and Aerospace grease Mobil 28. Grease was injected after each test condition was completed to ensure fresh grease was present for each test. The grease gun was weighed after re-lubrication to ensure that similar amounts of grease were inserted into the joint for each sliding velocity, angle of articulation and repeat. Tests were repeated 3 times to ensure reliability.

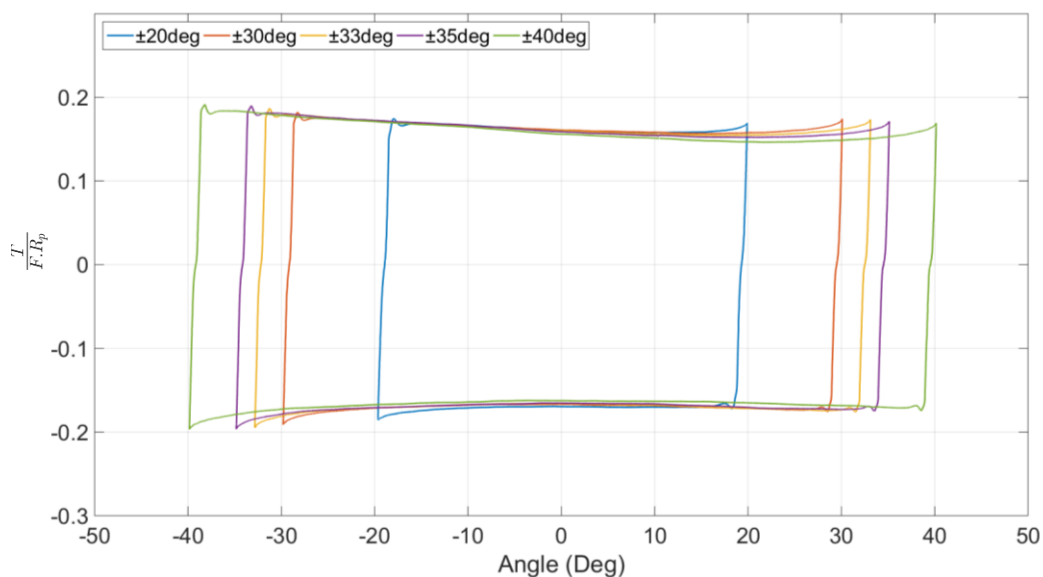


Figure 7.8: A single COF cycle for a range of articulation angles at 20MPa. COF is seen to decrease slightly for a longer stroke

Figure 7.8 shows a single COF cycle for a low velocity test condition for each of the articulation angles tested. From this it can be seen that increasing the angle of articulation reduces the COF by a small amount. This is the result of the increased sliding distance, leading to the entrainment of more grease into the contact, developing a thicker film between the surfaces, and therefore a slight reduction in the COF. However due to the oscillatory nature of the joint, the COF rapidly rises again as the sliding velocity begins to drop as the oscillation approaches the end of travel, before reversing, and the collapse of the film.

This process was repeated for a range of velocities, and an average kinetic COF taken for each articulation angle and velocity tested to generate a Stribeck plot, Figure 7.9. Care should be taken when interpreting these results as one may mistakenly assume that the lowest range of Hersey numbers is the transition from the mixed lubrication regime to the Hydrodynamic regime.

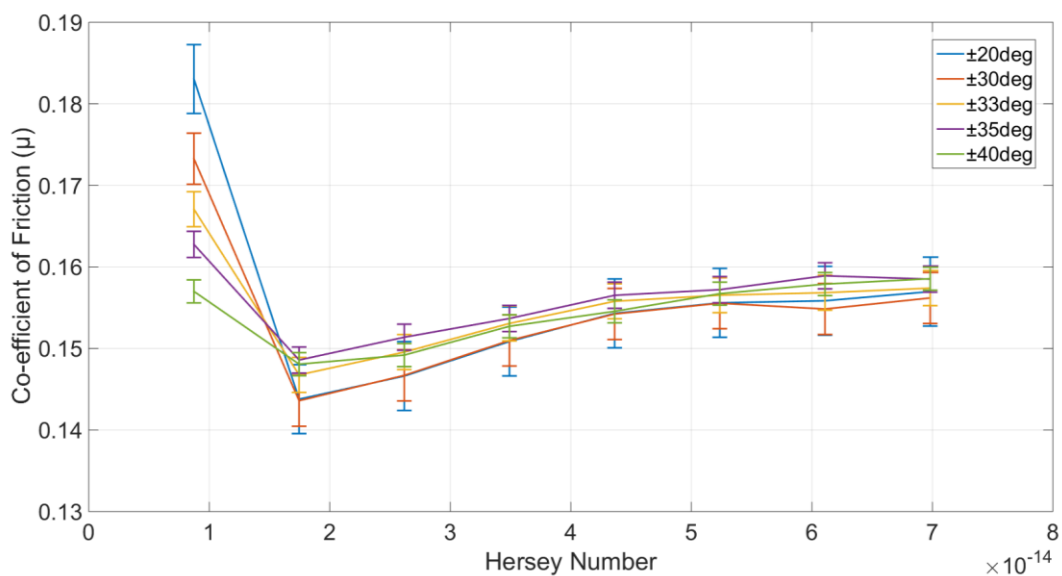


Figure 7.9: Averaged Stribeck curve showing little change to COF with varying articulation angle, Mobil 28, 20MPa

Upon closer evaluation one will notice the scale of the y axis of Figure 7.9 shown is 0.1, whereas on a Stribeck diagram it is typically a factor of 10 greater. For each of the 3 results<sup>4</sup>, the COF values typically lie between 0.18 and 0.22, which is a narrow band on the Stribeck diagram. Therefore indicating that the joint is still operating in the same mixed regime.

<sup>4</sup> See Appendix C1

It should be highlighted here that at first there appears to be little agreement of Figure 7.9 with Figure 7.5. Typical COF values for Figure 7.9 are in the region of 0.18 and 0.22, for a bearing pressure of 20 MPa with Mobil 28, whereas Figure 7.5 shows COF values of up to 1.3 using the same lubricant at a lower bearing pressure of 15 MPa. The first comment to be made about this observation is that much slower reciprocating velocities were used for the testing conducted in Figure 7.9. In addition, as already mentioned above an increased bearing pressure was also used for the testing, and it can quickly be observed from Figure 7.5 that a greater bearing pressure results in a greater rate of change of the COF with Hersey number. The most significant difference however is the fact that the bushes and pin were changed. Both bushes and pin were standard aircraft spares and therefore satisfy the relevant quality assurance and MIL-SPECs, however the Aluminium Bronze bushes are supplied oversize on the OD to minimise the cost of landing gear overhaul if the bore in the housing, or strut wears. In this eventuality the housing can be re-machined and the required bush OD can be increased to a larger diameter. For the case of the test rig, while wear of the housing is unlikely, there is possibility for the OD of the bush to be machined to a slightly different tolerance. An increased interference fit results in a reduced bearing ID, and therefore more favourable conditions for the generation of a lubricating film, resulting in a lower value for the COF.

The additional machining process of “line boring” the bushes was also completed, where the OD of the bush is machined to size, the bushes all fitted and then the ID’s of all the bushes machined in situ in the housing. This technique reduces the likelihood of bush misalignment occurring. This was completed only for the aluminium bronze bushes as they were not subjected to the constant fitting and removal process required during testing.

While it is highly unlikely, it must be considered that the calibration settings for the test frame’s load cell may have been altered during the test programme as a result of other operators running very different tests. It is highly unlikely that this would be a cause of the discrepancy as calibration was checked before and during the test programme, but a factor that must be considered none the less. The difference in COF values is therefore attributed to the change of bushes.

### 7.5.2. General purpose grease

Tests were repeated using a general purpose grease, at the same pressures and velocities, in order to determine if the phenomenon of the decreasing COF with increasing angle of articulation at low velocities was system or grease related. Shell Alvania EP (LF) 2 is typically a general purpose grease, and was therefore expected to perform worse than the aviation grease.

Shell Alvania showed repeatable results for all velocities and articulation angles, Figure 7.10. Therefore it can be confirmed that the Shell Alvania did not exhibit the same phenomenon as Mobil 28, but did however show a general decreasing COF with increase in velocity. Opposite to the general trend for that of the Mobil 28 trend, which showed a general increase.

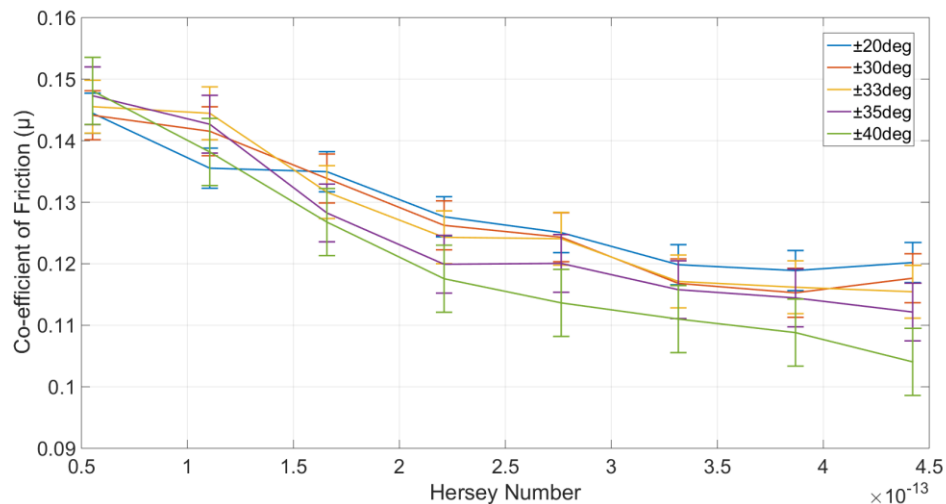


Figure 7.10: Averaged Stribeck curve showing little change to COF with varying articulation angle, Shell Alvania, 20 MPa

Shell Alvania also showed a much lower COF than that of the aerospace grease, almost consistently 0.1. Examining the averaged graph for Shell Alvania, there is some indication that for higher velocities than those tested, the angle of articulation may have a greater effect than what is observed here. There is an increasing divergence between the  $\pm 20^\circ$  and  $\pm 40^\circ$  cases, with  $\pm 20^\circ$  requiring slightly more torque than the  $\pm 40^\circ$  case.

Given the order of magnitude difference of the Hersey Number and the lower COF, it can be determined that Shell Alvania is operating more in the mixed lubrication regime than Mobil 28. Given that the bearing pressure, sliding velocities and angles of articulation were all maintained constant between the tests, the only variable in the dimensionless group is the viscosity. The base oil viscosities were 29 cSt and 189 cSt at  $40^\circ$  for the Mobil 28 and the Shell

Alvania respectively (ASTM D445). This therefore indicates that a grease with a higher viscosity performs better for a joint operating in the mixed regime.

The test was repeated using half the pressure (10 MPa) to determine if a reduction in arc of contact would show a greater divergence between the  $\pm 20^\circ$  and  $\pm 40^\circ$  cases, as more of the lubricant would be swept out and back into the loaded zone, for a smaller arc of contact.

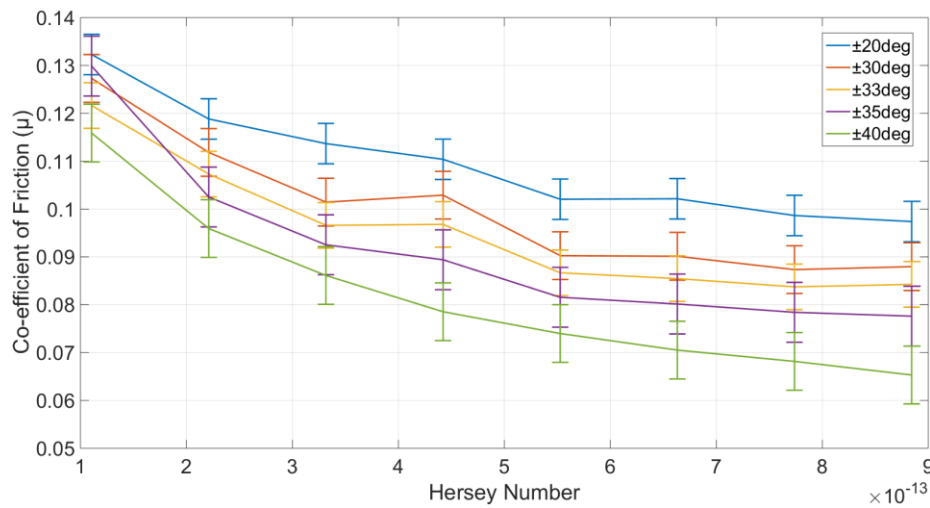
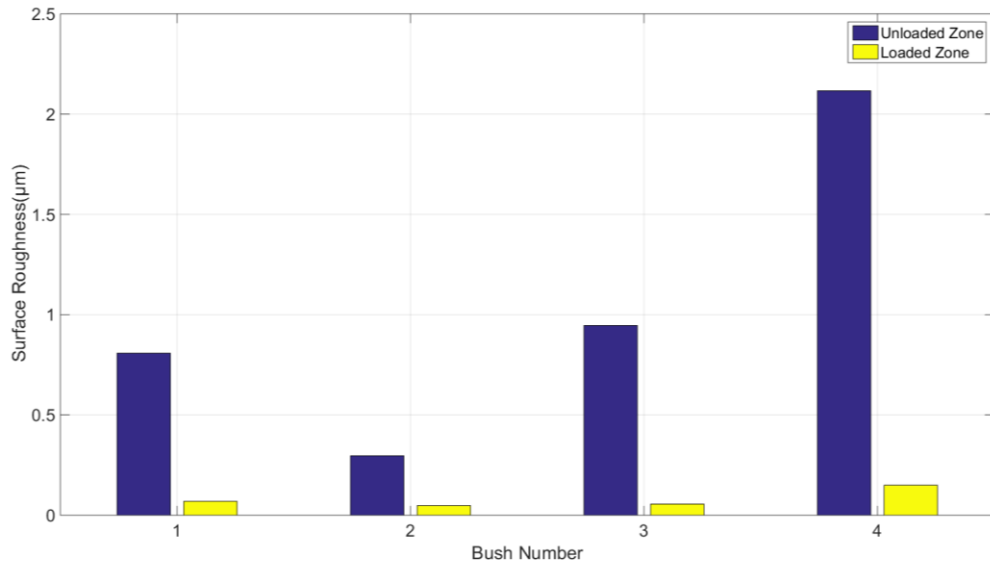


Figure 7.11: Averaged Stribeck curve showing little change to COF with varying articulation angle, Shell Alvania, at a reduced pressure of 10 MPa

It can be seen that there is a growing divergence between the largest and smallest angles tested, but at a very small rate. General trends of decreasing COF with increasing velocity are comparable with that of the higher pressure.

Given the lack of the anomalous behaviour at 0.02 m/s for Shell Alvania and the continued separation occurring for Mobil 28 in section 7.5.1 but both lubricants showing strong general trends for all the other cases, surface roughness measurements ( $R_q$ ) were recorded in two locations of each bush. One in the loaded zone and one outside of the loaded region. Averaged results are shown below.



**Figure 7.12: Reduction of surface roughness values (Rq) for the bore of the AlBr bushes in the loaded zone and unloaded zone**

The variation in surface roughness is as a result from the “running in” of the bushes. The bushes were new when fitted. Therefore during the testing of Mobil 28, the bushes were subjected to a small amount of running in. This should be negligible given the lubricated contact, however it is proposed that at the low velocities the film thickness was not great enough to adequately lubricate the contact, and separate the asperity to asperity contact. The bushes were not replaced during this testing as tolerances were deemed to be more of an influencing factor, and running in wear was assumed to be negligible given the typical service life of a joint.

The pressure required to inject new grease into the contact was recorded, using a pressure transducer fitted in line with a grease lubrication point on the clevis. The maximum pressures obtained during re lubrication<sup>5</sup> are shown below in Figure 7.13 for each lubricating grease.

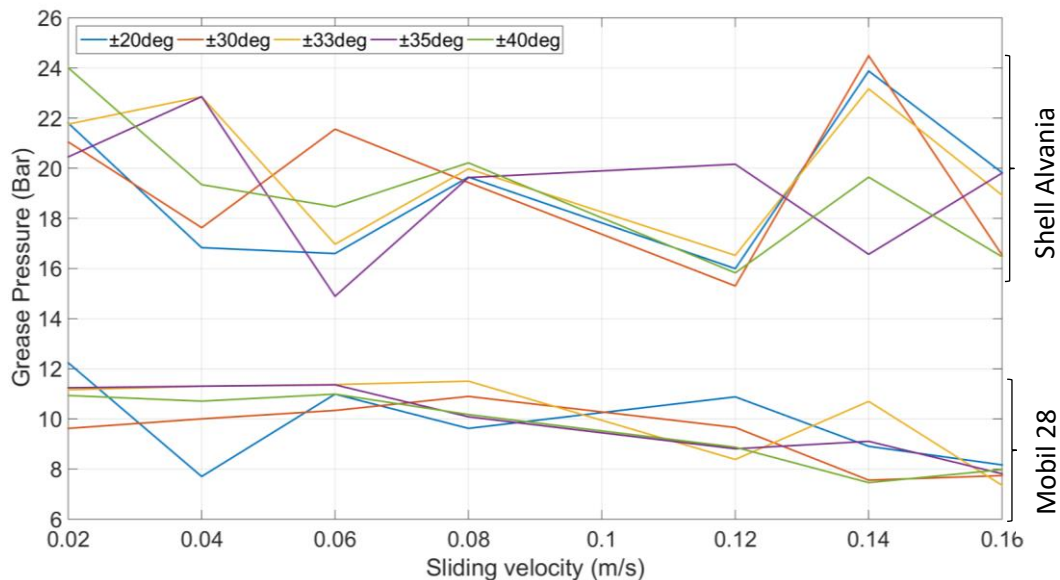


Figure 7.13: Pressure required to re-lubricate contact using two greases at a bearing pressure of 20 MPa

From this it can be seen that Shell Alvania consistently requires a greater pressure for the injection of the grease into the contact. Given the higher viscosity and also the slightly higher NLGI consistency number of 2, as opposed to Mobil 28 with 1.5, it can be confirmed that Shell Alvania is a harder grease, and therefore requires a greater pressure to insert the grease into the contact. Due to the greater resistance to flow Shell Alvania is less susceptible to be swept out of the loaded zone, and therefore stays in the contact for longer providing improved lubrication. Additionally a greater resistance to leakage would help to prevent the loss of the base oil. The improved co-efficient of friction performance of the Shell Alvania seen in section 7.5.2 is as a result of the higher NLGI.

<sup>5</sup> See Appendix C2

### 7.5.3. Number of cycles

Testing was conducted to evaluate the degradation of Aeroshell 22, given that it performed the worst in section 7.3, if it was not replenished at the recommended 250 cycle mark. A bearing pressure of 10 MPa was applied and the joint articulated by  $\pm 40^\circ$  for 1500 cycles at a sliding velocity of 0.373 m/s. The test was then repeated, lubricating at 500 cycle intervals, until the 1500 cycle mark. An interval of 500 cycles was chosen to investigate the implications of an extended maintenance programme, and also to negate the influence of temperature rise of the joint on the COF. Temperature was seen to rise at a greater rate in the first 250 cycles, than for the remainder of the test<sup>6</sup>.

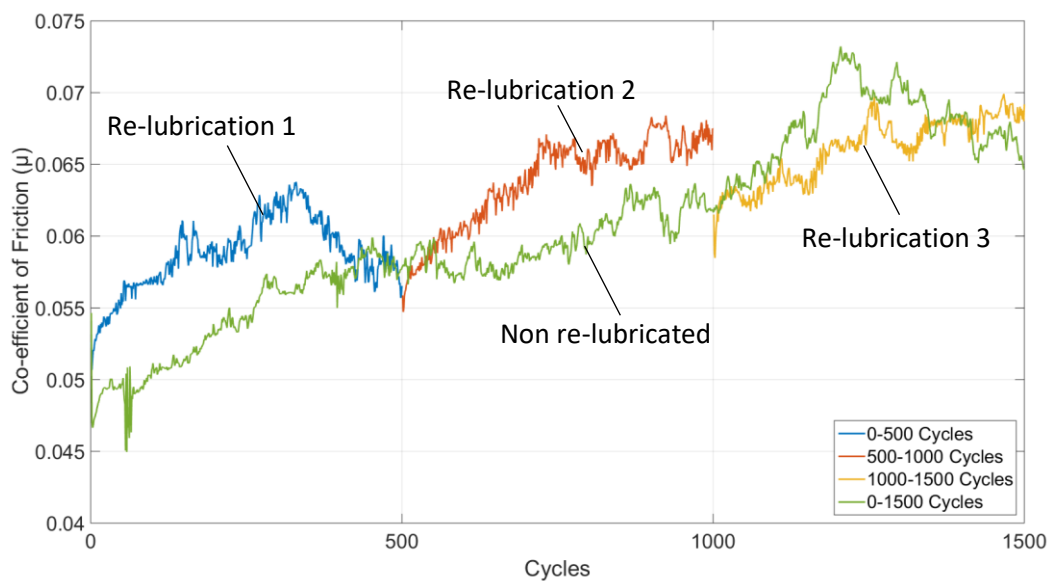


Figure 7.14: Rise in COF with 1500 cycles of operation at 10 MPa,  $\pm 40^\circ$ , 0.373 m/s, compared to re-lubrication every 500 cycles.

Figure 7.14 shows the results of the extended grease life testing. It can be seen that under the loading conditions imposed on the joint the performance of the grease does not rapidly deteriorate. A steady rise in the COF can be observed for the 0 - 1500 cycle case and is also mimicked for the 3, 500 cycle cases.

Re-lubrication at 250 cycles would reduce the COF by only 0.005, and for the testing conducted here there is still some influence from temperature increase of the clevis. Therefore it can be concluded that at these test conditions the COF is more influenced by the temperature, than the degradation of the lubricant. Under operating conditions similar to the ones tested, re-lubrication intervals can be increased by at least a factor of 2, and depending on the COF limitations there is potential for increasing by a factor of 5.

<sup>6</sup> See Appendix C3 for the corresponding grease temperatures

## 7.6. Self-lubricating bushes

To determine the suitability of self-lubricating maintenance free polymer composite bearings, preliminary work was conducted with HDPE bearings, which were manufactured to be a direct replacement for the lubricated aluminium bronze bushes. The HDPE bearings were then tested to first assess the COF of unlubricated contact in a pin joint application. The bearings were loaded initially to 10 MPa, and the COF determined. Testing was again conducted at a range of velocities and also articulation angles to enable a direct comparison to the lubricated aluminium bronze case. Figure 7.15 shows a typical single cycle at a velocity of 0.08 m/s for each of the articulation angles tested.

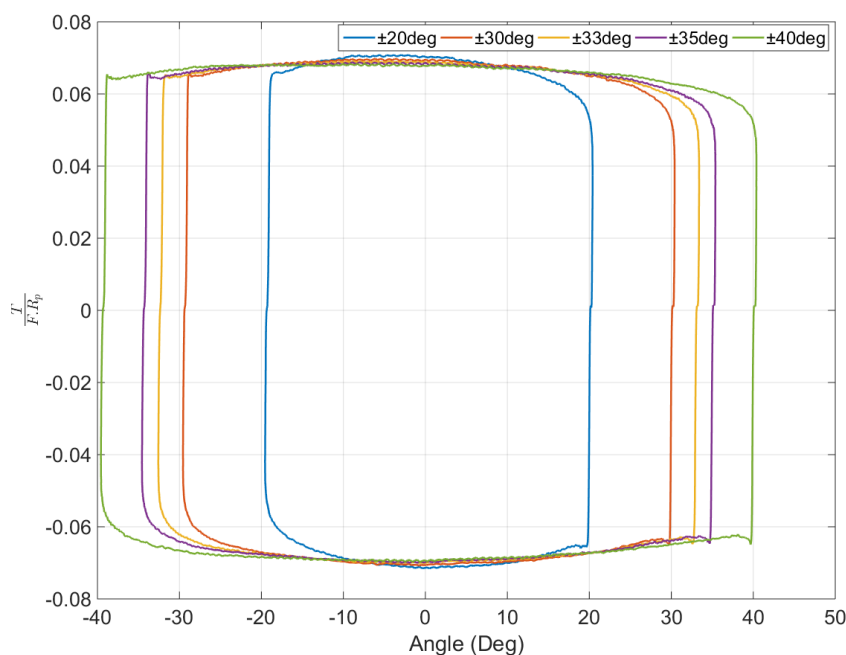


**Figure 7.15: A single cycle for each of the articulation angles tested with HDPE at 0.08 m/s and 10 MPa**

It can be observed here that the corners of each of the cycles are much more rounded, indicating stick slip is less prominent, than for the grease lubricated case (Figure 7.8). Interestingly at the maximum speed of the joint, the force resisting motion is also at its maximum, unlike the lubricated case, while the corners of the cycle have the lowest force resisting motion. Therefore for bearing applications where frequent starting and stopping occurs and a hence a low starting torque is required self-lubricating bushes provide the answer.

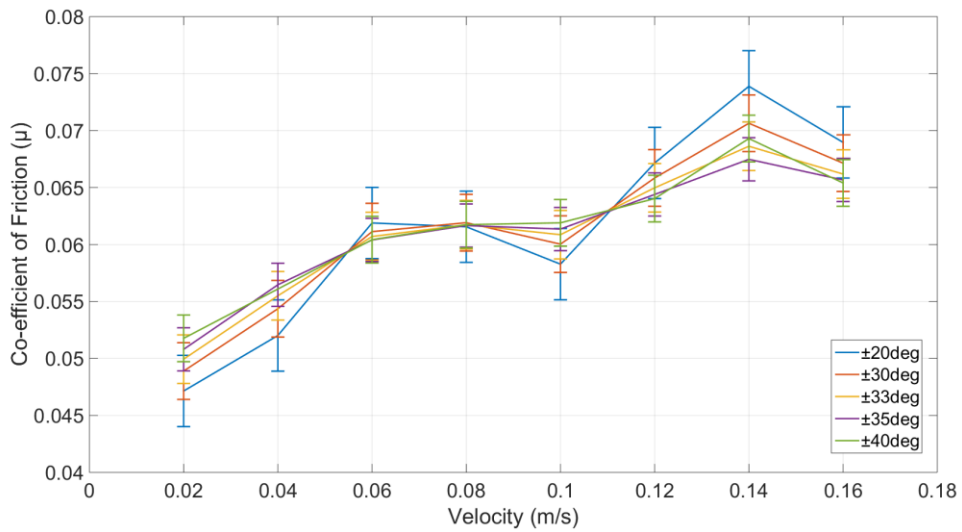


Figure 7.16: COF for HDPE bearings operating at 10 MPa, with a range of surface sliding velocities and angle of articulation

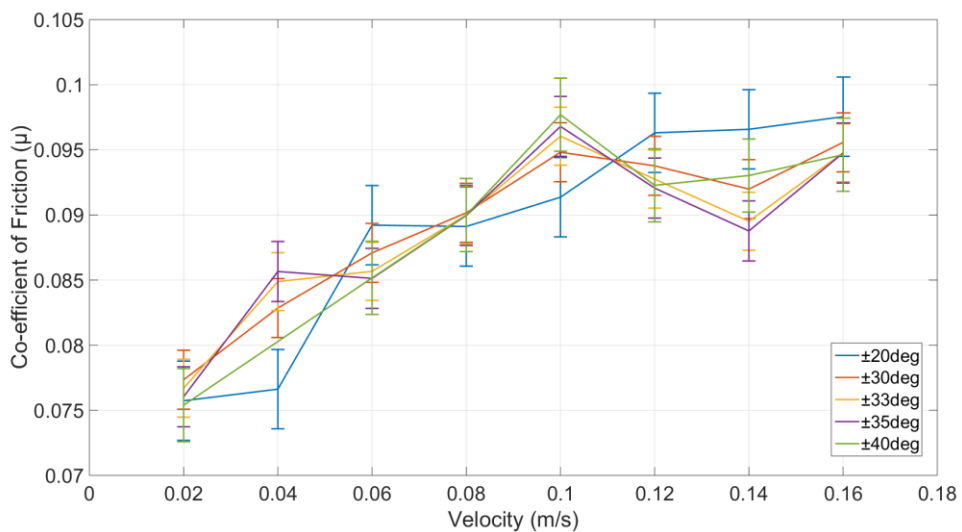


Figure 7.17: COF for HDPE bearings operating at 20 MPa, with a range of surface sliding velocities and angle of articulation

A systematic error occurred during the testing programme, resulting in the duplication of the 0.14 m/s case instead of 0.04 m/s for the  $\pm 40^\circ$  articulation angle. The results at this velocity have been averaged and no data point plotted for the 0.04 m/s,  $\pm 40^\circ$  case for both bearing pressures.

The friction co-efficient of the 10 MPa case shows little difference for the angle of articulation, but differs from that of grease in that the general trend is an increase with increasing velocity. The higher pressure 20 MPa shows much less of a consistent general trend. This was due to the failure of the HDPE bearing, as it extruded in the axial direction

along the pin. No visible signs of excessive heating were observed, therefore it is assumed to be as a result of the yield stress of HDPE being exceeded.

Testing with UHMWPE was attempted prior to testing with commercial self-lubricating bearings. During this testing it was found that the interference fit between the OD of the UHMWPE bearing and the ID of the housing was not great enough and the bearing slowly unscrewed itself.

The use of HDPE as a polymer bearing was shown to be a success, however it was highlighted that higher performance materials were required to survive the pressures. The UHMWPE highlighted the importance of the fit between the bush and the housing.

### 7.6.1. Co-efficient of friction comparison

Two long duration tests were conducted, to evaluate frictional performance of a self-lubricating polymer bearing against a lubricated aluminium bronze bearing. The Aluminium bronze bearings were lubricated once at the start of the test with Aeroshell 22, while the HDPE bearings were fitted dry. Both sets of bearings were run against a steel counter face. Identical test conditions were used 10 MPa bearing pressure, 0.373 m/s sliding velocity and an articulation angle of  $\pm 40^\circ$  for 1500 cycles.

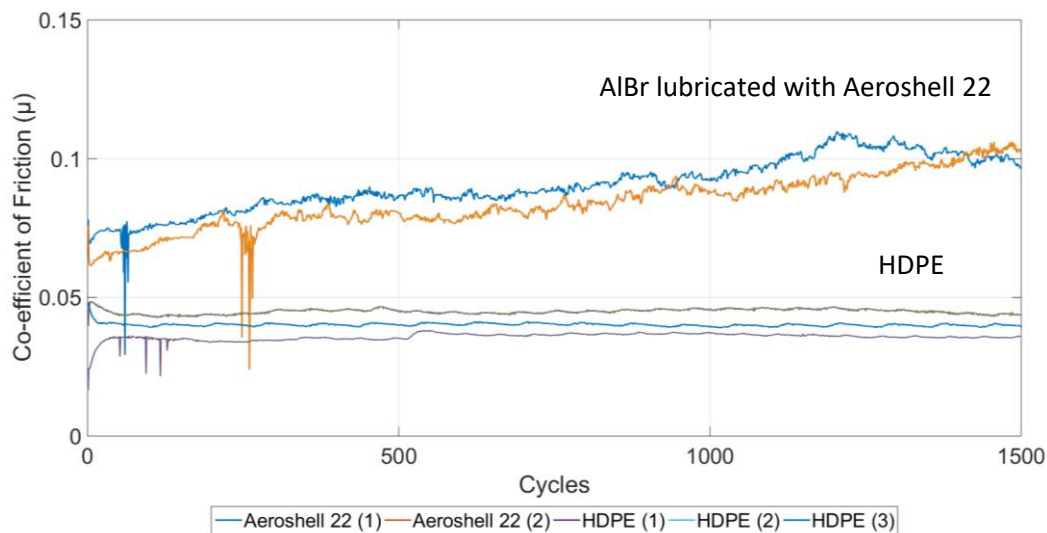


Figure 7.18: COF of Aluminium Bronze lubricated with Aeroshell 22 compared to HDPE, 10 MPa, 0.373 m/s,  $\pm 40^\circ$

Figure 7.18 shows the results from the testing. It can be seen that the HDPE has a consistently lower COF than that of the lubricated scenario. The lubricated case shows a general increase in COF with cycles, while the HDPE shows a very steady constant value. There is some inconsistency at the start of the tests for the HDPE, however this is due to temperature

effects. These tests being of a relatively long duration were run during the night to maximise machine time. This however resulted in a steady rise in temperature of the test clevis over the course of the day from other tests conducted, hence the third repeat of HDPE was started while the test clevis was still warm, and therefore a drop in COF can be seen as the clevis cools down. The same phenomenon can be seen for the second repeat however in the opposite direction, the temperature rose slightly as the testing began until a steady state temperature was achieved.

### 7.7. Commercial self-lubricating bushes

Four self-lubricating maintenance free bearings were identified in section 4 and tested under a reciprocating motion, at a variety of pressures, speeds, and angles of articulation. Tests were conducted starting with a low contact pressure of 4.5 MPa, representative of those observed in service, and a range of articulation angles was explored 20°, 30°, 33°, 35° and 40° the velocity was then adjusted and the test repeated, and then the load increased and the test repeated. No run in procedure was conducted for any of the materials tested. The average COF value was recorded for each sliding velocity 0.02 – 0.16 m/s and for each articulation angle at each of the bearing pressures 4.5 MPa, 8 MPa, 15 MPa, 30 MPa and 45 MPa for each of the materials tested and the values plotted.

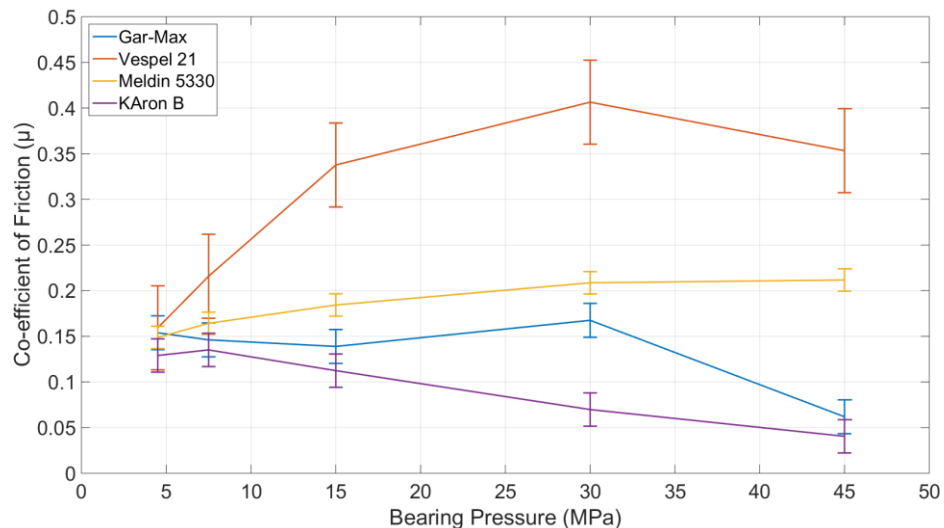


Figure 7.19: Average COF for articulation angles ±20°, ±30°, ±33°, ±35° and ±40° and velocities 0.02 – 0.16 m/s vs bearing pressure for 4 maintenance free bearings

The average of the sliding velocities and articulation for each bearing pressure and each material have been condensed to compare the four self-lubricating materials as shown in Figure 7.19. The data has been condensed in to a single figure as little difference in COF was

observed for the various sliding velocities investigated here. The effects of velocity and articulation angle are investigated in more depth in Section 7.7.1 for a single bearing pressure of 30 MPa. The error bars on Figure 7.19 therefore indicate the deviation as a result of the sliding velocities and the articulation angle.

KAron B typically shows a reduction in COF as the amount of teflon released into the contact increases, forming a transfer film. This would typically be expected with increased wear rather than load, however according to Archard's law, an increase in the applied load results in a greater wear rate. Given that only a small number of cycles have been conducted here it would be fair to say that no significant wear occurs, and any that has occurred could be considered to be running in wear. Manufacturers published data (Kamatics, n.d.) gives COF values of 0.08, 0.07 and 0.06 at bearing pressures of 15 MPa, 30 MPa and 45 MPa. From Figure 7.19 it can be shown that the results are a close match to those given by the manufacturer.

Gar-Max also shows a decrease in co-efficient with increasing bearing pressure. A sharp decrease is observed for the highest pressure. This sharp decrease is believed again to be a result of running in in which the rough asperities are worn down to release debris into the contact to reduce the COF. The expected COF value at 45 MPa predicted by the manufacturers after a 24 hour run in period of 103 MPa is approximately 0.085 (GGB, 2009). For the testing conducted here an average value of 0.06 was found, with no run in other than the previous tests displayed. Agreement with lower pressures could not be confirmed as manufacturer's data was only available for bearing pressures greater than 45 MPa. However it is expected that data will correlate well for the run in period.

Meldin 5330 shows a small but general increase in COF with increasing bearing pressure. No manufacturer's data was available for comparison with test data obtained here.

VespeL 21 shows much higher COF than the other materials tested here, it can also be seen that there is a more dramatic rise as the bearing pressure increases. This data is contradictory to manufacturer's data (DuPont, 2002) which averages a COF value of approximately 0.2.

During testing at 45 MPa, one of the bearings migrated out of the test clevis. A failsafe was triggered on the MOOG SimatestOne controller which was monitoring the hydraulic pressure applying the radial load. As the bush moved out of the housing the hydraulic pressure dropped and the test was stopped. A quick visual inspection of the bush was made and it could be observed that the bush had rotated with the pin and slowly unscrewed itself. Figure

7.20 shows the bush that had migrated out of the housing. It was also observed that the bush had extruded slightly in the axial direction, along the pin. The bush was carefully re-inserted and the testing restarted.

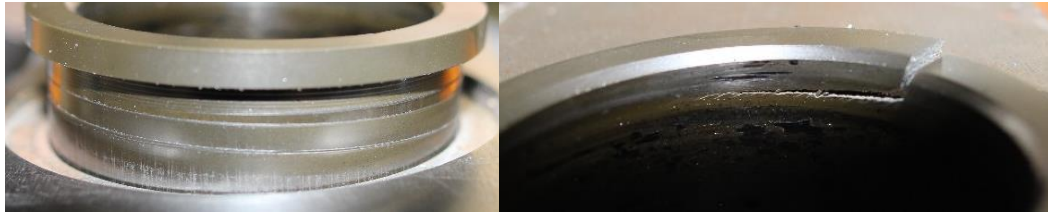


Figure 7.20: Score marks on the bush OD indicate bush has walked out of the contact with oscillations (left), Crack initiation on the flange of the migrated bush upon completion of testing (right)

Upon removal of Vespel 21 after testing had been completed, it was observed that a crack had begun to initiate along the flange on the same bush that had migrated during the testing. It should be noted here that the initiation point of the crack is on the same side as the loaded region of the bush.

Given the large interference fit of 0.3 mm between the housing and the bearing as recommended by the manufacturers it was deemed unlikely that the bush had simply migrated out of the housing. Investigation of the bore of the bush indicated that galling had occurred, resulting in seizure. This seizure is thought to have occurred due to too little clearance between the pin and the bush. Seizure resulted in increased COF values as seen in Figure 7.19. The reduction in COF at 45 MPa is due to reinsertion of the bush after the failsafe occurred. Extrusion of the bush resulted in a greater clearance between the pin and bearing, resulting in a lower value of COF. Extrusion of the bearing occurred as a result of the contact area reducing, but the applied force remaining constant as the bush worked its way out of the housing. It should be noted here that the design of the landing gear would resist migration of the bush in the axial direction, as the flange would press against the flange of the adjacent bearing. While this would reduce the likelihood of extrusion due to a reduction in area, it would lead to an increase in torque requirement and hence COF performance as Vespel to Vespel contact would occur, resulting in higher wear rates.

### 7.7.1. Angle of articulation

The angle of articulation was investigated to determine if co-efficient of friction performance was affected by an increase or decrease in the magnitude of rotation, for any of the materials. Each time the angle of articulation was adjusted, the rotation frequency was also adjusted in order to maintain the same surface sliding velocity for each articulation angle under test. Figure 7.21 shows that the angle of articulation had no effect on the COF performance at bearing pressure of 30 MPa. Testing was also conducted for a range of surface sliding velocities (0.02 – 0.16 m/s) also shown in Figure 7.21 for each of the materials. Additionally it can also be seen that the velocity of testing had little effect on the COF, with no correlation between sliding velocity and COF. This was observed for all the materials tested, for all the articulation angles at all of the bearing pressures over the range of sliding velocities tested, therefore the COF values were averaged across the range of sliding velocities, for each articulation angle and for each of the articulation angles to obtain the average COF value for each bearing pressure, which is plotted in Figure 7.19, and the deviation represented by the error bars.

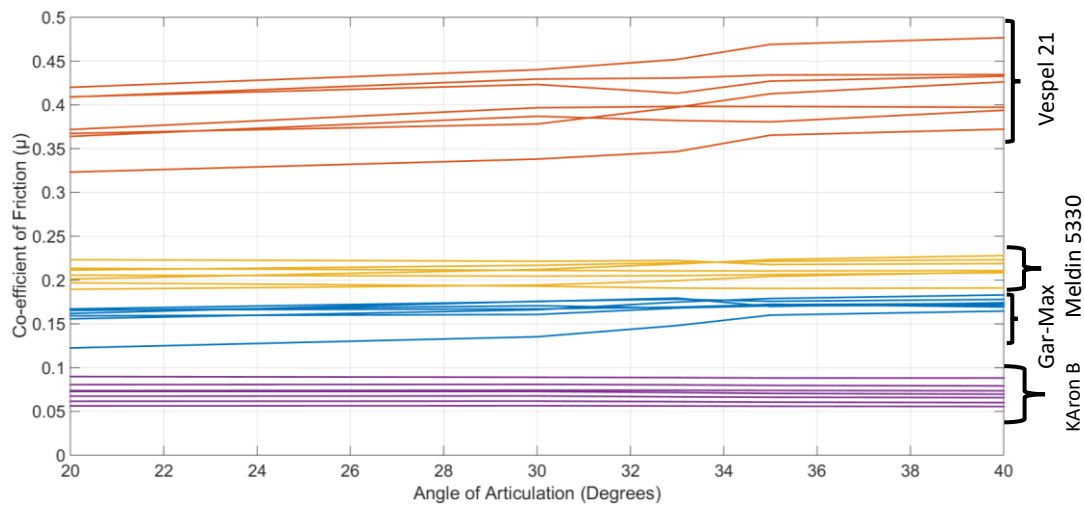


Figure 7.21: Effect of articulation angle on the COF for the maintenance free bearings at 30 MPa tested with a range of sliding velocities 0.02 – 0.16 m/s

### 7.7.2. Assessment of wear and dimensional change

The mass of the bushes was recorded before testing, following drying for 24 hours at 70°C. Bushes that were not being tested were stored in a desiccator as described in section 3.2.5. Testing was conducted under atmospheric conditions. Following testing, bushes were carefully removed and re-dried for 24 hours and re-weighed following the removal of wear debris. The change in mass of the specimens as a result of testing was less than 0.5% for all materials tested. The small mass loss that has occurred is as a result of the fitting and removal of the bearing. However for Vespel 21 and Gar-Max an increase in the mass can be observed, this is as a result of moisture absorption and contamination of the bushes during the weighing process. Therefore it can be identified that mass loss techniques have limited use for the determination of wear in self-lubricating bushes.

	Bush 2		Bush 3	
	Before (g)	After (g)	Before (g)	After (g)
Vespel 21	18.2473	18.2605	18.2545	18.2556
Gar-Max	21.7328	21.7331	21.8937	21.8927
Meldin 5330	17.0315	17.0262	17.0398	17.0359
KAron B	87.0919	87.0904	87.2673	87.2646

Table 7.1: Bush masses before and after testing

Deviation from round measurements were taken both before and after testing in the pin joint function tester, at the heights outlined in section 4.4 for bushes 2 and 3. Vespel 21 was the only material that showed significant deviations, as would be expected following the extrusion mentioned in section 7.7. Gar-Max showed some initial deviation from round prior to testing and is therefore replicated for the measurements after. Given the manufacturing process of Gar-Max it is to be expected that there will be some deviations due the fibres. KAron B showed no measureable change. Meldin 5330 showed a small amount of deviation on bush 3 closest to the flange.

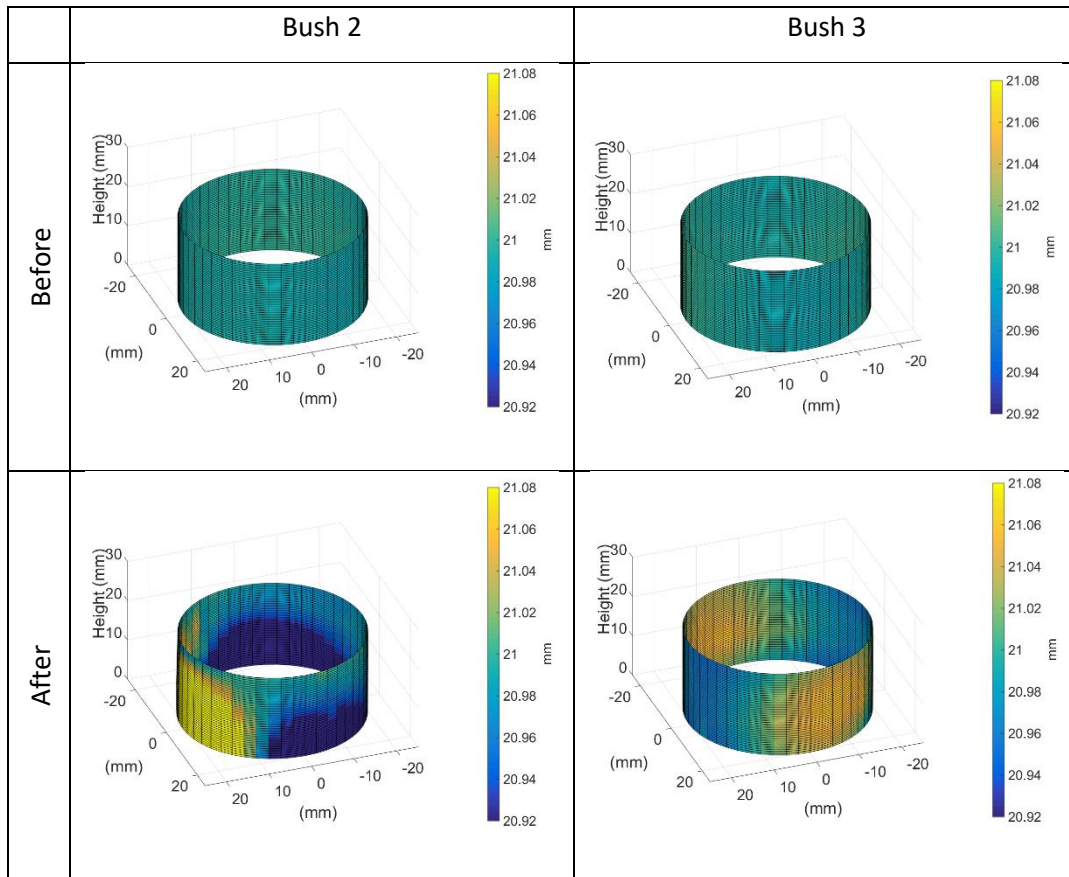


Table 7.2: Vespel 21 Bush ID before and after testing

	Bush 2	Bush 3
Before		
After		

Table 7.3: Gar-Max Bush ID before and after testing

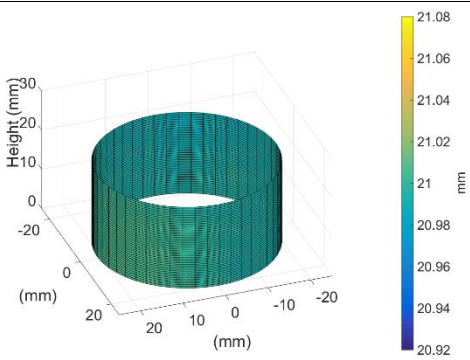
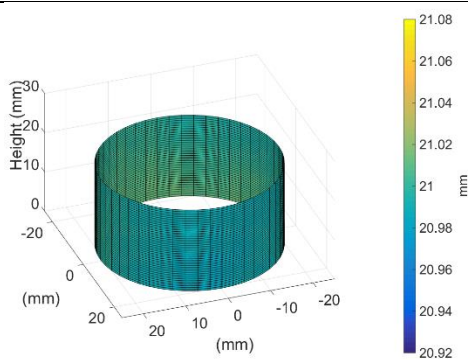
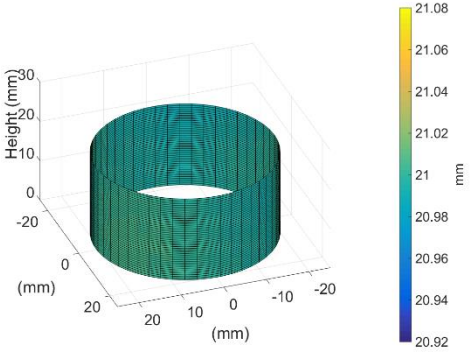
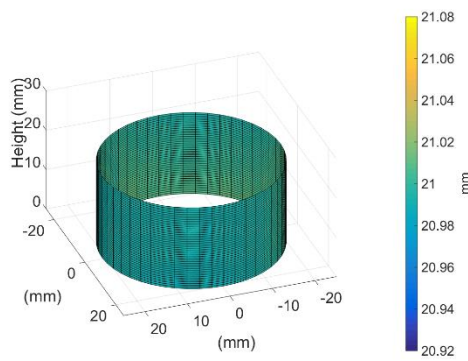
	Bush 2	Bush 3
Before		
After		

Table 7.4: Karon B Bush ID before and after testing

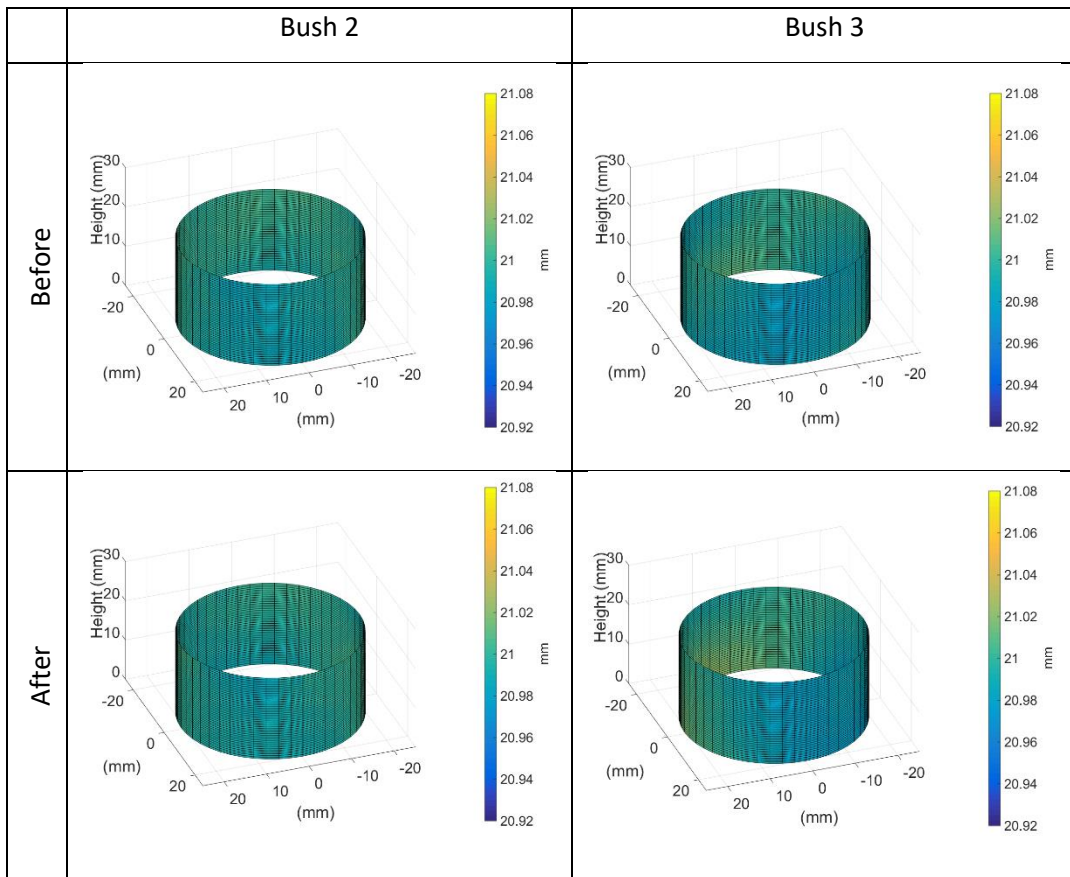


Table 7.5: Meldin 5330 Bush ID before and after testing

Peak deviations from round were taken for each half of each bush at a height of 5.5 mm. The results are compared in Figure 7.22 for 180-360° and Figure 7.23 for 0-180°. The load was applied in the 180-360° half, therefore any wear or deformation would be expected to be observed in this region first. As would be expected, Vespel 21 has the largest change of 98 and 65 μm, in the 180-360° half due to the migration and failure as described in section 7.7. Gar-Max shows a small amount of running in wear approximately 16 μm, on bush 2. Karon B appears to deviate less than before with a reduction of 13 μm, however closer inspection of the data revealed this to be an anomalous data point. Therefore it can be said that Karon B and Meldin 5330 show no significant change. Table 7.6 shows the difference between the two measured values for each bush in the 180-360° range.

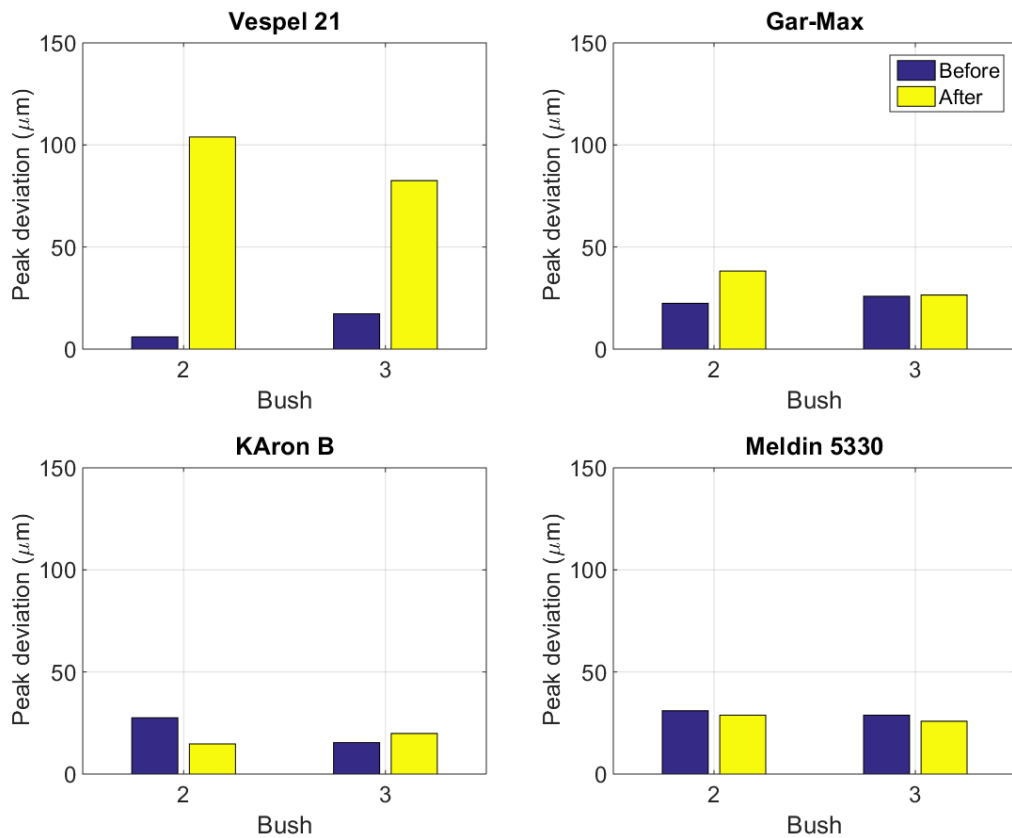


Figure 7.22: Peak deviations in roundness at measurement height of 5.5 mm, for 180°-360°

180-360°	Bush 2 (μm)	Bush 3 (μm)
Vespel 21	98	65
Gar-Max	16	1
KAron B	-13	4
Meldin 5330	-2	-3

Table 7.6: Difference between peak deviations 180°-360°

For the 0-180° measurements again Vespel 21 showed the largest change of 65 and 67 μm, as a result of the bush rotating in the housing and also the deformation of the bushes on the opposite side. The other 3 materials were shown to be either within or comparable to the accuracy of the Talyrond probe at ±5 μm. Again Table 7.7 shows the difference between the two measured values for each bush.

0-180°	Bush 2 ( $\mu\text{m}$ )	Bush 3 ( $\mu\text{m}$ )
Vespel 21	65	67
Gar-Max	3	0
KAron B	6	-2
Meldin 5330	3	-6

Table 7.7: Difference between peak deviations 0-180°

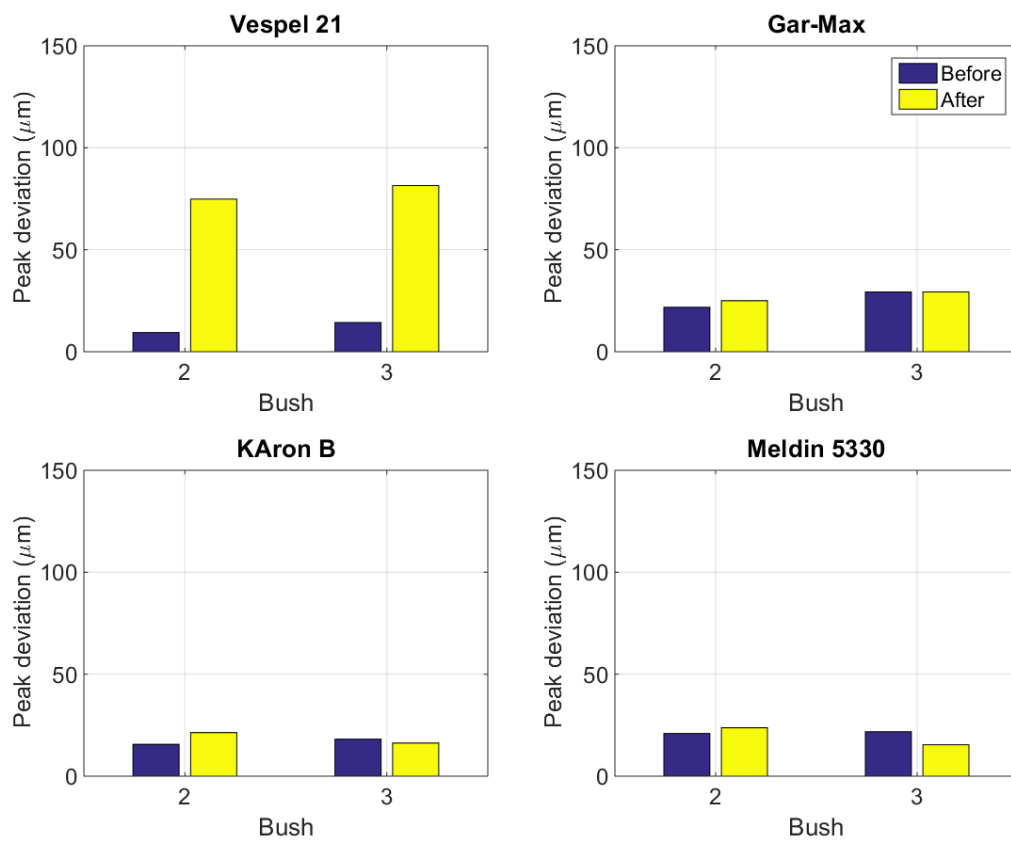


Figure 7.23: Peak deviations in roundness at measurement height of 5.5 mm, for 0-180°

## 7.8. Conclusion

The performance of dry, lubricated and self-lubricating reciprocating pin joints was studied using a servo-hydraulic test frame. At a bearing pressure of 10 MPa and surface sliding speed of 0.145 m/s, the dry joint was found to have a COF of 0.33. When lubricated it was found to be 0.19 and 0.14, for Aeroshell 22 and Mobil 28 grease respectively. The lower COF was attributed to the clay based thickener, as viscosity of the base oil was similar. For Mobil 28 the joint was beginning to generate a hydro-dynamic film, but due to the reciprocating motion the velocity dropped and the film broke down. Both lubricating greases were shown to be operating in the boundary to mixed regime at representative aircraft loads and speeds.

The articulation angle was investigated to determine if a larger oscillation angle could generate a film and result in a lower COF. Sliding velocity was maintained constant for the different angles of articulation tested, and a range of frequencies and pressures tested. At 20 MPa Mobil 28 showed evidence of the aluminium bronze bushes being run in, producing COF values between 0.18-0.22. It was also identified that there was a significant discrepancy between the COF values for the initial tests conducted and those using a higher bearing pressure and slower sliding velocity as a result from a change in bush clearance caused by a new set of bushes and pin for the articulation angle testing. A general purpose grease Shell Alvania was tested at the same pressure, and also did not show any effect of the articulation angle on the COF with values between 0.12-0.145. A lower bearing pressure of 10 MPa was also used to determine if a smaller arc of contact would emphasise the effect of articulation angle, but had little success. The lower COF of the general purpose grease compared to the aerospace grade was attributed to it being a thicker grease. The pressure required to inject the grease into the contact was found to be greater than Mobil 28, and the higher NLGI number confirmed this further.

Investigation into the re-lubrication life of the grease was conducted by cycling Aeroshell 22 for 1500 cycles, 6 times longer than the recommendation for aircrafts. Results were compared to a joint re-lubricated every 500 cycles, and showed little difference for COF. For 500 cycles the COF was shown to increase by only 0.005.

HDPE was initially selected for comparison of self-lubricating bushes with lubricated aluminium bronze and showed success with a COF value of 0.04 in contrast to 0.06-0.1 for Aeroshell 22 at 10 MPa. Further research was conducted using 4 commercially available self-lubricating bushes over a range of bearing pressures from 5 MPa to 45 MPa. The sliding velocity and the angle of articulation was investigated with regards to the COF, and was

found to have no impact. Gar-Max was shown to have COF values between 0.15-0.06, decreasing with increasing load. Karon B was similar with values 0.12-0.05, again decreasing with load. Results were in very close agreement with manufacturers supplied data. The decrease in COF with increasing load for both materials was due to a transfer film developing. Meldin 5330 showed a slight increase in COF from 0.15-0.2 with applied load, which was lower than the manufacturers limited data predicted. Vespel 21 suffered catastrophic failure due to poor clearances and fits, resulting in migration of the bearing from the housing due to galling. Failure of the bearing then occurred through both extrusion and fracture. COF values were found to be 0.15-0.4, much higher than predicted by the manufacturers. The amount of deformation of the bushes was measured using a roundness tester, with measurements taken both before and after testing, and the change calculated. Given that Vespel 21 catastrophically failed values of 98  $\mu\text{m}$  and 65  $\mu\text{m}$  for bushes 2 & 3 respectively were the highest out of all the materials. Gar-Max showed some change of 16  $\mu\text{m}$  for bush 2, which was attributed to the running in and the release of wear particles into the contact, as part of the lubricating mechanism. Measurements for the remaining bushes were found to be in the region of 5  $\mu\text{m}$ , the accuracy of the roundness tester.

Temperature of the joint was seen to be a significant factor in the lubricated testing. An increase in joint temperature, resulted in a decrease in the diametral clearance as the bushes expanded and therefore an increase in the COF. For the investigation into the re-lubrication interval this was seen to happen most significantly in the first 200 cycles, following this the recirculating cooling water was able to reduce the effects of temperature increase on the COF. The self-lubricating bushes were less sensitive to changes in temperature due to the reduced thermal conductivity of the bushes, however the COF was still seen to vary depending on the temperature of the clevis, which caused the fluctuation in COF at the beginning HDPE runs when compared to the lubricated AlBr (Figure 7.18).

Consideration was given to the calibration of the load cells on the test frame, however given that the calibration was checked before testing commenced and during, it is highly unlikely to be the cause of any inaccuracies. In addition the data for self-lubricating materials was acquired at a much later date, soon after a full calibration had been completed and was shown to be in excellent agreement with the manufacturers data, therefore there is little question about the validity of the data due to calibration.

[Blank Page]

# 8.

## Conclusions and Recommendations

In this chapter conclusions are drawn from the wear tests conducted and the development and validation of the load displacement model. The COF testing is summarised for both lubricated aluminium bronze and the self-lubricating alternatives. Recommendations for further work are also given.

## 8.1. Wear performance of self-lubricating bearings

A bespoke wear and fatigue test head was designed and manufactured for the testing of self-lubricating bushes in an aircraft landing gear application. Representative geometry was used to maintain similarity with the full scale component to avoid any scaling errors. The test head was mounted to a servo-hydraulic test frame which was capable of applying representative field loading of the aircraft as it taxis along the runway, developing a shock loading on the bracing struts of the landing gear. The displacement of one half of the test head was measured relative to the other with an LVDT to isolate the test clevis from any external deformations such as that in the load cell. The displacement of the joint was recorded during the test programme, the travel per cycle was calculated and the elastic component subtracted to give any permanent deformation occurring. The experimental results produced by the LVDT showed changes in displacement of 27  $\mu\text{m}$  to 127  $\mu\text{m}$  which was deemed to be within the source of error of the servo-hydraulic system. For the roundness measurements taken extensively during the second aircraft life the bushes were removed from the test clevis which involved the removal of the LVDT. While the location of this LVDT was marked there was a slight margin for error in the repositioning if misaligned in the vertical of the two planes, a slightly larger displacement may be recorded. The application of the load was controlled using closed loop feedback from the load cell, therefore the control of the actuator to less than  $\pm 100 \mu\text{m}$  during the cyclic application of up to 167 kN over a prolonged period becomes a difficult task, and a potential for error.

Roundness measurements were taken to confirm plastic deformation and were found to vary by 20  $\mu\text{m}$  for all materials during the test program, which was within the measurement error of the Talyrond. For the roundness measurements recorded it was shown that the peak measurements for out round occasionally decreased, indicating that following an application of load, the bush had become more round. While this is possible in how the Talyrond is configured to measure, it is extremely unlikely that this will have occurred from the nature of the applied load. It is more likely that the bush has crept back towards its original shape. The Talyrond probe has been calibrated to only 10  $\mu\text{m}$ , therefore any attempt to draw conclusions from measured data with only a few microns difference would not be feasible.

It would be highly recommended that a bespoke roundness tester be developed, which could be mounted to the radial load test rig. If the roundness tester was developed in such a manner, only the removal of the pin would be required, and the bushes measured in situ. This would not only remove errors of misalignment but would also reduce measurement

time, and eliminate completely inaccuracies due to fitting and removal of the bushes. Furthermore the effects of creep would also be reduced, given the reduced measurement time required and also the dimensional changes due to the fits and tolerances of the bushes themselves.

Mass loss measurements are a common approach to quantifying the amount of wear that has occurred in a system. However given the nature of the materials under test considerations to moisture absorption were taken into account. This coupled with their comparably soft nature to that of steel, it was evident that material was removed from the OD of some of the bushes, simply by inserting them into the test clevis. Therefore given that the bushes were to be removed and re-fitted numerous times, it was deemed not to be a representative measure of the wear. Material transfer to the pin provides evidence for wear of all the materials. Meldin 5330 and KAron B showed the least and Vespel 21 showed the most. However for all of the materials, this is to be expected, as the lubricating behaviour of the joint is achieved through a transfer of material. The visual inspection showed a greater amount of material transfer at the head end of the pin, rather than the far end, which was confirmed with the use of the load sensing pin. It was concluded that the retaining collar induced unequal loading of the bushes due to a pivoting action of the pin and mild fretting occurred between the pin and the retaining collar.

Visual inspection of the OD of the bushes showed that micro oscillations took place between the bushes and the housing, resulting in the most severe case for KAron B with local welding of the asperities. The combination of the micro oscillation and the unequal loading induced by the retaining collar is proposed as the most likely solution to the failure of the Vespel 21 bush prior to life cycle 3, as a fatigue load will have developed on the flange as a result of the axial motion.

The wear performance of four commercially available self-lubricating bearings was investigated under a cyclic radial loading regime, representative of aircraft in service loading. The work conducted here has shown through several types of tribological analysis that very little wear of the bearings has resulted from 3 complete aircraft lives. The measured wear was found to be of comparable magnitude to that of the measurement error. Additionally it was identified that the wear debris produced were the formation of a lubricating film consisting of either PTFE or graphite. Therefore it was identified that for the preliminary testing conducted here of 3 aircraft lives, the self-lubricating bushes showed significant potential for the application in aircraft landing gear.

## 8.2. Load displacement model

The Hertzian and Persson models (section 2.4) are the classic models used for the analysis of cylindrical conformal contact problems. For many conformal contacts analysed with the Hertzian contact theory, the assumption of the contact region being small in comparison to the contacting bodies is broken, but results produced often still give an acceptable answer (Zhu, 2012). However for the polymer composite bushes with a large amount of elastic dissimilarity the Hertzian model was not applicable, as the calculated half width of contact rapidly approached the radius of the contacting bodies at low loads.

Persson's model was originally only given in quadrature form, but a closed form solution developed by Ciavarella and Deccuzi (2001a; 2001b), was given for numerical solution for both cases of elastic similarity and dissimilarity.

An important parameter that is required for accurate analysis of cylindrical conformal contact when considering polymer composite bushing materials is the thickness of the bush itself. The stiffness of the joint, or its resistance to deformation under the application of an applied vertical load is directly related to the wall thickness of the polymer composite bushing.

A load displacement model has been developed, based on the intersection of circles for conformal contact between a polymer bush and steel pin in order to analyse the displacement of the joint under an applied load. Given that for an aircraft landing gear application, when the gear is in the down locked position the most demanding loading regime is that of the applied radial load. The loading capacity of self-lubricating bushes was identified through the literature to be highly dependent on the wall thickness of the bush. Therefore the model developed considers the influence of the bush thickness on the load carrying capacity of the bushing, and requires only geometrical and material properties. The model was extended to predict arc of contact from the displacement calculated. The model does not consider however plastic deformation of the bushes, as it is assumed to be operating only in the elastic range. Additionally the model is only valid if the contacting bodies are significantly elastically dissimilar, such as a steel shaft loaded against a polymer bush. This therefore means that care must be exercised when using the model for high displacements to ensure that the displacement does not exceed the thickness of the bush.

### 8.2.1. Experimental Validation

The load displacement model developed here was experimentally validated in this work using the radial load test rig and also a small scale clevis with PVC bushes of varying wall thickness. An LVDT was used to measure the stiffness of the contact in both a static and dynamic application, and was shown to be in close agreement with the model developed. PVC bushes with wall thicknesses of 1.5 and 2 mm were initially used for the validation and were found to be in agreement. For the aircraft geometry, Meldin 5330 and Gar-Max were found to be in excellent agreement with the model. Vespel 21 unexpectedly showed a large discrepancy between the experimental data and the simulated data. It was proposed that the elastic modulus quoted for Vespel 21 is greater than stated by the manufacturer due to the anisotropy of the material. Therefore when loaded in this application, the elastic modulus being measured is perpendicular to the direction of applied force during the manufacture. The elastic modulus quoted for Vespel 21 is measured in the same direction of applied force during manufacture, which is a lower value than the perpendicular. This can be supported by the experimental data obtained which was similar to that of Gar-Max and Meldin 5330, but the modulus of elasticity for these two materials was an order of magnitude greater. In addition, it was observed that there was a very heavy interference fit between the bush wall and housing, which resulted in a reduced clearance at the bush pin interface. Therefore the arc of contact was much greater, resulting in a more linear response for the force displacement curve as the result of a constant joint stiffness. The displacement calculated by the simulation for Karon B was under predicted when compared to the experimental results. Given that the composition of the bearing is a liner bonded to a steel backing, the results were unsurprising. The simulation used only the liner thickness of 0.3 mm for the bush thickness, rather than the whole bush. This approach was taken as the substrate material had similar properties to that of the clevis and was therefore neglected. In this circumstance the assumption that the arc of contact is small in comparison to the size of the contacting bodies may still be valid and the contact more accurately predicted by Hertzian analysis.

Experimental validation of the arc of contact was conducted using two methods. Indexing of the load pin at a constant load and calculating the change in angular position for a force, proved to be unsuccessful in validation. However the use of a lightly knurled pin imprinted into the PVC bushes, which were sectioned and the marked width measured, showed the model to provide a close approximation to the arc of contact. When the model was compared to that of the closed form Persson solution, it was shown to be a closer

approximation for higher loads. This verification highlighted the importance of selecting the correct value of E for the bushing.

One important parameter is still missing from the analysis of conformal contacting bodies, and that is the surface roughness. The assumption of smooth contacting surfaces was made for simplification purposes (Johnson, 1982). For the successful application of surface roughness to the contact, the surface roughness must be considered in both the radial and axial directions of the pin and bush.

The work conducted here has shown the successful development and experimental verification of a model to predict the displacement, and arc of contact of self-lubricating polymer bushes, which includes a term for the thickness of the bush in the joint. The model was developed and experimentally verified to obtain a greater understanding of the load carrying capacity for polymer composite bearings and the effect of bush wall thickness. The model can be utilised in the analysis and design of new aircraft landing gear to establish how the lower joint stiffness of the polymer composite materials may impact the rigidity of the landing gear. Furthermore the model can be extended and combined with the work conducted earlier, investigating the wear performance of the bushes resulting from the cyclic radial loads developed, and how this will impact the life of the bearings in the landing gear by minimising the extent of initial expensive experimental testing.

### 8.3. Effect of articulation angle on COF

The effect of the articulation angle in both lubricated and self-lubricating reciprocating pin joints was studied using a servo-hydraulic test frame. For lubricated contact it was shown for a range of velocities that the angle of articulation had little effect on the COF despite a constant surface sliding velocity for the different angles tested. The COF was found to range from 0.18-0.22 for Mobil 28 at 20 MPa, and a general purpose grease Shell Alvaina was found to be 0.12-0.145. The lower COF was attributed to the thickness of the grease being greater, and therefore not as easily removed. This was confirmed by the consistently higher pressure required to insert the grease into the contact and the NLGI number of the grease. A lower contact pressure was tested to determine if a smaller arc of contact would emphasise the effect, but made little difference.

The four commercially available self-lubricating bushes were extensively tested in the reciprocating pin joint test rig for a range of bearing pressures from 5 MPa to 45 MPa. Again the effect of articulation angle and sliding velocity showed no impact on the COF. The change

in mass of the specimens as a result of testing was less than 0.5% for all materials tested. The small mass loss that has occurred is as a result of the fitting and removal of the bearing.

#### 8.4. COF for Reciprocating Journal Bearings

The unlubricated aluminium bronze bushes were found to have a COF of 0.33 at a bearing pressure of 10 MPa, when lubricated with Aeroshell 22 and Mobil 28 aerospace greases it was reduced to 0.19 and 0.14 respectively. The lower COF of Mobil 28 was attributed to the initial generation of a hydrodynamic film which then broke down as a result of the reciprocating motion. For both lubricants used, the joint was experimentally determined to be operating in the boundary to mixed regime.

The re-lubrication interval of the grease lubricated pin joints was investigated, using Aeroshell 22. The joint was cycled for 6 times longer than the recommended re-lubrication interval, and then a repeat conducted with the joint re-lubricated every 500 cycles, and the results compared. Little difference was shown. An increase in COF over 500 cycles was found to be 0.05.

A HDPE bearing was selected for preliminary investigation into self-lubricating polymer bushes in an aircraft landing gear application. A steady COF value of 0.04 was recorded for a bearing pressure of 10 MPa. Compared with the lubricated aluminium bronze which increased steadily from 0.06-0.1 showed that there was significant potential.

Out of the four commercially available self-lubricating bearings Karon B and Gar-Max performed the best in terms of COF over the range of 5 MPa to 45 MPa. A decreasing COF value for an increasing pressure was obtained, and experimental data was found to be in excellent agreement with the manufacture's predicted values. Both materials reached low COF values of 0.05. Meldin 5330 maintained a reasonably constant COF value of 0.2. Vespel 21 however showed catastrophic failure through galling induced seizure which caused the bearing to migrate from the housing with a peak COF value of 0.4. The bush extruded on migration, and the flange also fractured.

## 8.5. Metrology of self-lubricating bushes

The surface roughness of the four maintenance free bearings was analysed with both a linear profilometer and an optical surface profilometer. Measurements showed that Vespel 21 was the smoothest and KAron B and Gar-Max were the two roughest due to their fibrous nature. There was a slight discrepancy between the two measurements due to the linear profile being taken in the bore of the bush, and the surface profile taken as a representative sample on the flange of the bush.

The surface roughness of the counter face mating components was also measured. For the standard aircraft pin the roughness measured using a linear profilometer was found to be 0.14  $\mu\text{m}$ , while the bespoke load sensing pin was found to be 0.63  $\mu\text{m}$ . The hardness of the pins was also measured to be 48 Rockwell C for the standard aircraft pin and 47 Rockwell C for the load sensing pin.

The mass of each set of bushes was compared to establish the potential weight savings by replacing the aluminium bronze bush with a polymer composite material. Meldin 5330 was shown to be the lightest and KAron B with the stainless steel backing was found to be the heaviest.

## 8.6. Summary of materials tested

Even though Vespel 21 showed the lowest surface roughness and a relatively low weight, it is not recommended for use in this type of joint on the aircraft landing gear. Given that one bush in each test failed in a similar manner, with a crack initiation on the flange and then propagating in the high stress concentration region.

Re-design of the joint, for the removal of the flange may prove to make the bushing more reliable in terms of resistance to fracture. However galling was observed between the pin and bushing, and was responsible for the migration. The bushes were not loaded outside of their normal operating loads in the radial load test programme. However it is proposed that Vespel 21 is loaded to failure following the result of the extrusion as the bearing was migrating out of the housing. This indicates that an overload may come close to or exceed the yield stress of the material.

Meldin 5330 proved to be a suitable lightweight alternative bearing solution as it combined a low surface roughness with the lowest weight and a COF comparable to that of the current grease lubricated aluminium bronze bushes. An element for concern is the similar value of

COF to Vespel before galling and hence migration occurred, coupled with the less evident transfer film to the pin. It would be recommended that further testing in the pin joint function tester be completed to establish if a full transfer film develops, or if failure in the same manner as Vespel 21 occurs.

KAron B proved to be a safe self-lubricating alternative with stiffness values comparable to those of aluminium bronze. The high surface roughness values measured were shown to be of no concern given that KAron B proved to have the lowest COF out of all the materials. From an aviation point of view KAron B carries a big penalty in terms of weight, however given that the majority of the weight is in the substrate, it is possible for the substrate material to be changed to further enhance the performance of the joint.

Gar-Max offers the best all round solution. The COF is the lowest of all the polymer composite materials, despite the high surface roughness measured, and is in good agreement with the manufacture's data. Additionally it can be seen to decrease with an increased bearing pressure. The joint mass is highest out of the polymer composite materials, but still significantly lower than KAron B and the current lubricated aluminium bronze bushes.

The work conducted here has investigated the performance of self-lubricating bearings in an aircraft landing gear application, where the joints are subjected to two types of motion: dynamic radial loading and an oscillatory motion. The development and successful experimental verification of a theoretical model that predicts the displacement and arc of contact when under an applied radial load, while considering the bush thickness has been developed. Experimental investigation of the wear performance of four commercially available self-lubricating bushes was conducted under a fatigue style loading regime representative of aircraft loading and geometry. For the materials tested, they were all shown to be within acceptable levels of wear. The self-lubricating bushes were compared to the current technology, lubricated metallic journal bearings, under a reciprocating oscillatory motion and were found to have lower values for the COF. Furthermore for some of the self-lubricating materials tested the COF was shown to decrease with increasing bearing pressure. In addition the effect of the articulation angle was investigated for both grease lubricated and self-lubricating bearings and was found to have no significant impact at the loads and speeds tested in this work. The cyclic loading, representative of 3 aircraft lives, radially applied to the self-lubricating polymer composite bushes was shown to cause little change in the bushes in terms of either wear or fatigue. The combination of the results from

both test programmes indicates that there is significant potential for the successful application of self-lubricating polymer composite bushes to aircraft landing gear.

### 8.7. Future work

This research has addressed three of the main mechanisms at work in pin jointed structures, the static loading and contact size, fatigue loading and wear, and the COF in an oscillatory nature. Based upon the work conducted some recommendations for further work are given below.

One area for further work would be the extension of the load displacement model to be able to model polymer bushes to failure through overload. The model developed here does not take into account the yield stresses of the materials, and therefore failure can only be determined when the displacement is greater than or equal to the thickness of the bush. Experimental determination of the modulus of elasticity would greatly improve the accuracy of the model. As some materials tested stated a large range of values for the modulus. Experimental determination was not possible with the samples supplied due to their specific application.

Fatigue testing of the aircraft landing gear joint identified the retaining collar to be inducing unequal loading in the clevis. This phenomenon occurred only for the polymer materials with a low modulus of elasticity and hence low joint stiffness. This promoted accelerated deformation of the bushes at the head end of the pin. Therefore for the successful application of polymer joints subjected to a fatigue type loading, further investigation into suitable pin retention mechanisms that will not wear either the bushes or the housing dramatically must be conducted. In an attempt to improve the accuracy of the measured wear data it is suggested that a bespoke roundness tester be developed that can be fitted to the test clevis to minimise the effects of misalignment during measuring and reduce the influence of creep on the results.

The combination of the radial fatigue loading and also the oscillatory loading would provide a yet more representative test, as this would allow for variable radial loads to be applied to the contact as the joint is oscillating meaning that any wear debris generated would either be redistributed around the joint, or would be released from the contact, depending on the nature of the lubricating particles.

## References

- Aarrass, I., Badal, O., van de Bogaart, J., van Grieken, S., Pehlivan, A., Wennink, B. & Yali, R., 2008. Project Landing gear- Boeing 737-800. Hogeschool van Amsterdam.
- Ahmad, M.A., Kasolang, S. & Dwyer-Joyce, R., 2013. The effects of oil supply pressure at different groove position on frictional force and torque in journal bearing lubrication. *Procedia Engineering*, 68, pp.70–76.
- Airbus, *A320 Flight Crew Operating Manual*,
- Airbus, 2005. *Aircraft Characteristics Airport and Maintenance Planning*,
- Airbus, 2008. *Getting to grips with A320 Family Performance Retention and Fuel Savings*,
- Airbus, 2000. Global Market Forecast 2000- 2019., (July), pp.1–86.
- ASM, 1987. Fractography. In *ASM Handbook*. pp. 479–480.
- ASTM, 2013. D618-13 Standard Practice for Conditioning Plastics for Testing.
- Bahadur, S., 2000. The development of transfer layers and their role in polymer tribology. *Wear*, 245(1-2), pp.92-99.
- Bentham, P.P., Crawford, R.J. & Armstrong, C.G., 1996. *Mechanics of Engineering Materials* Second., Pearson Education Limited.
- Biehl, F.A., 1983. Aircraft landing gear brake squeal and strut chatter investigation. In W. W. Mutch, ed. *The Shock and Vibration Bulletin*. Long Beach: The Shock and Vibration Information Center, pp. 179–190.
- Biswas, S.K. & Vijayan, K., 1992. Friction and wear of PTFE — a review. *Wear*, 158(1–2), pp.193–211.
- Boeing, 2014. *Boeing Current Market Outlook 2014*, Seattle.
- Booser, E.R. & Wilcock, D.F., 1953. Minimum oil requirements of ball bearings. *Lubrication Engineering*, 9(140–3), pp.156–8.
- Bradford, L.J., Barber, E.M. & Muenger, J.R., 1961. Grease Lubrication Studies with Plain Bearings. *J.Basic Eng*, 83, pp.153–161.
- Briscoe, B., 1981. Wear of polymers: an essay on fundamental aspects. *Tribology International*, 14(4), pp.231–243.
- Briscoe, B.J., & Sinha, S.K., 2002. Wear of polymers. *Proceedings of the Institution of Mechanical Engineers, Part J: Journal of Engineering Tribology*, 216(6), pp.401-413.
- Briscoe, H.M., 1990. Why space tribology? *Tribology International*, 23(2), pp.67–74.
- Brito, F.P., Miranda, A.S., Claro, J.C.P. & Fillon, M., 2012. Experimental comparison of the performance of a journal bearing with a single and a twin axial groove configuration. *Tribology International*, 54, pp.1–8.

- Bushan, B., 2001. Surface roughness Analysis and Measurement Techniques. In *Modern Tribology Handbook*. CRC Press.
- Cann, P.M., Webster, M.N., Doner, J.P., Wikstrom, V. & Lugt, P., 2007. Grease Degradation in ROF Bearing Tests. *Tribology Transactions*, 50(2), pp.187–197.
- Cann, P.M., Doner, J.P., Webster, M.N. & Wikstrom, V., 2001. Grease Degradation in Rolling Element Bearings. *Tribology Transactions*, 44(3), pp.399–404.
- Cann, P.M., 2001. Grease film thickness and friction in EHL contacts. *WTC Tribology*, pp.159–164.
- Cann, P.M., 2007. Grease lubrication of rolling element bearings — role of the grease thickener. *Lubrication Science*, 19(3), pp.183–196.
- Cann, P.M., 1999. Starved Grease Lubrication of Rolling Contacts. *Tribology Transactions*, 42(4), pp.867–873.
- Cann, P.M. & Lubrecht, A.A., 1999. An analysis of the mechanisms of grease lubrication in rolling element bearings. *Lubrication Science*, 11(3), pp.227–245.
- Careless, J., 2008. Landing Gear Maintenance “Best Practices.” *Aircraft Maintenance Technology*.
- Chen, H.H. & Marshek, K.M., 1988. Effect of Clearance and material property on contact pressure in two-dimensional Conforming Cylinders., 23(1), pp.55–62.
- Ciavarella, M. & Decuzzi, P., 2001a. The state of stress induced by the plane frictionless cylindrical contact. I. The case of elastic similarity. *International Journal of Solids and Structures*, 38(26–27), pp.4507–4523.
- Ciavarella, M. & Decuzzi, P., 2001b. The state of stress induced by the plane frictionless cylindrical contact. II. The case of elastic dissimilarity. *International Journal of Solids and Structures*, 38(26–27), pp.4507–4523.
- Clarke, A. Weeks, I.J.J, Evans, H.P. & Sindle, R.W., 2014. An investigation into mixed lubrication conditions using electrical contact resistance techniques. *Tribology International*, 93, pp.1–8.
- Colbert, R.S., Alvarez, L.A., Hamilton, M.A., Steffens, J.G., Ziegert, J.C., Burris, D.L. & Sawyer, W.G., 2010. Edges, clearances, and wear: Little things that make big differences in bushing friction. *Wear*, 268(1), pp.41–49.
- Cranfield University, 2010. *Fuel and air transport, A report for the European Commission*,
- Curry, N.S., 1988. *Aircraft Landing Gear Design: Principles and Practices* J. S. Przemieniecki, ed., Marietta: American Institute of Aeronautics and Astronautics, Inc.
- Dally, J.W., Riley, W.F. & McConnell, K.G., 1993. *Instrumentation For Engineering Measurements* 2nd ed. C. Robichaud, ed., John Wiley & Sons, Inc.
- Darby, A. & Fishwick, D., 2011. Beryllium: A review of the health effects and the evidence for screening or surveillance in workers exposed to beryllium. *Health and Safety Executive*.
- Denti, E., & Fanteria, D., 1995. Aanalysis and control of the flexible dynamics of landing gear in the presence of antiskid control systems. In *AGARD*. Pisa.

- Depei, Z., 1989. Some aspects of nose-wheel shimmy damper of the aircraft. *Foreign Technology Division*.
- Deters, L., Mueller, F. & Berger, M., 2003. Self-Lubricating Dry Rubbing Bearings - Fundamentals and Methods of Calculation. In *Tribological Research and Design for Engineering Systems*. pp. 183–194.
- Dillingham, G.L. (United S.G.A.O., 2014. *Impact of Fuel Price Increases on the Aviation Industry*,
- DuPont, 2002. Vespel S Line Design Handbook.
- ESDU 87007, 2010. Design and Material Selection For Dry Rubbing Bearings ESDU 87007. In *ESDU Tribology Series*. London: IHS Inc.
- Evans, D.C., 1981. Self-lubricating Bearings. , 1(August), pp.132–138.
- Fabre, C., Balay, J.M. & Mazars, A., 2004. A380 Pavement Experimental Programme / Rigid Phase. In *2004 FAA Worldwide Airport Technology Transfer Conference*. Atlantic City: FAA, pp. 1–22.
- Fusaro, R.L., 1990. Self-lubricating polymer composites and polymer transfer film lubrication for space applications. *Tribology International*, 23(2), pp.105-122.
- Gander, W. & Hrebicek, J., 2012. *Solving Problems in Scientific Computing Using MAPLE and MATLAB*, Berlin: Springer-Verlag.
- Gawarkiewicz, R. & Wasilczuk, M., 2007. Wear measurements of self-lubricating bearing materials in small oscillatory movement. *Wear*, 263(1–6 SPEC. ISS.), pp.458–462.
- Gay, R., 2013. *Friction and wear behaviour of self lubricating bearing liners*. Cardiff University.
- GGB, 2009. Filament Wound High Load Self-lubricating Bearings.
- Glaeser, W.A. & Dufrane, K.F., 1976. Performance of Heavily-Loaded Oscillatory Journal Bearing. *ASLE Transactions*, 20(4), pp.309–314.
- Godet, M., Play, D. & Berthe, D., 1980. An attempt to provide a unified treatment of tribology through load carrying capacity, transport, and continuum mechanics. *Journal of Lubrication Technology*, 102(1), pp.153-164.
- Godfrey, D., 1964. Friction of Greases and Grease Components during Boundary Lubrication. *ASLE Transactions*, 7(1), pp.24–31.
- Goldsmith, W., 1960. *Impact, The Theory and Physical Behaviour of Colliding Solids*, London, England: Edward Arnold Ltd.
- Goodman, L.E. & Keer, L.M., 1964. The Contact Stress Problem for an Elastic Sphere Indenting an Elastic Layer. *Journal of Applied Mechanics*, 31(1), p.143.
- Hinson, D.R., 1993. National Transportation Safety Board Safety Recommendation. *National Transportation Safety Board*, pp.1–6.

- Hirayama, T., Yamaguchi, N., Sakai, S., Hishida, N., Matsuoka, T. & Yabe, H., 2009. Optimization of groove dimensions in herringbone-grooved journal bearings for improved repeatable run-out characteristics. *Tribology International*, 42(5), pp.675–681.
- Holligan, P.T., 1968. Plastic Bearing Materials. *Tribology*, (August).
- Hooke, C.J., Kukureka, S.N., Liao, P., Rao, M. & Chen, Y.K., 1996. The friction and wear of polymers in non-conformal contacts. *Wear*, 200(1–2), pp.83–94.
- Horth, A.C., 1968. Friction Reduction with Greases. *NLGI Spokesman*, (32), pp.155–161.
- Hunt, K.H. & Crossley, F.R.E., 1975. Coefficient of Restitution Interpreted as Damping in Vibroimpact. *Journal of Applied Mechanics*, 42(2), p.440.
- Johnson, K.L., 1997. Adhesion and friction between a smooth elastic spherical asperity and a plane surface. , pp.163–179.
- Johnson, K.L. 1994. *Contact Mechanics*, Cambridge, England: Cambridge University Press.
- Johnson, K.L., 1982. One Hundred Years of Hertz Contact. In *Proceedings Institution of Mechanical Engineers*. Cambridge: SAGE, pp. 363–378.
- Kamatics, 2010. Karon B Material Data Sheet.
- Kamatics, Miscellaneous Karon Information/Data.
- Kawabata, N., Ozawa, Y., Kamaya, S. & Miyake, Y., 1989. Static Characteristics of the Regular and Reversible Rotation Type Herringbone Grooved Journal Bearing. *Journal of Tribology*, 111(3), p.484.
- Kennedy, F.E., Smidhammar, L. & Play, D., 1985. Wear of polyethylene in small-amplitude oscillatory motion. *EUROTRIB*, 2, p.5.
- Khapane, P.D., 2003. Simulation of asymmetric landing and typical ground maneuvers for large transport aircraft. *Aerospace Science and Technology*, 7(8), pp.611–619.
- Kirk, C.L., 1973. Analysis of Taxiing Induced Vibrations in Aircraft by the Power Spectral Density Method., (15).
- Krabacher, W.E., 1995. A Review of Aircraft Landing Gear Dynamics. In *The Design, Qualification and Maintenance of Vibration-Free Landing Gear*. Banff.
- Krauss, A., 1995. *Technical Evaluation Report*,
- Krüger, W., 2001. Integrated design process for the development of semi-active landing gears for transport aircraft. *D L R - Forschungsberichte*, (27), pp.6–126.
- Lancaster, J.K., 1971. Estimation of the limiting PV relationships for thermoplastic bearing materials. *Tribology*, 4(2), pp.82–86.
- Lancaster, J.K., 1972a. Lubrication of carbon fibre-reinforced polymers: Part II- Organic fluids. *Wear*, 20, pp.335–351.
- Lancaster, J.K., 1972b. Polymer-based bearing materials. The role of fillers and fibre reinforcement. *Tribology*, 5(6), pp.249–255.

- Lankarani, H.M. & Nikravesh, P.E., 1994. Continuous Contact Force Models for Impact Analysis in Multibody Systems. *Nonlinear Dynamics*, 5(2), pp. 193-207.
- Lee, E.H. & Radok, J.M., 1960. The Contact Problem for Visoelastic Bodies. *ASME. Journal of Applied Mechanics*, 3(27), pp.438-444.
- Lee, J.J., Lukachko, S.P., Waitz, I.A. & Schafer, A., 2001. Historical and Future Trends in Aircraft Performance, Cost, and Emissions. *Annual Reviews Energy Environment*, (26), pp.167–200.
- Ligterink, D.J. & de Gee, A.W.J., 1996. Measurement of wear in radial journal bearings. *Tribotest*, (September), pp.45–54.
- Lim, C.T. & Stronge, W.J., 1999. Oblique elastic-plastic impact between rough cylinders in plain strain. *International Journal of Engineering Science*, 37(1), pp.97-122.
- Lu, X. & Khonsari, M.M., 2007a. An experimental investigation of dimple effect on the stribeck curve of journal bearings. *Tribology Letters*, 27(2), pp.169–176.
- Lu, X. & Khonsari, M.M., 2007b. An Experimental Investigation of Grease-Lubricated Journal Bearings. *Journal of Tribology*, 129(1), p.84.
- Lu, Z. & McKellop, H., 1997. Frictional heating of bearing materials tested in a hip joint wear simulator. *Proceedings of the Institution of Mechanical Engineers. Part H, Journal of engineering in medicine*, 211(1), pp.101–108.
- McCarthy, R.F.J., Haines, G.H. & Newley, R. a., 1994. Polymer composite applications to aerospace equipment. *Composites Manufacturing*, 5(2), pp.83–93.
- Merzbach, U.C. & Boyer, C.B., 2011. *A History of Mathematics* 3rd ed., John Wiley & Sons, Inc.
- Mindlin, R.D. & Deresiewicz, H., 1953. *Journal of Applied Mechanics*, 75.
- MOOG, 2014. Servo Valves Pilot Operated Flow Control Valve With Analog Interface 730 Series., (F).
- Mota, V. & Ferreira, L. a., 2009. Influence of grease composition on rolling contact wear: Experimental study. *Tribology International*, 42(4), pp.569–574.
- Muijderman, E.A., 1979. Grease-lubricated spiral groove bearings. , (June), pp.131–137.
- Mullet, G.W., 1973. Grease lubrication of rolling bearings. *Critical Reviews in Tribology* 1970, 1(4), p.351.
- Neale, M.J., 2013. *Bearings: A Tribology Handbook* Revised., Elsevier.
- Noble, B. & Hussain, M.A., 1969. Exact solution of certain dual series of indentation and inclusion problems. *International Journal of Engineering Science*, 7, pp.1149–1161.
- Parr, A., 2011. *Hydraulics and Pneumatics. A technician's and engineer's guide* 3rd ed., Milton Keynes: Elsevier B.V.
- Pereira, C.M., Ramalho, A.L. & Ambrósio, J. a., 2011. A critical overview of internal and external cylinder contact force models. *Nonlinear Dynamics*, 63(4), pp.681–697.

- Persson, A., 1964. *On the stress distribution of cylindrical elastic bodies in contact*. Chalmers Tekniska Hogskola.
- Pettersson, U. & Jacobson, S., 2003. Influence of surface texture on boundary lubricated sliding contacts. *Tribology International*, 36(11), pp.857–864.
- Pfestorf, H., Weiss, F., Matucha, K. H. and Wincierz, P. 2000. Bearing Materials. Ullmann's Encyclopedia of Industrial Chemistry.
- Pinchbeck, P.H., 1961. A Review of Plastic Bearings. *Wear*, 5(12), pp.85–113.
- Play, D., 1985. Mutual Overlap Coefficient and Wear debris Motion in Dry Oscillating Friction and Wear tests. *American Society of Lubrication Engineers Transactions*, 28, pp.527-535.
- Play, D. & Godet, M. 1977. Design of high performance dry bearings. *Wear*, 41(1), pp.25-44.
- Prabhu, B.S., 1997. An Experimental Investigation on the Misalignment Effects in Journal Bearings. *Tribology Transactions*, 40(2), pp.235–242.
- Pratt, G., 1973. Plastics lined bearings for dry, pre-lubricated and water lubricated applications. *Tribology International*, 6(4), pp.135–139.
- Quaglini, V., Dubini, P., Ferroni, D. & Poggi, C., 2009. Influence of counterface roughness on friction properties of engineering plastics for bearing applications. *Materials and Design*, 30(5), pp.1650–1658.
- Radzimovsky, E.I., 1953. Stress Distribution and Strength Condition of Two Rolling Cylinders Pressed Together. *University of Illinois Engineering Experimental Station*, 408.
- Raymer, D.P., 1999. *Aircraft Design: A Conceptual Approach* 3rd ed. J. S. Przemieniecki, ed., Sylmar: American Institute of Aeronautics and Astronautics, Inc.
- Reinhoudt, J.P., 1970. A Grease-lubricated Hydrodynamic Bearing System for A Satellite Flywheel. *Journal American Society Lubrication Engineers*, 3(26), pp.95–100.
- Rezaei, A., Ost, W., Van Paepegem, W., De Baets, P. & Degrieck, J., 2011. Experimental study and numerical simulation of the large-scale testing of polymeric composite journal bearings: Three-dimensional and dynamic modeling. *Wear*, 270(7–8), pp.431–438.
- Ronen, A., Etsion, I. & Kligerman, Y., 2001. Friction-Reducing Surface-Texturing in Reciprocating Automotive Components. *Tribology Transactions*, 44(3), pp.359–366.
- Ruishen, L., 1989. The Analysis for dynamic response during airplane taxiing.
- Russo, M., 2013. Oil Grooves for Bronze Bushings. *National Bronze News*. Available at: <http://www.nationalbronze.com/News/410/> [Accessed August 18, 2015].
- Saint-Gobain, 2014. Product Handbook.
- Scarlett, N.A., 1996. Use of Grease in Rolling Bearings On Use of Grease in Rolling Bearings Lubricants for fluid film and hertzian contact conditions. *Proceedings of the Institution of Mechanical Engineers. Part H, Journal of engineering in medicine*, 210(4), pp.259–266.
- Schaeffler Group, 2006. *INA FAG Rolling Bearing Technical Compendium*,

- Schuller, F.T., Fleming, D.P. & Anderson, W.J., 1968. Experiments on the Stability of Water Lubricated Herringbone-Groove Journal Bearings. I - Theoretical Considerations and Clearance Effects. *National Aeronautics and Space Administration*.
- Sep, J., Pawlus, P. & Galda, L., 2013. The effect of helical groove geometry on journal abrasive wear. *Archives of Civil and Mechanical Engineering*, 13(2), pp.150–157.
- Shell, AeroShell Greases. *Premium military approved greases*.
- Silsby, N.S., 1962. An Analytical Study of Effects of Some Airplane and Landing-Gear factors on the Response to Runway Roughness with Application to Supersonic Transports. *National Aeronautics and Space Administration*.
- Sinanoğlu, C., Nair, F. & Karamiş, M.B., 2005. Effects of shaft surface texture on journal bearing pressure distribution. *Journal of Materials Processing Technology*, 168(2), pp.344–353.
- Strand, H., 2005. *Design, testing and analysis of journal bearings for construction equipment*,
- Strand, H., 2007. Journal bearing housing design-A statistical study with FEM. *Tribology International*, 40(4), pp.665–671.
- Stuart, B.H., 1998. Tribological studies of poly (ether ether ketone) blends. *Tribology International*, 31(11), pp.647–651.
- Sullivan, J.L. & Wong, L.F., 1985. Wear of aluminium bronze on steel under conditions of boundary lubrication. *Tribology International*, 18(5), pp.275–281.
- Thorp, J.M., 1982. Friction of some commercial polymer-based bearing materials against steel. *Tribology International*, 15(2), pp.69–74.
- Ugryumov, V.S. & Pedrik, B.G., 1982. Determination of Grease Replacement Periods in Hinge-Bolt Joints. *Khimiya i Tekhnologiya Topliv i Masel*, (4), pp.24–25.
- Unal, H., Mimaroglu, A., Kadioglu, U. & Ekiz, H., 2004. Sliding friction and wear behaviour of polytetrafluoroethylene and its composites under dry conditions. *Materials and Design*, 25(3), pp.239–245.
- Unal, H. & Mimaroglu, A., 2003. Friction and wear behaviour of unfilled engineering thermoplastics. *Materials and Design*, 24(3), pp.183–187.
- Unal, H., Sen, U. & Mimaroglu, A., 2004. Dry sliding wear characteristics of some industrial polymers against steel counterface. *Tribology International*, 37(9), pp.727–732.
- Ünlü, B.S., 2011. Tribological and mechanical properties of PM journal bearings. *Powder Metallurgy*, 54(3), pp.338–342.
- Ünlü, B.S. & Atik, E., 2007. Determination of friction coefficient in journal bearings. *Materials and Design*, 28(3), pp.973–977.
- Ünlü, B.S., Atik, E. & Köksal, S., 2009. Tribological properties of polymer-based journal bearings. *Materials and Design*, 30(7), pp.2618–2622.
- Ünlü, B.S., Atik, E. & Yilmaz, S.S., 2009. Tribological behaviors of polymer based journal bearings manufactured from particle reinforced bakelite composites. *Materials and Design*, 30(9), pp.3896–3899.

- Vincenti, W.G., 1994. The Retractable Airplane Landing Gear and the Northrop “ Anomaly ”: Variation-Selection and the Shaping of Technology. *Technology and Culture*, 35(1), pp.1–33.
- Wang, Y.Q. & Li, J., 1999. Sliding wear behavior and mechanism of ultra-high molecular weight polyethylene. *Materials Science and Engineering: A*, 266(1–2), pp.155–160.
- Wenger, E., 1964. Bestimmung des Lagerspiels von Kunstharzpreßstofflagern unter Berücksichtigung der Verformbarkeit des Werkstoffes. , 74, pp.1202–1212.
- Wentscher, H., Kortüm, W. & Krüger, W.R., 1995. Fuselage vibration control using semiactive front gear. *Proceedings of the 81st meeting of the AGARD SMP Panel on” The design, Qualification and Maintenance of Vibration-Free Landing Gears*, (October).
- Wilkie, J., Johnson, M. & Katebi, R., 2002. *Control Engineering an introductory course* 1st ed., New york: Palgrave.
- Williams, J., 2005. *Engineering Tribology*, Cambridge University Press.
- Wilson, W., Selecting dry rubbing bearings.
- Yousif, A.E., 1951. Rheological properties of a lubricating grease. *Journal of Colloid Science*, 6(2), pp.171–189.
- Yousif, A.E., 1983. The Tribological Characteristics of Lubricating Greases in Heavily Loaded Contacts. *Wear*, 85, pp.273–291.
- Zhang, S.W., 1998. State-of-the-art of polymer tribology. *Tribology International*, 31(1–3), pp.49–60.
- Zhejun, G., 1987. Semi-prepared airfield and design of double-action shock absorber. *Hangkong Xuebao*,, 8(12).
- Zhu, J., Pugh, S., Dwyer-Joyce, R.S., Beke, A., Cummer, G. & Ellaway, T., 2010. Experiments on the pressure distribution and frictional torque in articulating pin joints. *Proc Institute Mechanical Engineers Part J: J Engineering Tribology*, 224(J10), pp.1153–1162.
- Zhu, J., 2012. Simulation Model and Ultrasound Study for Engineering Interfaces.
- Zhu, J., Pugh, S. & Dwyer-Joyce, R.S., 2012. Model and experiments to determine lubricant film formation and frictional torque in aircraft landing gear pin joints. In *Proceedings of the Institution of Mechanical Engineers, Part J: Journal of Engineering Tribology*. Sheffield: SAGE, pp. 315–327.

# Appendix A

## Material Data Sheets

The data sheets of the four commercial bearing materials are given in this appendix, as mentioned in Section 4.1

# DuPont™ Vespel® SP-21

## POLYIMIDE ISOSTATIC SHAPES

### Typical ISO Properties

DuPont™ Vespel® SP-21 parts and shapes provide low wear and friction for bearing, thrust washers, and dynamic seals. SP-21 is a graphite-filled polymer.

*Some data presented below are based on limited production runs and are subject to revision as new knowledge and experience become available.*

Mechanical Property	Temperature	ASTM	Units	Typical Values
Tensile Strength	23 °C (73 °F) 260 °C (500 °F)	D-1708 or E8 <sup>†</sup>	MPa (kpsi)	65.5 (9.5) 37.9 (5.5)
Strain at Break	23 °C (73 °F) 260 °C (500 °F)	D-1708 or E8 <sup>†</sup>	%	4.5 3.0
Flexural Strength	23 °C (73 °F) 260 °C (500 °F)	D-790	MPa (kpsi)	110.3 (16.0) 62.0 (9.0)
Flexural Modulus	23 °C (73 °F) 260 °C (500 °F)	D-790	MPa (kpsi)	3792 (550) 2551 (370)
Compressive Stress at 1% strain at 10% strain at 0.1% offset	23 °C (73 °F) 23 °C (73 °F) 23 °C (73 °F)	D-695	MPa (kpsi)	29.0 (4.2) 133.1 (19.3) 45.5 (6.6)
Compressive Modulus	23 °C (73 °F)	D-695	MPa (kpsi)	2895 (420)
Axial Fatigue, Endurance Limit at 10 <sup>3</sup> cycles  at 10 <sup>7</sup> cycles	23 °C (73 °F) 260 °C (500 °F) 23 °C (73 °F) 260 °C (500 °F)	—	MPa (kpsi)	46.2 (6.7) 22.8 (3.3) 32.4 (4.7) 16.5 (2.4)
Flexural Fatigue, Endurance Limit at 10 <sup>3</sup> cycles at 10 <sup>7</sup> cycles	23 °C (73 °F) 23 °C (73 °F)	—	MPa (kpsi)	65.5 (9.5) 44.8 (6.5)
Shear Strength	23 °C (73 °F)	D-732	MPa (kpsi)	77.2 (11.2)
Izod Notched Impact Strength	23 °C (73 °F)	D-256	J/m	42.7
Izod Unnotched Impact Strength	23 °C (73 °F)	D-256	J/m	320
Poisson's Ratio	23 °C (73 °F)	—	—	0.41
<b>Wear and Friction</b>				
Wear Rate <sup>††</sup>	—	—	m/s x 10 <sup>-10</sup>	6.30
Friction Coefficient <sup>**</sup> PV = 0.875 MPa·m/s PV = 3.5 MPa·m/s	—	—	—	0.24 0.12
In Vacuum	—	—	—	—
Static in Air	—	—	—	0.30



The miracles of science™

DuPont™ Vespel® SP-21 Typical ISO Properties (continued)

Thermal Property	Temperature	ASTM	Units	Typical Values
Coefficient of Linear Expansion	23 °C (73 °F) to 260 °C (500 °F) -62 to +23 (-80 to 73° F)	D-696	µm/m/°C (in/in/°F)	49 (27) 34 (19)
Thermal Conductivity	40 °C (104 °F)	—	W/m·°C	0.87
Specific Heat	—	—	J/kg/°C	—
Deformation Under 14 MPa Load	50 °C (122 °F)	D-621	%	0.10
Deflection Temperature at 2 MPa	—	D-648	°C	~360
Electrical Property				
Dielectric Constant at 10 <sup>2</sup> Hz at 10 <sup>4</sup> Hz at 10 <sup>6</sup> Hz	23 °C (73 °F)	D150	—	13.53 13.28 13.41
Dissipation Factor at 10 <sup>2</sup> Hz at 10 <sup>4</sup> Hz at 10 <sup>6</sup> Hz	23 °C (73 °F)	D150	—	0.0053 0.0067 0.0106
Dielectric Strength, Short Time 2 mm Thick	23 °C (73 °F)	D149	MV/m	9.84 (1.4)
Volume Resistivity	23 °C (73 °F)	D257	Ω·m	10 <sup>12</sup> -10 <sup>13</sup>
Surface Resistivity	23 °C (73 °F)	D257	Ω	—
Other Properties				
Water Absorption 24 h 48 h Equilibrium, 50% RH	23 °C (73 °F) 50 °C (122 °F)	D570	%	0.19 0.57 0.8-1.1
Specific Gravity	—	D792	—	1.51
Oxygen Index	—	D2863	%	49

† Machined isotstic tensile specimens made per D1708

†† Unlubricated in air (PV 0.875 MPa·m/s).

\*\* Steady state, unlubricated in air.

Visit us at [kalrez.dupont.com](http://kalrez.dupont.com) or [vespel.dupont.com](http://vespel.dupont.com)

Contact DuPont at the following regional locations:

**North America**  
800-222-8377

**Latin America**  
+0800 17 17 15

**Europe, Middle East, Africa**  
+41 22 717 51 11

**Greater China**  
+86-400-8851-888

**ASEAN**  
+65-6586-3688

**Japan**  
+81-3-5521-8484

The information provided in this data sheet corresponds to our knowledge on the subject at the date of its publication. This information may be subject to revision as new knowledge and experience becomes available. The data provided fall within the normal range of product properties and relate only to the specific material designated; these data may not be valid for such material used in combination with any other materials, additives or pigments or in any process, unless expressly indicated otherwise.

The data provided should not be used to establish specification limits or used alone as the basis of design; they are not intended to substitute for any testing you may need to conduct to determine for yourself the suitability of a specific material for your particular purposes. Since DuPont cannot anticipate all variations in actual end-use and disposal conditions, DuPont does not guarantee favorable results, makes no warranties and assumes no liability in connection with any use of this information. All such information is given and accepted at the buyer's risk. It is intended for use by persons having technical skill, at their own discretion and risk. Nothing in this publication is to be considered as a license to operate under or a recommendation to infringe any patent. DuPont advises you to seek independent counsel for a freedom to practice opinion on the intended application or end-use of our products.

**CAUTION:** Do not use DuPont materials in medical applications involving implantation in the human body or contact with internal body fluids or tissues unless the material has been provided from DuPont under a written contract that is consistent with DuPont policy regarding medical applications and expressly acknowledges the contemplated use. For further information, please contact your DuPont representative. You may also request a copy of DuPont POLICY Regarding Medical Applications H-50103-4 and DuPont CAUTION Regarding Medical Applications H-50102-4.

Copyright © 2014 DuPont. The DuPont Oval Logo, DuPont™, The miracles of science™, Kalrez®, and Vespel® are trademarks or registered trademarks of E.I. du Pont de Nemours and Company or its affiliates. All rights reserved.

(09/10) Reference No. VPE-A10863-00-B0614



The miracles of science™

## Meldin® 5000 – Technical Properties

	Condition	Test Method	Units	Meldin® 5055	Meldin® 5210	Meldin® 5301	Meldin® 5302	Meldin® 5320	Meldin® 5330	Meldin® 5350	Meldin® 5390	Meldin® 5530
<b>Mechanical Properties</b>												
Tensile Strength	Yield RT	ASTM D638	psi (MPa)			14,000 (97)	17,000 (117)					
Tensile Strength	Break RT	ASTM D638	psi (MPa)	16,300 (112)	10,200 (70)		17,000 (117)	24,000 (166)	33,000 (228)	20,000 (138)	20,500 (141)	24,700 (170)
Tensile Strength	Break 480°F (249°C)	ASTM D638	psi (MPa)		1,400 (10)			3,600 (25)	5,100 (35)	4,800 (33)	5,700 (39)***	7,100 (49)
Tensile Elongation	RT	ASTM D638	%	1.2	6.6	65	20	2.1	2	2.2	1.9	1.9
Tensile Modulus	RT	ASTM D638	psi*10 <sup>5</sup> (GPa)	23 (15.9)	4.6 (3.2)	5.1 (3.5)	6.4 (4.4)	14 (9.7)	32 (22.3)	14.7 (10.1)	20.3 (14)	26 (18)
Flexural Strength	RT	ASTM D790	psi (MPa)	26,400 (182)	16,800 (123)*	22,600 (156)	26,400 (182)	33,500 (231)	48,000 (331)	30,600 (211)	31,000 (214)	34,800 (240)
Flexural Strength	480°F (249°C)	ASTM D790	psi (MPa)	2,600 (18)	1,200 (8)*	1,000 (7)		4,100 (28)	5,100 (35)	4,800 (33)	5,800 (40)*	6,500 (45)
Flexural Modulus	RT	ASTM D790	psi*10 <sup>5</sup> (GPa)	21.2 (14.5)	4.6 (3.2)	6 (4.1)	6.7 (4.6)	14.5 (10)	27.6 (19)	13.8 (9.5)	17.7 (12.2)	24.7 (17)
Compressive Strength	RT	ASTM D695	psi (MPa)	18,000 (124)	15,700 (108)**	17,200 (119)		31,200 (215)	34,800 (240)	21,700 (150)	22,900 (158)**	25,500 (176)
Compressive Strength	392°F (200°C)	ASTM D695	psi (MPa)		2,300 (16)****	9,700 (67)		4,300 (30)	3,600 (25)		3,800 (26)****	5,100 (35)
Compressive Modulus	RT	ASTM D695	psi*10 <sup>5</sup> (GPa)	4.5 (3.1)	4.2 (2.9)		5.1 (3.5)				10.4 (7.1)	
<b>Thermal Properties</b>												
Melting Point		ASTM D3418	°F (°C)	650 (343)	650 (343)	650 (343)	707 (375)	650 (343)	650 (343)	650 (343)	651 (343)	650 (343)
Glass Transition T <sub>g</sub>	Onset	ASTM D3418	°F (°C)	290 (143)	290 (143)	290 (143)	320 (160)	290 (143)	290 (143)	290 (143)	290 (143)	290 (143)
Coefficient of Thermal Expansion	Along Flow < T <sub>g</sub>	ASTM E831	in/in/°F (m/m/°C) x 10 <sup>-5</sup>	1.8 (3.3)		2.5 (4.5)	2.8 (5)	1 (1.8)	0.8 (1.4)	0.84 (1.5)		0.7 (1.2)
Coefficient of Thermal Expansion	Along Flow > T <sub>g</sub>	ASTM E831	in/in/°F (m/m/°C) x 10 <sup>-5</sup>	2.1 (3.8)		6.7 (12)		1 (1.8)	0.8 (1.4)	0.84 (1.5)		0.7 (1.2)
Coefficient of Thermal Expansion	Average < T <sub>g</sub>	ASTM E831	in/in/°F (m/m/°C) x 10 <sup>-5</sup>	2.3 (4.1)		3.1 (5.5)	3.4 (6)	2.5 (4.5)	2.2 (4)	2.5 (4.5)		2 (3.5)
Coefficient of Thermal Expansion	Average > T <sub>g</sub>	ASTM E831	in/in/°F (m/m/°C) x 10 <sup>-5</sup>	2.8 (5)		7.8 (14)		6.2 (11)	5.6 (10)	6.2 (11)		5 (9)
Heat Deflection Temperature		ASTM D648	°F (°C)	600 (316)		305 (152)		617 (325)	626 (330)	600 (316)		626 (330)
Thermal Conductivity	RT	ASTM F433	BTU in/hr ft <sup>2</sup> (W/m°C)	5.3 (0.76)		2 (0.29)		2.1 (0.3)	6.6 (0.95)	6.1 (0.87)		9.1 (1.3)
<b>Electrical Properties</b>												
Dielectric Strength	2.5 mm thickness	ASTM D149	V/mil (kV/mm)			407 (16)		510 (20)				
Dielectric Constant	RT, 1 kHz	ASTM D150				3.1		3.2				
Volume Resistivity	RT	ASTM D257	Ohm*cm			10 <sup>16</sup>		10 <sup>16</sup>	10 <sup>5</sup>	10 <sup>10</sup>		10 <sup>6</sup>
<b>General Properties</b>												
Specific Gravity	RT	ASTM D792		1.4	1.36	1.3	1.31	1.51	1.4	1.45	1.45	1.44
Water Absorption	RT, 24h	ASTM D570	%	0.2	0.17	0.5		0.11	0.06	0.06	0.06	

Data reported are typical of grades processed by injection molding

\*Value reported at 5% strain if strain exceeded 5% per ASTM D790

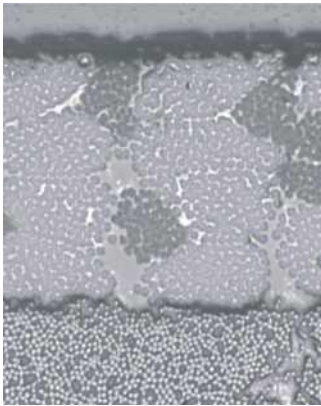
\*\*2% offset yield stress reported if no peak stress observed

\*\*\*Data obtained at 235°C

\*\*\*\*Data obtained at 249°C, 2% offset yield stress reported if no peak stress observed

## 2.0 Product Descriptions

### GAR-MAX®



Sliding layer -  
Continuous wound PTFE and  
high-strength fibers encapsulated  
in an internally lubricated, high  
temperature filled epoxy resin.

Backing -  
Continuous wound fiberglass  
encapsulated in a high  
temperature epoxy resin.



CHARACTERISTICS	POSSIBLE APPLICATIONS	AVAILABILITY
<ul style="list-style-type: none"> <li>• High load capacity</li> <li>• Excellent shock and misalignment resistance</li> <li>• Excellent contamination resistance</li> <li>• Very good friction and wear properties</li> <li>• Good chemical resistance</li> </ul>	<ul style="list-style-type: none"> <li>• Steering linkages</li> <li>• Hydraulic cylinder pivots</li> <li>• King pin bearings</li> <li>• Boom lifts, scissor lifts</li> <li>• Cranes, hoists, lift gates</li> <li>• Backhoes, trenchers</li> <li>• Skid steer loaders</li> <li>• Front end loaders</li> </ul>	<p>Standard Plain cylindrical bushes Inner diameter range: Metric: 12 - 150 mm Standard: 1/2 - 6"</p> <p>Special order Plain cylindrical bushes Inner diameter range: Metric: 10 - 500 mm Standard: 3/8 - 20"</p> <p>Customized bushing designs. Cylindrical bushes with non-standard lengths and wall thickness, flanged bearings, hexagonal and square bores, liner on outer diameter.</p>

BEARING PROPERTIES	METRIC	IMPERIAL
Ultimate compressive strength $\sigma_c$	414 N/mm <sup>2</sup>	60 000 psi
Maximum static load $p_{sta,max}$	210 N/mm <sup>2</sup>	30 000 psi
Maximum dynamic load $p_{dyn,max}$	140 N/mm <sup>2</sup>	20 000 psi
Maximum sliding speed U	0.13 m/s	25 fpm
Maximum pU factor	1.05 N/mm <sup>2</sup> x m/s	30 000 psi x fpm
Maximum temperature $T_{max}$	160 °C	320 °F
Minimum temperature $T_{min}$	- 195 °C	- 320 °F

## **KAron B Data Self-Lubricating Liner Material**

### **1. Characteristics:**

- 1.1. Nominal liner thickness: .010 to .015 in. (.25 to .38 mm), Max thickness .060 in. (1.52 mm)
- 1.2. Operating temperature range: -100° F to +450°F (-73 to +232°C)
- 1.3. Coefficient of friction range: .03 to .10, depending upon pressure, and velocity.
- 1.4. Compatible backing substrate materials: stainless steel, carbon steel, titanium, aluminum bronze, aluminum, phenolic, fiberglass, inconel and others.
- 1.5. Surface speeds to 3 fpm (0.9 m/min)

### **2. Physical Properties:**

- |                                      |                                     |
|--------------------------------------|-------------------------------------|
| 2.1. Specific gravity:               | 1.508                               |
| 2.2. Density                         | 1.505 gm/cc                         |
| 2.3. Hardness                        | Rockwell M 90/100                   |
| 2.4. Approximate Compression Modulus | 7 x 10 <sup>5</sup> psi (4,828 MPa) |

### **3. Typical Load Carrying Capabilities:**

- |                               |                       |
|-------------------------------|-----------------------|
| 3.1. Static Ultimate *        | 120,000 psi (827 MPa) |
| 3.2. Static Limit **          | 80,000 psi (551 MPa)  |
| 3.3. Dynamic (max.)           | 50,000 psi (344 MPa)  |
| 3.4. Dynamic (continuous) *** | 35,000 psi (241 MPa)  |

Notes: \* Equivalent to 1.5 times the static limit load, local liner distress may occur.

\*\* Maximum load which will result in a permanent set in the liner no greater than .003 (0.08mm) inches after the load is applied for 3 minutes.

\*\*\* .0045 inches (0.114 mm) maximum permitted wear after 25,000 cycles of oscillation at ± 25° at 10 cpm (8 rms mating surface, R<sub>c</sub>50 min.).  
Typical liner thickness 0.012 in. (0.3 mm).

### **4. Applicable Specifications:**

- 4.1 SAE AS-81820 – Bearings, plain, self-aligning, self-lubricating, low speed oscillation. (MS14101, MS14102, MS14103 & MS14104), (Kamatics KR-CNB, KR-CNGB, KR-CWB, KR-CWGB).
- 4.2 SAE AS-81934 – Bearings, sleeve, plain and flanged, self-lubricating (AS-81934/1-plain, AS-81934/2-flanged) (Kamatics KRJ-B & KRJ-USB).

### **5. Typical Applications:**

- 5.1. Airframe controls, flaps, etc., industrial applications requiring high load carrying capability and self-lubricating features.
- 5.2. The above information is to be considered as a guide only. Kamatics Corporation Engineering should be consulted for proposed applications.

# Appendix B

## Radially Loaded Pin Joint

Additional information is provided in this appendix, such as the two additional load distribution plots for Vespel 21 and KArOn B. Additionally consideration is given briefly to the element of creep occurring in each of the materials tested over a 70 Hour period.

## B1. Load Profiles

Load profiles were conducted for Vespel 21 and Karon B at the same time and in the same manner as described in section 6.4. The findings given in section 5.2.1. show that the simulation did not accurately predict the displacement for Vespel 21 and Karon B, therefore using the predicted displacement to calculate the arc of contact would have introduced a significant error.

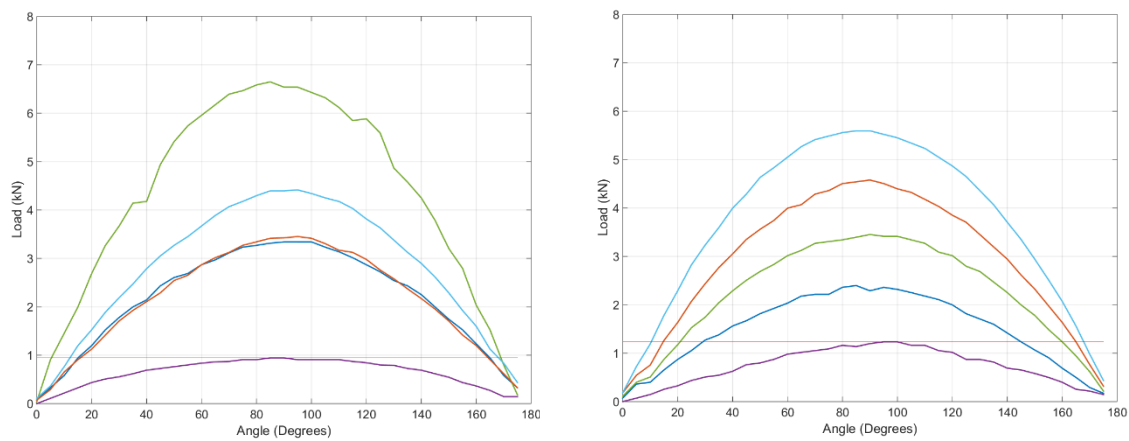


Figure B.1: Load distribution plot, recorded with the load pin for Vespel 21 (left), Karon B (right)

## B2. Creep

Given the nature of the polymer materials, consideration must be given to creep of the materials. While this was not the main focus of the project investigation into how each material responded under an applied static load. Each material was fitted into the radial load test clevis, and mounted on a deadweight machine with a static load of 38 kN. A dial test indicator was positioned between the two halves of the clevis and time lapse camera set to photograph the dial test indicator every hour, for 70 hours. Figure B2 shows the results. It can be seen that Gar-Max, Meldin 5330 and Karon B showed no change in the 70 hour period. Vespel 21 however shows an initial change in the first few hours, and then another change at the 10 hour mark. It is predicted that the two step behaviour of Vespel 21 is the change for the bushes in each half of the test head, with the different contact areas causing the different rates of creep. Loading of the joint was completed prior to measurements being taken.

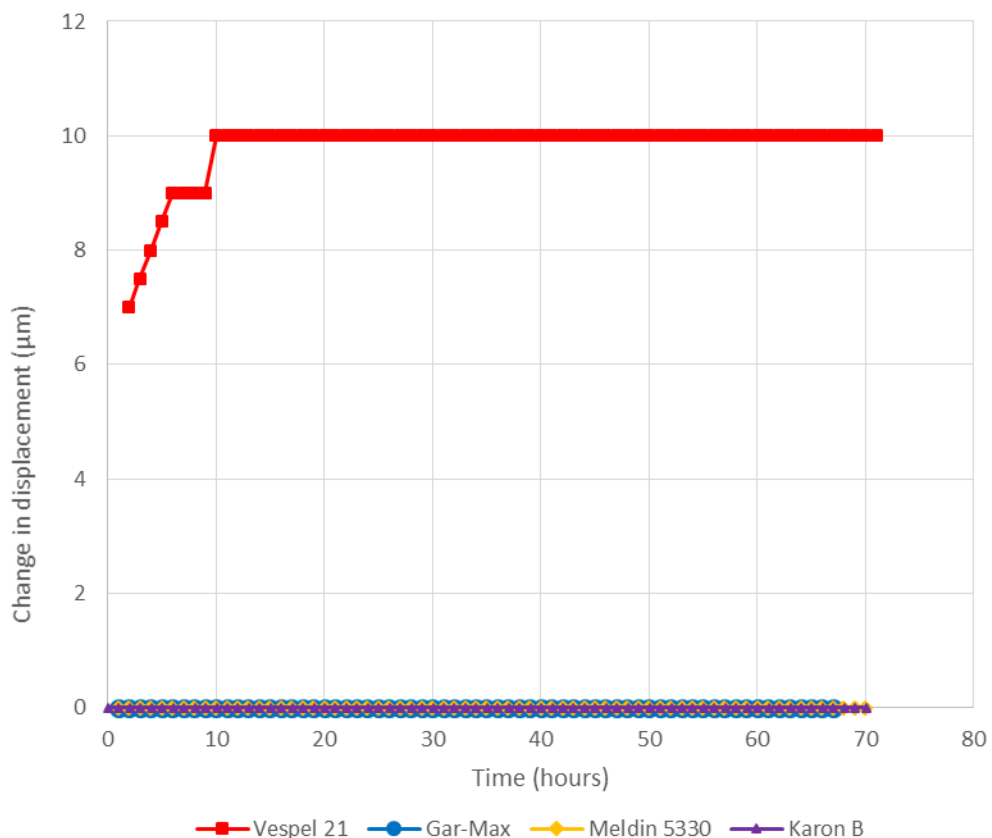


Figure B.2: Change in displacement for each material under an applied static load of 38 kN

[Blank Page]

# Appendix C

## Grease Lubricated Testing

Additional information is provided here detailing the results for each of the three repeats conducted for Mobil 28 when investigating the effect of articulation angle on the co-efficient of friction. Further information is given regarding the pressure required to inject fresh grease into the joint for both Mobil 28 and Shell Alania. Finally details are given for how the number of cycles oscillated effects the grease temperature.

## C1. Articulation angle Mobil 28 Running in

Figures C1 to C3 show the Mobil 28 lubricated aluminium bronze bearing running in. It can be seen for each test that the average value is around the same magnitude of 0.155. However for the lower sliding velocities there is a growing divergence between the angles of articulation. The averaged graph is shown in Figure 7.9 section 7.5.1.

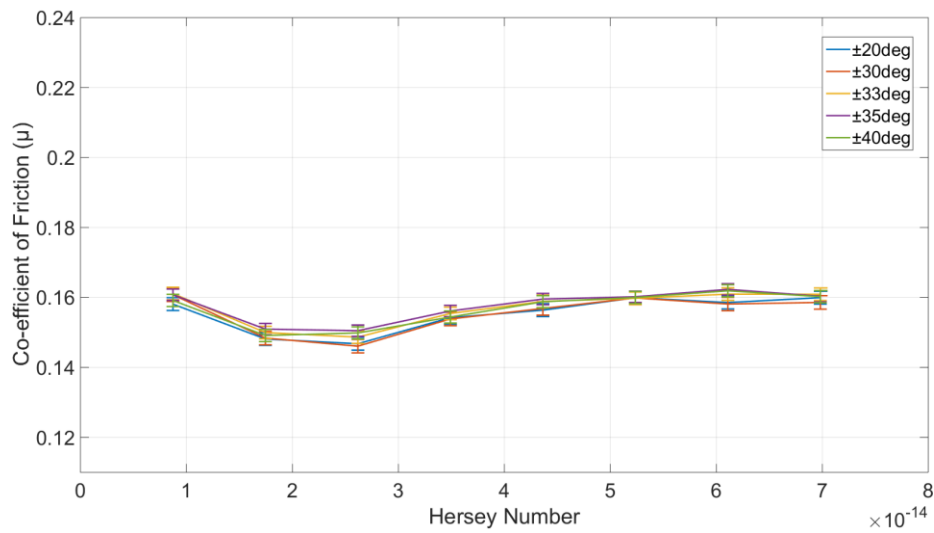


Figure C.1: Stribeck curve Mobil 28 test 1 20MPa

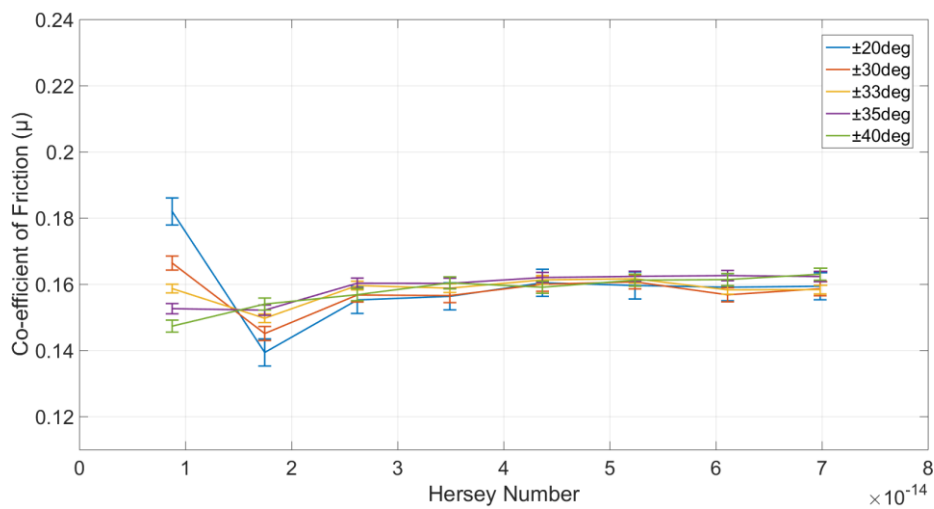


Figure C.2: Stribeck curve Mobil 28 test 2 20MPa

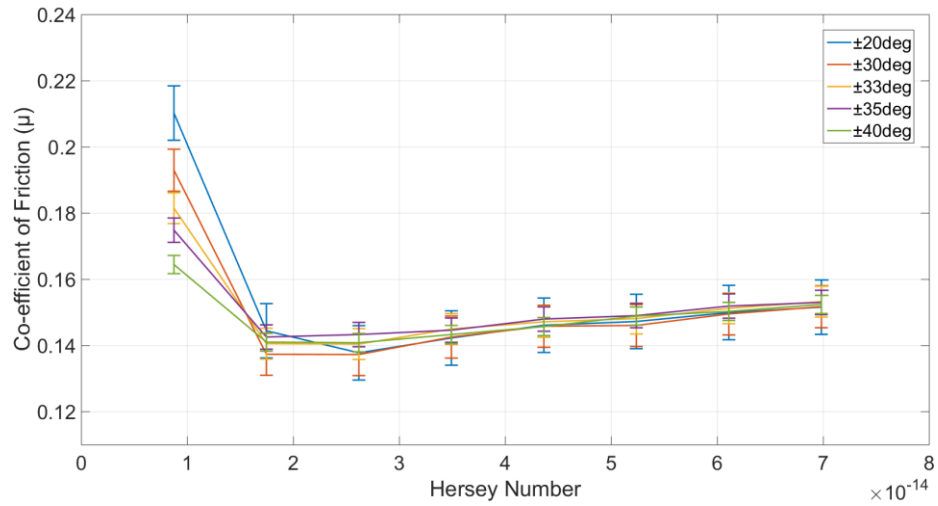


Figure C.3: Stribeck curve Mobil 28 test 3 20MPa

The co-efficient of friction for  $\pm 20^{\circ}$  case is higher than all the other articulation angles in the second and third repeats. For these two repeats, it can be seen that as the angle of articulation grows to  $\pm 30^{\circ}$ ,  $\pm 33^{\circ}$ ,  $\pm 35^{\circ}$  and then  $\pm 40^{\circ}$  the co-efficient of friction was seen to reduce. This effect was observed most obviously for the last repeat, where there was a significant difference at the lowest sliding velocity for the  $\pm 20^{\circ}$  and  $\pm 40^{\circ}$  cases.

## C2. Grease Pressure

Figure C.4 shows the pressure required to re-lubricate the joint with respect to time during section 7.5.2. It can be seen that for Mobil 28, the pressure requirement was significantly lower than that of Shell Alvania. Additionally the individual injections from the grease gun can be identified, two for Mobil 28 and three for Shell Alvania. An extra injection was required for grease to escape from the bearing, and to remove the dis-coloured grease. The same process was followed for Mobil 28, however fresh grease was ejected from the bearing after only two injections. The pressure in the system once the joint had been re-lubricated can be seen to be higher than the initial, reducing with time, indicating that the grease was supporting a part of the loaded pin joint.

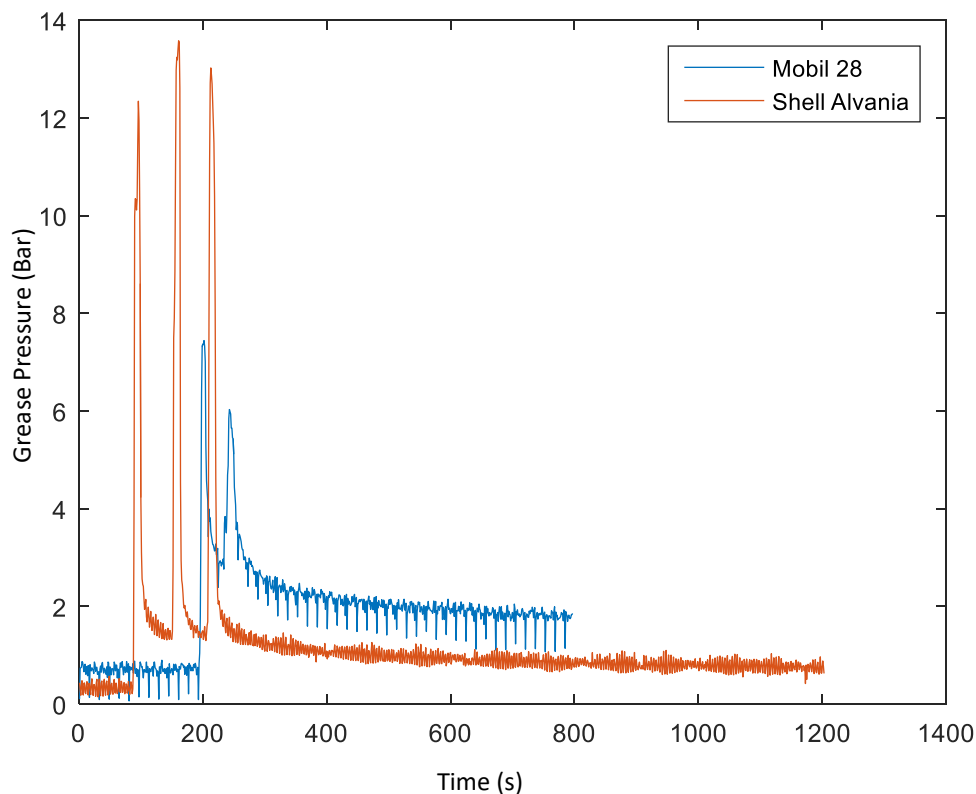


Figure C.4: Example plot of the pressure required to re-lubricate the joint with a bearing pressure of 20 MPa, for the two greases tested Shell Alvania and Mobil 28

### C3. Grease Temperature

Given the significance that heating effects can have on an articulating pin joint. When conducting experiments on the number of cycles for the re-lubrication interval testing particular attention was given to the temperature of the joint, in particular the temperature of the grease in the joint. Figure C5 shows the increase in temperature with the duration of testing. It can be seen that the rate of which the temperature increases is the same for all the tests conducted. The offset in temperature is as a result of the laboratory room temperature and the length of time that the chiller unit had been running, either with or without a test in progress. For 0-1500 cycles, testing commenced when the chiller had been running, without a test running hence the low starting temperature of the test.

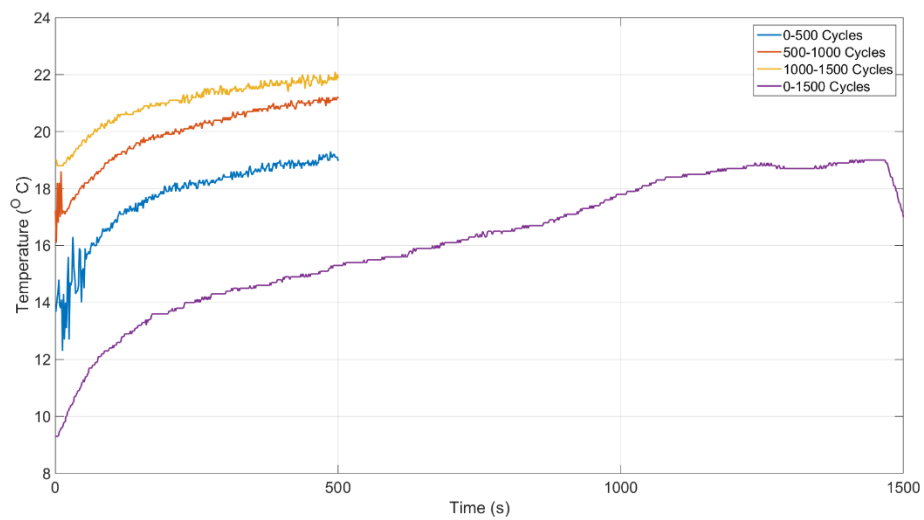


Figure C.5: Grease temperature for the number of cycles re-lubrication test (Figure 7.14, Section 7.5.3)